SAPIENZA
UNIVERSITÀ DI ROMA

Energy Dissipation in Suspended Microchannel Resonators: theoretical, numerical and experimental validation

Facoltà di Ingegneria Civile e Industriale
Corso di laurea in Ingegneria Meccanica

Supervisor
Prof. Giuseppe Ruta

Co-supervisor
Prof. Daniele Andreucci

External supervisors
Prof. Sandro Carrara (EPFL)
Prof. Luis Guillermo Villanueva (EPFL)
Ph.D. Annalisa De Pastina (EPFL)

Candidate
Andrea Gerbino
1551668

A/A 2016/2017

Tesi discussa il 22 Gennaio 2018
di fronte a una commissione esaminatrice composta da:

Prof. Enrico Sciubba (presidente)

Prof. Roberto Capata

Prof. Alessandro Corsini

Prof. Giovanni Delibra

Prof. Leone Martellucci

Prof. Giuseppe Ruta

Prof.ssa Claudia Toro

Energy Dissipation in Suspended Microchannel Resonators: theoretical, numerical and experimental validation

Tesi di Laurea Magistrale. Sapienza – Università di Roma

Questa tesi è stata composta con LaTeX e la classe Sapthesis.

Versione: 20 gennaio 2018

Email dell'autore: andreagerbino@gmail.com

To Family,

Friendship,

Love,

Nature.

A G

"Laudato si', mi' Signore, per sora nostra matre Terra, la quale ne sustenta e governa, e produce diversi frutti con coloriti fiori et herba"

San Francesco D'Assisi

Summary

Suspended Microchannel Resonators (SMRs) are hollow resonant structures containing an embedded U-shaped microfluidic channel. This configuration reduces the losses due to the damping caused by the fluid, which are deleterious for the quality factor in traditional solid resonators immersed in fluid. As bio-sensors, SMRs enable real time detection of liquid compounds, by added mass resonance frequency shift, with very high quality factors, and weighing of nanoparticles, bacterial cells and single bacterial cells and sub-monolayers of adsorbed proteins in water with sub-femtogram resolution. Theoretical and experimental results have proved that in these devices the energy dissipation is a non-monotonic function of the fluid viscosity (or Reynolds number), while in conventional cantilevers it always increases with the viscosity as the damping from the fluid on the solid structure increases. Furthermore, a variation in the device quality factor by several orders of magnitude was discovered when the microfluidic channel axis was placed away from the beam neutral axis, which is expected to happen always for fabrication limits, and a change in the behaviour of the Quality Factor Q at high viscosities was noticed when varying fluid compressibility.

The author would like to declare that this project has been carried out during a six months long experience at the École polytechnique fédérale de Lausanne, thanks to a collaboration between the Advanced NanoElectroMechanical Systems Laboratory and the Integrated Systems Laboratory of EPFL. Thus, the author had the chance to include in his Master of Science experience several secondary activities such as:

- joining an international environment, being constantly supervised and helped by Professors and PhD students;
- attending weekly group meetings;
- getting to know about the nowadays research interests in the field of nano-sized resonators;

- attending a compulsory course to access the EPFL Cleanroom;
- attending a course of French language (level A2/B1).

In this project, both a Mathematica (release 10.4) code and a 3D COMSOL (release 5.3) model are produced to validate the theoretical and experimental results on the energy dissipation in these devices [32]. To reduce the computational effort an eigenvalue study is performed. The incompressible and compressible cases are investigated while changing the fluid and device characteristics. The effects of the rigid lead channel length have been studied and some differences have been found with respect to the reference paper [32]. Importantly, numerical results seem to match quite well with the theoretical results everywhere but at high viscosities, while a slightly bigger difference exists between numerical and experimental results. Our numerical model works fine where the experimental data are provided but it is in contrast with the theoretical model at low Reynolds number. We consider it valid in the region of interest and send to further investigation the difference at low β between theory and numerics. Throughout the work some improvements to the theoretical model have been proposed as a few mistakes were proved to exist in the equations developed in [32].

The student's main tasks are here summed up:

- Reviewing and understanding the state of the art of energy dissipation in hollow beam resonators;
- Analytically proving and coding in Mathematica (release 10.4) the theoretical model proposed by Sader[32];
- Developing a 3D COMSOL model to compare experimental [33], theoretical [32] and numerical results;
- Taking part to some experimental sessions in the ANEMS Laboratory of the EPFL.

Finally, an Abstract and a Poster on this work have been accepted by the 1^{st} International Workshop on Nanofluidics and Nanomechanics, held in Turin on 14^{th}-15^{th} September 2017.

Acknowledgments

These pages humbly contain and express the experience and all the skills that five years of University with Sacrifice left to me; application of all the teachings was my main goal, by emulation of what I was taught I tried to achieve as amazing results as those which shook my Soul as a Student. This text reflects my 24-years-old sensitivity, in the Resonating Emotive period of my life; when, aged, I read these pages again, my heart will Vibrate and bring me back to these days of Satisfaction. I owe these joyful moments to all those who spent time to answer my uncountable Questions; among these, I consider the two best Professors of my life my Mum and my Dad, who motivated and always supported me; to them I owe possibilities and self-belief, the love for internationality and adventure. I thank them for what I am today and what I have been given.

Desidero donare dei pensieri, frutto di un percorso personale realizzato nel tempo, scritti ogni volta che, pensandovi, ho percepito tutt'a un tratto una sensazione che mi ha mostrato ciò che chi mi è caro rappresenta per me.

Ti ringrazio, Mamma, per l'Amore di cui mi nutri, donandomi possibilità senza pretese. Di te desidero portare in me la Determinazione e la Forza con cui si realizzano opere che soddisfano l'Animo.

Ti ringrazio, Papà, per le Opportunità che sempre mi doni e per il modo in cui sostieni la mia Intelligenza e le mie Capacità. Il modo in cui mi accompagni mi dona Sicurezza e mi aiuta a scegliere. Di te desidero portare in me la Semplicità dei Bambini.

Ti ringrazio, Francesco, per la Pazienza con cui mi sei Fratello Maggiore: di te desidero portare in me l'Equilibrio.

In me, Ammiri Tanto Orgogliosamente Molti Ideali, Giorgia, e sostieni e stimoli la mia Creatività e il mio Pensiero. Con te e con la Compagnia dei Giallo Canarino realizzo l'Arte ed esprimo Gioia:

insieme, tra le risate, produciamo l'Irrazionale.

Ringrazio i miei amici di sempre, Daniele, Federico, Mattia, Andrea amico del Pelide, Alice, Lorenzo, Giulia, Matteo, Francesca, Giulia, Luca e Alessandro per le risate in compagnia. *On ne voit bien qu'avec le coeur. L'essentiel est invisible pour les yeux.*

Ringrazio la Famiglia dell'Oratorio, che costantemente mi protegge col suo abbraccio, e soprattutto Andrea, con cui condivido Genio e Sregolatezza.

Ringrazio le Famiglie Gerbino e Franchini: un Ringraziamento speciale va ai miei Zii Luisa e Bruno, per i quali io e Francesco fummo "primi nipoti" e sempre si interessano a noi, e a mio cugino Lorenzo, le cui storie da tutto il Mondo incrementano la mia sete d'Avventura.

Ti ringrazio, Moreno, per essermi Maestro di Matematica. Grazie a te ora vedo in essa il Modello Perfetto di un Mondo Armonicamente Imperfetto, strumento di comunicazione tra l'Uomo e la Natura.

Ringrazio Elvira e Carmen per avermi sempre fatto sentire capace di tutto. E' questo forse lo stimolo più importante che spinge un Uomo a Camminare.

Ringrazio i miei Amici dell'Università, ai quali devo gran parte dell'obiettivo raggiunto e la serenità di questo percorso: a Edoardo, Francesco, Dario, Marco, Alessandro, Isabella, Chiara, Silvia, Federico, Matteo, Valeria, Christian, Giuseppe ed Edoardo ricordo che la soddisfazione si valuta con una scala di misura personale costruita sulla base delle proprie ambizioni. Sapere Aude!

I thank my Spanish friend Álvaro, who I consider incredibly wise, skilled and surely an example of Eclecticism. He is an excellent Thinker and Listener, an enjoyable person to share true Friendship with.

In the last two years I have had the chance to experience Erasmus twice. The people I met in Delft and in Lausanne shared with me Cultures, Ideas, Lives. Angel, Michaela, Francisco, Will, Matthew, Raphael, Ricardo, Nacho, Enrique, Filipe, José, Afonso, Andrea, Saverio, Livio, Alessandro, Francesca, Federico, Daniele, Natalia, Andrea, Roberto, Guillermo, An, Mauricio, Damien, Will, Chiara, Arianna, Xavier, Teo, Javi, Pawel, Elisabetta, Mariana are part of my best memories.

I will always be infinitely grateful to the people of the ANEMS laboratory in EPFL for the cheerful environment where I could carry out this thesis: I thank Prof. Guillermo Villanueva, Prof. Sandro

Carrara, Prof. François Gallaire and Ph.D. Annalisa De Pastina for their collaboration and the opportunity they gave me to prove my "Quality Factor". Guillermo and Annalisa stimulated me to improve my understanding of SMRs and taught me how to discuss on results professionally; our weekly meetings were instructive and always managed to get a smile from me.
To them I remind that *"Ma il cielo è sempre più blu"*.

Ringrazio, infine, il mio Relatore Prof. Giuseppe Ruta e il mio Correlatore Prof. Daniele Andreucci, della cui Sapienza ho potuto fruire in questi anni, crescendo intellettualmente e sviluppando una metodologia di cui sono fiero. La loro Professionalità è stato un grande stimolo a migliorarmi. *Magister interrogantibus libenter respondeat, non interrogantes percontetur ultro.*

Contents

List of Figures

List of Tables

Chapter 1

Introduction

> "I felt it as a sensual delight that I should become one with – become this earth which is forever radiated by the sun in such a constant ferment and which lives – lives – and which will grow plants from my decaying body – trees and flowers – and the sun will warm them and I will exist in them – and nothing will perish – and that is eternity."
>
> *Edvard Munch*

Contents

This introductory chapter aims to give a general overview of this MSc project. Firstly, an overview on the Micro-NanoElectroMechanicalSystems state of the art is provided. Starting from a literature survey on the advances in the M/NEMS industry, we move on discussing the peculiarities of resonant systems.

Secondly, application of M/NEMS technology in bio-sensing is discussed, whereupon the key parameter known as quality factor is introduced and the attention is focused on the innovative microfluidic devices referred to as Suspended Microchannel Resonators (SMRs).

The last two sections have the purpose to show the aim of the study with the research goal that justifies this project and the outline of this Master Thesis project.

1.1 Literature Survey

1.1.1 MEMS and NEMS

Micro-Electro-Mechanical Systems, or MEMS, are miniaturized mechanical and electro-mechanical devices made using the techniques of microfabrication. They have been developed and broadly produced to perform specific functions, typically acting as sensors, controllers and actuators at the micro-scale, having dimensions in the range of a few to hundreds of microns [6]. Their diffusion is due as well to the versatility, good mechanical properties, low cost, biocompatibility and abundance of their main material, compatible with most batch-processed integrated circuits technologies: silicon. Therefore, the last decades have seen a boost in the use of silicon for the fabrication of miniaturized systems with moving parts. Advanced fabrication procedures, such as lithography, thin film deposition and etching, have turned MEMS into a well-established industry. Their applications span the automotive industry, communications, defence systems, national security, health care, information technology, avionics, environmental monitoring, cell weighing, mass spectrometry, magnetometry and surface science (phase transitions and diffusion). Accelerometers (for automotive airbag sensors), gyroscopes (for orientation determination in vehicles, smartphones, games consoles, etc.), inkjet printer nozzles, microphones, video projector display chips, blood pressure sensor are well-known examples of MEMS commercial products, as well as Scanning Tunneling Microscope (STM) and Atomic Force Microscope (AFM)[15] [38].

Recently, innovative manufacturing technologies and materials have enabled the scaling down of MEMS to a smaller size-domain. These sub-micron MEMS have been naturally defined NanoElectroMechanical Systems (NEMS) and allow for exploiting of MEMS aforementioned characteristics at a higher level, with light and astonishing sensitive sensors, minimally invasive bio-medical tools and ultra-high data storage. MEMS and their extension NEMS are collected in the category referred

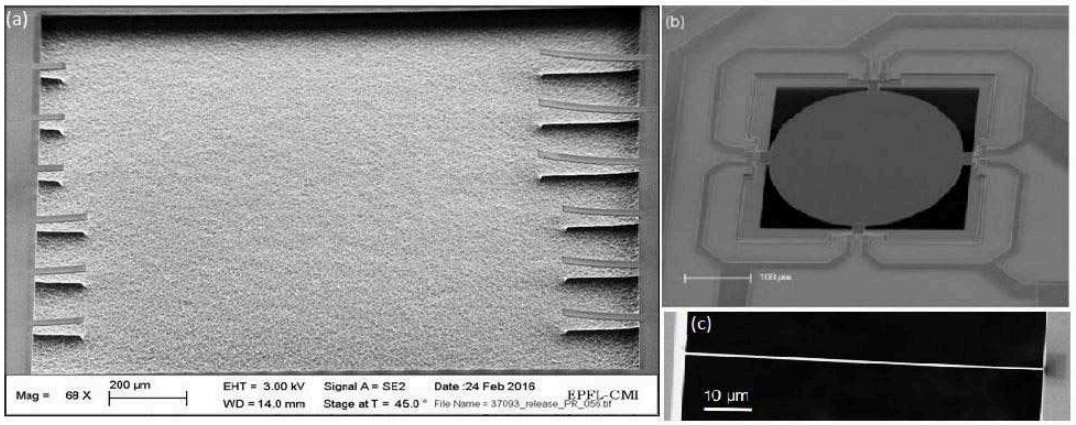

Figure 1.1.1: *Scanning electron microscopy images of different mechanical resonators: a) microcantilever array (with courtesy of Annalisa De Pastina from EPFL), b) surface stress membrane-like sensor c) resonant nanostring (with courtesy of An Hoang Tran)*

to as "M/NEMS", where the physical principles and theoretical background on which they are based are in common, while their size differs of almost an order of magnitude.

Mechanical structures such as beams, plates, strings, wires and membranes that exhibit resonance, vibrating at some specific resonance frequencies (determined by geometry, dimensions, stiffness and mass density) with bigger amplitude than at others, are all mechanical resonators. Hence, M/NEMS resonators are simply miniaturised mechanical resonators consisting of suspended micro- or nanostructures free to oscillate at high frequencies (in the order of kHz and MHz), much bigger than their macroscopic counterparts due to their small sizes.

Figure 1.1.1 shows examples of different configurations of M/NEMS. In all case, small sizes and new properties of M/NEMS resonators have endowed many sensors with incredibly high sensitivity to changes in relative humidity, temperature, pressure, flow, viscosity, charge, mass, force, etc. External physical stimuli can strongly affect the oscillations of the resonators, especially at their resonance frequency, at which these devices are often driven. Observing the changes in vibrational properties such as resonant frequency, vibration amplitude, phase or damping and correlating them back to the stimuli define the fundamentals of the sensing principle of resonant M/NEMS. Extremely high sensitivity, ultralow power requirements, device robustness and very high mechanical responsivity have been achieved in these innovative sensors thanks to the reduced dimensions, high mechanical properties and low mass, also leading to an increase in the resonator's resonant frequency.

1.1.2 Nanomechanical bio-sensors

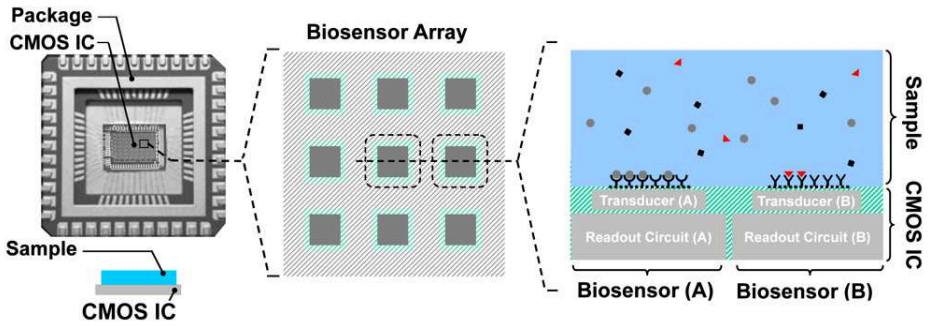

Figure 1.1.2: *CMOS technology applied to bio-sensing: the biosensors are immersed in a sample and linked to a CMOS Integrate circuit; the interaction of biological molecules with the device surface is one of the most relevant phenomena when it occurs at the interfaces between CMOS circuits and biological systems [25]*

MEMS/NEMS technology has found wide application in bio-sensing. A biosensor is a device which measures the physicochemical changes that a biological recognition layer attached to a solid transducer undergoes when it interacts with a sample that contains the targeted molecules: some biomolecules (receptors or probes) specifically bind (recognize) complementary biomolecules (ligands or targets); the surface of the micro- or nanomechanical element is sensitised with receptor or "probe" molecules that selectively recognize the targeted substance.

For example, if we develop an implantable system for measuring human glycemia (the measure of glucose in the blood), then glucose must be the only molecule to interact with our interface. Functionalization can be achieved in several ways like evaporating, sputtering, or spraying a thin layer of bio-material on a gold or silicon surface [19]. Common molecular recognition mechanisms in biology occur in systems such as, for example, receptors/ligands in cell membranes, antigens/ antibodies in the immune system, DNA-DNA and DNA-RNA pairings in cell nuclei. Molecular complementarity is a concept of utmost importance: it assures the correct pairing in target/probe recognition at the Bio/CMOS interface. Targets may

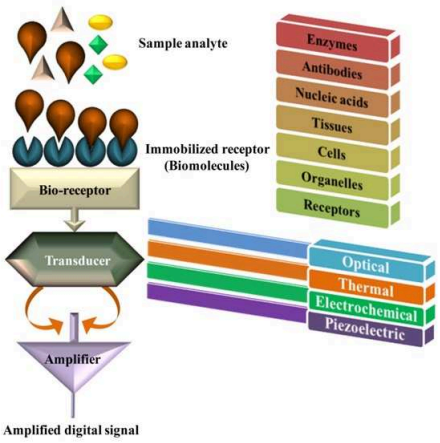

Figure 1.1.3: *Bio-sensing working principle: binding of target molecules with receptors of the functionalized surface produces a stimuli which is transduced into a measurable signal*

be metabolites, genes, proteins, enzymes, cells, bacteria or particular base sequences in a single-stranded DNA or RNA extracted from cells [13]. In all cases, immobilization of the probes onto the chip surface is mandatory to create a stable Bio/CMOS interface. Typical interactions are hybridization of complementary nucleic acids and antibody–antigen binding. These devices are broadly requested in biological studies, health science research, drug discovery, on-chip cell cultures monitoring, pH monitoring and clinical diagnosis. Their use is based on the detection of the forces, motion, mechanical properties and masses that emerge in biomolecular interactions and fundamental biological processes. An important step is the transduction of the physicochemical change into a measurable signal: optical, electrical or mechanical. MMS and microcantilever systems include systems based on cantilevers having a fixed end and a movable end; in these systems, the displacement and/or movement of the "free" end is usually detected. However, there are also systems based on cantilevers clamped at both ends, in which the movement of the central part can be detected. This displacement can be in the order of about 1- 100 nanometres (nm) and in many cases it is necessary to obtain a resolution better than 1 nm, depending on the application. For the readout of the displacement, there are several techniques such as capacitive detection, detection based on tunnel current, optical interferometry, piezoresistive readout and the optical beam deflection technique.

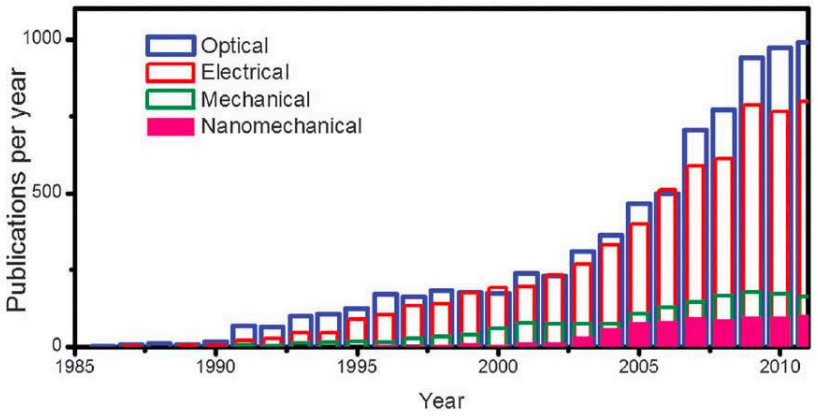

Figure 1.1.4: *Chronogram of the publication rate in optical, electrical, mechanical and nanomechanical biosensors. Up to now, optical and electrical transduction techniques clearly dominate the research on biosensors. It is expected that emerging nanomechanical biosensors will play an increasing role during the next decade [26]*

Biosensors based on micro- and nanomechanical resonators have gained considerable relevance in the last decade and are expected to be widely used in the next years (Figure 1.1.4). The key point of their spread is the high sensitivity of deformation and vibrational characteristics to molecular adsorption thanks to the advances in micro- and nanofabrication technologies that nowadays enable

us to achieve increasingly smaller mechanical transducers with micro- and nanosized moving parts. These ultrasensitive nanomechanical biological and chemical sensors take advantage of their small dimensions to measure with very high resolution physicochemical changes of biological particles. Common devices consist on suspended mechanical structures when either biological adsorption or interactions take place on their surface. Mass, surface stress, effective Young's modulus and viscoelasticity are typical parameters that change as a consequence of biomolecular adsorption, while common issues are the immobilization of biomolecular receptors on the surface of the sensors.

In comparison to other technologies such as quartz crystal resonators, the smaller size of nanomechanical systems produces outstanding mass resolution (up to single atoms), thanks to the comparable sizes of the biomolecules and one of the dimensions of the mechanical system, typically its thickness.

Displacements in nanomechanical biosensors range from angstroms to hundreds of nanometres, and they can be measured by means of optical and electrical techniques.

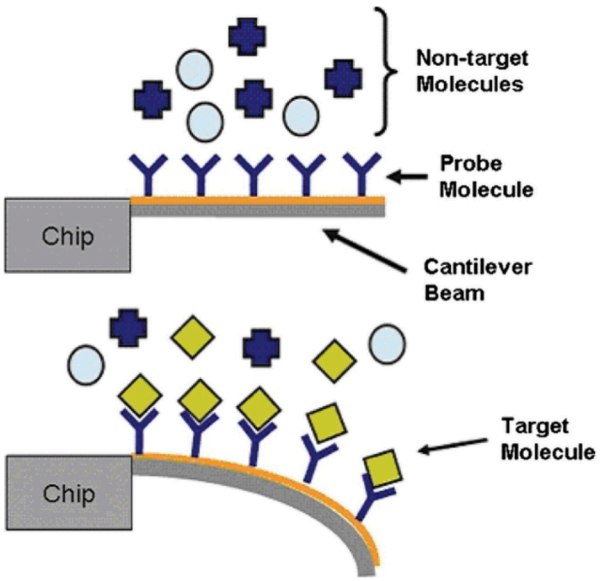

(a) *Bio-functionalized micro-cantilever experiencing a static deflection due to molecular binding between target and probe bio-molecules [39]*

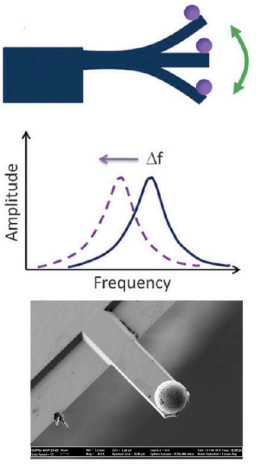

(b) *Top: conceptual model of a cantilever with an added mass at the tip; centre: frequency shift of a mechanical system due to the effect of an added mass after molecular recognition; bottom: SEM image of a silver microsphere attached to a silicon cantilever [16]*

Figure 1.1.5: *Bio-sensing working principle of nanomechanical cantilevers immersed in biological fluid samples*

Nanomechanical biosensors commonly operate in two modes: static and dynamic. In the former, one side of the device, often a microcantilever, is functionalized with a layer of biomolecular receptors

which exhibit high affinity to the targeted biomolecules. Surface stress changes on one side of the structure induce the cantilever bending, which is optically detected. In the dynamic mode, piezoelectric actuators, magnetic forces or light-induced forces drive the cantilever at its resonance frequency. The exquisite and unprecedented sensitivity (mass change over frequency shift) and resolution (minimum detectable mass) in mass measuring of micro- and nanomechanical resonators has been widely proven [21], [37], [23] and allowed for mass detection of individual virus particles, with measurement of the cantilever resonant frequency often performed using a microscope scanning laser Doppler vibrometer. Femtogram-level mass sensitivity using photothermally actuated NEMS was attained by Lavrik and Datskos[23]: their conventional Si microcantilevers with resonance frequencies in the range of 1 to 10 MHz were exposed to vapours of 11-mercaptoundecanoic acid; to estimate an additional cantilever mass due to attached 11-mercaptoundecanoic acid molecules, they used a model of a weakly damped resonator where $\Delta m = 2G\frac{k\Delta f}{\pi^2 {f_0}^3}$, with f_0 as the cantilever frequency before adsorption, k as the spring constant, G as a geometrical factor and Δf=2 KHz as the frequency shift, corresponding to an added mass of 5.5 fg. In 2006, Yang and Roukes [37] demonstrated in situ measurements in real time with mass noise floor $\sim$ 20 zg and mass resolution of $\sim$ 7 zg. Their doubly clamped NEMS were maintained at high vacuum ($< 10^{-7}$ Torr) at T=300 K, fundamental resonant frequency was of 133 MHz and a controlled flux of atoms or molecules was shot onto the NEMS. In recent years, detection limits have been even further reduced, attaining yoctogram resolution (10^{-24} g) and enabling to measure the mass of single protons [36], [14].

Figure 1.1.6: *Frequency shift in the cantilever resonance curve observed by Lavrik and Datskos [23] after adsorption of 11-mercaptoundecanoic acid, corresponding to an added mass of 5.5 fg*

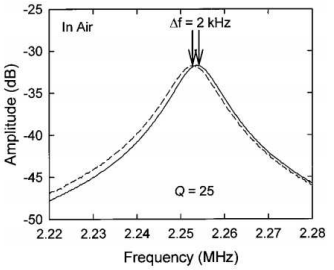

1.1.3 Quality factor

A key parameter of a resonator is the so-called quality factor Q, defined as the ratio between the energy stored and the energy lost during one cycle at resonance. It can also be computed from the vibrational frequency spectrum as $Q = \frac{f_0}{\Delta f_0}$, with f_0 the resonance frequency and $\Delta f_0 = f_2 - f_1$ the bandwidth at -3dB from the peak, Figure 1.1.8. The quality factor determines the accuracy of the resonance frequency measurement, thus a high quality factor is desired for applications of mechanical resonators as it means a sharp peak of the measurement.

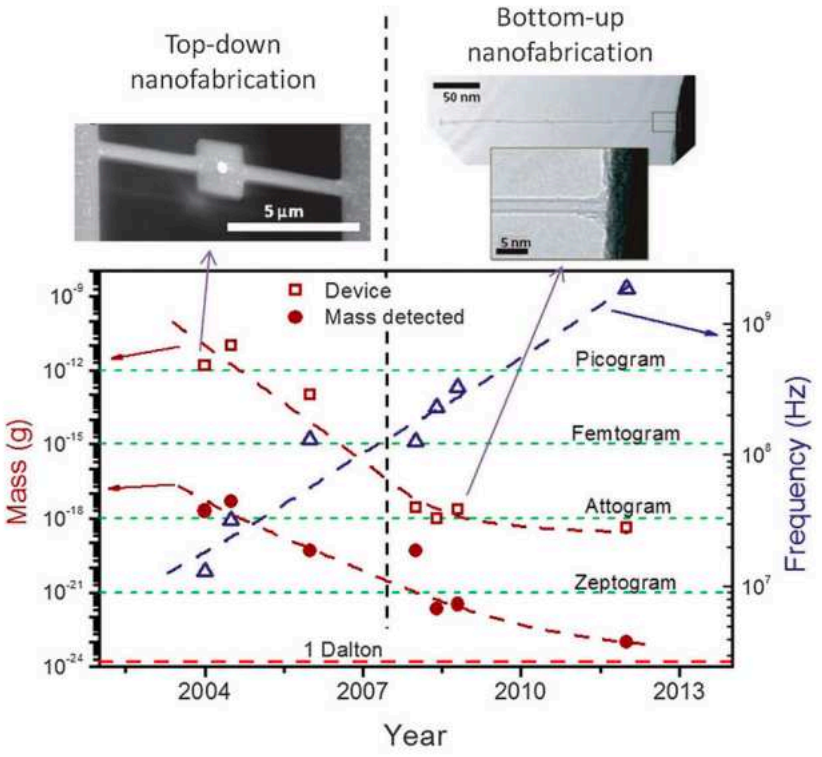

Figure 1.1.7: *Chronology of the advances in nanofabrication of mechanical resonators that have increasingly enhanced the mass detection limits: the device mass, the detected mass levels and the resonance; huge quality factors (1000–10 000) and high resonance frequencies are measured in vacuum with high sensitivity. The advances in nanofabrication have led to smaller devices, smaller mass detection limits approaching Dalton resolution and higher resonance frequencies. Data are from [21], [14] and [36]*

Energy dissipation in mechanical systems is due to the sum of different dissipation mechanisms, among which we mention viscous dissipation through the surrounding medium, clamping to the substrate and intrinsic dissipative mechanisms whithin the material of the resonator; obviously, operation in vacuum and proper structural design can bring up the Q factor of some orders of magnitude. Fluid damping has always limited the use of resonating microcantilevers immersed in liquid as a micro- and nanomechanical sensor as it severely degrades the signal-to-noise ratio of measurements by lowering the mass responsivity and the quality factor of these sensors. Desired yoctogram resolutions require nanoscale resonators with huge quality factors (1000 - 100000), only obtainable with measurements performed in vacuum, while bio-sensing commonly needs aqueous solutions; the development of bio-cantilever sensors for detection in liquid presents two drawbacks: (i) long-term drift of the cantilever deflection induced by slow electrochemical processes at the cantilever/solution interface [28] and (ii) the quality factor of the cantilever is reduced by about two orders of magnitude, from more than 10^4 in vacuum [36] to few units in liquid [9].

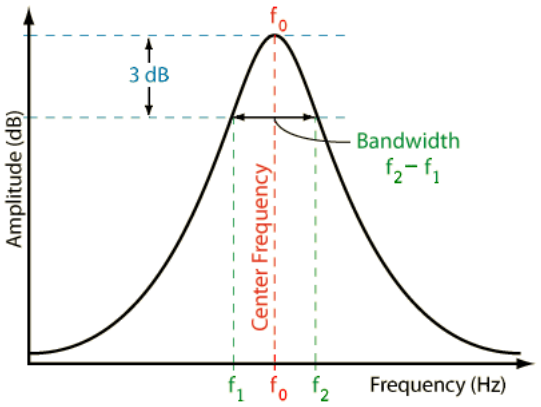

Figure 1.1.8: *Quality factor computed from the frequency spectrum of a mechanical resonator*

Therefore, current challenges concern the development of resonators in contact with viscous fluids with limited energy loss [20], [30]. Tamayo [35] enhanced the sensitivity of the cantilever response by up to three orders of magnitude through Q-control electronic positive feedback technique.

Sader [30] found out that viscous effects strongly depend on the dimensions of the beam: miniaturization of these devices always results in broadening of the resonant peak from its value in vacuum, thus lowering the quality factor and not being a good strategy for the purpose of increasing Q. To sum up, the low quality factor together with the low mass responsivity leads to low sensitivity of M/NEMS when immersed in liquid for bio-sensing applications. A clever solution to this problem has been recently proposed [10]: rather than having the resonator immersed in a liquid environment, the liquid sample is enclosed and let flow in an embedded channel placed within the resonator itself. This easily allows to actuate the device in vacuum, leading to almost equal quality factors for empty and filled resonators [12]. This turns microfluidic technologies into an even more suitable and efficient option for measuring single cells biophysical properties such as density and monitoring cell growth when applied to cancer, immunology and microbial systems. These devices are called Suspended Microchannel Resonators (SMRs).

1.1.4 Suspended Microchannel resonators

Microcantilevers immersed in fluids have been developed for a broad range of applications, from sensing of environmental conditions to imaging with molecular resolution. The quality factor determines the precision to which small changes in resonant frequency can be measured, therefore using microcantilevers as sensors in fluid environments is a challenge, being the quality factor often of order of unity.

One of the very first differences between microcantilevers and macrocantilevers immersed in fluids is that the former are strongly affected by fluid viscosity, while the latter are almost not at all. This produces a big dissimilarity in the fluid dynamics developed by the mechanical oscillations of these similar-in-shape devices. However, the scaling is a major issue that differs them. In fact, quality factors of microcantilevers are orders of magnitude smaller than those of macro-scale cantilevers, because of energy dissipation enhanced with miniaturization. As discussed in the previous subsection, a good quality factor means a very pure resonance peak that enhances the signal-to-noise ratio of resonant frequency measurements and Suspended Microchannel Resonators (SMRs) have been proposed as an alternative to cantilevers immersed in fluids to overcome the issue of high energy dissipation: confining the fluid inside a hollow cantilever significantly increased sensitivity by surrounding the whole device with vacuum and eliminating high damping.

The idea of using microfabricated resonant channels for sensing was developed by Enoksson et al. in 1995 [17]. They developed a device made of a silicon tube whose resonance frequency changed according to the density of fluid flowing through. In 2003 Manalis and Burg [10] developed the first SMR, overcoming the major drawback of conventional immersed resonators: low quality factor, low mass responsivity and low sensitivity.

Figure 1.1.9: *Chip layout and typical chip dimensions for an array of SMRs. Inset: fluidic channel inlet dimensions. Image taken from CleWin (with courtesy of Mauricio Loucena Couto)*

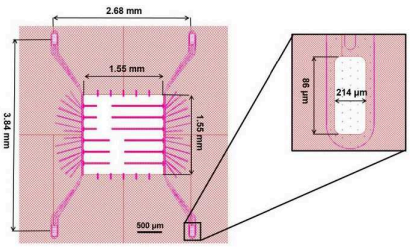

Surprisingly, a non-monotonic energy dissipation due to fluid viscous dissipation was observed while increasing viscosity, in contrast to the monotonic degradation of Q in conventional cantilevers; as a direct consequence enhancement of the quality factor upon miniaturization has been possible [32], [33], [31].

In 2006 Burg and Manalis [11] demonstrated a new type of vacuum-packaged sensor known as the suspended microchannel resonator (SMR) that effectively solved the problems of a limited quality factor in resonators immersed in liquids. They successfully described the fabrication, packaging and testing of a resonant mass sensor for the detection of biomolecules in a microfluidic format with a suspended microchannel as the resonating element of their sensor, such to avoid the problems of viscous damping that degrade the sensitivity of resonant sensors in liquids. It has been showed that these devices exhibit quality factors as high as 10000, comparable to their macro-scale counterpart and orders of magnitude higher than traditional microcantilevers immersed in fluid. Furthermore,

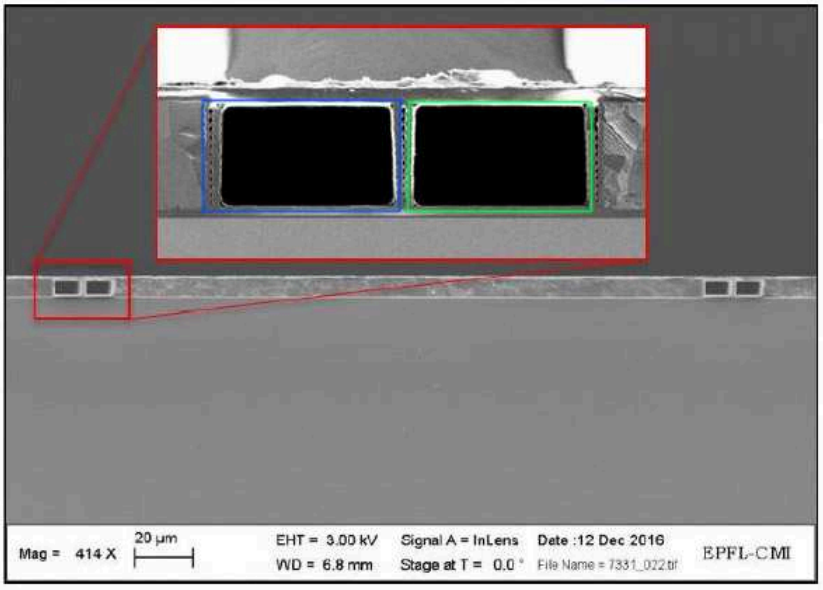

Figure 1.1.10: *SEM image of the inlet (blue framed) and outlet (green framed) channels for a Suspended Microchannel Resonator (with courtesy of Annalisa De Pastina)*

quite surprisingly no change was observed in these devices when air or water was passed through the channel. Such behaviour is in contrast with traditional microcantilevers immersed in fluid whose quality factor drops by 2 orders of magnitude when the surrounding fluid is changed from air to water, because of the increased damping exerted by water on the mechanical system (fluid structure interaction, acoustic impedance).

Such a tool constitutes a micromechanical resonator, modelled as a harmonic oscillator, in which the effective spring constant k and the total effective mass m^* of the system (channel walls mass, liquid mass and the mass of any adsorbed matter) determine the mechanical resonance frequency [34]:

$$\omega_n = \sqrt{\frac{k}{m^*}} \tag{1.1.1}$$

Microcantilevers incorporating a microfluidic channel in their interior constitute a promising solution to the problem of low Q factors: the basic idea is to fill the internal environment of the cantilever with the fluid to be investigated and surround the whole device with vacuum.

These devices have enabled many important measurements through two main modalities of operation:

- flow-through detection: real time monitor of resonance frequency over time, as particles are

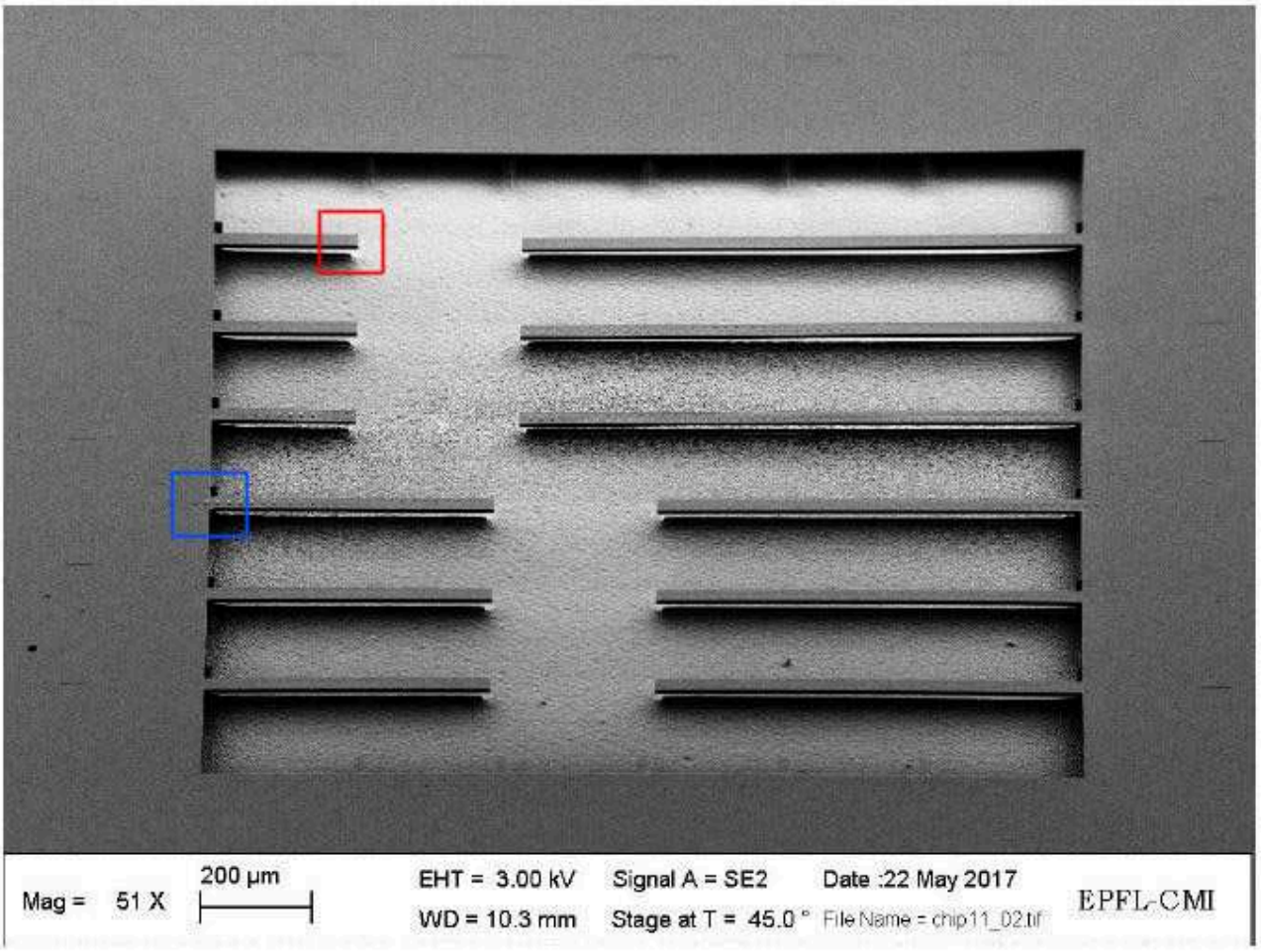

(a) *Chip of 12 Suspended Microchannel Resonators in silicon nitride ($ls - SiNx$) of different sizes fabricated at the CMi Laboratory at EPFL; image taken with a SEM microscope (with courtesy of Annalisa De Pastina)*

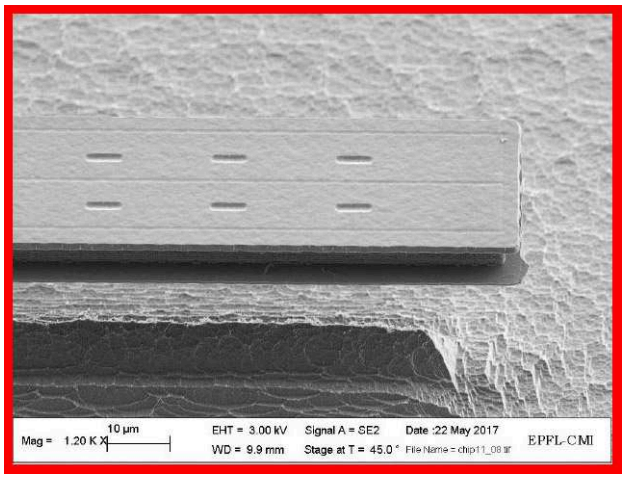

(b) *Zoom at the tip of a SMR*

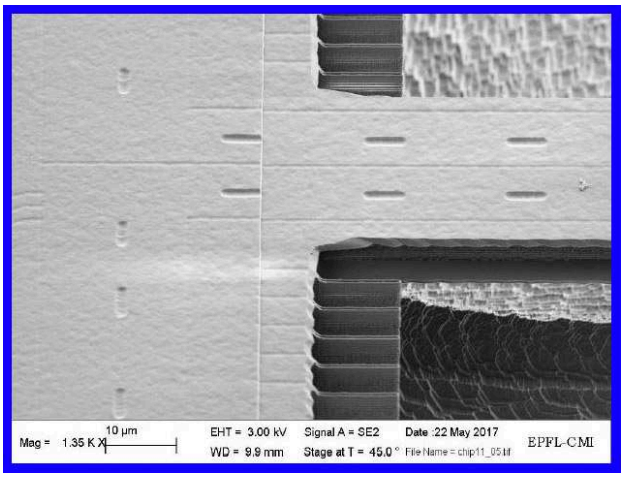

(c) *Zoom at the clamping of a SMR*

flown in diluted suspesion inside the microchannels (Figure 1.1.12c).

- affinity-based capture: channel inner walls are functionalized in order to immobilize the targeted particles by molecular recognition (not real time measurement). At the microscopic scale, any small increase in mass of the cantilever will affect the global resonant frequency of the mechanical vibrating system (Figure 1.1.12b).

Other possible applications are fluid density and mass flow measurements. Research is now making efforts to measure tiny changes in single cell properties, achieving miniaturization of the microchannel to enable the weighing of single virus cells and ultimately single molecules. This will be possible if the microresonator is well fabricated at the micro-scale and structural defects are avoided. Furthermore, a deep insight into the fluid dynamics of the internal fluid may help to "tune" the system properties to achieve any specific sensing task.

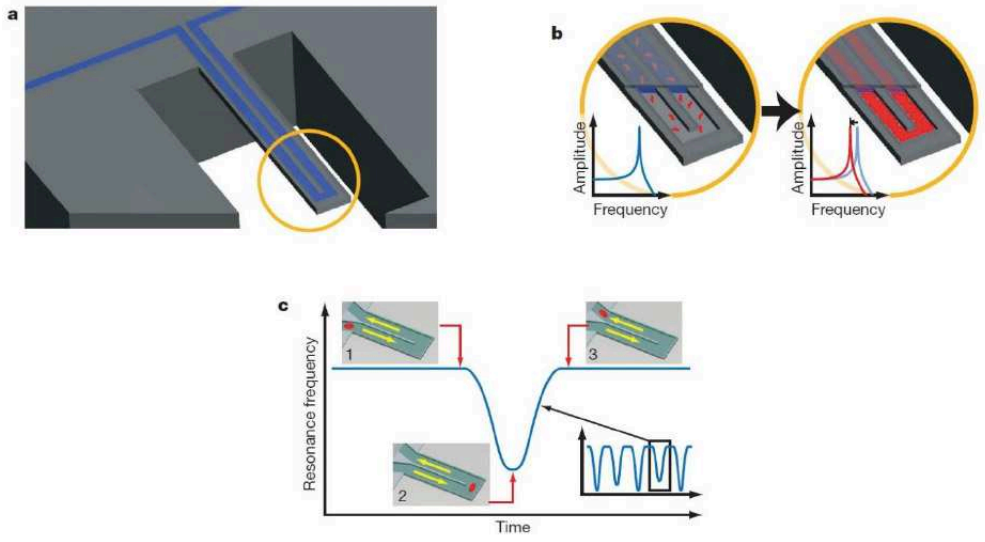

Figure 1.1.12: *Representation of the two mass measurement capabilities of a SMR; a) SMR translates mass changes into resonance frequency shifts. The fluid continuously flows through the channel delivering biomolecules, cells or other particles; b) surface adsorption mechanism: molecules that bind to the channel wall accumulate inside the device. This enables specific detection by way of immobilized receptors; c) particles flow through the cantilever without binding to the surface. The observed signal depends on the position of the particles along the channel. The exact mass excess of a particle can be quantified by the frequency peak shift induced at the apex [12]*

This MSc project focuses on studying the energy dissipation due to the motion of the fluid contained inside these new devices, and it is found that the complexity in fluid dynamics exceeds that of fluid surrounding conventional microcantilevers, which has been widely solved numerically [29]. Comparison between theoretical, numerical and experimental results is our main task.

Importantly, the effects of fluid density and viscosity are considered in the model and investigated, similarly to popular works on the vibration of microcantilevers immersed in fluid. However, in internal problems the effects of compressibility must be investigated. Thus, it is found that this fluid property is of utmost importance in certain cases. Compressibility and other fluid properties are responsible for the rich behaviour of the fluid, in contrast with the external problem counterpart. The most important result following this particular flow field developed inside the resonator is that the quality factor is not a monotonic function of fluid viscosity (or Reynolds number), allowing for a reduction in energy dissipation which is unprecedented in micromechanical systems. It is of paramount importance to underline that the model focuses on energy dissipation due to the fluid motion only and neglects all the effects of structural dissipation in the solid structure such as thermo-elastic dissipation, clamping/anchor losses (acoustic losses due to energy radiated at the clamping), electrostatic interactions, dislocations, internal friction and damping due to residual gas in the vacuum chamber. Importantly, it is found that positioning of the fluid channel in the beam cross-section strongly affects the fluid dynamics and the quality factor.

The model is developed dividing the solution in two sub-problems: on-axis placement and off-axis placement of the channel. The complete flow is given by the linear combination of the two solutions.

1.2 Aim of the Study

The main objective of this thesis is to develop a reliable numerical model to describe dissipation in Suspended Microchannel Resonators, through determination of the Quality Factor, as a costless and quickly reproducible procedure to determine the effectiveness and performance of these innovative MEMS for bio-sensing. Through comparison of numerical results with theoretical and experimental results available in literature we aimed to contribute to the research and understanding of the physical phenomena occurring in these recently developed devices, putting under question some of the previous results and opening to new possible interpretations and discussions.

Importantly, after finding a good match between numerics and experiments, we encourage to re-analyse the findings in the approximated bi-dimensional theoretical model, which seems to give controversial results in the high viscosity regime.

1.3 Thesis outline

This report has been organized in the following structure:

- *Chapter 1* gives an introduction to the main topic studied in this thesis: MicroElectroMechanical Systems (MEMS) and NanoElectroMechanicalSystems (NEMS) are presented before focusing on Suspended Microchannel Resonators (SMRs) and their innovative aspects. Their application as bio-sensors is also discussed and the importance of the Quality Factor in the design of SMRs is underlined. The chapter is concluded with the presentation of the aim and structure of the thesis.
- *Chapter 2* shows the derivation of the theoretical model and all the relevant equations used to describe the physical phenomenon behind dissipation in SMRs.
- *Chapter 3* is dedicated to the discussion of results in the theoretical model, done by plotting functions and variables with the help of Mathematica (release 10.4), which the author suggests as a powerful symbolic tool.
- *Chapter 4* focuses on the description of the numerical model built in COMSOL (release 5.3), with details on the geometry, the dimensions, the boundary and initial conditions, the mesh, the materials and the type of study performed in the numerical analysis. Both a 2D and 3D models are developed and presented and their strengths and weaknesses are discussed.
- *Chapter 5* contains a discussion on the numerical results and a comparison with their theoretical and experimental counterpart[1].
- *Chapter 6* sums up what has been achieved in this thesis, followed by an outlook on the future work. Suggestions and recommendations conclude the text.
- *Appendices* are included at the very end of the thesis, as the aforementioned Abstract, the Poster and the Mathematica codes used to discuss on the theoretical model.

[1] An *Abstract* and a *Poster* on this part have been submitted and accepted by the 1st International Workshop on Nanofluidics and Nanomechanics held in Turin on 14th and 15th September 2017

Chapter 2

Theoretical Model

> Voglio fare dei disegni che vadano al cuore della gente... Sia nella figura che nel paesaggio vorrei esprimere, non una malinconia sentimentale, ma il dolore vero. Voglio che la gente dica delle mie opere: "Sente profondamente, sente con tenerezza"
>
> *Vincent Van Gogh*

Contents

A theoretical model to explain the physical mechanisms of the energy dissipation in the SMRs was proposed by Sader et al. and validated through measurements [32]. We will here prove and discuss on the theoretical model, used as a reference to compare numerical and experimental results. It is important to note that the model focuses on the energy dissipation due to the fluid only, neglecting all the other dissipative mechanisms happening in the solid cantilever structure.

In such a model, the quality factor is defined as the ratio between the energy stored and the energy dissipated per cycle when the resonator is driven at the resonance frequency:

$$Q = 2\pi \left. \frac{E_{stored}}{E_{diss/cycle}} \right|_{\omega_n} \tag{2.0.1}$$

2.1 Model hypotheses

Several hypothesis are stated to simplify the problem and allow for an analytical solution:

1. Cantilever width b_{cant} and thickness h_{cant} are much smaller than its length L; as such, Euler-Bernoulli beam theory can be applied to describe the beam motion.
2. Fluid channel thickness h_{fluid} and channel width b_{fluid} are in a ratio such that we can take the limit $\frac{h_{fluid}}{b_{fluid}} \to 0$; as such, a bi-dimensional analysis in the x-z plane passing through the beam neutral axis can be performed, representing the fluid channel as a single channel with total width the sum of the two channels widths.
3. The beam vibrates at its fundamental mode.
4. The lead channel is rigid and does not move.
5. The amplitude of vibration is so small compared to any geometric scaling factor of the beam that the non-linear convective term in the Navier-Stokes equations can be neglected and linearized Navier-Stokes equations can be used.

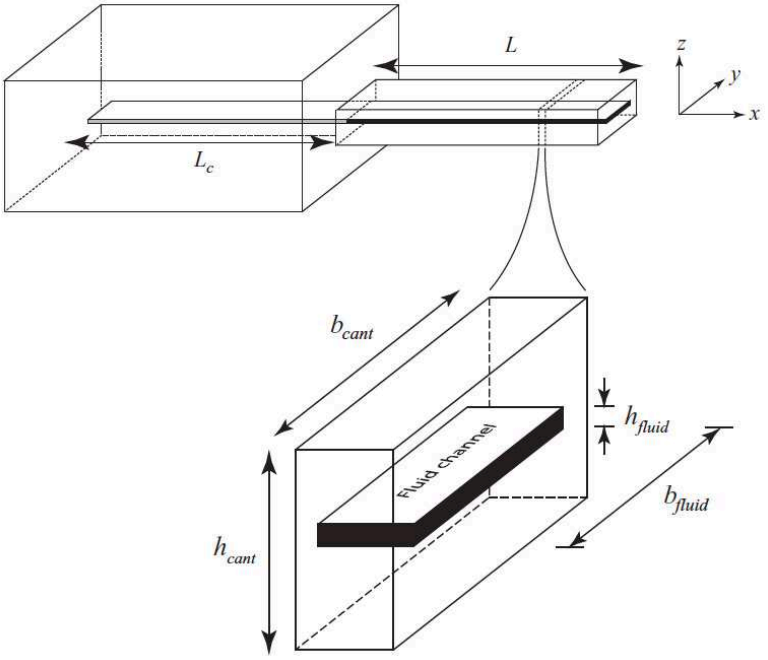

Figure 2.1.1: *Mid-plane section where the theoretical is developed*

2.2 Structural Euler-Bernoulli model

From Euler-Bernoulli beam theory [8] the displacement field of a beam is given by:

$$\mathbf{u_b}(x,z,t) = W(x,t)\hat{\mathbf{z}} - z\frac{\partial W(x,t)}{\partial z}\hat{\mathbf{x}} \tag{2.2.1}$$

Assuming harmonic motion we can write all the functions as the product of a spatial complex function, parametric in the frequency ω, and a temporal oscillating function:

$$X(x,z,t) = \tilde{X}(x,z;\omega)e^{-i\omega t} \tag{2.2.2}$$

We will clearly focus on $Re\left[X(x,z,t)\right]$ and deriving 2.2.1 with respect to time and neglecting all $\tilde{}$ for $W(x;\omega)$ we obtain:

$$\mathbf{v_b}(x,z,t) = \tilde{\mathbf{v}}_\mathbf{b}(x,z;\omega)e^{-i\omega t} = -i\omega\left(W(x;\omega)\hat{\mathbf{z}} - z\frac{\partial W(x;\omega)}{\partial z}\hat{\mathbf{x}}\right)e^{-i\omega t} = -i\omega\mathbf{u_b}(x,z,t) \tag{2.2.3}$$

which gives the beam velocity, therefore also the boundary condition for the velocity field of the fluid inside the channel. Notice that the velocity is correctly shifted of 90° with respect to the displacement.

Real and imaginary parts of each field (pressure, velocity,...) will be combined in time:

$$\begin{aligned} Re\left\{\tilde{X}(x,z;\omega)e^{-i\omega t}\right\} = Re\left\{(Re\left[\tilde{X}(x,z;\omega)\right] + i\ Im\left[\tilde{X}(x,z;\omega)\right])(cos(\omega t) - i\ sin(\omega t))\right\} = \\ = Re\left[\tilde{X}(x,z;\omega)\right] cos(\omega t) + Im\left[\tilde{X}(x,z;\omega)\right] sin(\omega t) \end{aligned} \tag{2.2.4}$$

2.3 Fluidynamics model

The equations used to solve for the fluid field are the Continuity Equation and the Navier-Stokes Equations; in the general form, these are:

$$\frac{\partial \rho_f}{\partial t} + \nabla \cdot (\rho_f \mathbf{v}) = 0 \qquad \mathbf{a} + \mathbf{v} \cdot \nabla \mathbf{v} = -\frac{\nabla P}{\rho_f} + \nu_f \nabla^2 \mathbf{v} + \mathbf{f} \tag{2.3.1}$$

where **a** describes the time-derivative of the fluid velocity and **f** is any external force applied to the fluid. The complete flow is divided into an on-axis flow and an off-axis correction, as in Figure 2.3.1. The former does not include a boundary condition at the tip wall, thus introducing an error but allowing for an analytical solution, the latter does consider the presence of the end-wall by defining a reduced velocity V and stating that its value in $x = L$ is 0, as discussed in Section 2.5. In this way, the velocity v in the original frame of reference is solved, matching the wall velocity according to Euler-Bernoulli.

2.3.1 Turbulence

As the boundary conditions in Figure 2.3.1 clearly state, the fluid motion is due to the oscillation of the solid boundaries: as a consequence, the velocity varies periodically with respect to time even at large Reynolds numbers and the governing equations can be linearized; the main approximation in the case in which no mean flow is imposed on the fluid, as in our case, is that

$$\left|\frac{\partial \mathbf{u}}{\partial t}\right| \gg |\mathbf{u}\nabla\mathbf{u}| \tag{2.3.2}$$

which is of order $\frac{U_0^2}{L}$ where U_0 and L are the characteristic velocity and length of the problem, in our case ωh_f and L. The linearization assumption is thus satisfied when $\frac{\omega L}{U_0} = \frac{L}{h_f} \gg 1$. In cases in which the periodic variation of **u** is forced on the fluid by oscillations of a solid boundary, as in our case, the vorticity arises wholly from the boundaries and the rate of generation of vorticity is

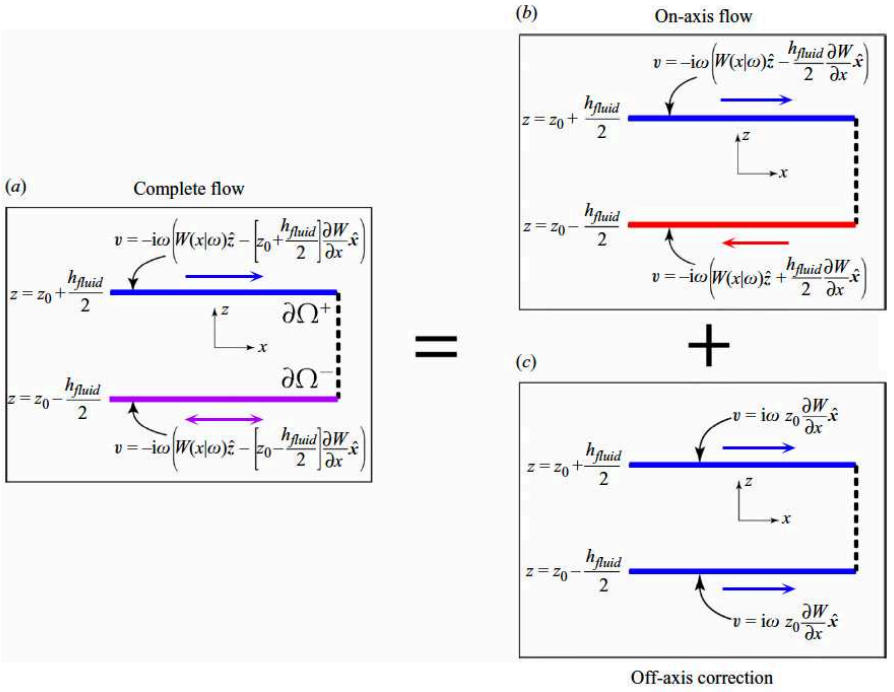

Figure 2.3.1: *Bi-dimensional theoretical model: the complete flow (a) is divided into an on-axis flow (b) and an off-axis correction (c); colours help to have immediate sense of motion in the x-direction: in (b) blue and red coloured walls are moving in opposite verses, in (c) blue coloured walls are straining in the same verse, in (a) the verses depend on the combination of (b) and (c). In the z-direction, each point of the channel moves proportionally to W(x;ω). Dashed line is the wall at the tip: no boundary condition is set on it for simplicity. Notice that the off-axis correction affects only the x component.*

alternately positive and negative: therefore, it is wise to assume as a good approximation that no net vorticity is generated in one cycle and that the vorticity is zero outside a very narrow region close to the boundary layer [7]. It is known that convection carries vorticity and, with this approach, we are inherently assuming that vorticity does not move far from the oscillating boundary before the convection velocity is reversed. However, all this is true if separation of the boundary layer does not occur: bodies with salient edges should be excluded, because separation occurs almost immediately when such bodies move. As the frequency increases, edges of smaller radii of curvature can be admitted. All these concepts are linked to our case when considering the importance of the sharp edges at the end of the cantilever, which can surely be sources of vorticity, neglected in a linearized solution. However, the importance of this neglected term is linked to the time available for diffusion of vorticity of one sign from the boundary, which is $\frac{2\pi}{\omega}$, and so the thickness of the layer of non-zero vorticity is of order $\delta = \left(\frac{\mu}{\omega}\right)^2$

2.3.2 Energy dissipation: viscous dissipation function

We consider the energy equation of a fluid in motion from Batchelor [7], where the rate of change of internal energy per unit mass of a material element of fluid is:

$$\frac{DE}{Dt} = -\frac{\sigma_{ij}e_{ij}}{\rho} + \frac{1}{\rho}\frac{\partial}{\partial x_i}\left(k\frac{\partial T}{\partial x_i}\right) \tag{2.3.3}$$

Substitution of the expression for the stress tensor σ_{ij} gives:

$$\frac{DE}{Dt} = -\frac{p\Delta}{\rho} + \frac{2\mu}{\rho}\left(e_{ij}e_{ij} - \frac{1}{3}\Delta^2\right) + \frac{1}{\rho}\frac{\partial}{\partial x_i}\left(k\frac{\partial T}{\partial x_i}\right) \tag{2.3.4}$$

where

$$\phi = \frac{2\mu}{\rho}\left(e_{ij}e_{ij} - \frac{1}{3}\Delta^2\right) \tag{2.3.5}$$

is the rate of dissipation of mechanical energy (viscous dissipation function), per unit mass of fluid, due to viscosity, equivalent to an irreversible addition of heat, while the first term on the right-hand side of equation 2.3.4 is the rate of change of energy of compression (Δ is the trace of the rate-of-strain tensor $\bar{\bar{e}}$), which can be returned to the mechanical system without loss in a cycle of expansion-compression. This is true approximately for small departures from the equilibrium pressure p. Indeed, a more general expression is:

$$-\frac{p\Delta}{\rho} = -\frac{p_e}{\rho} + \frac{\lambda\Delta^2}{\rho} \tag{2.3.6}$$

where the first term on the right-hand side represents a reversible transformation of energy, while the second one represents a dissipation of mechanical energy. The parameter λ is an empirical coefficient called "bulk viscosity" (alternative names are "second coefficient of viscosity" or "expansion viscosity") and is often negligible (Stokes hypothesis), fact that allows us to conclude that dissipation only comes from the "Viscous dissipation function" ϕ. The value of λ, when large enough to be measured, turns out to be not a fluid property but dependent on the rate of expansion $\nabla \cdot \mathbf{v}$. The Stokes hypothesis states that $\lambda\nabla \cdot \mathbf{v} = 0$: this term is associated with the dilation of the fluid particles and has a strength much smaller than that of the dilation of fluid volumes, because of the much smaller scale at which the phenomenon occurs. An alternative equation to 2.3.6 is $p_m = p - \lambda\nabla \cdot \mathbf{v}$ which reveals that the thermodynamic pressure (instantaneous pressure in the fluid) tends to be higher than the mechanical pressure (waves of pressure due to fluid volumes motion only) when the mechanical pressure is increasing (volume decreasing, $\nabla \cdot \mathbf{v} < 0$). In other words, it takes more

time to the instantaneous pressure to react to volume changes because the particles haven't relaxed yet when the volumetric pressure waves have passed through.

2.3.3 Dissipated energy over a cycle of vibration

The energy dissipated within the fluid after a cycle of vibration of the solid cantilever can be computed from equation 2.3.5 as:

$$\phi_{v,cycle} = \int_0^T \phi_v dt = \int_0^T 2\mu(\bar{\bar{e}} : \bar{\bar{e}}^* - \frac{1}{3}|tr(\bar{\bar{e}})|^2)dt \tag{2.3.7}$$

and having all square terms in the equation and being all the fields harmonic ($\bar{\bar{e}} = \tilde{\bar{\bar{e}}}(x, y, z)\cos\omega t$)

$$\phi_{v,cycle} = \int_0^T \tilde{\phi}_v \cos^2\omega t dt = 2\mu(\tilde{\bar{\bar{e}}} : \tilde{\bar{\bar{e}}}^* - \frac{1}{3}|tr(\tilde{\bar{\bar{e}}})|^2)\frac{T}{2} = \frac{\pi}{\omega}\tilde{\phi}_v \tag{2.3.8}$$

2.4 On-axis placement of the channel

2.4.1 Governing equations

In the case where the channel mid-plane lies on the neutral axis of the cantilever ($z_0 = 0$), we define the scaled variables

$$\bar{x} = \frac{x}{h_{fluid}} \tag{2.4.1}$$

$$\bar{W} = \frac{W}{L} \tag{2.4.2}$$

and use the following definitions:

$$\beta = \frac{\rho\omega h_{fluid}^2}{\mu} \tag{2.4.3}$$

$$U(\bar{x};\omega) = -i\omega W(\bar{x};\omega) \tag{2.4.4}$$

We then expand the function $U(\bar{x};\omega)$ as a Taylor series expansion around the local point $\bar{x}_0$:

$$U(\bar{x};\omega) = U_0 + A(\bar{x} - \bar{x}_0) + B(\bar{x} - \bar{x}_0)^2 + ... \tag{2.4.5}$$

where

$$U_0 = U(\bar{x}_0;\omega) = -i\omega W(\bar{x}_0;\omega) \tag{2.4.6}$$

and

$$A = \left.\frac{\partial U(\bar{x};\omega)}{\partial \bar{x}}\right|_{\bar{x}_0} \tag{2.4.7}$$

$$B = \left.\frac{\partial^2 U(\bar{x};\omega)}{\partial \bar{x}^2}\right|_{\bar{x}_0} \tag{2.4.8}$$

$$\bar{x}_0 = \frac{x_0}{h_{fluid}} \tag{2.4.9}$$

From the chain rule of the derivative of the composition of two functions we obtain:

$$A = -i\omega h_{fluid} \left.\frac{\partial W(x;\omega)}{\partial x}\right|_{x_0} \tag{2.4.10}$$

As $\frac{h_{fluid}}{L} \longrightarrow 0$, we can write:

$$U(\bar{x};\omega) = U_0 + A(\bar{x} - \bar{x}_0) + \mathcal{O}\left(\left(\frac{h_{fluid}}{L}\right)^2\right) \tag{2.4.11}$$

The velocity of the beam 2.2.3 in the scaled variables and in the ω space becomes a linearized function of $\bar{z}$ and $\bar{x}$:

$$\begin{aligned}\tilde{\mathbf{v}}_{\mathbf{b}}(\bar{x},\bar{z};\omega) = -i\omega W(\bar{x};\omega)\hat{\mathbf{z}} + (\bar{z}h_{fluid})i\omega \left.\frac{\partial W(\bar{x};\omega)}{\partial \bar{x}}\right|_{\bar{x}_0} \hat{\mathbf{x}} = \\ = U(\bar{x};\omega)\hat{\mathbf{z}} - A\bar{z}\hat{\mathbf{x}} = U_0\hat{\mathbf{z}} + A[-\bar{z}\hat{\mathbf{x}} + (\bar{x} - \bar{x}_0)\hat{\mathbf{z}}]\end{aligned} \tag{2.4.12}$$

or in matrix form:

$$\tilde{\mathbf{v}}_b = \begin{pmatrix} -A\bar{z} \\ U_0 + A(\bar{x} - \bar{x}_0) \end{pmatrix} = \begin{pmatrix} i\omega h_{fluid} \left.\frac{\partial W(x;\omega)}{\partial x}\right|_{x_0} \bar{z} \\ U_0 - i\omega h_{fluid} \left.\frac{\partial W(x;\omega)}{\partial x}\right|_{x_0} (\bar{x} - \bar{x}_0) \end{pmatrix} \tag{2.4.13}$$

The general form of the continuity equation and Navier-Stokes equation is:

$$\frac{\partial \rho}{\partial t} + \nabla \cdot (\rho \mathbf{v}) = 0 \qquad \mathbf{a} + \mathbf{v} \cdot \nabla \mathbf{v} = -\frac{\nabla P}{\rho} + \nu \nabla^2 \mathbf{v} + \mathbf{f} \tag{2.4.14}$$

We now solve the continuity equation coherently assuming that when the channel is perfectly centred on the neutral axis of the beam, no change of total volume takes place in the channel hence in the on-axis case the density is constant and the Navier-Stokes equation, in agreement with the assumption that $W(x;\omega) \gg L$, can be linearized, neglecting the convective inertial term; assuming $\mathbf{f} = 0$ and being $\mathbf{a} = -i\omega\mathbf{v}$ turns 2.4.14 into:

$$\nabla \cdot \mathbf{v} = 0 \qquad -i\omega\rho\mathbf{v} = -\nabla P + \mu \nabla^2 \mathbf{v} \tag{2.4.15}$$

where the second one is a vectorial equation in 2 dimensions. Notice that we are studying the stationary spatial functions having omitted all the ˜. The problem for the fluid inside the channel can be written as:

$$\begin{cases} \nabla \cdot \mathbf{v} = 0 & in \quad \Omega \\ -i\omega\rho\mathbf{v} = -\nabla P + \mu\nabla^2\mathbf{v} & in \quad \Omega \\ \mathbf{v} = \mathbf{v}_{beam} & on \quad \partial\Omega \end{cases} \tag{2.4.16}$$

which means:

$$\begin{cases} \nabla \cdot \mathbf{v} = 0 & in \quad \Omega \\ -i\omega\rho\mathbf{v} = -\nabla P + \mu\nabla^2\mathbf{v} & in \quad \Omega \\ \mathbf{v} = -i\omega[W(x;\omega)\hat{z} - \frac{h_{fluid}}{2}\left.\frac{\partial W(x;\omega)}{\partial x}\right|_{x_0}\hat{x}] & on \quad \partial\Omega^+ \\ \mathbf{v} = -i\omega[W(x;\omega)\hat{z} + \frac{h_{fluid}}{2}\left.\frac{\partial W(x;\omega)}{\partial x}\right|_{x_0}\hat{x}] & on \quad \partial\Omega^- \end{cases} \tag{2.4.17}$$

Let us now divide the solution in:

1. non-viscous solution (which needs to respect the normal boundary condition only)
2. corrective term necessary to respect the horizontal boundary condition

$$\mathbf{v} = \mathbf{v_{inv}} + M(\bar{z})\hat{\mathbf{x}} \tag{2.4.18}$$

Notice that the corrective term must not affect the inviscid solution along $\hat{z}$ because that part already respects the vertical boundary condition.

It is wise to believe that the solution to the inviscid part is:

$$\mathbf{v}_{inv} = A\bar{z}\hat{\mathbf{x}} + (U_0 + A(\bar{x} - \bar{x}_0))\hat{\mathbf{z}} \tag{2.4.19}$$

which clearly satisfies the $\hat{\mathbf{z}}$ components of the boundary conditions in 2.4.17. Clearly, we couldn't choose $v_{inv,x} = -A\bar{z}$, otherwise no corrective term would have been necessary and we would have stated that the flow field matches completely the beam velocity field, which is of course not true. Substituting 2.4.19 in 2.4.17 we can easily satisfy the continuity equation and the $\hat{\mathbf{z}}$ component of the boundary conditions. We can also derive the pressure from the $\hat{\mathbf{z}}$ component of the Navier-Stokes equations, using the supposed expression 2.4.19:

$$-i\omega\rho v_z = -\frac{\partial P}{\partial z} + \mu\left[\frac{\partial^2 v_z}{\partial x^2} + \frac{\partial^2 v_z}{\partial y^2} + \frac{\partial^2 v_z}{\partial z^2}\right] \tag{2.4.20}$$

$$-i\omega\rho[U_0 + A(\bar{x} - \bar{x}_0)] = -\frac{\partial P}{\partial \bar{z}}\frac{1}{h_f} \tag{2.4.21}$$

from which

$$P(\bar{x}, \bar{z}) = \int_0^{\bar{z}} \frac{\partial P}{\partial \bar{z'}} d\bar{z'} = i\omega\rho h_f[U_0 + A(\bar{x} - \bar{x}_0)]\bar{z} \tag{2.4.22}$$

which can be easily proved to satisfy both components of Navier-Stokes equations (second equation of 2.4.17). We can now write:

$$\begin{cases} \mathbf{v} = \mathbf{v_{inv}} + M(\bar{z})\hat{\mathbf{x}} = [M(\bar{z}) + A\bar{z}]\hat{\mathbf{x}} + [U_0 + A(\bar{x} - \bar{x}_0)]\hat{\mathbf{z}} \\ P = i\omega\rho h_f[U_0 + A(\bar{x} - \bar{x}_0)]\bar{z} \\ \nabla \cdot \mathbf{v} = 0 \\ -i\omega\rho\mathbf{v} = -\nabla P + \mu\nabla^2\mathbf{v} \end{cases} \tag{2.4.23}$$

Substituting the first two equations in the second two, the continuity equation and the z-component of Navier-Stokes are again satisfied (having introduced a correction for the x-component) and, from the x-component of Navier-Stokes:

$$-i\omega\rho v_x = -\frac{\partial P}{\partial x} + \mu\left[\frac{\partial^2 v_x}{\partial x^2} + \frac{\partial^2 v_x}{\partial z^2}\right] \tag{2.4.24}$$

we get:

$$-i\omega\rho[M(\bar{z}) + A\bar{z}] = -i\omega\rho h_f A\bar{z}\frac{1}{h_f} + \mu\frac{d^2M(\bar{z})}{d\bar{z}^2}\frac{1}{h_f^2} \tag{2.4.25}$$

$$-i\frac{\omega\rho h_f^2}{\mu}M(\bar{z}) = \frac{d^2M(\bar{z})}{d\bar{z}^2} \tag{2.4.26}$$

or finally:

$$-i\beta M(\bar{z}) = \frac{d^2M(\bar{z})}{d\bar{z}^2} \tag{2.4.27}$$

Importantly, the boundary conditions obtained from the beam theory do not change after the introduction of the corrective term. Computing 2.4.18 in $\bar{z} = \pm\frac{1}{2}$ gives the boundary conditions for $M(\bar{z})$:

$$\begin{cases} M(\frac{1}{2}) = -A \\ M(-\frac{1}{2}) = A \end{cases} \tag{2.4.28}$$

The problem for $M(\bar{z})$ becomes:

$$\begin{cases} \frac{d^2M(\bar{z})}{d\bar{z}^2} + i\beta M(\bar{z}) = 0 \\ M(\frac{1}{2}) = -A \\ M(-\frac{1}{2}) = A \end{cases} \tag{2.4.29}$$

which is a simple harmonic equation, solved by:

$$\begin{cases} M(\bar{z}) = C\sin(\Omega\bar{z} + \phi) \\ \Omega^2 = i\beta \\ \phi = 0 \\ C = -\frac{A}{\sin\left(\frac{\Omega}{2}\right)} \end{cases} \tag{2.4.30}$$

$$M(\bar{z}) = -\frac{A\sin\left(\sqrt{i\beta}\bar{z}\right)}{\sin\left(\frac{\sqrt{i\beta}}{2}\right)} \tag{2.4.31}$$

Using some trigonometric relationship, the latter can be written also as

$$M(\bar{z};\beta) = -\frac{A\sinh\left[(1-i)\sqrt{\frac{\beta}{2}}\bar{z}\right]}{\sinh\left[\frac{1-i}{2}\sqrt{\frac{\beta}{2}}\right]} \tag{2.4.32}$$

which gives the corrective term for the x-component of the velocity field, parametric in β and dependent on the specific $\bar{x}$-coordinate through A. We finally obtain the total velocity field in the on-axis case:

$$\mathbf{v} = \underbrace{A\left\{\bar{z} - \frac{\sinh\left[(1-i)\sqrt{\frac{\beta}{2}}\bar{z}\right]}{\sinh\left[\frac{1-i}{2}\sqrt{\frac{\beta}{2}}\right]}\right\}}_{G(\beta)}\hat{\mathbf{x}} + [U_0 + A(\bar{x} - \bar{x}_0)]\hat{\mathbf{z}} \tag{2.4.33}$$

It's worth mentioning that the velocity field is made up of a real and an imaginary part, which are 90° and will then need to be properly combined in the time domain.

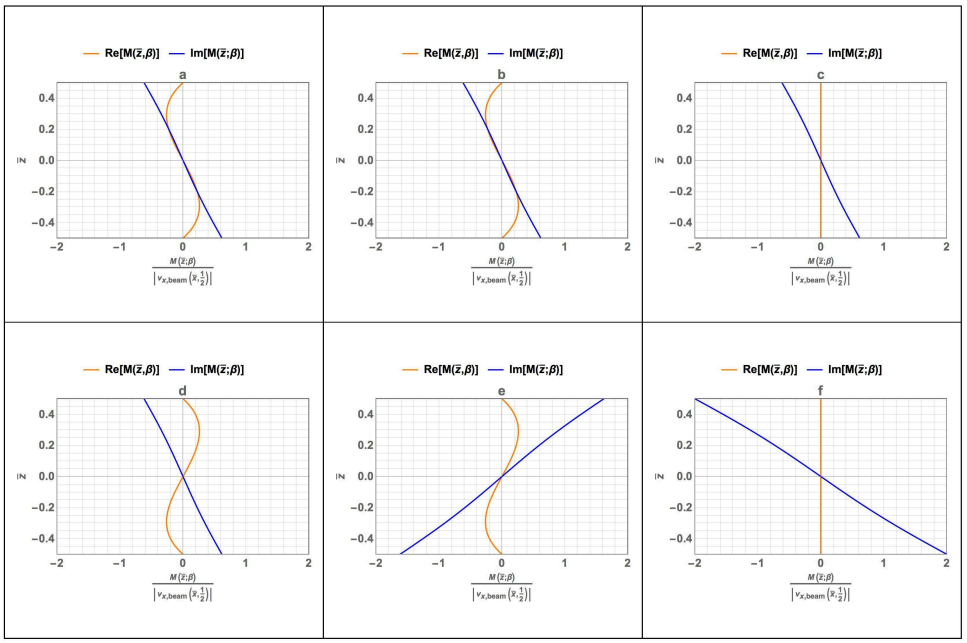

Figure 2.4.1: *Real and imaginary parts of the corrective function $M(\bar{z};\beta)$ for the x-component of the velocity field, normalized with respect to $\left|v_{x,beam}(\bar{x},\frac{1}{2})\right|$, for $\beta = 10$ and $\bar{x} = \frac{L}{h_f}$ (tip) and different fractions of the period T: a) $t = \frac{T}{6}$, b) $t = \frac{2T}{6}$, c) $t = \frac{3T}{6}$, d) $t = \frac{4T}{6}$, e) $t = \frac{5T}{6}$, f) $t = T$*

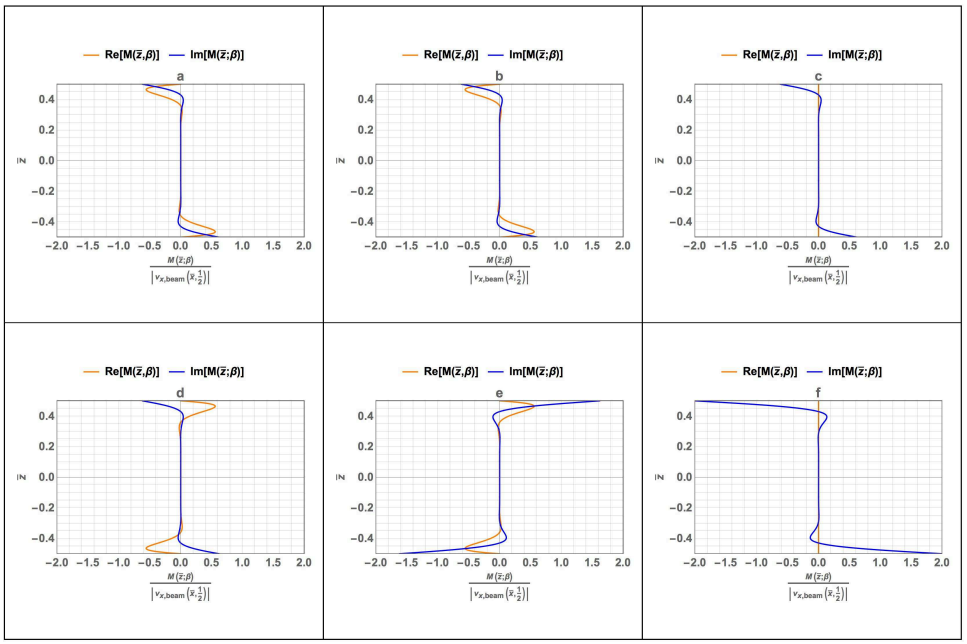

Figure 2.4.2: *Real and imaginary parts of the corrective function $M(\bar{z};\beta)$ for the x-component of the velocity field, normalized with respect to $\left|v_{x,beam}(\bar{x},\frac{1}{2})\right|$, for $\beta = 1000$ and $\bar{x} = \frac{L}{h_f}$ (tip) and different fractions of the period T: a) $t = \frac{T}{6}$, b) $t = \frac{2T}{6}$, c) $t = \frac{3T}{6}$, d) $t = \frac{4T}{6}$, e) $t = \frac{5T}{6}$, f) $t = T$*

The velocity gradient tensor $\nabla\bar{v} = \frac{\partial v_i}{\partial x_j}$ can be written as the sum of a symmetric part e_{ij} and an

antisymmetric part Ω_{ij} where:

$$e_{ij} = \frac{1}{2}\left(\frac{\partial v_i}{\partial x_j} + \frac{\partial v_j}{\partial x_i}\right) \tag{2.4.34}$$

is the rate-of-strain tensor of the fluid. In our bi-dimensional case, the tensor reduces to a 2x2 matrix and, from 2.4.33, we learn that the terms on the diagonal are null, while for the symmetry of the tensor the off-diagonal terms are equal. Therefore:

$$\bar{\bar{e}} = \frac{1}{2}\left(\frac{\partial v_x}{\partial z} + \frac{\partial v_z}{\partial x}\right)(\hat{\mathbf{x}}\hat{\mathbf{z}}) + \frac{1}{2}\left(\frac{\partial v_z}{\partial x} + \frac{\partial v_x}{\partial z}\right)(\hat{\mathbf{z}}\hat{\mathbf{x}}) = \frac{1}{2}\left(\frac{\partial v_z}{\partial x} + \frac{\partial v_x}{\partial z}\right)(\hat{\mathbf{x}}\hat{\mathbf{z}} + \hat{\mathbf{z}}\hat{\mathbf{x}}) \tag{2.4.35}$$

$$= -i\omega \left.\frac{\partial W}{\partial x}\right|_{x_0} \left\{1 - \frac{1-i}{2}\sqrt{\frac{\beta}{2}}\frac{\cosh[(1-i)\sqrt{\frac{\beta}{2}}\bar{z}]}{\sinh[\frac{1-i}{2}\sqrt{\frac{\beta}{2}}]}\right\}(\hat{\mathbf{x}}\hat{\mathbf{z}} + \hat{\mathbf{z}}\hat{\mathbf{x}}) \tag{2.4.36}$$

The energy dissipated per cycle per unit volume is:

$$E_{diss/cycle/volume} = \frac{2\pi\mu}{\omega}(\bar{\bar{e}} : \bar{\bar{e}}^* - \frac{1}{3}|tr(\bar{\bar{e}})|^2) \tag{2.4.37}$$

where $\bar{\bar{e}} : \bar{\bar{e}}^*$ indicates the colon product (dyadic) and returns $2|e_{12}|^2$, while $tr(\bar{\bar{e}}) = 0$ in our case. The total dissipated energy in the channel is:

$$\begin{aligned} E_{diss/cycle} &= \int_{-\frac{h_f}{2}}^{\frac{h_f}{2}} \int_0^{b_f} \int_0^L E_{diss/cycle/volume} dV = \\ &= \int_{-\frac{1}{2}}^{\frac{1}{2}} \left|1 - \frac{1-i}{2}\sqrt{\frac{\beta}{2}}\frac{\cosh[(1-i)\sqrt{\frac{\beta}{2}}\bar{z}]}{\sinh[\frac{1-i}{2}\sqrt{\frac{\beta}{2}}]}\right|^2 d\bar{z} \int_0^{b_f} dy \int_0^L 4\pi\mu\omega h_f \left[\left.\frac{\partial W}{\partial x}\right|_{x_0}\right]^2 dx_0 \end{aligned} \tag{2.4.38}$$

The displacement function of the beam is taken as the first vibrational mode, which is believed to contribute most to the total displacement; a higher order expansion of the displacement as a sum of more modes would barely increase the accuracy of the result:

$$W(x) = (\cos B_1 x - \cosh B_1 x) - \frac{\cos B_1 L + \cosh B_1 L}{\sin B_1 L + \sinh B\ L}(\sin B_1 x - \sinh B_1 x) \tag{2.4.39}$$

and for the first mode of a clamped beam

$$B_1 = \frac{1.8751}{L} \tag{2.4.40}$$

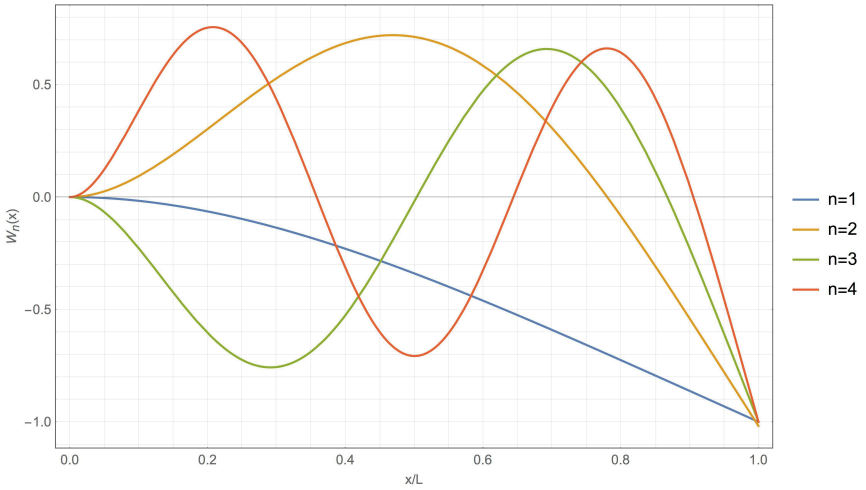

Figure 2.4.3: *Schematics of the first four bending modes $W_n(x)$ of a clamped cantilever seen from the side. The amplitude is in units of the Fourier coefficients and the position is in units of the length L, where 0 indicates the base of the cantilever*

The energy stored is computed following [34]:

$$E_{stored} = \frac{1}{2}A_c\rho_c\int_0^L\left(\frac{\partial W}{\partial t}\right)^2 dx = W_{kin,max} = \omega^2 W_{kin}(W(x,y;\omega)) = \frac{1}{2}\omega^2 A_c\rho_c\int_0^L W(x)^2 dx \tag{2.4.41}$$

Applying the definition of Q and normalizing, we finally obtain the normalized Quality Factor $F(\beta)$:

$$Q = 2\pi\left.\frac{E_{stored}}{E_{diss/cycle}}\right|_{\omega_n} = 2\pi\frac{\frac{1}{2}\omega^2 A_c\rho_c\int_0^L\left(\frac{\partial W}{\partial t}\right)^2 dx}{2\pi\frac{\mu}{\omega}2\int_V |e_{12}|^2 dV} = F(\beta)\frac{\rho_c}{\rho_f}\frac{h_c}{h_f}\frac{b_c}{b_f}\left(\frac{L}{h_c}\right)^2 \tag{2.4.42}$$

$$\begin{aligned} F_{on}(\beta) = \frac{1}{4L^2}\frac{\int_0^L W(x)^2 dx}{\int_0^L\left[\left.\frac{\partial W}{\partial x}\right|_{x_0}\right]^2 dx_0}\beta\left(\int_{-\frac{1}{2}}^{\frac{1}{2}}\left|1-\frac{1-i}{2}\sqrt{\frac{\beta}{2}}\frac{\cosh[(1-i)\sqrt{\frac{\beta}{2}}\bar{z}]}{\sinh[\frac{1-i}{2}\sqrt{\frac{\beta}{2}}]}\right|^2 d\bar{z}\right)^{-1} = \\ = 0.05379\beta\left(\int_{-\frac{1}{2}}^{\frac{1}{2}}\left|1-\frac{1-i}{2}\sqrt{\frac{\beta}{2}}\frac{\cosh[(1-i)\sqrt{\frac{\beta}{2}}\bar{z}]}{\sinh[\frac{1-i}{2}\sqrt{\frac{\beta}{2}}]}\right|^2 d\bar{z}\right)^{-1} \end{aligned} \tag{2.4.43}$$

2.4.2 Small β limit

A Taylor series expansion around $\beta_0 = 0$ arrested at the first order of 2.4.33 (easily obtainable exploiting de l'Hôpital's rule) gives:

$$\mathbf{v} = \left(-A\bar{z} + \frac{Ai}{12}(4\bar{z}^3 - \bar{z})\right)\hat{\mathbf{x}} + [U_0 + A(\bar{x} - \bar{x}_0)]\hat{\mathbf{z}} \tag{2.4.44}$$

from which the rate-of-strain is:

$$\bar{\bar{e}} = \frac{1}{2}\left\{\omega\beta \left.\frac{\partial W}{\partial x}\right|_{x_0}\left(\bar{z}^2 - \frac{1}{12}\right)\right\}(\hat{\mathbf{x}}\hat{\mathbf{z}} + \hat{\mathbf{z}}\hat{\mathbf{x}}) \tag{2.4.45}$$

and

$$F(\beta) = \frac{0.05379\beta}{\frac{\beta^2}{4}\int_{-\frac{1}{2}}^{\frac{1}{2}}\left(\bar{z}^2 - \frac{1}{12}\right)^2 d\bar{z}} = \frac{38.73}{\beta}, \qquad \beta \ll 1 \tag{2.4.46}$$

2.4.3 Large β limit

For $\beta \to \infty$ we can approximate the velocity field with 2.4.19 in all the channel but in a small boundary layer where the boundary condition of no-slip must be satisfied. Therefore, the complete solution 2.4.33 must be used and the small terms in β can be neglected after integration. Exploiting the fact that, for $\beta \gg 1$:

$$\frac{1}{\sinh\left(\frac{(1-i)}{2}\sqrt{\frac{\beta}{2}}\right)} = \frac{2}{e^{\frac{(1-i)}{2}\sqrt{\frac{\beta}{2}}} - e^{-(1-i)\sqrt{\frac{\beta}{2}}}} \simeq \frac{2}{e^{\frac{(1-i)}{2}\sqrt{\frac{\beta}{2}}}} \tag{2.4.47}$$

we can write $G(\beta)$ in equation 2.4.33 as:

$$G(\beta) = A\bar{z} - 2Ae^{-\frac{(1-i)}{2}\sqrt{\frac{\beta}{2}}}\sinh\left((1-i)\sqrt{\frac{\beta}{2}}\bar{z}\right) \tag{2.4.48}$$

Therefore,

$$\bar{\bar{e}} = -i\omega \left.\frac{\partial W}{\partial x}\right|_{x_0}\left(1 - (1-i)\sqrt{\frac{\beta}{2}}e^{-\frac{1-i}{2}\sqrt{\frac{\beta}{2}}}\cosh\left((1-i)\sqrt{\frac{\beta}{2}}\bar{z}\right)\right)(\hat{\mathbf{x}}\hat{\mathbf{z}} + \hat{\mathbf{z}}\hat{\mathbf{x}}) \tag{2.4.49}$$

which, integrating and neglecting small terms in β, gives:

$$F(\beta) = \frac{0.05379\beta}{\int_{-\frac{1}{2}}^{\frac{1}{2}}\left|1 - (1-i)\sqrt{\frac{\beta}{2}}e^{-\frac{1-i}{2}\sqrt{\frac{\beta}{2}}}\cosh\left((1-i)\sqrt{\frac{\beta}{2}}\bar{z}\right)\right|^2 d\bar{z}} \simeq \frac{0.215616\beta}{\sqrt{2}\sqrt{\beta}} = 0.1521\sqrt{\beta} \tag{2.4.50}$$

2.5 Off-axis placement of the channel

2.5.1 Governing equations

Scaling considerations allow to state that the Continuity and Navier-Stokes equations for compressible flows 2.4.14 become:

$$\frac{\partial\rho}{\partial t} + \rho\nabla\mathbf{v} = 0, \qquad \rho\frac{\partial\mathbf{v}}{\partial t} = -\nabla P + \mu\nabla^2\mathbf{v} + \frac{1}{3}\mu\nabla(\nabla\mathbf{v}) \tag{2.5.1}$$

where the Stokes hypothesis has been used (bulk viscosity $\mu_b = 0$). In contrast with the on-axis case, in the off-axis sub-solution the walls are straining in the same verse along x and the total volume of fluid domain is changing, with frequency ω. For reference, see Figure 2.3.1. Hence, it is wise to introduce and exploit the following relationship, which moves the origin of the reference frame to the free end of the beam:

$$\mathbf{v} = \mathbf{v}|_{x=L} + \mathbf{V} \tag{2.5.2}$$

with boundary conditions

$$\mathbf{V}|_{z=z_0 \pm h_{fluid}/2} = \begin{cases} i\omega z_0 \left(\frac{dW}{dx} - \frac{dW}{dx}\Big|_{x=L} \right) \hat{\mathbf{x}} & 0 \leq x \leq L \\ -i\omega z_0 \left. \frac{dW}{dx} \right|_{x=L} \hat{\mathbf{x}} & -L_c \leq x \leq 0 \end{cases} \tag{2.5.3}$$

By so doing, we build a reduced problem which represents a channel held fixed at its closed end, whose sidewalls are straining in their plane in an infinite fluid reservoir.

The scaling factors are:

$$x_s = L, \qquad z_s = h_{fluid}, \qquad u_s = i\omega z_0 \left. \frac{dW}{dx} \right|_{x=L}, \qquad w_s = \frac{h_{fluid}}{L} u_s, \qquad P_s = \frac{\mu u_s L}{h_{fluid}^2} \tag{2.5.4}$$

Substituting the scaling factors and equation 2.5.2 into 2.5.1, the governing equations become:

$$\frac{\partial \bar{u}}{\partial \bar{x}} + \frac{\partial \bar{w}}{\partial \bar{z}} = i\alpha \bar{P}, \qquad -i\beta(1 + \bar{u}) = -\frac{d\bar{P}}{d\bar{x}} + \frac{\partial^2 \bar{u}}{\partial \bar{z}^2} \tag{2.5.5}$$

At this stage, we define:

$$\beta = \frac{\rho_0 \omega h_{fluid}^2}{\mu}, \qquad \gamma = \left(\frac{\omega L}{c} \right)^2, \qquad \alpha = \frac{\gamma}{\beta} \tag{2.5.6}$$

with

$$\rho = \rho_0 + \rho_0 k P \qquad k = \frac{1}{(\rho_0 c^2)} \tag{2.5.7}$$

where k is the fluid compressibility [$Pa^{-}1$], c is the speed of sound and ρ_0 is the density at ambient pressure. By making use of the Helmholtz decomposition of a general vector field [27], we define:

$$\bar{u}(\bar{x}, \bar{z}) = f(\bar{x})k'(\bar{z}) + h(\bar{x}), \qquad \bar{w}(\bar{x}, \bar{z}) = -f'(\bar{x})k(\bar{z}) \tag{2.5.8}$$

and, substituting 2.5.8 into 2.5.5 we obtain the following problems:

$$\frac{dh}{d\bar{x}} = i\alpha \bar{P}, \qquad \frac{d\bar{P}}{d\bar{x}} = Bf(\bar{x}) + i\beta \left[1 + h(\bar{x}) \right] \tag{2.5.9}$$

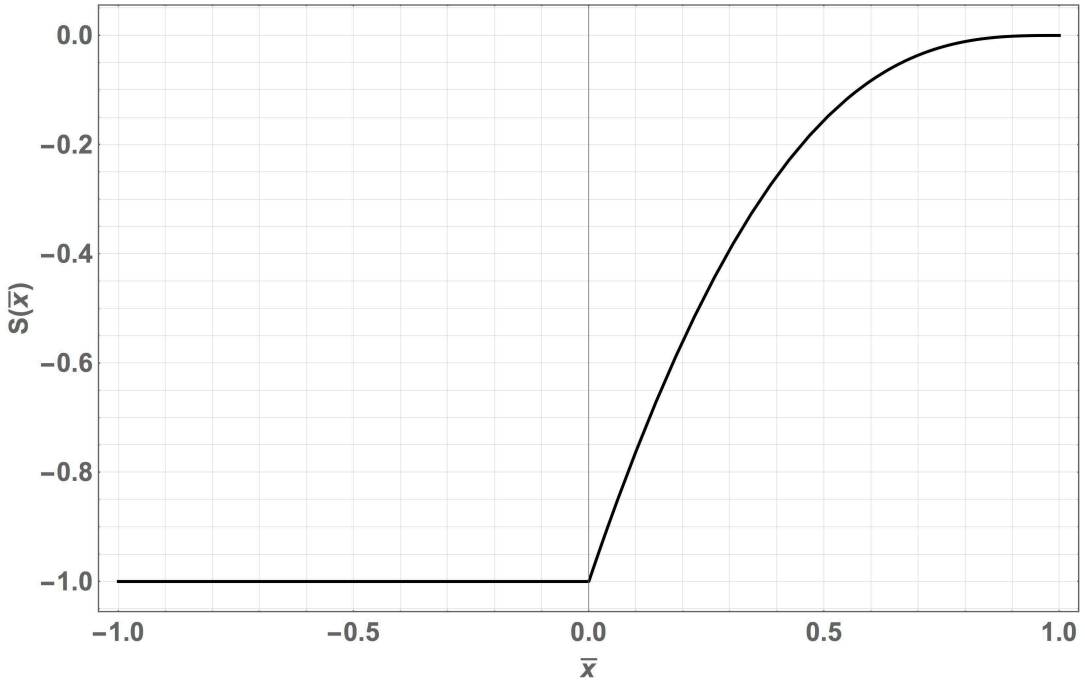

Figure 2.5.1: *$S(\bar{x})$ for both the components of fluid velocity field in the Helmholtz decomposition approach*

$$\begin{cases} k'''(\bar{z}) + i\beta k'(\bar{z}) = B \\ k\left(\pm\frac{1}{2}\right) = 0 \\ k'\left(\pm\frac{1}{2}\right) = 1 \end{cases} \tag{2.5.10}$$

$$f(\bar{x}) = S(\bar{x}) - h(\bar{x}) \tag{2.5.11}$$

$$S(\bar{x}) = \begin{cases} -1 + \dfrac{\dfrac{dW}{d\bar{x}}}{\left.\dfrac{dW}{d\bar{x}}\right|_{\bar{x}=1}} & : 0 \leq \bar{x} \leq 1, \\ -1 & : -\bar{L}_c \leq \bar{x} < 0 \end{cases} \tag{2.5.12}$$

The solutions for $k(\bar{z})$ and $B(\beta)$ are obtained in Mathematica (release 10.4):

$$k(\bar{z};\beta) = \frac{\sinh\left((1-i)\sqrt{\frac{\beta}{2}}\bar{z}\right) - 2\bar{z}\sinh\left(\frac{1-i}{2}\sqrt{\frac{\beta}{2}}\right)}{(1-i)\sqrt{\frac{\beta}{2}}\cosh\left(\frac{1-i}{2}\sqrt{\frac{\beta}{2}}\right) - 2\sinh\left(\frac{1-i}{2}\sqrt{\frac{\beta}{2}}\right)} \tag{2.5.13}$$

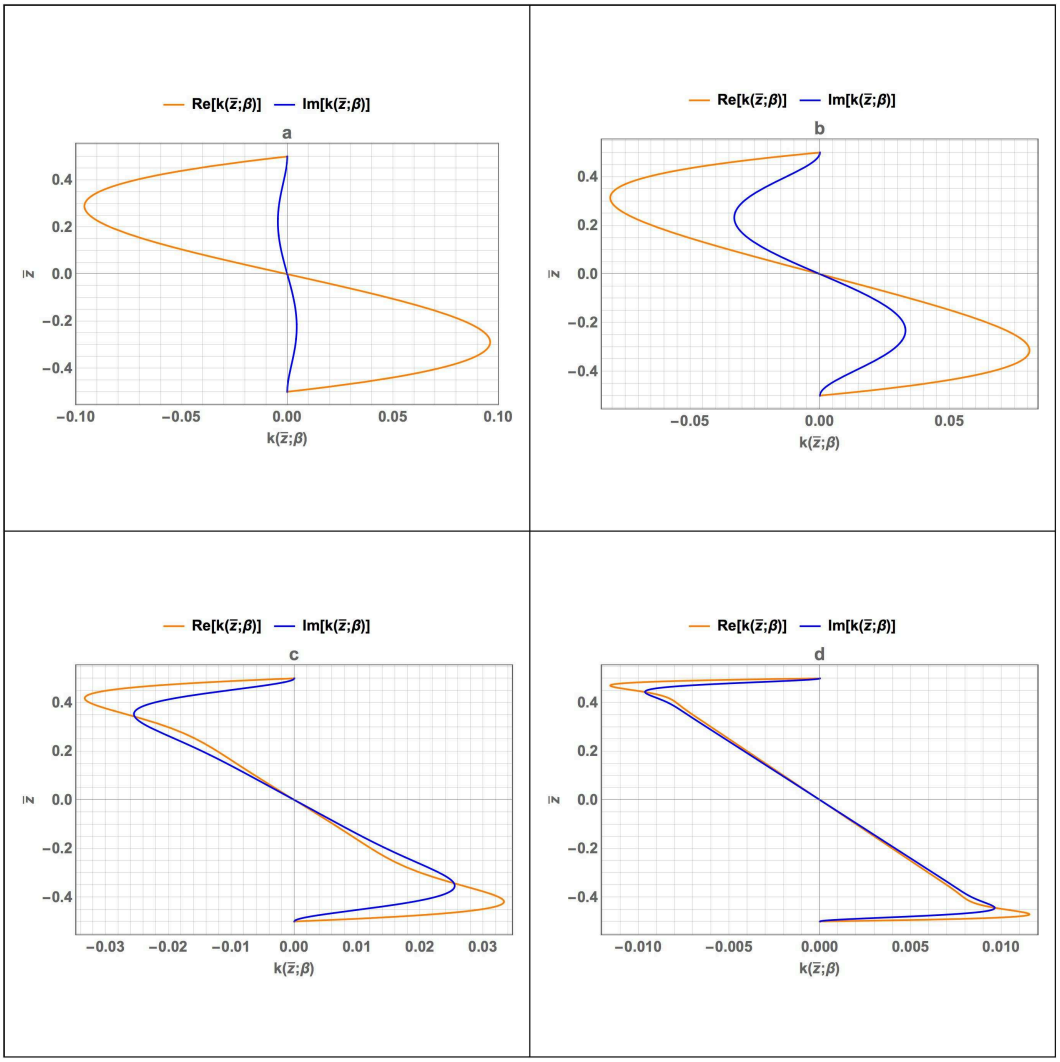

Figure 2.5.2: *Real and imaginary parts of $k(\bar{z})$ for both the components of fluid velocity field in the Helmholtz decomposition approach, with $\gamma = 0.0337$, $L = 250$ μm and for several β and α, showing the effect of decreasing viscosity (increasing β): a) β=5 and α=0.0067, b) β=50 and α=0.00067 , c) β=500 α=0.000067, d) β=5000 α=0.000067*

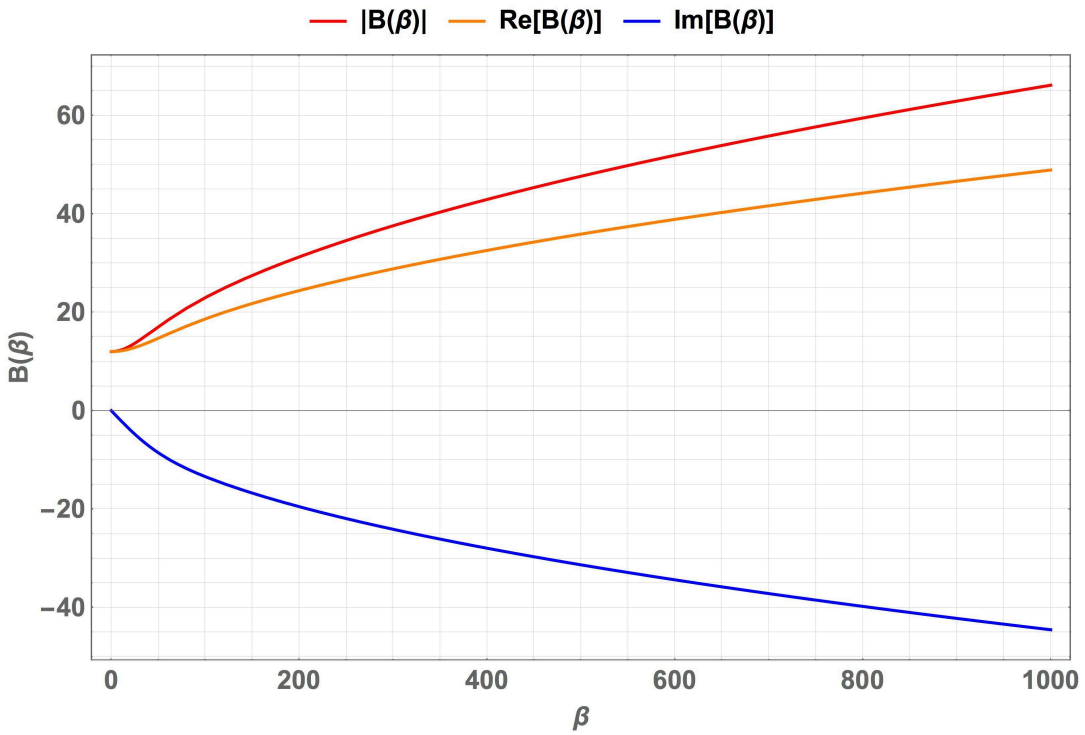

Figure 2.5.3: *Real part, imaginary part and absolute value of B(β)*

$$B(\beta) = \frac{-2i\beta \sinh\left(\frac{1-i}{2}\sqrt{\frac{\beta}{2}}\right)}{(1-i)\sqrt{\frac{\beta}{2}}\cosh\left(\frac{1-i}{2}\sqrt{\frac{\beta}{2}}\right) - 2\sinh\left(\frac{1-i}{2}\sqrt{\frac{\beta}{2}}\right)} \tag{2.5.14}$$

with

$$\lim_{\beta\to 0} Re[B(\beta)] = 12$$

Combining equations 2.5.8, 2.5.11 and 2.5.9 we obtain the problem for $h(\bar{x};\alpha,\beta)$:

$$\frac{d^2h}{d\bar{x}^2} + \alpha(\beta + iB)h = i\alpha BS(\bar{x}) - \alpha\beta \tag{2.5.15}$$

whose solution is found through the Green's function method [18] obtaining:

$$\begin{aligned} h(\bar{x}) = -\frac{\alpha}{Mcos[M(1+\bar{L}_c)]}\Bigg\{ & sin[M(1-\bar{x})]\int_{-\bar{L}_c}^{\bar{x}} [iBS(x') - \beta]cos[M(x'+\bar{L}_c]dx' \\ & + cos[M(\bar{x}+\bar{L}_c)]\int_{\bar{x}}^{1} [iBS(x') - \beta]sin[M(1-x')]dx'\Bigg\} \end{aligned} \tag{2.5.16}$$

with

$$M = \sqrt{\alpha(\beta + iB)} \qquad and \qquad \bar{P} = \frac{1}{i\alpha}\frac{dh}{d\bar{x}} \tag{2.5.17}$$

From Mathematica, we computed:

$$\lim_{\alpha\to 0} h(\bar{x};\alpha,\beta) = 0 \tag{2.5.18}$$

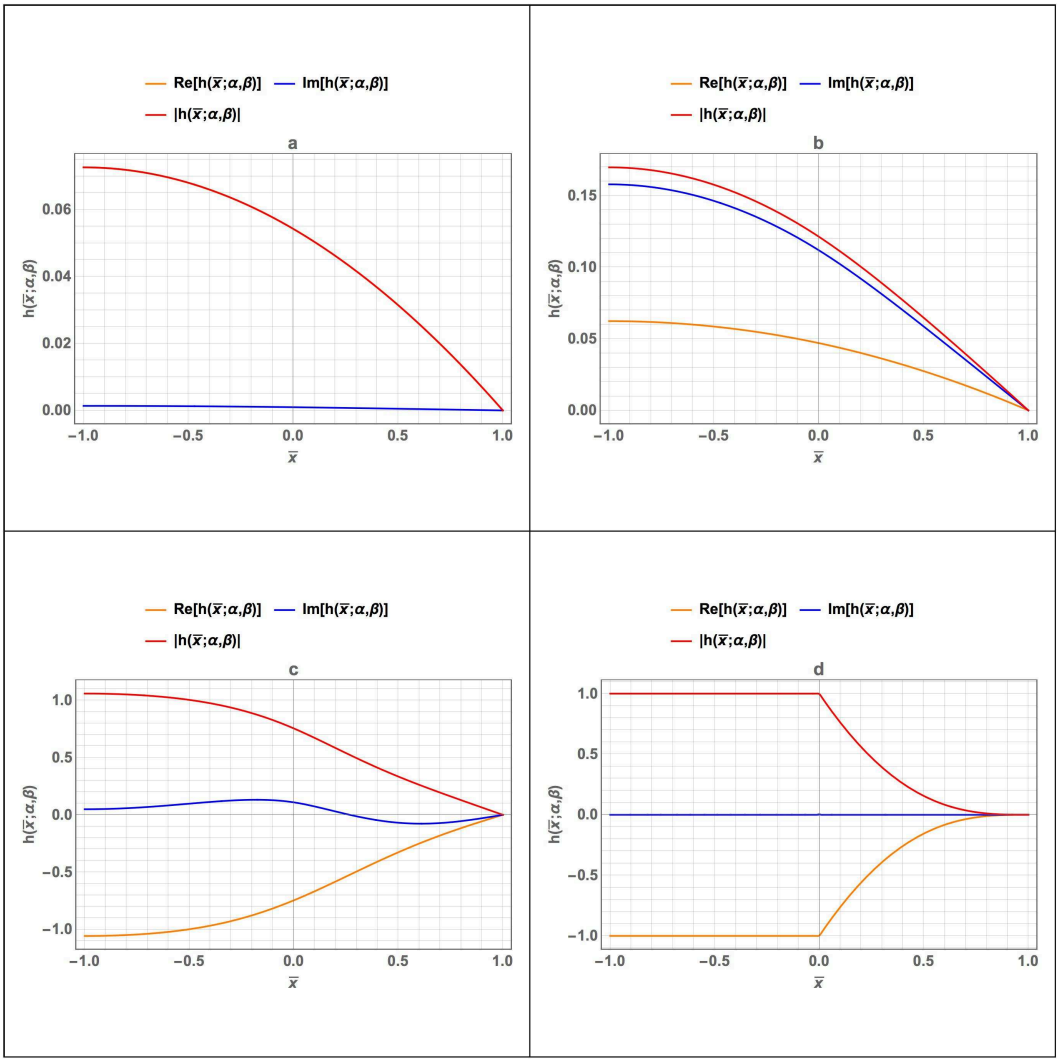

Figure 2.5.4: *Real part, imaginary part and absolute value of $h(\bar{x};\alpha,\beta)$ obtained with the Green's function method, with γ = 0.0337, L = 250 μm and for several β and α, showing the effect of decreasing viscosity (increasing β): a) β=500 and α=0.000067, b) β=0.5 and α=0.067 , c) β=0.005 and α=6.7, d) $\beta \to 0$ and $\alpha \to \infty$*

Incompressible flow: $\alpha \to 0$ In this case, the velocity field is given by:

$$\mathbf{v} = i\omega z_0 \frac{dW}{dx}\bigg|_{x=L} \left((1 + S(\bar{x})k'(\bar{z}))\hat{\mathbf{x}} - \frac{h_{fluid}}{L} S'(\bar{x})k(\bar{z})\hat{\mathbf{z}} \right) \tag{2.5.19}$$

Compressible flow: $\alpha > 0$ In this case, the velocity field is given by:

$$\mathbf{v} = i\omega z_0 \frac{dW}{dx}\bigg|_{x=L} \left(\left(1 + h(\bar{x}) + [S(\bar{x}) - h(\bar{x})]k'(\bar{z})\right) \hat{\mathbf{x}} - \frac{h_{fluid}}{L}[S'(\bar{x}) - h'(\bar{x})]k(\bar{z})\hat{\mathbf{z}} \right) \tag{2.5.20}$$

Hereinafter, we neglect the z-component, as much smaller than the x-component of a factor $\frac{h_{fluid}}{L}$. This means that the flow is expected to be locally directed parallel to the neutral axis of the beam.

2.5.1.1 Normalized wavenumber

As said, the parameter $\gamma = \left(\frac{\omega L}{c}\right)^2$ has been defined "Normalized wavenumber". The reason why this is done is here provided: it is known that $\frac{\omega}{c} = \frac{2\pi}{\lambda}$, which is used to give $\gamma = \left(\frac{L}{\lambda} 2\pi\right)^2$. The last equation shows that $\gamma = \left(\frac{cantilever\ length}{acoustic\ wavelength}\, 2\pi\right)^2$ and, apart from a factor 2π, it is the inverse of a normalized wavelength. Importantly, acoustic effects are important if $\gamma \gg 1$, which also means $L \gg \lambda$. Therefore, the frequency of acoustic waves is so big that "many pressure waves" are being transmitted in the fluid domain defined by $x \in [0, L]$ and these will affect the fluid flow and, consequently, the energy dissipation.

2.5.2 Volumetric flux

The volumetric flux is given by:

$$q(\bar{x}) = \iint_A \mathbf{v} \cdot \mathbf{dA} = \int_0^{b_f} \int_{-\frac{h_f}{2}}^{\frac{h_f}{2}} \mathbf{v} \cdot \hat{\mathbf{n}} dy dz = \int_0^{b_f} dy \int_{-\frac{1}{2}}^{\frac{1}{2}} u(\bar{x}, \bar{z}) h_f d\bar{z} = \tag{2.5.21}$$

$$= \frac{j\omega z_0}{L} \frac{\partial W}{\partial \bar{x}}\bigg|_{\bar{x}=1} h_f b_f \left(\int_{-\frac{1}{2}}^{\frac{1}{2}} (1 + h(\bar{x}) d\bar{z} + \int_{-\frac{1}{2}}^{\frac{1}{2}} (S(\bar{x} - h(\bar{x})k'(\bar{z}) d\bar{z} \right) \tag{2.5.22}$$

and finally the volumetric flux entering the system at the normalized position $\bar{x} = \bar{L}_c$ is:

$$q(-\bar{L}_c) = \frac{j\omega z_0}{L} \frac{\partial W}{\partial \bar{x}}\bigg|_{\bar{x}=1} h_f b_f [1 + h(\bar{L}_c)] \tag{2.5.23}$$

From Mathematica (release 10.4) we computed the limit case when compressibility $\alpha \to \infty$ and found out that

$$\lim_{\alpha\to\infty} h(-\bar{L}_c;\alpha,\beta) = -1, \tag{2.5.24}$$

thus the volumetric flux is zero. This was expected as the infinitely compressible case ideally corresponds to an infinitely rarefied fluid, such as vacuum.

2.5.3 Energy dissipation

In the off-axis case the rate-of-strain of energy dissipation in the compressible case is given by:

$$\bar{\bar{e}} = \frac{i\omega z_0}{2h_{fluid}} \frac{\partial W}{\partial x}\bigg|_L [S(\bar{x}) - h(\bar{x})]k''(\bar{z})(\hat{\mathbf{x}}\hat{\mathbf{z}} + \hat{\mathbf{z}}\hat{\mathbf{x}}) \tag{2.5.25}$$

In the incompressible case it reduces to:

$$\bar{\bar{e}} = \frac{i\omega z_0}{2h_{fluid}} \frac{\partial W}{\partial x}\bigg|_L [S(\bar{x})]k''(\bar{z})(\hat{\mathbf{x}}\hat{\mathbf{z}} + \hat{\mathbf{z}}\hat{\mathbf{x}}) \tag{2.5.26}$$

Notice that if the off-placement is null, there is no energy dissipation in the fluid. The complete flow energy dissipation will be due only to the on-axis solution.

Using now the scaling factor

$$E_s = 4\pi\rho L b_f h_{fluid}|u_s|^2 \tag{2.5.27}$$

the normalized energy dissipated per cycle is:

$$\begin{aligned} E(\beta)_{diss/cycle} &= \frac{\frac{2\pi\mu}{\omega}\int_{-L_c}^{L}\int_0^{b_f}\int_{-\frac{h_f}{2}}^{\frac{h_f}{2}} 2|e_{12}|^2 dxdydz}{E_s} = \\ &= \frac{2\pi\mu}{\omega} b_f \frac{\int_{-L_c}^{L}\int_{-\frac{h_f}{2}}^{\frac{h_f}{2}} \frac{|u_s|^2}{4h_f^2}|[S(\bar{x}) - h(\bar{x})]k''(\bar{z})|^2 dxdz}{4\pi\rho L b_f h_{fluid}|u_s|^2} = \\ &\frac{\mu}{\omega h_f^2\rho}\frac{1}{4}\int_{-\bar{L}_c}^{1}\int_{-\frac{1}{2}}^{\frac{1}{2}}|[S(\bar{x}) - h(\bar{x})]k''(\bar{z})|^2 d\bar{x}d\bar{z} = \\ &= \frac{1}{4\beta}\int_{-\bar{L}_c}^{1}\int_{-\frac{1}{2}}^{\frac{1}{2}}|[S(\bar{x}) - h(\bar{x})]k''(\bar{z})|^2 d\bar{x}d\bar{z} \end{aligned} \tag{2.5.28}$$

In the incompressible case it reduces to:

$$E(\beta)_{diss/cycle,inc} = \frac{1}{4\beta}\int_{-\bar{L}_c}^{1}\int_{-\frac{1}{2}}^{\frac{1}{2}}|S(\bar{x})k''(\bar{z})|^2 d\bar{x}d\bar{z} \tag{2.5.29}$$

2.6 Complete case: linear combination of on-axis and off-axis solutions

2.6.1 Normalized Quality factor

To derive the normalized quality factor in the complete case, we exploit the fact that the complete fluid flow within the fluid channel is a linear combination of the two flows derived in the on-axis and off-axis case separately: $v_{tot} = v_{on} + v_{off}$. We recall that these two flows have been found solving two different sub-problems with different boundary conditions, the combination of which well describes the physics of the original problem, as discussed in Section 2.1. Using the definition of Q (eq. 2.0.1) and applying the definition of the rate of strain tensor $\bar{\bar{e}}$ (eq. 2.4.34) to the total velocity field, we obtain:

$$Q = F(\beta)C \tag{2.6.1}$$

where $C = \frac{\rho_c}{\rho_f}\frac{h_c}{h_f}\frac{b_c}{b_f}\left(\frac{L}{h_f}\right)^2$ is a normalizing factor and

$$F(\beta) = \frac{\beta}{16\int_{-L_c}^{1}\int_{-\frac{1}{2}}^{\frac{1}{2}}|G(\bar{x},\bar{z})|^2 d\bar{x}\bar{z}} \tag{2.6.2}$$

with

$$\begin{aligned} G(\bar{x},\bar{z}) = &\left(1 - \frac{1-j}{2}\sqrt{\frac{\beta}{2}}\frac{\cosh\left((1-j)\sqrt{\frac{\beta}{2}}\bar{z}\right)}{\sinh\left(\frac{1-j}{2}\sqrt{\frac{\beta}{2}}\right)}\right)\frac{d\bar{W}}{d\bar{x}} + \frac{j\beta\bar{z}_0}{2} \\ &\left(\frac{\sinh\left((1-j)\sqrt{\frac{\beta}{2}}\bar{z}\right)}{(1-j)\sqrt{\frac{\beta}{2}}\cosh\left(\frac{1-j}{2}\sqrt{\frac{\beta}{2}}\right) - 2\sinh\left(\frac{1-j}{2}\sqrt{\frac{\beta}{2}}\right)}\right)[S(\bar{x}) - h(\bar{x},\alpha)]\left.\frac{d\bar{W}}{d\bar{x}}\right|_{\bar{x}=1} \end{aligned} \tag{2.6.3}$$

$$\bar{x} = \frac{x}{L}, \bar{z} = \frac{z - z_0}{h_{fluid}}, \bar{z}_0 = \frac{z_0}{h_{fluid}} \tag{2.6.4}$$

Equation 2.6.2 gives the quality factor of a Suspended Microchannel Resonator (SMR) in the general case of a device with normalized off-placement $\bar{z}_0$ and a fluid with compressibility number α.

2.6.2 Effect of Poisson's ratio

As far as Poisson's effect is concerned we mention the findings in [31], which give an extension of equation 2.6.3; importantly, we underline that the on-axis case is not affected by Poisson's effect, because the total volume doesn't change anyhow. On the contrary, the off-axis term is affected by Poisson through a factor $(1 - 2\nu)$ multiplying $S(\bar{x})$ in 2.6.3.

2.6.3 Effect of Mode number

In this thesis, the effect of the mode number is not investigated deeply: we only remind the reader that the mode number, and more in general the mode shape, surely affects the results, entering the quality factor equation 2.6.2 through $W(\bar{x})$ in $G(\bar{x}, \bar{z})$. In this study, we focus on the first two vibrational modes for each device described in Chapter 4; therefore, to compare with the theoretical results, we just apply equation 2.6.3 changing $W(\bar{x})$ coherently. For further information, we send to [33].

Chapter 3

Theoretical results and discussion

Per aspera ad astra

Marcus Tullius Cicero

Contents

In this chapter, the main theoretical results concerning the flow field developed in the fluid by the solid beam walls movement and the normalized quality factor are presented. Results are split in three parts, in agreement with the theoretical approach: firstly, the on-axis case is investigated, followed by the off-axis pumping mechanism and finally by the results on the linear combination of the two sub-flows.

3.1 On-axis flow and F(β)

3.1.1 Flow field within the channel

Figure 3.1.2 shows the qualitative fluid flow field at different x-positions along the beam for a value of the Reynolds number $\beta = 60$. We immediately notice that the field is split in real and imaginary parts and their combination at different fractions of the period T is also shown, to learn how they interact. The grey dashed line shows the beam velocity field. The beam has an aspect ratio of $\frac{L}{h_f} = 50$. We notice that the no-slip condition is respected everywhere and at the tip of the cantilever there is some difference in velocity between the beam and the fluid: therefore, as also evident from the imposed boundary conditions, the on-axis part of the model does not include any closing wall at the end of the channel.

As a matter of fact, the fluid is not forced to bounce back when in lag with the beam and an unrealistic suction phenomenon takes place and keeps the fluid inside the channel. The only source of momentum onto the fluid comes from the up and bottom wall along z, not strong enough to hold the fluid. We refer to this error as the "tip drop-effect". A plausible real phenomenon would consider a matching of the fluid movement with that of the channel end wall, whatever the viscosity of the fluid is. Figures 3.1.3 and 3.1.4 show similar results for higher β, namely 600 and 6000, showing the effect of viscosity changes. In $\bar{z} = 0$ there is no difference between the beam (which is not straining in $\bar{x}$ along the neutral axis) and the fluid, which is changing verse on the neutral axis.

Figure 3.1.1: *Middle section (red) of a SMR where the theoretical model is developed: the inlet and outlet channels are merged to find an analytical solution; symmetry condition is exploited (X-Y plane)*

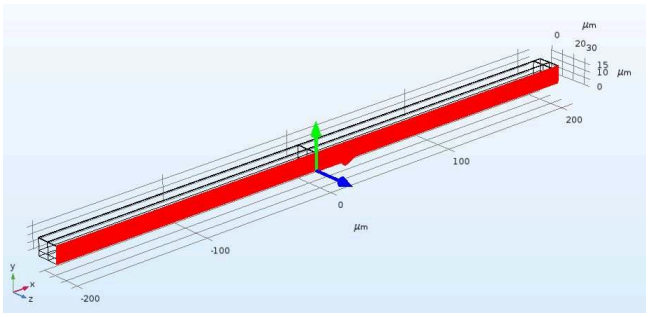

Figure 3.1.5 is more suitable to understand how the fluid moves within the channel: in this case the flow field is computed relatively to the local beam velocity, with the difference calculated point by point; therefore, what we see is how many times the fluid is faster than the theoretical beam that the channel is substituting in that point; furthermore, all values are normalized by the wall velocity

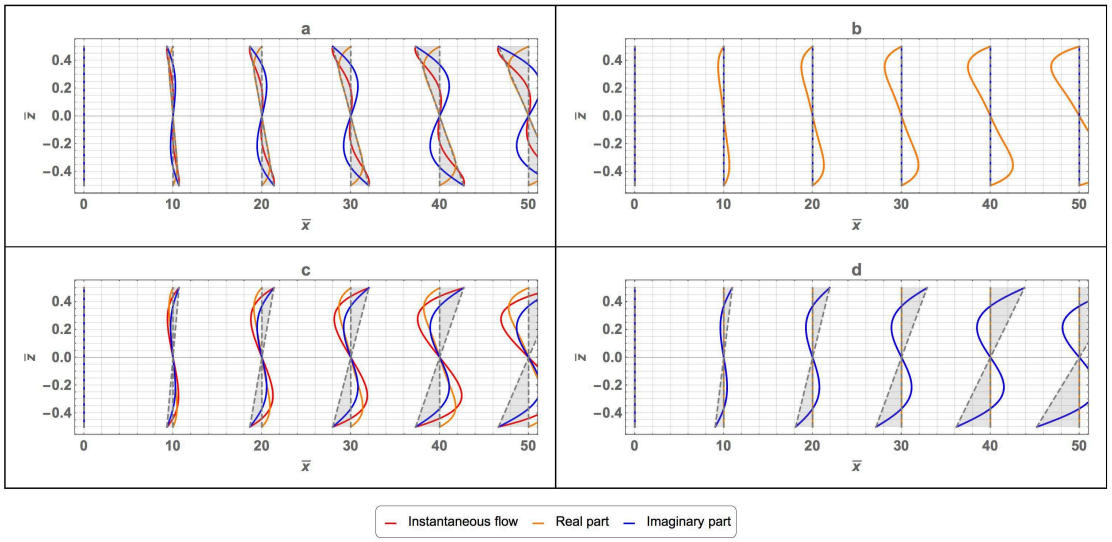

Figure 3.1.2: *On-axis qualitative flow field (not relative) and beam linear velocity field (grey dashed line) for a SMR with* $\frac{L}{h_f} = 50$ *and* $\beta = 60$*; the channel domain is shown and the velocities are scaled by a factor of 1000 for presentation only; the velocity profiles are shown at different* $\bar{x}$*-positions with* $\Delta\bar{x} = 10$ *and at different fractions of the period T; a)* $t = \frac{T}{8}$*, b)* $t = \frac{2T}{8}$*, c)* $t = \frac{3T}{8}$*, d)* $t = \frac{4T}{8}$

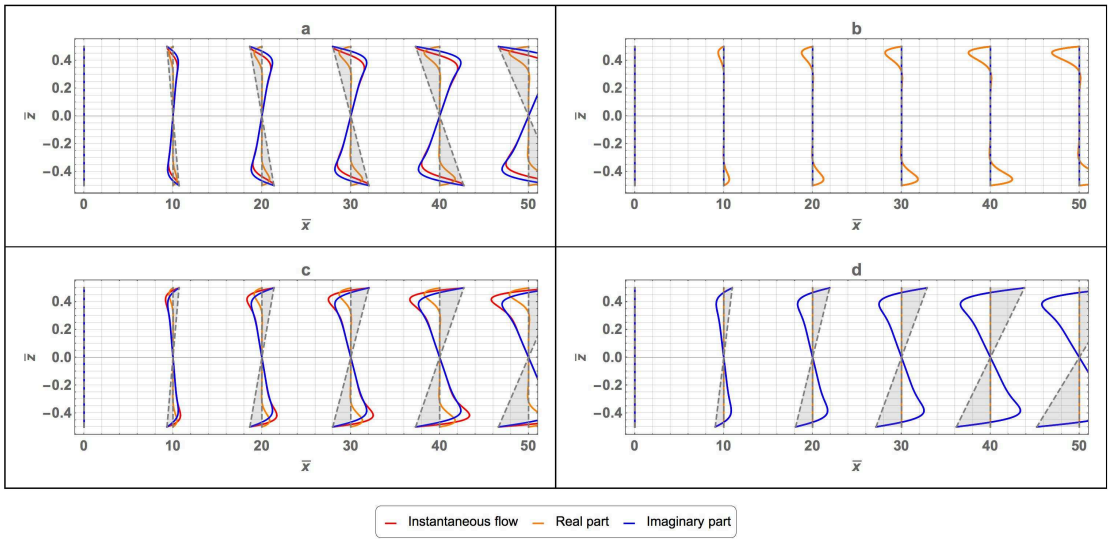

Figure 3.1.3: *On-axis qualitative flow field (not relative) and beam linear velocity field (grey dashed line) for a SMR with* $\frac{L}{h_f} = 50$ *and* $\beta = 600$*; the channel domain is shown and the velocities are scaled by a factor of 1000 for presentation only; the velocity profiles are shown at different* $\bar{x}$*-positions with* $\Delta\bar{x} = 10$ *and at different fractions of the period T; a)* $t = \frac{T}{8}$*, b)* $t = \frac{2T}{8}$*, c)* $t = \frac{3T}{8}$*, d)* $t = \frac{4T}{8}$

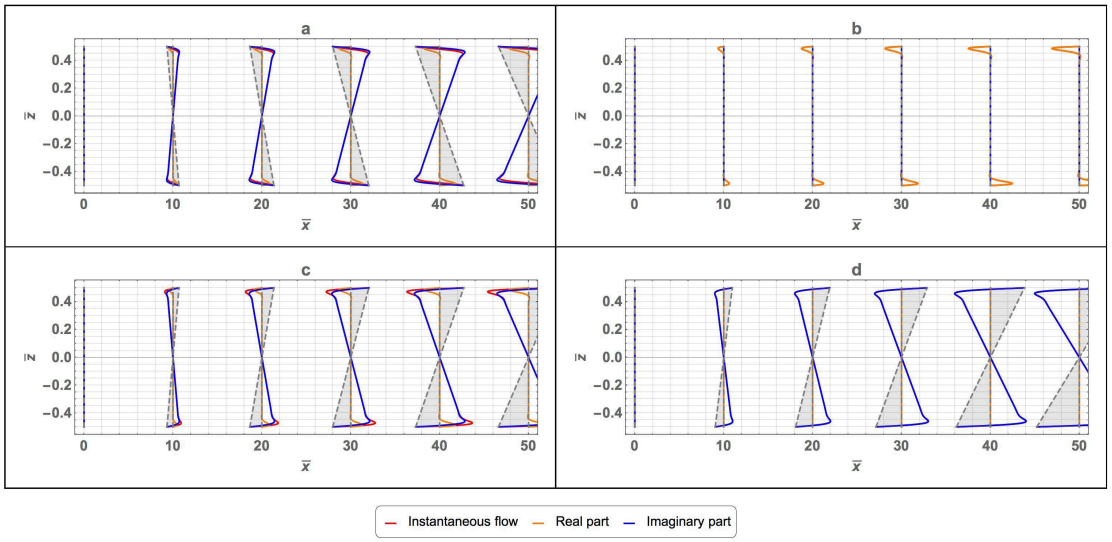

Figure 3.1.4: *On-axis qualitative flow field (not relative) and beam linear velocity field (grey dashed line) for a SMR with* $\frac{L}{h_f} = 50$ *and* $\beta = 6000$*; the channel domain is shown and the velocities are scaled by a factor of 1000 for presentation only; the velocity profiles are shown at different* $\bar{x}$*-positions with* $\Delta\bar{x} = 10$ *and at different fractions of the period T; a)* $t = \frac{T}{8}$*, b)* $t = \frac{2T}{8}$*, c)* $t = \frac{3T}{8}$*, d)* $t = \frac{4T}{8}$

(in $|\bar{z}| = 1/2$) corresponding to the same normalized abscissa. We notice that for very viscous fluids, the relative velocity is almost zero. With this approach, we are pushed to believe a counter-intuitive fact: for very high viscosities, the fluid moves in tandem with the part of solid of which it occupies the place, therefore showing linear behaviour as described by Euler-Bernoulli equation; we will see that increasing viscosity thus leads to zero dissipation and increasing Quality Factor. For inviscid fluids (case c: $\beta \to \infty$), the maximum relative velocity is attained and it is lower or equal to 2.

In $|\bar{z}| = \frac{1}{2}$ the no-slip condition is verified, while for a generic x, the beam velocity is linear in z and the fluid velocity differs from it, depending on β. For high μ, the fluid velocity tends to be linear and in phase with the solid velocity, hence the difference tends to vanish. For low μ, the flow tends to be in counter-phase with respect to the beam. The higher β, the thinner the boundary layer and the bigger the region that is π out-of-phase with the beam. We underline that along $\bar{z}$ the fluid is moving exactly as the beam, being however the z-velocities higher than the x-velocities. The fluid is being pushed up and down, with strength depending on x, by the no-penetration boundary condition. For this reason, we neglect including the z-component in our analysis and only focus on the flow along x. The imaginary part, which dominates the global magnitude of the flow, is chasing the real part.

The "tip drop effect" is again shown in Figure 3.1.6, where the instantaneous velocities, normalized

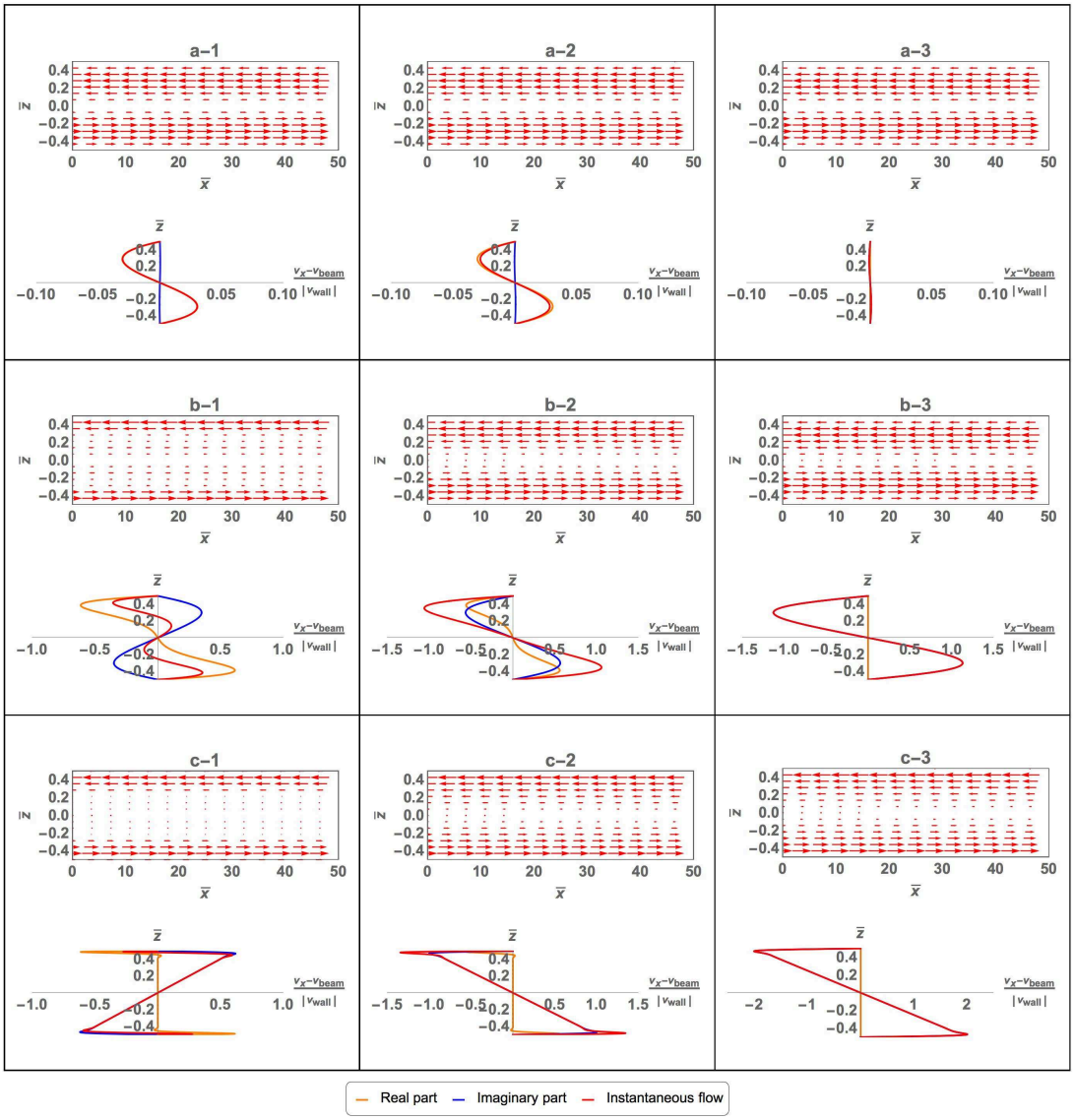

Figure 3.1.5: *On-axis qualitative flow field relative to beam velocity (point by point) and normalized to beam wall velocity for a SMR with* $\frac{L}{h_f} = 50$ *for different* β*: a)* $\beta = 1$*, b)* $\beta = 100$*, c)* $\beta = 10000$ *and at several fractions of the period T: 1)* $t = \frac{T}{5}$*, 2)* $t = \frac{T}{3}$*, 3)* $t = \frac{T}{2}$

with respect to the beam wall velocity, of fluid and beam at the tip for a given β and different fractions of the period T are shown together.

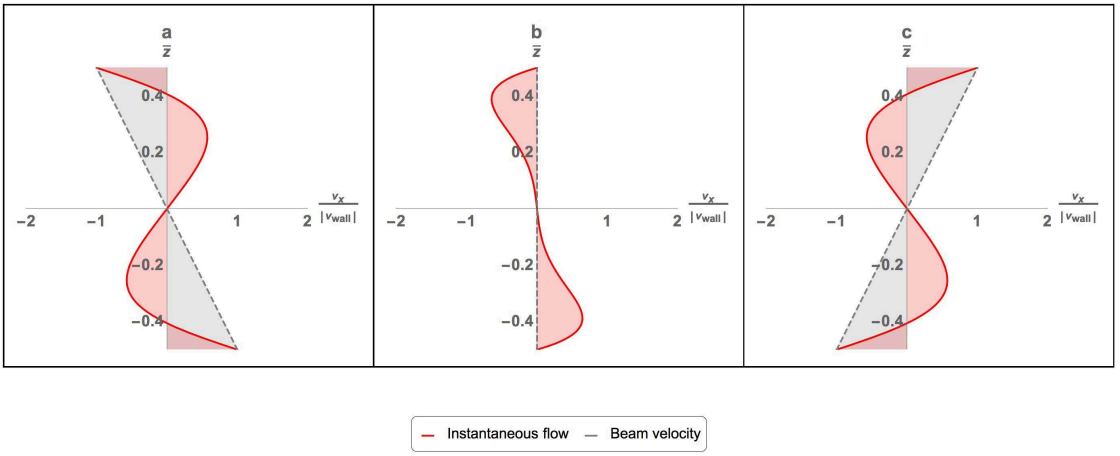

Figure 3.1.6: *On-axis case fluid velocity (not relative) and beam linear velocity (grey dashed line) for a SMR at the tip ($\bar{x} = \frac{L}{h_f} = 50$) with $\beta = 100$; instantaneous velocities, normalized with respect to the beam wall velocity, of fluid and beam are shown at different fractions of the period T; a) $t = \frac{T}{4}$, b) $t = \frac{T}{2}$, c) $t = \frac{3T}{4}$*

3.1.2 Energy Dissipation

The minimum in the Normalized quality factor in the On-axis case occurring at $\beta \simeq 46$ is due to the fact that the distribution of energy dissipation along the channel assumes such a shape that its integral over the volume of the channel itself is maximized. This happens even though the maximum of the energy dissipation distribution (which is always at the wall, regardless the particular value of μ) is getting higher and higher for higher values of β. However, we also underline that the on-axis model is neglecting the closing of the tip, for simplification reasons. This is believed to introduce an error of the order of $\mathcal{O}(\frac{h_f}{L})$, which is reasonably small for small ratios $\frac{h_f}{L}$, as in the practical cases. However, a more precise model would include the tip closing and a corrective term (weighing factor) which would allow the fluid to move in tandem with the channel end-wall in $x = \frac{L}{h_f}$. Whenever such a fluid-solid coincidence happens, the dissipated energy reduces (in the same way of when μ is so high that the fluid tends to the beam) to zero. This is not being described by our model, as shown in the distribution of energy dissipation in Figure 3.1.7, where the dissipation is not going to zero at the channel end-wall, independently from β.

This simplification and other errors of the order of $\mathcal{O}(\frac{h_f}{L})$ are believed to be responsible of the slight

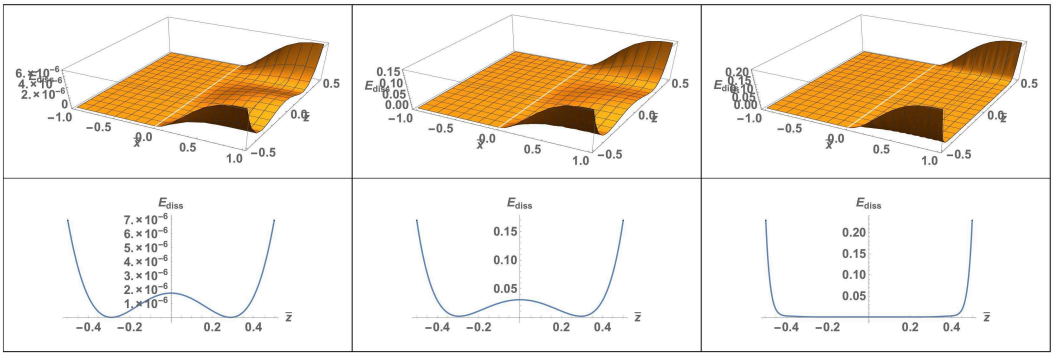

Figure 3.1.7: *Rate of energy dissipation within the channel in the on-axis case; the whole dissipation takes place in the cantilever proper: integration of the distribution of dissipated energy over the channel gives the dissipated energy, inverse of the Quality Factor. Top: $\beta = 0.001$, $\beta = 46$, $\beta = 1000$; Bottom: same, at $\bar{x} = 1$ (channel end) only, proving slip-condition or missing channel-end boundary condition in the on-axis case*

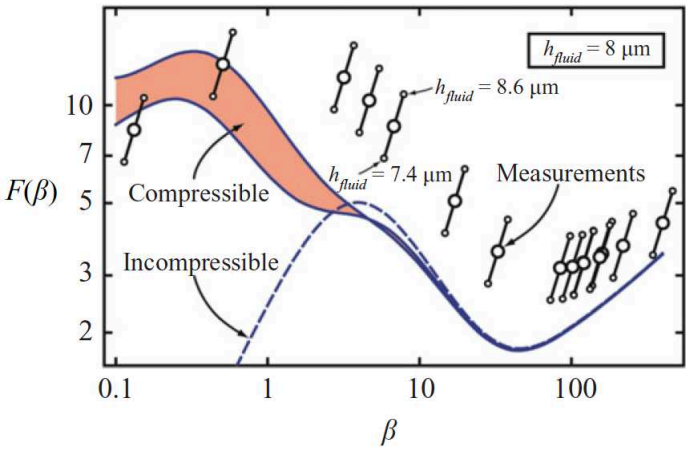

Figure 3.1.8: *Comparison of theoretical model with measurements taken from [32] showing overestimation of energy dissipation by the theoretical model*

discrepancy in the quality factor between experiments and theory, at high β, where the on-axis problem dominates the complete solution. In particular, the theoretical model is predicting lower values of the quality factor because of this overestimation of the energy dissipation, as seen in Figure 3.1.8.

We also recall that the whole dissipation is taking place in the cantilever proper, as the on-axis problem model doesn't include any rigid lead channel: this is trustworthy because the flow is developed only after the entrance of the fluid in the cantilever, as no change in volume occurs and no flow can be developed before the cantilever proper, the vibrations of which are causing the skew-symmetric flow field.

3.1.3 Normalized Quality factor F(β)

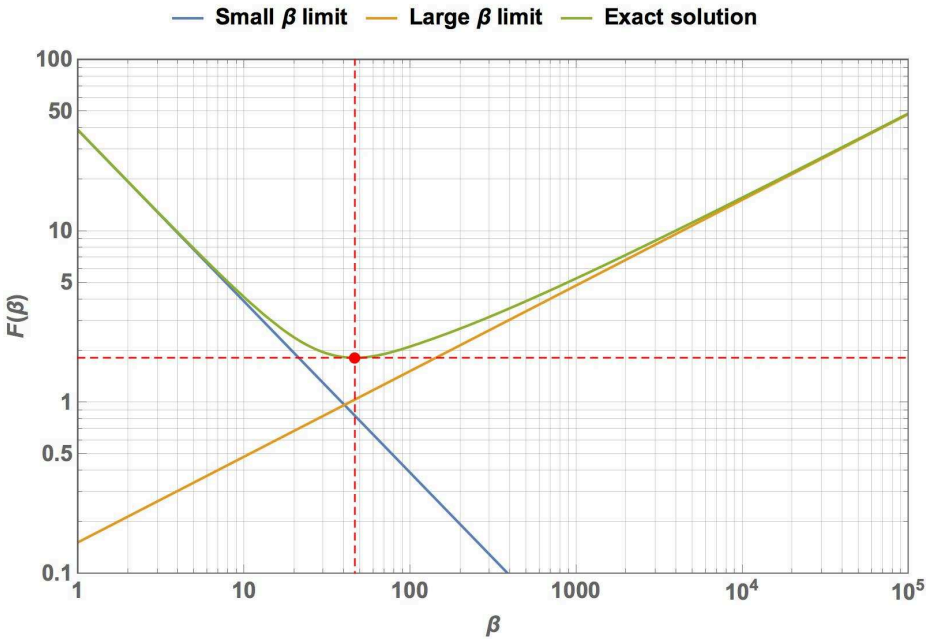

Figure 3.1.9: *On-axis Normalized Quality Factor F(β); both the small β, large β approximations and the exact solution are shown; red dot (46.4348,1.81751) is the minimum of the quality factor*

As previously discussed, the on-axis case does not depend on compressibility. Equations 2.4.46 and 2.4.50 give the Quality Factor in the on-axis case in the small and large β approximations respectively. Together with the exact solution, equation 2.4.43, their trends are shown in Figure 3.1.9. The minimum in this case is F(β)=1.81751 and occurs at β=46.435. We learn that the whole dissipation is taking place in the cantilever proper, as the on-axis problem model coherently does not include any rigid lead channel: this is trustworthy because the flow is developed only after the entrance of the fluid in the cantilever, as no change in volume occurs and no flow can be developed before the cantilever proper, the vibrations of which are causing the skew-symmetric flow field. We underline that the reason why there is no difference in the quality factor if the fluid is compressible or incompressible is that there is no change of volume in the on-axis case, which makes the fluid not change volume too, giving constant density ρ. Thus, there is no difference in the behaviour of a compressible or incompressible fluid, because they both do not experience any $\delta\rho$.

3.2 Off-axis flow and F(β)

3.2.1 Flow field within the channel

3.2.1.1 Incompressible case

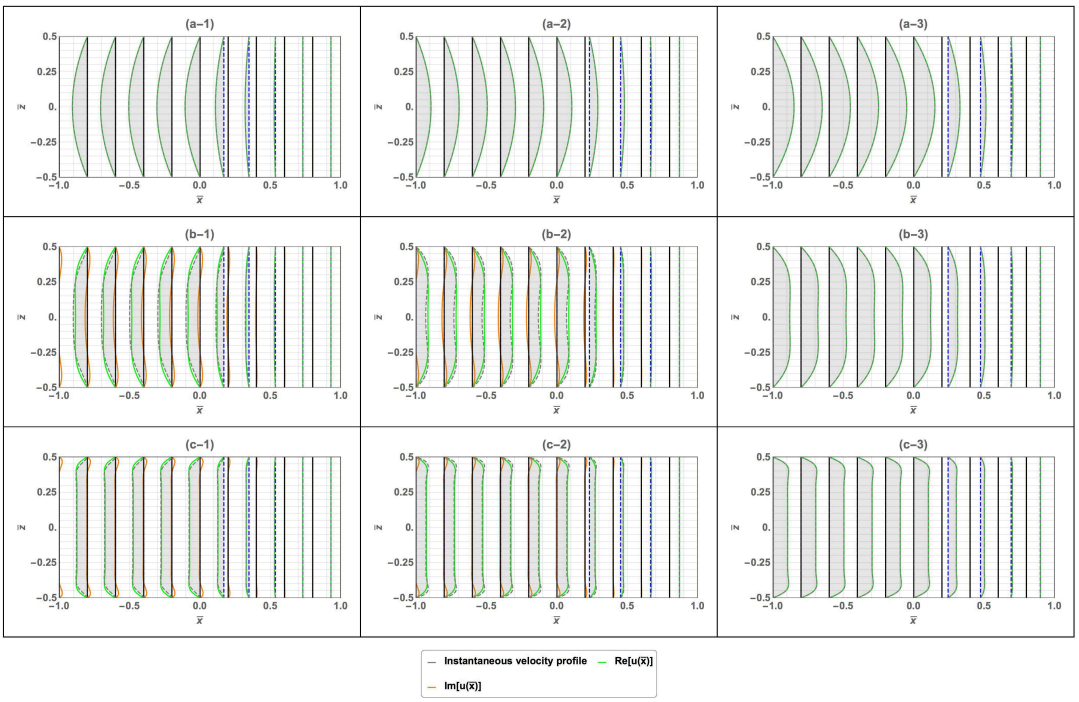

Figure 3.2.1: *Incompressible case qualitative flow field relative to the cantilever wall velocity in the off-axis case at different fractions of the period T and for several values of β: a) β = 0.0001, b) β = 100, c) β = 1000, 1) $t = \frac{3T}{8}$, 2) $t = \frac{5T}{8}$, 3) $t = \frac{6T}{8}$; real (green) and imaginary (orange) parts of the field are shown together with the instantaneous field (grey dashed line and grey filling); black solid lines show the reference positions and the blue dashed lines show the wall velocities for each $\bar{x}$-coordinate; on the walls ($|\bar{z}|$= 0.5) the fluid velocity matches with the wall velocity*

Asymptotic behaviour at small and large β From equation 2.5.19 we can easily obtain an asymptotic behaviour for small and large β of the incompressible flow in the off-axis case. We only need to compute the Taylor series expansion around β=0 (arrested at the first order) and the limit for $\beta \to \infty$ of **v**.

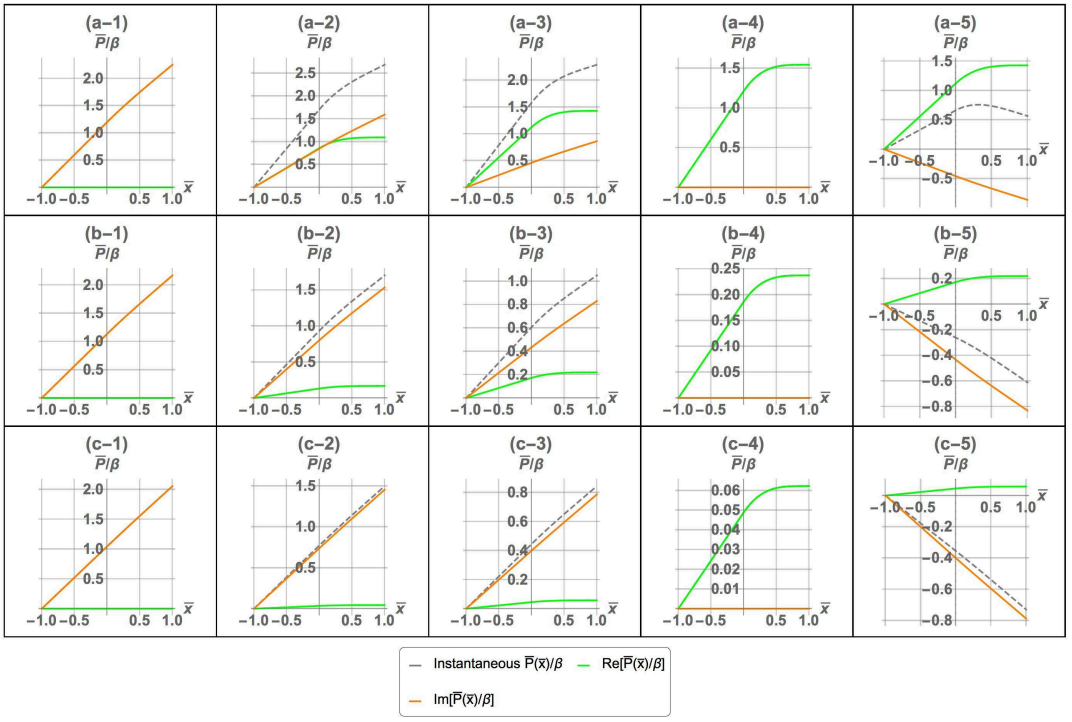

Figure 3.2.2: *Incompressible case scaled pressure (scaled also by β) in the off-axis case ($\bar{z}_0 = 0.1$) with $L = L_c = 250\mu m$ at different fractions of the period T and for several values of β: a) $\beta = 10$, b) $\beta = 100$, c) $\beta = 1000$, 1) $t = 0$, 2) $t = \frac{T}{8}$, 3) $t = \frac{3T}{16}$, 4) $t = \frac{4T}{16}$, 5) $t = \frac{5T}{16}$; real (green) and imaginary (orange) parts of the pressure are shown together with the instantaneous one (grey dashed line)*

1. small β:

   as β doesn't appear in $S(\bar{x})$ or $S'(\bar{x})$, we only focus on $k(\bar{z})$ and $k'(\bar{z})$:

   $$\lim_{\beta \to 0} k(\bar{z}) = -\frac{\bar{z}}{2} + 2\bar{z}^3 \tag{3.2.1}$$

   Instead, the series expansion of $k'(\bar{z})$ gives:

   $$k'(\bar{z}) \approx -\frac{1}{2} + 6\bar{z}^2 - \frac{1}{160} i\beta \left(1 - 24z^2 + 80z^4\right) \tag{3.2.2}$$

   A higher order expansion is useless because the first term dominates the asymptotic behaviour. The vertical component in k(z) is neglected because smaller than the horizontal component of a factor $\frac{h_f}{L}$.

2. large β:

   as far as the high β limit is concerned, we only need to compute the limits for $\beta \to \infty$, $\forall \bar{z} \in (-\frac{1}{2}, \frac{1}{2})$; Mathematica (release 10.4) returns:

   $$\lim_{\beta \to \infty} k(\bar{z}) = 0 \tag{3.2.3}$$

$$\lim_{\beta \to \infty} k'(\bar{z}) = 0 \tag{3.2.4}$$

Therefore, we obtain the following equation which is a good approximation for the two limits of low and high β:

$$v = i\omega z_0 \frac{dW}{dx}\bigg|_{x=L} \hat{\mathbf{x}} \cdot \begin{cases} 1 + S(\bar{x}) \left[6 \left(\frac{z - z_0}{h_{fluid}} \right)^2 - \frac{1}{2} \right] & : \quad \beta \to 0 \\ 1 & : \quad \beta \to \infty \end{cases} \tag{3.2.5}$$

We recall that $S(\bar{x}) = -1,\ \bar{x} < 0$ (Figure 2.5.1), therefore the parabolic profile is theorized constant in $\bar{x}$ in the incompressible case (Figure 3.2.1) before the fluid enters the proper cantilever, as the pressure function also prescribes (see Figure 3.2.2).

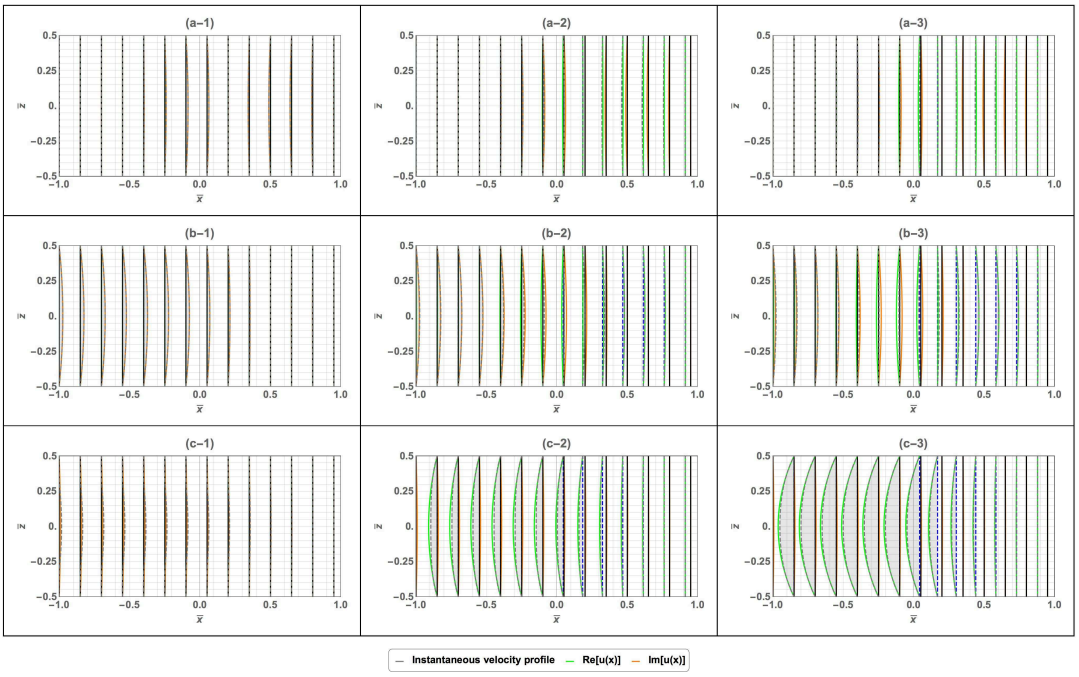

Figure 3.2.3: *Compressible case qualitative flow field relative to the cantilever wall velocity in the off-axis case ($\bar{z}_0 = 0.1$) with $L = L_c = 250\mu m$, $\gamma = 0.03$ at different fractions of the period T and for several values of β and $\alpha = \frac{\gamma}{\beta}$, showing effects of decreasing compressibility: a) ($\beta = 0.03$, $\alpha = 1$), b) ($\beta = 0.1$, $\alpha = 0.3$), c) ($\beta = 10$, $\alpha = 0.003$), 1) $t = \frac{3T}{8}$, 2) $t = \frac{5T}{8}$, 3) $t = \frac{6T}{8}$; real (green) and imaginary (orange) parts of the field are shown together with the instantaneous field (grey dashed line and grey filling); black solid lines show the reference positions and the blue dashed lines show the wall velocities for each $\bar{x}$-coordinate; on the walls ($|\bar{z}| = 0.5$) the fluid velocity matches with the wall velocity*

3.2.1.2 Compressible case

Equation 2.5.20 gives the off-axis flow field in the compressible case; Figure 3.2.3 shows how the fluid moves within the channel, relatively to the wall velocity, when the walls are straining along x.

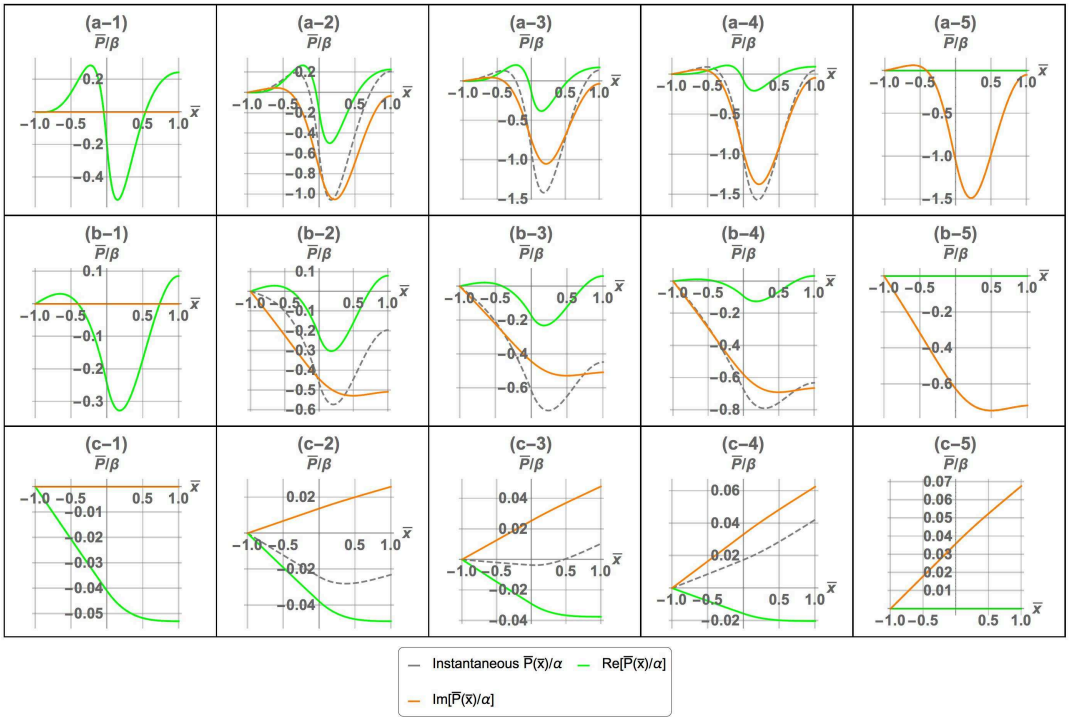

Figure 3.2.4: *Compressible case scaled pressure (multiplied by β) in the off-axis case ($\bar{z}_0 = 0.1$) with $L = L_c = 250\mu m$, $\gamma = 0.03$ at different fractions of the period T and for several values of β and $\alpha = \frac{\gamma}{\beta}$: a) $\beta = 0.01$, b) $\beta = 0.1$, c) $\beta = 10$, 1) $t = 0$, 2) $t = \frac{T}{16}$, 3) $t = \frac{T}{8}$, 4) $t = \frac{3T}{16}$, 5) $t = \frac{4T}{16}$; real (green) and imaginary (orange) parts of the pressure are shown together with the instantaneous one (grey dashed line)*

3.2.2 Normalized Volumetric flux

In the off-axis case we can introduce a new interesting variable, which was missing for physical reasons in the on-axis case: the volumetric flux due to the pumping phenomenon brought about by the coherent straining of the top and bottom walls of the channel. The normalizing factor for the volumetric flux is:

$$q_s = u_s h_{fluid} b_{fluid} \tag{3.2.6}$$

Substitution in equation 2.5.21 leads to:

$$\bar{q} = 1 + h(-\bar{L}_c) \tag{3.2.7}$$

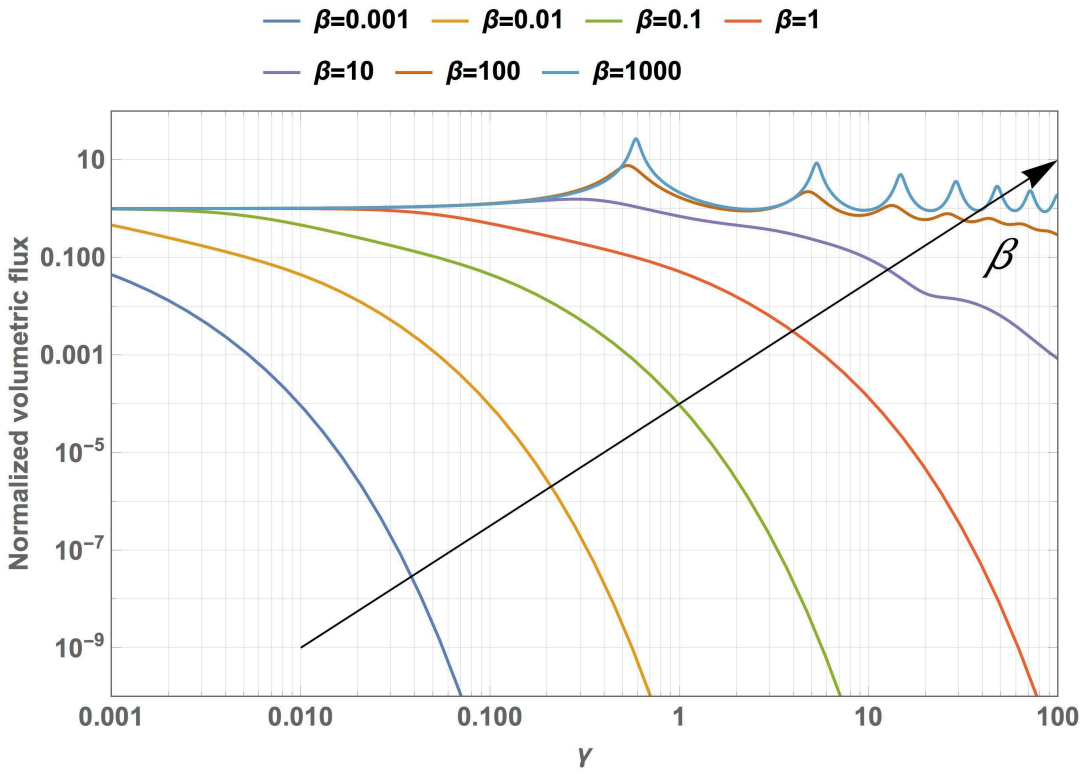

Figure 3.2.5: *Normalized volumetric flux as a function of the normalized wavenumber γ for different β*

Notice that the real flux depends on z_0 and the channel dimensions through the scaling factor. In figure 3.2.5 the normalized volumetric flux is shown for several values of β, and reasonings on its trend help to understand the phenomenology that causes strong oscillations in the quality factor in Figure 3.2.6. In previous sections, we discussed on how high values of β correspond to low values of viscosity μ, and vice-versa. At this point, when dealing with a compressible flow, we need to bear in mind how high viscosity not only brings up dissipation, but also damps out the volumetric flux due to the pumping mechanism. Figure 3.2.5 proves the existence of resonance phenomena within the fluid, strongly dependent on the value of β. We first notice that the system is becoming increasingly damped with increasing β: this corresponds to either a less viscous fluid or a higher resonance frequency (mode number).

We now discuss the effects of different values of β, γ and α on the volumetric flux (Figure 3.2.5). Independently from β, the general trend for increasing γ is a decreasing volumetric flux, which is coherent with the fact that $\alpha = \frac{\gamma}{\beta} \to \infty$ for $\gamma \to \infty$, giving zero volumetric flux as in equation 2.5.24. Physically, this was expected because infinite compressibility corresponds to an infinitely rarefied gas, such as vacuum. However, smaller β give high α earlier in the γ space. Therefore, it may happen that when β is very small (both high friction and high damping), even with small

γ, compressibility α could be very high, making resonance appear. As a matter of fact, increasing the acoustic wavenumber in this case returns an immediate drop in the volumetric flux, such that resonance behaviour is negligible. On the other hand, for high β, damping is really small and, as compressibility is included in the model, the fluid is provided with elastic properties. As α depends on γ, when γ is small $\alpha \to 0$, giving unitary volumetric flux, while when γ is high α increases and, for some combinations of these two values, resonance can manifest itself because viscosity is low for high β.

To sum up, for very small β (very high damping) the resonance peaks die out, while for very high β (very low damping) resonance peaks appear. At small γ, when β is high (low damping or high inertia), compressibility is already quite low (almost incompressible fluid) which means the normalized volumetric flux has already reached the unitary asymptotic value. At small γ, when β is small γ and β are comparable. The smaller β is, the smaller the volumetric flux at the entrance, because the fluid is more and more viscous for lower β and still compressible (as α is not yet 0), therefore it hasn't reached the asymptotic unitary value of an incompressible fluid yet.

3.2.3 Quality factor F(β)

Effect of γ The quality factor as a function of γ in the off-axis case is shown in Figure 3.2.6: reasonings in subsection 3.2.2 can be directly applied to this graph to get to the same conclusions.

The general trend of $F(\gamma;\beta)$ in the off-axis case is the following: increasing γ for a given β leads to an increase of the quality factor; the smaller the β, the larger the Q increase. However, the behaviour at intermediate γ strongly depends on the particular value of β. The energy dissipation mechanisms in the off-axis case give rise to the following situations:

- at small γ the volumetric flux is unitary, therefore friction between layers of fluid causes smaller quality factors for smaller β; this is due to the fact that the increase of viscosity, which increases the dissipation, dominates over the increase of damping (which should give benefits in terms of quality factor) for this combination of γ and β. The reduction (ultimately until the asymptotic unitary value) of the volumetric flux entering the channel is too little to give benefits while viscosity is increasing. Importantly, decreasing γ more will lead to an asymptotic unitary value of the normalized volumetric flux, which means the parabolic profile has reached an invariant shape and the shear and dissipation cannot change, hence the quality

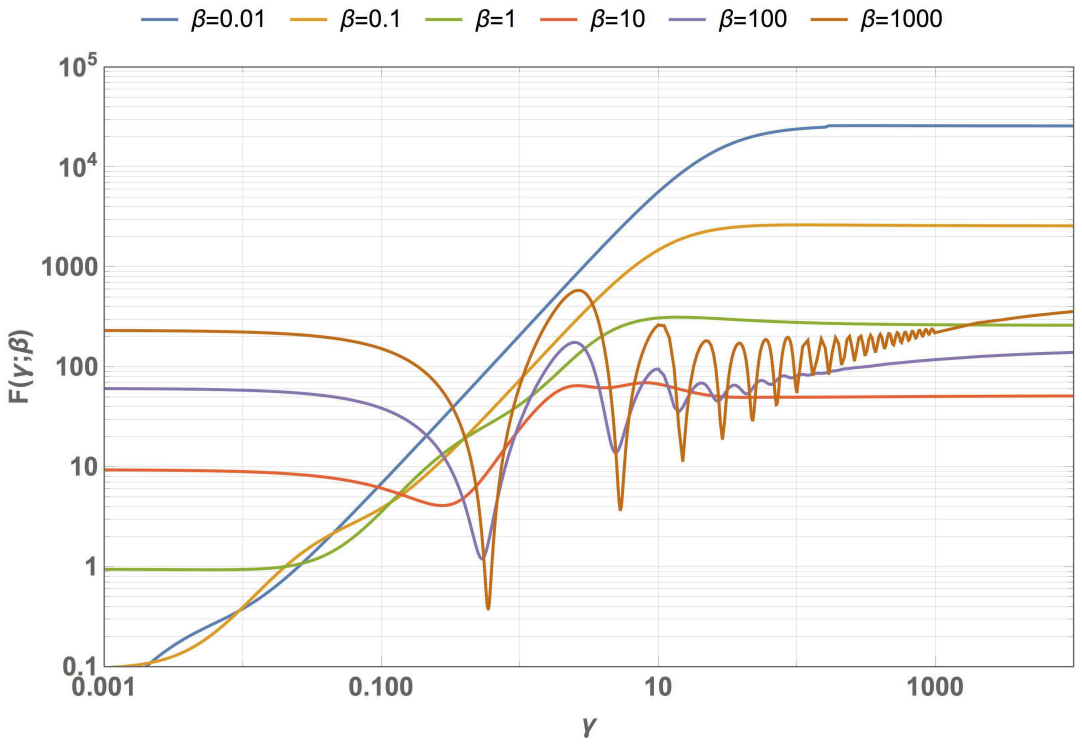

Figure 3.2.6: *Normalized quality factor due to the off-axis solution only in the compressible case as a function of the normalized acoustic wavenumber γ, with $\bar{z}_0 = 0.1$ and for several β*

factor has reached a constant value.

- at high γ, the opposite phenomenon takes place, with a constant value of $F(\gamma;\beta)$ reached when increasing γ. Smaller values of β will give higher constants as for the same γ the volumetric flux is much smaller and the fluid flow is more affected by the value of γ. We underline that intermediate values of β have lower constant value of $F(\gamma;\beta)$ because of the disadvantageous combination of the moderate viscosity value and fluid flow profile.
- at intermediate γ, resonance phenomena occur; low viscosity fluids are more affected by these phenomenon, coherently. For $\beta = 1000$, for $\gamma \simeq 1$ there is a peak in the volumetric flux (Figure 3.2.5), which corresponds to a drop in the quality factor

Effect of β By computing $F(\beta;\gamma)$ and running simulations in COMSOL by constraining the device to deform in-plane (longitudinally), one could compare the theoretical and numerical flow fields; indeed, in both cases the device would be deforming in such a way to produce a pumping mechanism at the origin of energy dissipation in the off-axis case; however, the numerical simulations would incorrectly give no importance to the value of the off-axis placement, while this is known to

increase dissipation; for this reason, quality factors wouldn't be comparable. For what said so far, the effect of β will be investigated in the next section, where the complete case is studied.

3.3 Complete flow and F(β)

We first of all recall that the complete case flow field will be a linear combination of the two sub-solutions (on-axis and off-axis flows), as described in Section 2.6.1, while the Quality factor will be a non-linear combination of Q_{on} and Q_{off} defined by:

$$\frac{1}{Q_{tot}} = \frac{1}{Q_{on}} + \frac{1}{Q_{off}} \tag{3.3.1}$$

from which we easily obtain

$$Q_{tot} = \frac{Q_{on}Q_{off}}{(Q_{on} + Q_{off})} \tag{3.3.2}$$

It is important to realize that when one of the two, say Q_{on} for instance, is much smaller than the other one, then the total quality factor will follow it, as $Q_{tot} \to Q_{on}$, and vice-versa for very small Q_{off}. This explains why the Q_{on} takes over at high β for small enough $\bar{z}_0$ or why Q_{off} dominates at low β in the incompressible case, as in figure 3.3.2. Energy dissipation from one of the two sub-solutions is dominating over the other one.

3.3.1 Incompressible fluid

In this section we compute $F(\beta)$, equation 2.6.2, assuming an incompressible flow ($\alpha \to 0$ and $h(x;\alpha,\bar{\beta}) \to 0$ in this limit) and integrating over the channel domain; we provide both the exact solution (obtained through numerical integration) and the approximated expressions for small β (by Taylor Series expansion around $\beta_0 = 0$, arrested at the first order, of the integrand $G(x,\bar{z})$) and large β. From equation 2.6.2, we obtain:

$$G(\bar{x},\bar{z}) \simeq -6\left(\bar{z}\frac{\partial\bar{W}}{\partial\bar{x}}\bigg|_1 \bar{z}_0 S(\bar{x})\right) + \tfrac{1}{120} i\left(-5\frac{\partial\bar{W}}{\partial\bar{x}} + 60\frac{\partial\bar{W}}{\partial\bar{x}}\bar{z}^2 - 18\,\bar{z}\frac{\partial\bar{W}}{\partial\bar{x}}\bigg|_1 \bar{z}_0 S(\bar{x}) + 120\,\bar{z}^3\frac{\partial\bar{W}}{\partial\bar{x}}\bigg|_1 \bar{z}_0 S(\bar{x})\right)\beta + \mathcal{O}(\beta)^{\frac{3}{2}} \tag{3.3.3}$$

and integrating over the normalized channel height:

$$\int_{-\frac{1}{2}}^{\frac{1}{2}}\int_{-1}^{1} |G(\bar{x},\bar{z})|^2 d\bar{x}d\bar{z} \simeq \int_{-1}^{1}\left[\frac{1}{720}\beta^2\left(\frac{\partial\bar{W}}{\partial\bar{x}}\right)^2 + 3\left(\frac{\partial\bar{W}}{\partial\bar{x}}\bigg|_1\right)^2 \bar{z}_0^2 S(\bar{x})^2 + \frac{\beta^2\bar{z}_0^2 S(\bar{x})^2}{2800}\right] d\bar{x} \tag{3.3.4}$$

Therefore, equation 2.6.2 becomes:

$$F_{small}(\beta) = \frac{38.73\beta}{\beta^2 + 4086.86\left(1 + \frac{\beta^2}{8400}\right)\bar{z}_0}, \qquad \beta \ll 1 \tag{3.3.5}$$

We underline that the same result has been found when computing the approximated rate-of-strain tensor (from the series expansion of the total velocity field), confirming the validity of this solution with respect to what given in [32][1].

Similarly to what done in section 2.4.3, integrating eq. 2.6.2, neglecting small terms for $\beta \to \infty$ and rearranging, we obtain the other limit:

$$F_{large}(\beta) = \frac{0.1521\sqrt{\beta}}{1 + 0.2613\ {\bar{z}_0}^2}, \qquad \beta \gg 1 \tag{3.3.6}$$

Notice that if $\bar{z}_0 = 0$ equations 3.3.5 and 3.3.6 give back the quality factor in the on-axis case for small and large β (eq. 2.4.46 and eq. 2.4.50). At this stage we underline a discrepancy with the result at small β provided by the reference work [32]; figure 3.3.1 shows the different behaviours: the own solution well follows the small β behaviour and is believed to be a better approximation than the reference paper one. The maximum occurs at $\beta < 46.434$ and, taking the expression for $\beta \ll 1$, for $\bar{z}_0 \to 0$, it takes place when:

$$\frac{\partial F_{small}(\beta; \bar{z}_0)}{\partial \beta} = 0 \tag{3.3.7}$$

which gives:

$$\beta_{max} = 63.92\bar{z}_0 + \mathcal{O}({\bar{z}_0}^2) \tag{3.3.8}$$

Similarly, we can find the condition for which the turnover in the quality factor vanishes, by imposing that:

$$F_{small}(\beta_{max}; \bar{z}_0) > F_{on}(\beta_{min}) = 1.8175 \tag{3.3.9}$$

which gives:

$$\bar{z}_0 > 0.2959 \tag{3.3.10}$$

Various $\bar{z}_0$ We now discuss the effects of the off-placement of the channel $\bar{z}_0$ on the complete case quality factor.

Increasing $\bar{z}_0$ in the incompressible off-axis case always lowers the quality factor as $\frac{1}{\bar{z}_0^2}$; this behaviour will be preserved in the compressible case, as in Figure 3.3.8.

[1] As a matter of fact, we found the same results as in [32] when integrating equation 3.3.4 using a value of $S(\bar{x}) = 0$ in $-\bar{L}_c \leq \bar{x} < 0$ in equation 2.5.1: we believe the authors of [32] made a typo in their Mathematica code

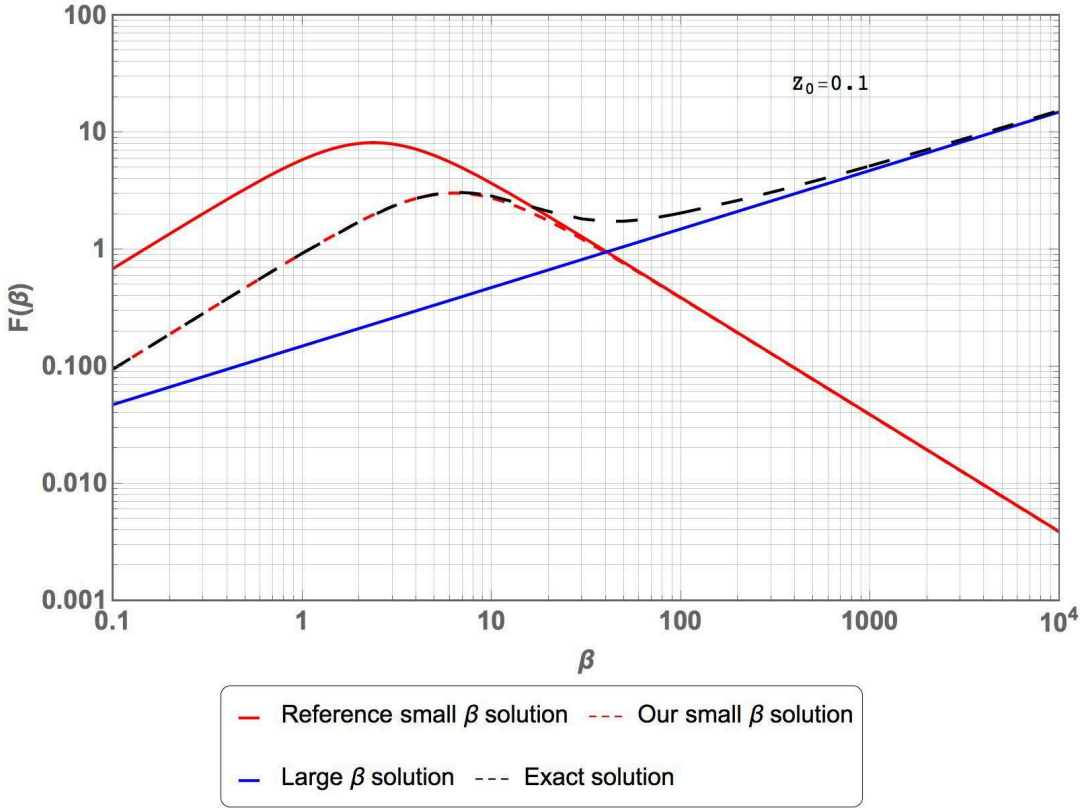

Figure 3.3.1: *Comparison between own solutions and analogous solutions in [32] for $\bar{z}_0 = 0.1$ for the quality factor in the complete incompressible case: red stands for small β solutions (eq. 3.3.5), black for exact solution (eq. 2.6.2), blue for large β solution (eq. 3.3.6); dashed lines refer to the good solutions; purple dot shows the maximum position*

From Figure 3.3.2 we notice that, for higher $\bar{z}_0$, the value of the local maximum in the quality factor decreases and the corresponding β_{max} at which this occurs is shifted at higher β. This means that a bigger off-placement increases the energy dissipation, as expected, and it does it especially at high μ. At low μ there is a slight uniform downshift of the quality factor while the qualitative behaviour of increasing F(β) for increasing β is preserved. Thus, $\bar{z}_0$ does not affect much F(β) at low μ because the off-axis component of the fluid is moving as a plug flow and, regardless the fact that the global intensity of the plug flow increases with $\bar{z}_0$, the shear (and thus dissipation) remains low because the "shape" of the flow does not change and dissipation is constrained in a thin boundary layer.

When $\bar{z}_0$ is very small, we need very high μ (very low β) to let the off-axis dissipation mechanism dominate over the nice fact that the fluid is tending to move as the solid beam, which means we need very high μ to let the off-axis parabolic profile be big enough to let the shear gradient cause big dissipation; furthermore, as soon as the off-axis starts dominating at high μ, μ is so high that the quality factor has a high rate of decrease, which explains the different slope of $F(\beta)$ at high and

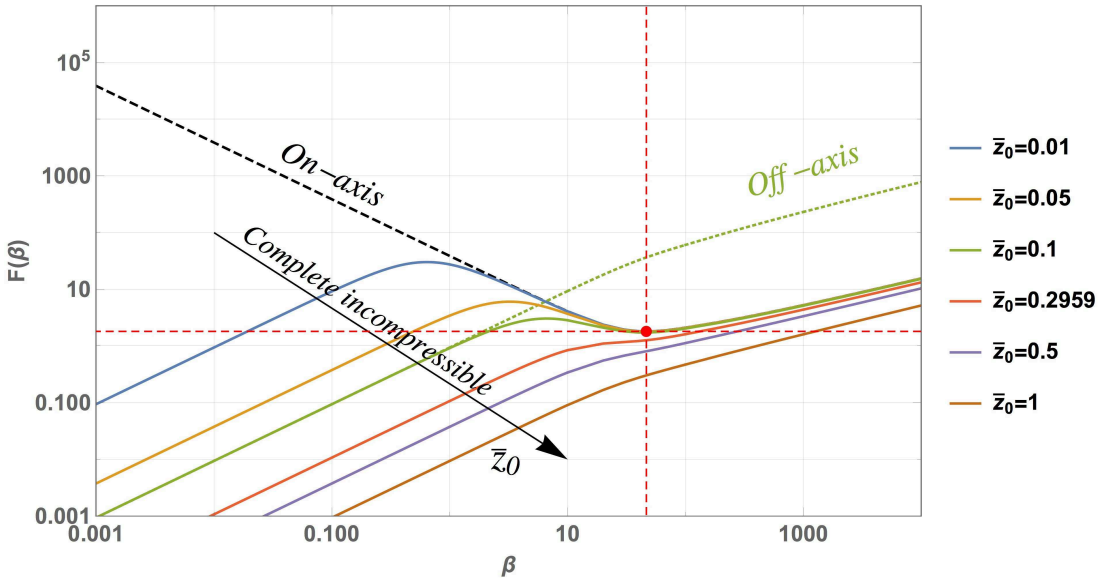

Figure 3.3.2: *Incompressible case Quality Factor for several off-placements of the channel; black dashed line is the on-axis case, whose dissipation mechanism dominates at high β for low $\bar{z}_0$; red dot is the minimum in the quality factor in the on-axis case, the appearance of which depends on the strength of the off-placement: for $\bar{z}_0 > 0.2959$, the non-monotonicity in the quality factor is lost and the off-axis dissipation mechanism dominates everywhere; green dashed line shows how the off-axis dissipation mechanism takes over at low β*

low β.

Ultimately, the off-placement is so big that the maximum disappears and the quality factor becomes monotonically increasing for decreasing viscosity. We therefore lose the nice feature of the maximum F(β) at intermediate β, which is basically due to the increase of F(β) for decreasing $\beta < \beta_{min}$ of the on-axis component. At high $\bar{z}_0$, therefore, the off-axis component of the flow dominates shifting down the whole curve and the maximum disappear; however, F(β) will keep increasing for decreasing μ. Combination of on-axis and off-axis quality factors is clear from figure 3.3.2.

The change in slope of the complete F(β) for high $\bar{z}_0$ is independent of $\bar{z}_0$ and occurs at β=46 where also the off-axis incompressible case quality factor slope slightly increases. This happens when the flow turns from parabolic flow into plug flow, with merging of the boundary layers.

We underline that the error of the order of $\mathcal{O}(\frac{h_f}{L})$ due to the missing boundary condition in the on-axis case model at the end of the channel is having effects only at high β, because at low β the off-axis flow, which correctly includes this boundary condition, dominates. Therefore, the error is coming only from the on-axis case and in [32] Sader et al. claim that it reduces to 0 when the on-axis

component is not bringing about any dissipation (high μ). We put this finding into question and send to Section 5.3.1 for further details on our believes.

All the aforementioned results find a direct explanation in the fluid motion; from equation 3.2.5 it is evident that $\bar{z}_0$, as well as ω, $S(\bar{x})$ and the mode shape through $\left.\frac{dW}{dx}\right|_{x=L}$, increases the off-axis case velocity magnitude, but at high β (low viscosity μ) this is not a big issue in terms of dissipation because the off-axis fluid component is given by a plug flow. However, when at low β, the profile is parabolic with strong shear gradients and, being μ high, dissipation will be higher. Figure 3.2.1 shows the relative motion of the fluid with respect to the lateral walls:

- in the proper cantilever the fluid is moving as the channel lateral walls, almost everywhere and for any β
- in the rigid lead channel the fluid is moving faster than the cantilever channel lateral walls everywhere but in a thin boundary layer if β is high, or with a parabolic profile with respect to the walls if β is low. The lower β, the higher μ and the higher the dissipation for the same parabolic profile.

Various $\frac{L_c}{L}$ Increasing the length of the leading channel will not bring up the stored energy; on the contrary, assuming some off-axis placement $\bar{z}_0$, the energy used to actuate the resonator will be dissipated to pump in and out a bigger amount of fluid, which is proportional to the volume change of the channel, but, being the reservoir further, a bigger amount of fluid will be displaced (at least according to the theoretical model), thus decreasing Q. In particular, more energy will be dissipated only in the rigid channel, while the energy dissipated in the cantilever proper should stay constant. As the rigid lead channel is not included in the on-axis case, it appears clear that any change in L_c will only affect the off-axis part.

In the incompressible case (Figure 3.3.3), reducing the length of the reservoir brings benefits to the normalized quality factor; in the limit of $L_c = 0$ the energy dissipation is confined to the proper cantilever and the off-axis component of dissipation cancels out. Any fluidic phenomenon occurring in the rigid part of the device can only be problematic: no more energy can be stored increasing L_c, but it can be easily dissipated because of shear between layers of fluid.

We also expected $\frac{L_c}{L}$ to have the same effect on the elbow as $\bar{z}_0$: higher values of the length ratio will monotonically increase dissipation (downshifting uniformly the off-axis contribution) making

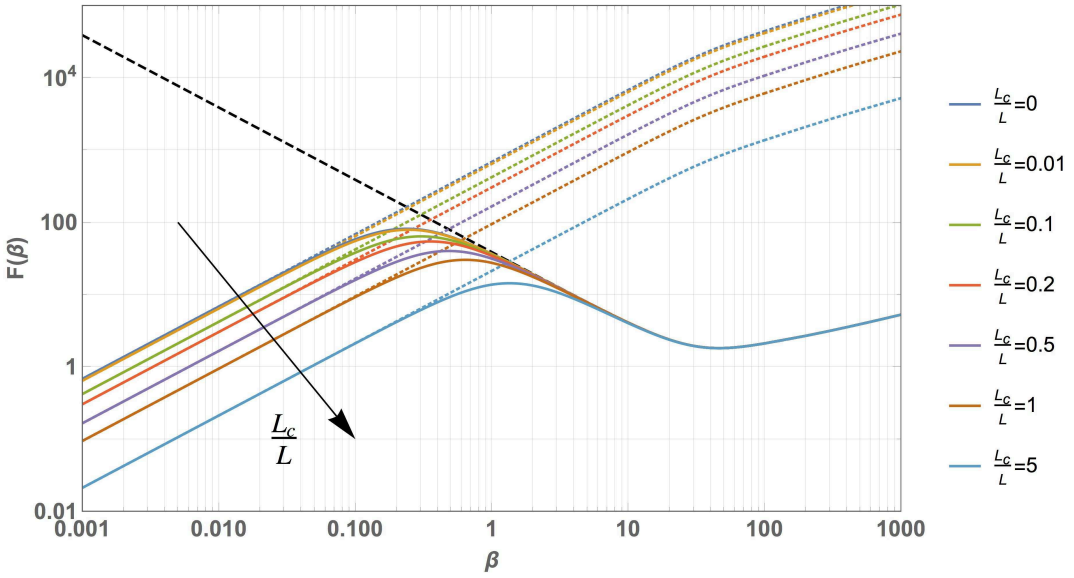

Figure 3.3.3: *Incompressible case Quality Factor for several rigid channel lenghts, with $\bar{z}_0 = 0.01$; black dashed line is the on-axis case, whose dissipation mechanism dominates at high β for low $\bar{z}_0$; coloured dashed lines show how off-axis dissipation mechanism takes over at low β; for $\frac{L_c}{L} = 0$ the highest curve is obtained*

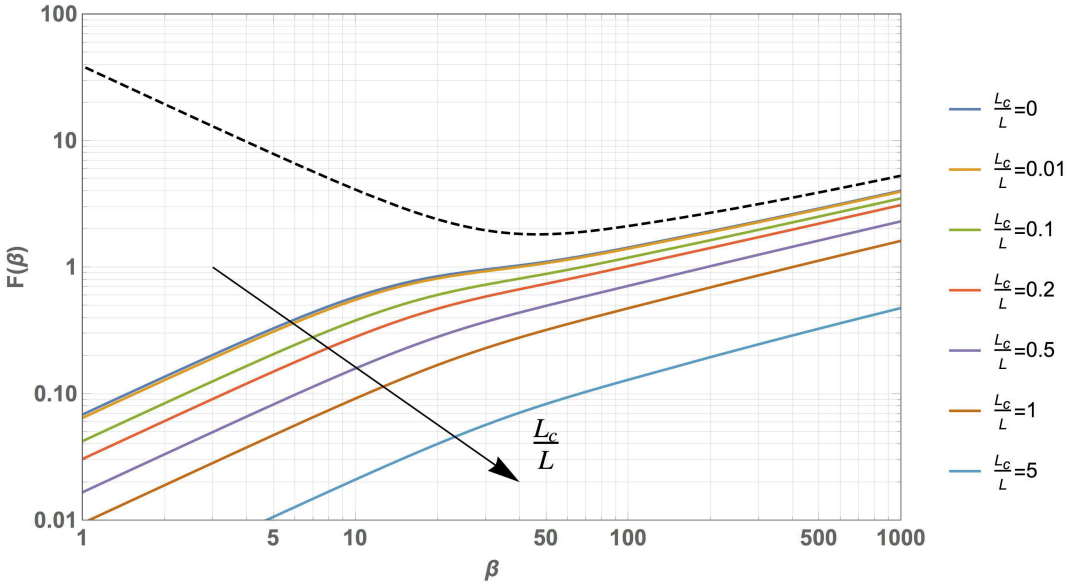

Figure 3.3.4: *Incompressible case Quality Factor for several aspect ratios of the channel, with $\bar{z}_0 = 1$; the effect is stronger at higher β than in Figure 3.3.3 and as $\bar{z}_0$ is so big, the minimum has disappeared; black dashed line is the on-axis case, whose dissipation mechanism dominates at high β for low $\bar{z}_0$; for $\frac{L_c}{L} = 0$ the highest curve is obtained;*

the elbow and the minimum vanish for very high ratios. Importantly, for $L_c = 0$ a maximum of the local maximum is reached, while for $L_c \gg L$, the maximum disappears as for very high $\bar{z}_0$: the way $\frac{L_c}{L}$ affects the incompressible off-axis part is independent of $\bar{z}_0$.

Various Poisson's ratios The effects of the Poisson's ratio are discussed in [33].

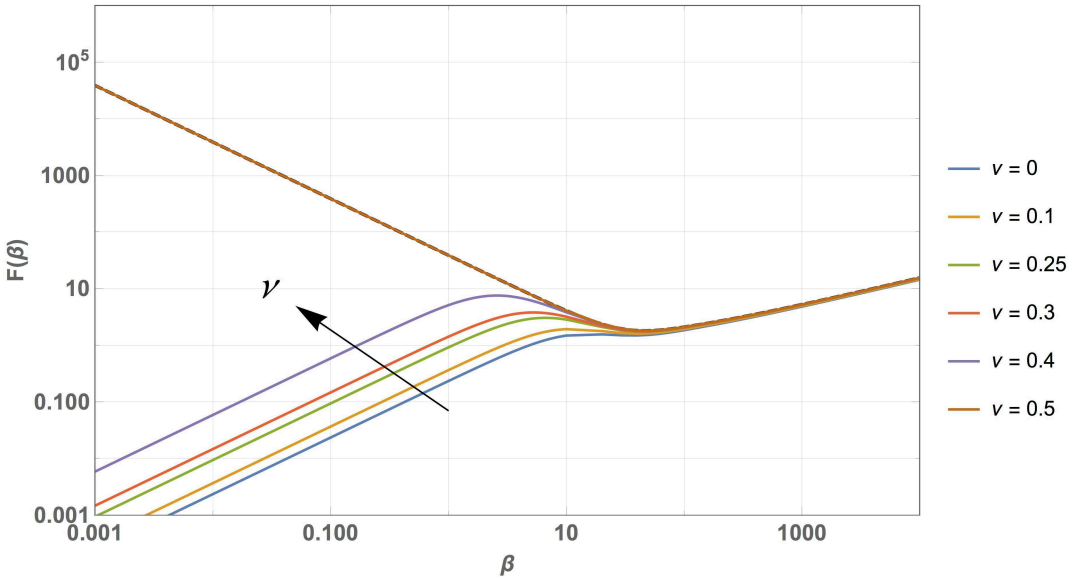

Figure 3.3.5: *Incompressible case Quality Factor for several Poisson's ratios ν, with $\bar{z}_0 = 0.2$ and $\frac{L_c}{L} = 1$; for $\nu = 0$ (incompressible solid) we get the same behaviour as without considering Poisson; for $\nu = 0.5$ the off-axis contribution cancels out and the quality factor overlaps the on-axis case (black dashed line); this is expected as explained in [31] because increasing Poisson's ratio to this limiting case leads to zero volumetric flux into the channel due to off-axis placement and energy dissipation disappears for any $\bar{z}_0$*

In this paper, the authors established that increasing Poisson's ratio brings benefits reducing the negative effects of off-axis channel placement. This is due to a reduced volumetric flux into the channel forced by the pumping mechanism, as the channel contracts laterally while expanding axially, giving zero volume change in the limit of $\nu = 0.5$ overall, as in Figure 3.3.6.

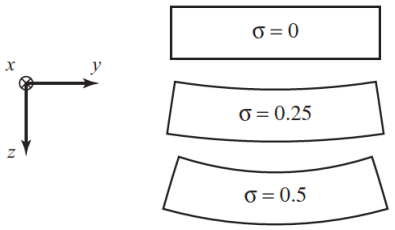

Figure 3.3.6: *Lateral walls contraction for different values of Poisson's ratios ν [31]*

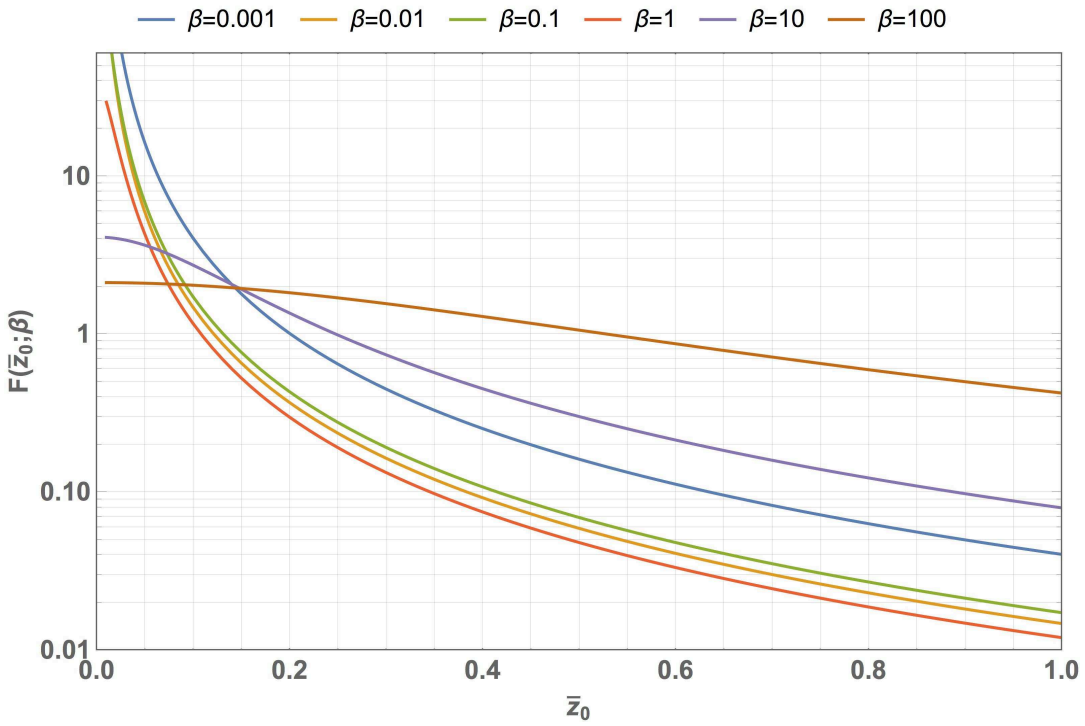

Figure 3.3.7: *Compressible case Quality Factor for several β, with $\gamma = 0.01$ and $\frac{L_c}{L} = 1$*

3.3.2 Compressible fluid

We now present results in the case of complete compressible flow ($\alpha \neq 0$ and $h(\bar{x};\alpha) \neq 0$). In this case, the quality factor exhibits a slightly more complex behaviour and is differently affected by changes of $\bar{z}_0$ and $\frac{L_c}{L}$.

Various $\bar{z}_0$ We begin by noticing that $\bar{z}_0$ has the negative effect on $F(\beta)$ as in the incompressible case, affecting it especially at low β. From Figure 3.3.9, we learn that in the compressible case two maxima and two minima occur. We recognize that the rightmost maximum corresponds to the only maximum in the incompressible case (Figure 3.3.2); accordingly, the result concerning the incompressible case for high $\bar{z}_0$ applies to the complete compressible case too: the rightmost maximum disappears after moving to higher β positions and merging with the on-axis case minimum at β=46.

Interestingly, on a broad range of 5 orders of magnitude, $\beta \in (0.001, 10)$, $F(\beta)$ keeps quite constant, being confined to values in 1 order of magnitude. Importantly, we notice that the theoretical model is predicting a counter-intuitive behaviour at low β, surprisingly qualitatively opposite to the incompressible case: it appears that increasing the viscosity brings benefits in terms of quality factor,

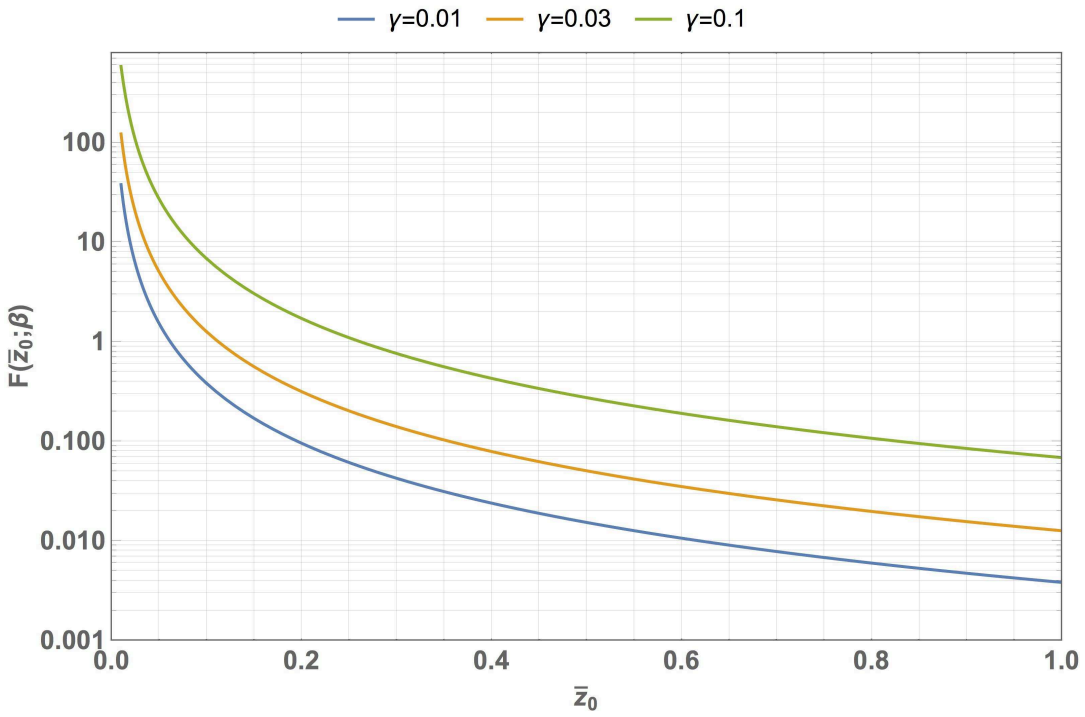

Figure 3.3.8: *Compressible case Quality Factor for several γ, with $\beta = 0.01$ and $\frac{L_c}{L} = 1$*

with $F(\beta) \to \infty$ for $\mu \to \infty$, while in the incompressible case this is not true. This behaviour is not confirmed by our COMSOL simulations and a plausible explanation of this discrepancy is given in Section 5.3.1.

Importantly, $F(\beta)$ is pseudo-hyperbolic in $\bar{z}_0$: Figures 3.3.7 and 3.3.8 show how γ and β modify this general trend: β affects the response to $\bar{z}_0$ changes, while γ simply uniformly reduces dissipation, theoretically.

Various $\frac{L_c}{L}$ For the same γ, $\frac{L_c}{L}$ theoretically strongly affects the quality factor, as in Figure 3.3.10. Importantly, in the complete compressible case it seems that when $L_c = 0$ the quality factor goes down for high viscosity μ, oppositely to the general case where $L_c \neq 0$ in which the quality factor, after some oscillations, goes up for. Increasing L_c decreases the rightmost maximum from the maximum value (F(β)=8 for $L_c = 0$) and makes the leftmost maximum appear and increase for increasing L_c. Both the righmost and leftmost maxima take place at higher β as L_c is increased. Being there two maxima, a minimum must occur for intermediate β and this takes place at higher β as L_c is increased and its value also slightly increases. The rightmost minimum due to the on-axis case is preserved.

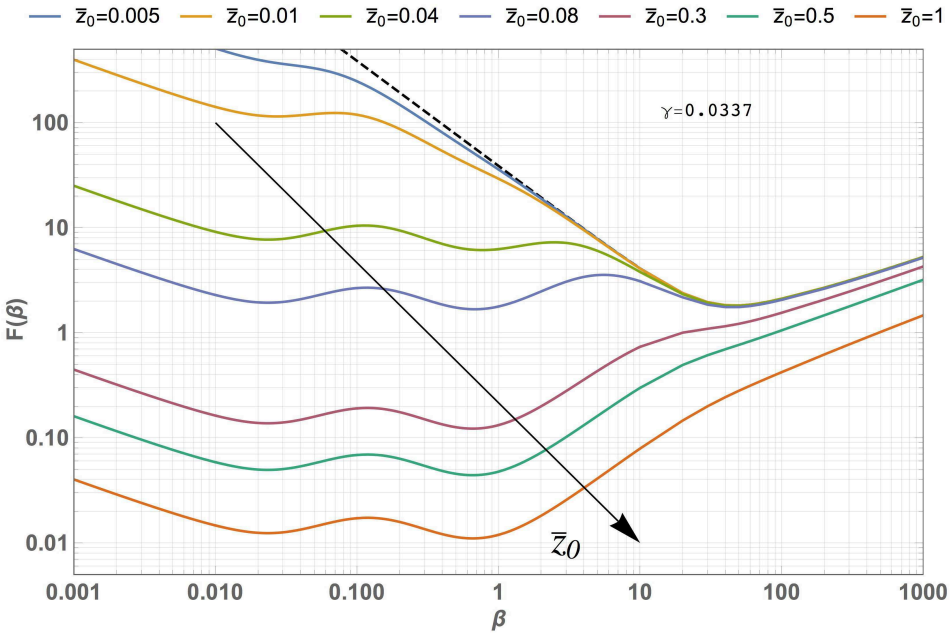

Figure 3.3.9: *Compressible case Quality Factor for several $\bar{z}_0$, with normalized acoustic wavenumber $\gamma = 0.0337$ and $\frac{L_c}{L} = 1$; black dashed line is the on-axis case; if $\bar{z}_0 < 0.2959$, increasing $\bar{z}_0$ brings down the quality factor especially at low β, where the off-axis dissipation mechanism dominates, while at high β the on-axis dissipation dominates; when $\bar{z}_0 > 0.2959$, the quality factor experiences a uniform dowhshift;*

Ultimately, increasing L_c leads to the disappearing of the rightmost maximum, which merges with the on-axis minimum, and to the increasing of the intermediate minimum which disappears too, flattening to a constant value which is equal to the leftmost maximum. After the merging, a uniform downshift of the quality factor at low μ occurs (which means L_c is so big that off-axis dissipation mechanism is dominating).

As mentioned, the behaviours for $L_c = 0$ and $L_c \neq 0$ are strongly different at low β. We already discussed on how introducing compressibility allows decreasing β to bring benefits, as damping is increased and the flow due to the pumping dies out (Section 3.2.2). However, when $L_c = 0$, one obtains the same decreasing trend as in the incompressible case, as if compressibility positive effects were cancelled out. This is due to an failure of the boundary conditions in the off-axis model when the reservoir merges with the entrance of the cantilever. We therefore assume $L_c = 0.001 \approx 0$.

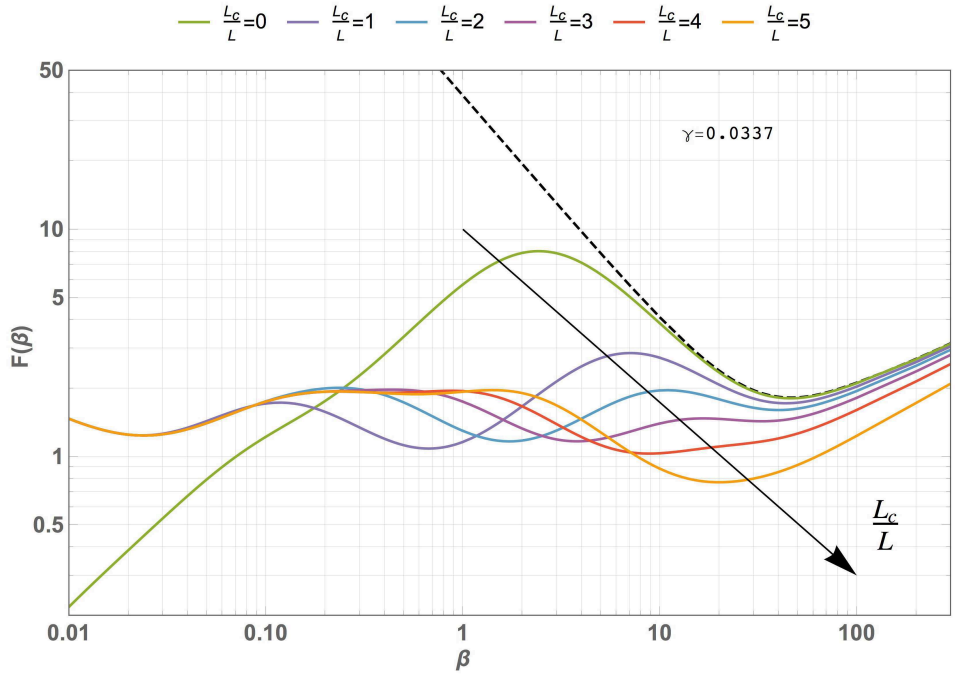

Figure 3.3.10: *Compressible case Quality Factor for several* $\frac{L_c}{L}$*, with normalized acoustic wavenumber* $\gamma = 0.0337$ *and* $\bar{z}_0 = 0.1$*; black dashed line is the on-axis case; green line shows the surprising different behaviour for* $\frac{L_c}{L} = 0$*.*

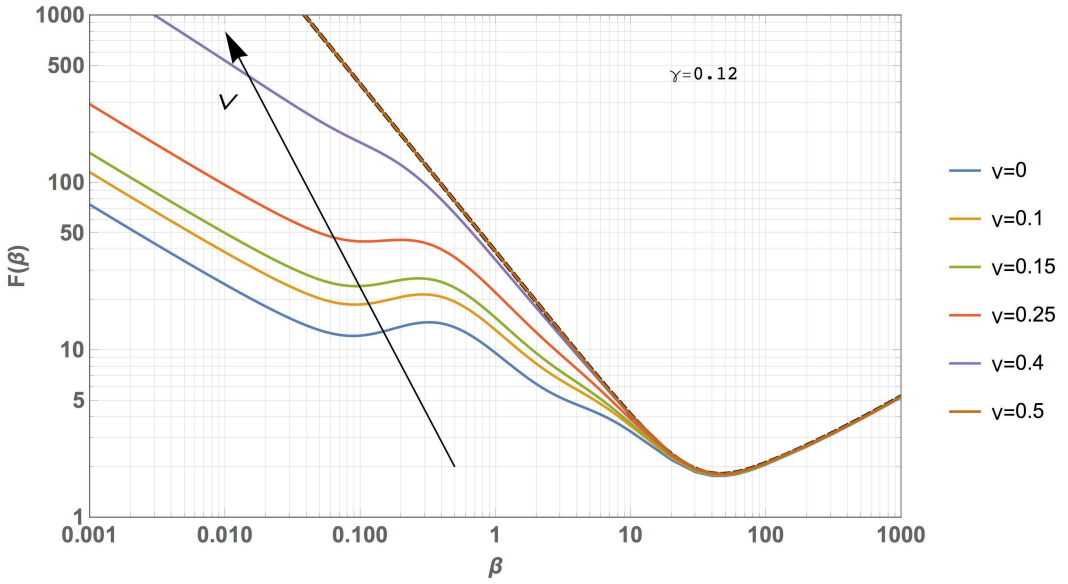

Figure 3.3.11: *Compressible case Quality Factor for several Poisson's ratios* ν*, with normalized acoustic wavenumber* $\gamma = 0.12$*,* $\frac{L_c}{L} = 1$ *and* $\bar{z}_0 = 0.06$*; black dashed line is the on-axis case;*

Poisson's ratios The benefits from increasing Poisson's ratios in the incompressible case discussed in paragraph 3.3.1 are preserved in the compressible case (Figure 3.3.11).

Chapter 4

Numerical Model

> On ne voit bien qu'avec le coeur. L'essentiel est invisible pour les yeux
>
> *Antoine de Saint-Exupéry*

Contents

The second part of the work consisted in developing a model in COMSOL (release 5.3) to compare numerical results with theoretical and experimental results. A 2D model was provided to the author as a reference for the geometry, the physics, the study and the boundary conditions to be used, and to get familiar with COMSOL environment. However, it was immediately clear that the 2D Model couldn't be a good tool of comparison for several reasons, which will be later discussed.

In this chapter we discuss on the theoretical numerical background to perform a benchmark with the analytical model and experimental data, which have been seen to match well enough [32],[33]. We also show the settings for our COMSOL model used to obtained results with an eigenvalue study on the system.

An important research goal of this study is to compare two different methods like the two-way coupled and the one-way coupled Fluid-Structure Interaction (FSI). In the former, a more realistic analysis can be conducted, but this approach requires good definition of the double coupling. In the latter, the stresses from the fluid are not affecting the motion of the solid.

4.1 Fluid-Structure Interaction (FSI)

A common example of Fluid Structure Interaction (FSI) problem in the field of Micro/Nano Electro Mechanical Systems (MEMS/NEMS) is a cantilever vibrating in fluid environment: this has been largely investigated theoretically, experimentally and numerically [29] [30]. Such FSI problem is dominated by viscous damping, rather than other damping mechanisms (acoustic radiation damping or internal structural damping) [24], which represents the most dissipative process occurring during the oscillation of any microstructure in a viscous fluid. Fluid damping imposes severe limitations by strongly degrading the signal-to-noise ratio of measurements.

Importantly, FSI problems can be solved either in time domain or in frequency domain, the former having many drawbacks:

- on equal mesh density, an eigenfrequency analysis is clearly less time consuming than a time domain one;
- in frequency domain, a convergence study concerns only the mesh density and quality: no

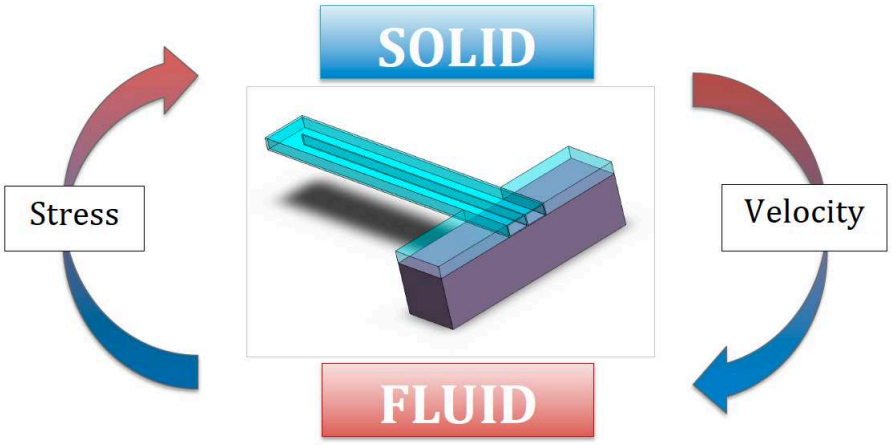

Figure 4.1.1: *Fluid-structure interaction double coupling concept: the solid structure exerts forces (no-slip boundary condition) on the fluid, transferring momentum to it. The fluid movement (inertial force) influences the structural behaviour through stresses; in a one-way coupling*

constraints on any time parameter (Courant condition,...) are to be verified, as happens in the time domain

As discussed in chapter 1, dynamic measurement in microcantilever based Bio-Sensors is conducted evaluating Q factors and Resonance Frequencies; as these parameters belong to the frequency domain, we decide to follow the approach of Ricci and Giuri [29], looking for the solution of an eigenvalue problem. By so doing, and exploiting symmetry conditions, we obtain a strong reduction of the computational time and a high degree of accuracy of results, avoiding long transient computations. Our numerical model is believed to help in design and optimization of Suspended Microchannel Resonators.

4.2 COMSOL equations and solver

COMSOL Multiphysics® is a general-purpose software platform, based on advanced numerical methods, for modelling and simulating physics-based problems. Importantly, it provides the user with a significant amount of physics modelling functionality, including multiphysics ability. By adding application-specific modules, the modelling power is increased with dedicated tools for electrical, mechanical, fluid flow, and chemical applications.

To simulate our phenomenon efficiently, we used the Acoustics and Structural Mechanics mod-

ules from COMSOL, which were then linked by an Aeroacoustic-Structure Boundary Multiphysics tool. Under Physics, we selected the "Solid Mechanics" and "Linearized Navier-Stokes, Frequency Domain" interfaces: this step allows to move from the time domain to the frequency domain, and transforms all the temporal terms $\frac{\partial}{\partial t}$ in $j\omega t$. An "Eigenfrequency" study has been performed while changing the fluid and structure properties.

4.2.1 Equations for fluids and solids from COMSOL

The equations and all the information on the solver were taken from COMSOL Documentation [1], COMSOL Multiphysics Reference Manual [2] and COMSOL Multiphysics User's Guide [3]. Aeroacoustic simulations would ideally involve solving the fully compressible continuity, momentum (Navier-Stokes equations), and energy equations in the time domain. This approach is often impractical for real-world computational aeroacoustic applications due to the required computational time and memory resources. Instead, for solving many practical engineering problems, a decoupled two-step approach is used: first solve for the fluid flow, then the acoustic perturbations of the flow. As far as the acoustic problem is concerned, the governing equations are linearized around the background mean flow p_0 and only solved for the acoustic perturbation p. Acoustic variables are assumed to be small and perturbation theory can be used, for example, the total pressure is

$$p_{tot} = p_0 + p \tag{4.2.1}$$

Fluid Dynamics The complex interaction of a stationary background flow and an acoustic field can be modelled using the linearized Navier-Stokes physics interfaces in the Acoustics Module. The interfaces allow for a detailed analysis of how a flow, which can be both turbulent and non-isothermal, influences the acoustic field in different systems. Basically, the equations solve for the full linear perturbation to the general equations of CFD (mass, momentum, and energy conservation).

The linearized Navier-Stokes equations are derived by linearizing the full set of fluid flow equations given in General Governing Equations. After some manipulation, the continuity, momentum, and energy equations become:

$$\begin{cases} \frac{\partial \rho}{\partial t} + \nabla \cdot (\rho_0 \mathbf{u} + \rho \mathbf{u}_0) = M \\ \rho_0 \left(\frac{\partial \mathbf{u}}{\partial t} + (\mathbf{u} \cdot \nabla)\mathbf{u}_0 + (\mathbf{u}_0 \cdot \nabla)\mathbf{u} \right) + \rho(\mathbf{u}_0 \cdot \nabla)\mathbf{u}_0 = \nabla \cdot \sigma + \mathbf{F} \\ \rho_0 C_p \left(\frac{\partial T}{\partial t} + \mathbf{u} \cdot \nabla T_0 + \mathbf{u}_0 \cdot \nabla T \right) + \rho C_p (\mathbf{u}_0 \cdot \nabla T_0) + \\ -\alpha_p T_0 \left(\frac{\partial p}{\partial t} + \mathbf{u} \cdot \nabla p_0 + \mathbf{u}_0 \cdot \nabla p \right) - \alpha_p T (\mathbf{u}_0 \cdot \nabla p_0) = \nabla \cdot (k \nabla T) + \mathbf{\Phi} + \mathbf{Q} \end{cases} \tag{4.2.2}$$

The equations are formulated in the frequency domain and assume harmonic variation of all sources and fields. They include viscous losses and thermal conduction as well as the heat generated by viscous dissipation, if relevant. All terms are defined in the COMSOL Reference Manual [2]. The physics interface solves for the acoustic variations in the pressure p, velocity field u, and temperature T. The background mean flow can be any stationary flow. The Linearized Navier-Stokes, Frequency Domain interface is formulated in the so-called scattered field formulation where the total acoustic field is the sum of the scattered field (the field solved for p, u, and T) and a possible background acoustic field, such that

$$p_t = p + p_b \qquad T_t = T + T_b \qquad \mathbf{u}_t = \mathbf{u} + \mathbf{u}_b \tag{4.2.3}$$

All governing equations and boundary conditions are formulated in the total field variables. When no Background Acoustic Fields feature is present, as in our case, the total field is simply the field solved for:

$$p_t = p \qquad T_t = T \qquad \mathbf{u}_t = \mathbf{u} \tag{4.2.4}$$

Coupling the interfaces to structures enables detailed vibration analysis of structures in the presence of flow, such as FSI in the frequency domain. The coupling in the frequency domain and time domain is readily performed using the predefined Aeroacoustic-Structure Boundary multiphysics coupling feature. [1] [2] [3]

Solid Mechanics Solid Mechanics Physics is found in the module Structural Mechanics of COMSOL Multyphysics.

Importantly, we neglected structural damping, therefore all results refer solely to the Quality Factor related to the fluid dissipation mechanisms.

4.2.2 Modal eigenfrequency analysis

Our numerical results make use of the eigenfrequency analysis, which solves for the eigenfrequency of the model. The time-harmonic representation of the generic field **p**

$$\mathbf{p}(\mathbf{r}, t) = Re(\tilde{\mathbf{p}}(\mathbf{r})e^{-\lambda t}) \tag{4.2.5}$$

includes a complex parameter in the phase, λ; this eigenvalue, $-\lambda = -\delta + j\omega$, has an imaginary part representing the eigenfrequency and a real part responsible for the damping. The complex time exponential expresses the time behaviour of the system; the quality factor Q is derived from the eigenfrequency and damping as:

$$Q = \frac{\omega}{2\delta} \tag{4.2.6}$$

Equation 4.2.6 is used to extract the numerical results on the quality factor in all our simulations. In the "Eigenfrequency search method" we selected Manual and inserted supposed eigenfrequency values around which to search for the larger real part of the complex eigenfrequency $\tilde{f} = -\frac{\lambda}{2\pi j} = f + j\frac{\delta}{2\pi}$. This step strongly speeds up convergence. We underline that this definition of Q is slightly different to the one proposed by Sader [32] and takes into account all the dissipative mechanisms within the fluid (for instance, the energy equation contains a temperature dependent term); therefore, comparison between numerical and theoretical results should be done carefully; when we applied Sader's definition of Q to our numerical model, we obtained the same qualitative behaviour as when using Equation 4.2.6; however, the plots were slightly shifted down of some units.

4.3 The 2D Model

A 2D Model was provided to the author to get confident with the software and as a reference to later develop the 3D Model. Even though optimal in terms of computational effort, such a model was unable to well describe the physics and provide coherent values of the quality factor for several reasons, which will be now discussed. Moreover, even in a simpler case where the fluid is around the beam [29], a 2D model would hold only when the length of the cantilever is much bigger than

its thickness and just for low mode numbers; therefore, a 3D model, if computationally feasible, is more appropriate for a deep analysis when short cantilevers and high mode numbers are to be investigated.

4.3.1 Geometry

A 3D Geometry has been built and the middle cross section has been selected to perform a 2D analysis. We immediately underline that the 3D characteristics are completely lost with this step: the physical domain under study becomes the central section of the beam (X-Z plane). If the 3D geometry included the internal wall separating the two channels, as in real devices, the central section would be clearly intersecting this wall: the study would be performed on a solid domain only, hence completely missing the fluid-structure interaction.

Believing valid the assumption that the internal wall can be neglected, as in the theoretical model, the middle section becomes as in Figure 4.3.2. Again, we encountered a limit: the eigenfrequencies solved for were 1 order of magnitude lower than the expected ones and the eigenshapes were wrong and viscosity dependent. This mistake is due to the fact that the software is not modelling the two lateral walls (parallel to the X-Z plane) which link the top and bottom walls (parallel to the X-Y plane). This fault reduces the stiffness (giving lower eigenfrequencies) and makes the structure behave as a so called "shear-type frame", as in Figure 4.3.6. Both ends cannot rotate, as in doubly clamped structures.

4.3.2 Tip error caused by the shear-type frame

To solve the aforementioned problem, we tried to force COMSOL to apply the good mode shape for all the eigenfrequencies. Two approaches were pursued:

- making the tip softer, by reducing its Young Modulus (Figure 4.3.4)
- including an additional solid domain (Figure 4.3.5)

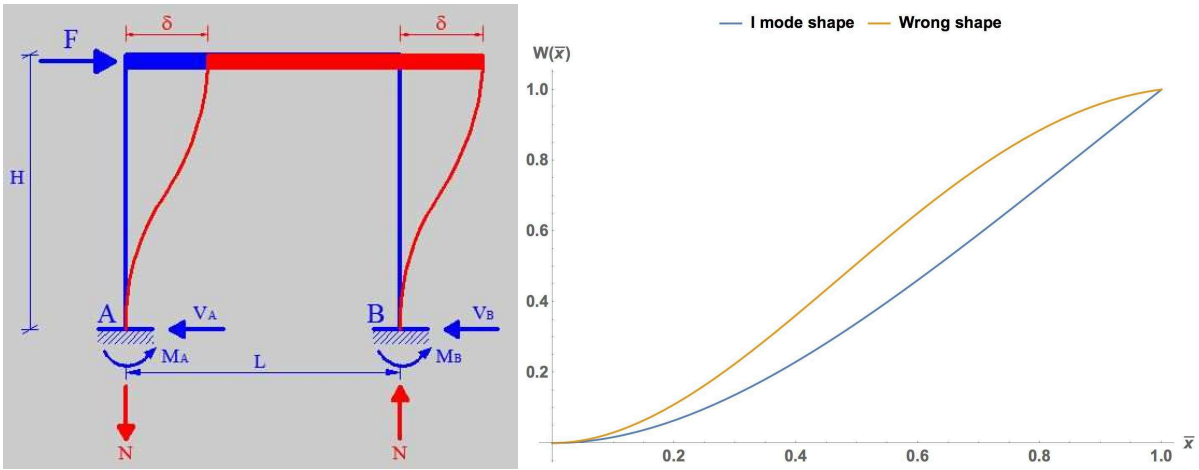

(a) (b)

Figure 4.3.1: *"Wrong" shape obtained in the 2D model: (a) Shear-type frame showing the prevented rotation of the free-end; (b) I mode shape and "wrong" shape*

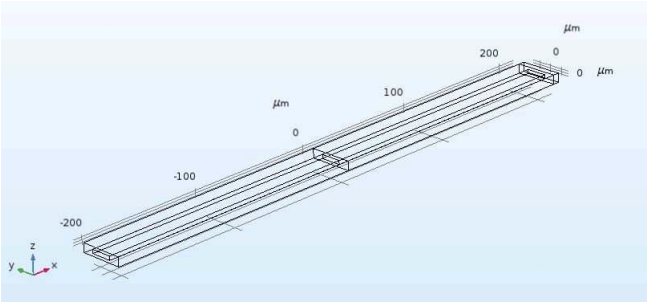

Figure 4.3.2: *3D CAD for Device B: a simplified geometry where the middle wall has been removed is built to compare results with the theoretical model; the 2D analysis focuses on the middle section (Z-X)*

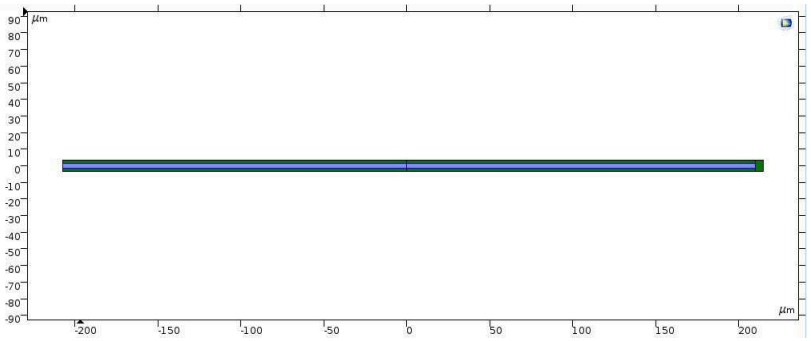

Figure 4.3.3: *2D middle section (Z-X) where the 2D analysis is performed*

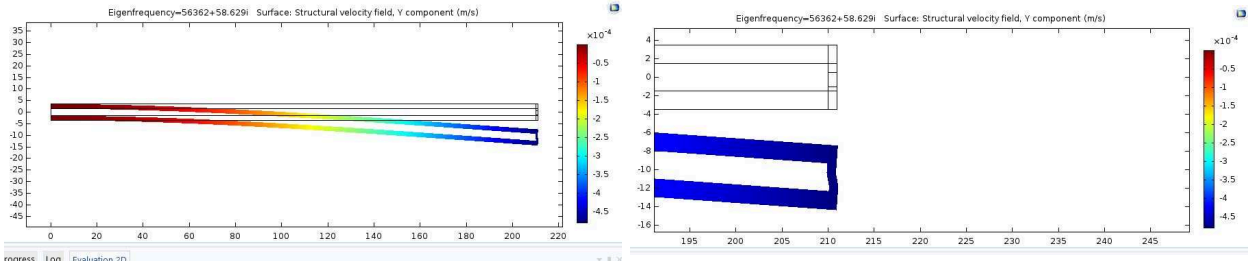

(a) **(b)**

Figure 4.3.4: *Approach 1: low Young Modulus is given to the tip to make it softer; (a) Eigenshape of the structure; (b) Zoom at the tip showing unrealistic structural deformation*

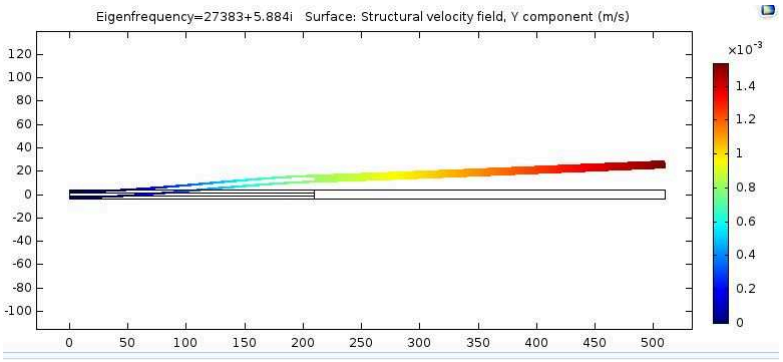

Figure 4.3.5: *Approach 2: Solid structure with extended tip to achieve the correct eigenmode*

The first approach gave back the good mode shape, but introduced an important error at the tip. The second approach did not introduce any error at the tip, but did not give back the good shape. In both case, the correct values of the eigenfrequencies were not obtained. In conclusion, we decided to move to a 3D model to well capture all the physics.

4.3.3 The "wrong" mode shape attempt

Before moving to the 3D model it is worth mentioning another attempt done to validate the theoretical model. We tried to apply the "wrong" mode shape obtained from COMSOL and fitted in Mathematica (Figure 4.3.1a) to the theoretical model to compute the Quality factor and compare it with the one obtained directly with COMSOL. In fact, equation 2.6.2 accepts any kind of mode shape $W(\bar{x})$.

However, we realized that this approach was not good for comparison because of the different boundary conditions that COMSOL was imposing to the fluid: the top and bottom walls of the

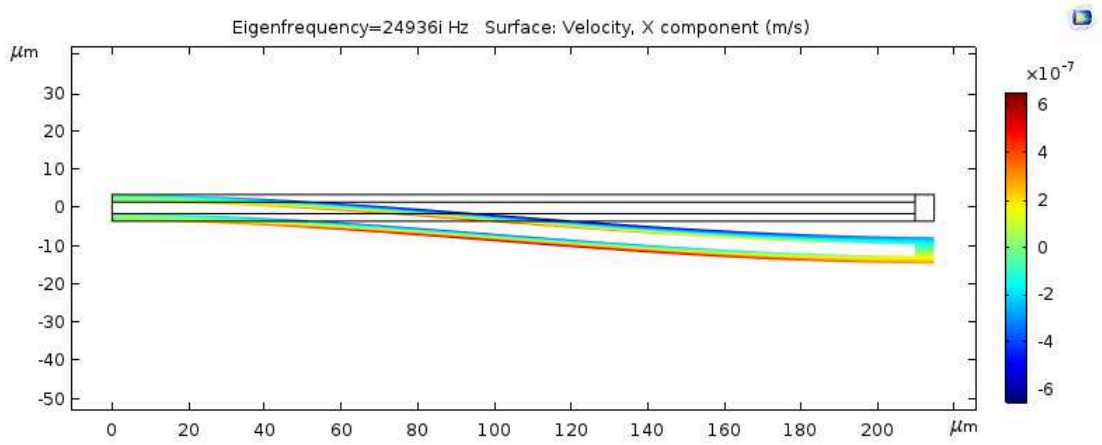

Figure 4.3.6: *Inexact deformation of the structure when solving for the first eigenmode: the top and bottom walls are considered separately by COMSOL in the 2D model, with one independent neutral-axis each; the internal walls have opposite deformation*

cantilever were considered as separate solid structures during deformation, each one having an own neutral axis; as such, the boundary conditions onto the fluid are in the same verse even in the simple case where $\bar{z}_0 = 0$, oppositely to the theoretical model (Figures 2.3.1 and 4.3.6).

4.4 The 3D Model

Most of the characteristics of the devices and fluid studied numerically are taken from [32], but some parameters had to be assumed by the author not being available in the reference paper. Three devices are investigated for comparison and all the relevant parameters are listed in Tables 4.3 and 4.1. In order to compare numerical results with the theoretical ones, a simplified model which didn't include the wall in the middle was firstly used. This preliminary analysis was conducted to get acquainted with the software and detect the first differences between theory and numerics, in order to give a first interpretation to the numerical results. Later, in order to match numerics with experiments, a complete geometry was used, including the wall in the middle, with a supposed value of b_{wall}. This had the main effect of increasing the stiffness of the cantilever and returning higher and more precise values of the eigenfrequency, which matched better with the experimental results. Secondly, the Quality factor was quantitatively affected and shifted up of some units, as a result of the decrease of the shear gradients. However, its general trend didn't change, as expected.

To quickly run simulations for different devices and fluid properties, the COMSOL model was

parameterized in function of relevant parameters such as h_{fluid}, $h_{channel}$, k, ρ_{fluid}, $\bar{z}_0$ and μ_{fluid} and Parametric Sweeps were performed.

4.4.1 Domain

In this section the domains for both the simplified and complete geometries are discussed and presented together with a list of all the relevant parameters. Both geometries were studied for the following purposes: at first, a simplified geometry with no wall separating the inlet and outlet channels was built and numerical results were compared with the 2D theoretical model; in this way we could validate the theoretical model more easily and find discrepancies which couldn't be due to the geometry, but to some theoretical uncaptured physics; secondly, a geometry closer to the devices on which experiments were performed [32],[33] was built and numerical results were compared.

Figures 4.4.1 and 4.4.2 show the physical domain of interest in the simple case of $\bar{z}_0 = 0$: the solid domain is coloured in green and the fluid domain is coloured in light blue. The geometrical parameters for Devices A, B and C are listed in Table 4.1, where also b_{wall} is included to take into account the wall in the middle in the model that better represents the real device. This last parameter and the size and position of the channel bending are not provided and are therefore tuned to match eigenfrequencies and quality factors.

Description	Geometry parameter	Device A, value [μm]	Device B, value [μm]	Device C, value [μm]
Channel height	h_{fluid}	3	8	15
Cantilever height	h_c	7	12	19
Channel width	b_{fluid}	16	16	40
Cantilever width	b_c	33	33	57
Middle wall width	b_{wall}	1	2	2
Channel length	L	204	204	315
Rigid Channel length	L_c	204	204	240
Tip length	L_{tip}	12	6	6
Total cantilever length	$length$	216	210	321

Table 4.1: *Geometrical properties of the experimented and simulated devices*

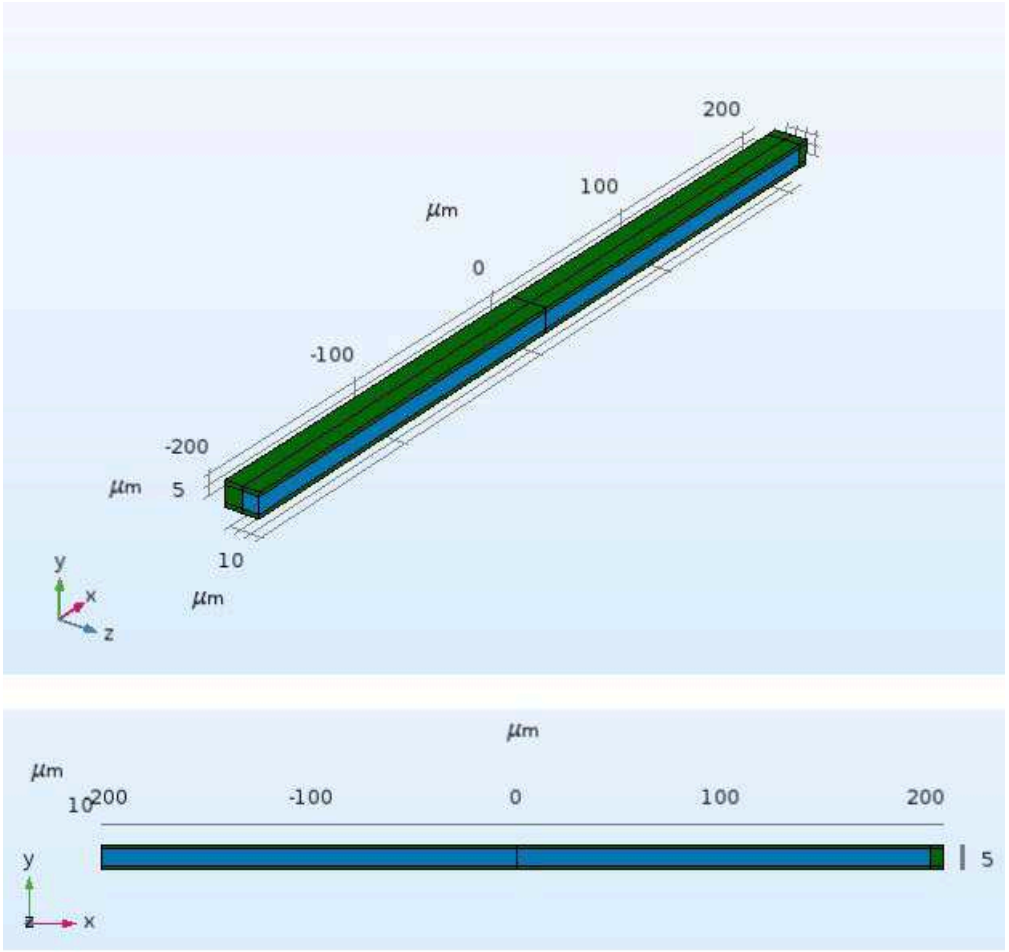

Figure 4.4.1: *3D Simplified geometry, with $\bar{z}_0 = 0$, for theoretical and numerical comparison; on the top an isometric view, on the bottom a later view*

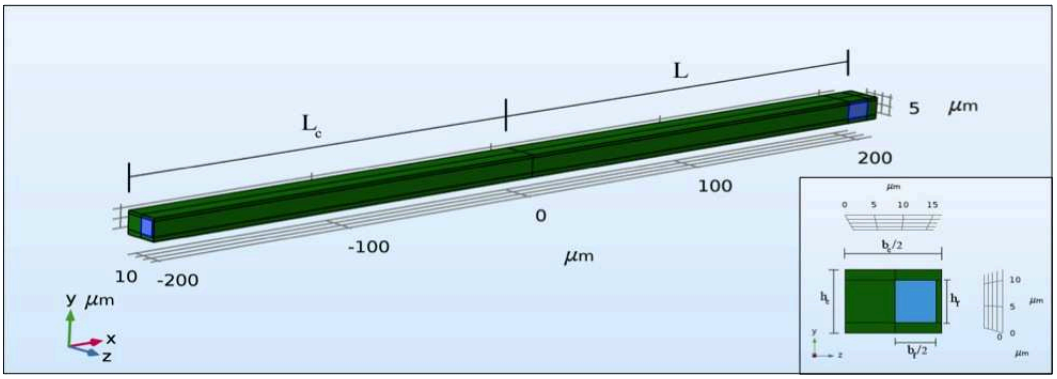

Figure 4.4.2: *3D complete geometry with a wall between the inlet and outlet channel, with $\bar{z}_0 = 0$, for experimental and numerical; inset: front view*

4.4.2 Mesh

The mesh resolution and mesh element quality are important aspects to consider when validating a model. Low mesh resolution — in relation to the variations in the solution and the geometry — can lead to inaccurate results. A low mesh element quality — which measures the regularity of the mesh elements' shapes — can lead to inverted mesh elements and to high condition numbers for the Jacobians, which in turn can cause convergence issues. The mesh element quality is a dimensionless quantity between 0 and 1, where 1 represents a perfectly regular element, in the chosen quality measure, and 0 represents a degenerated element. [1]

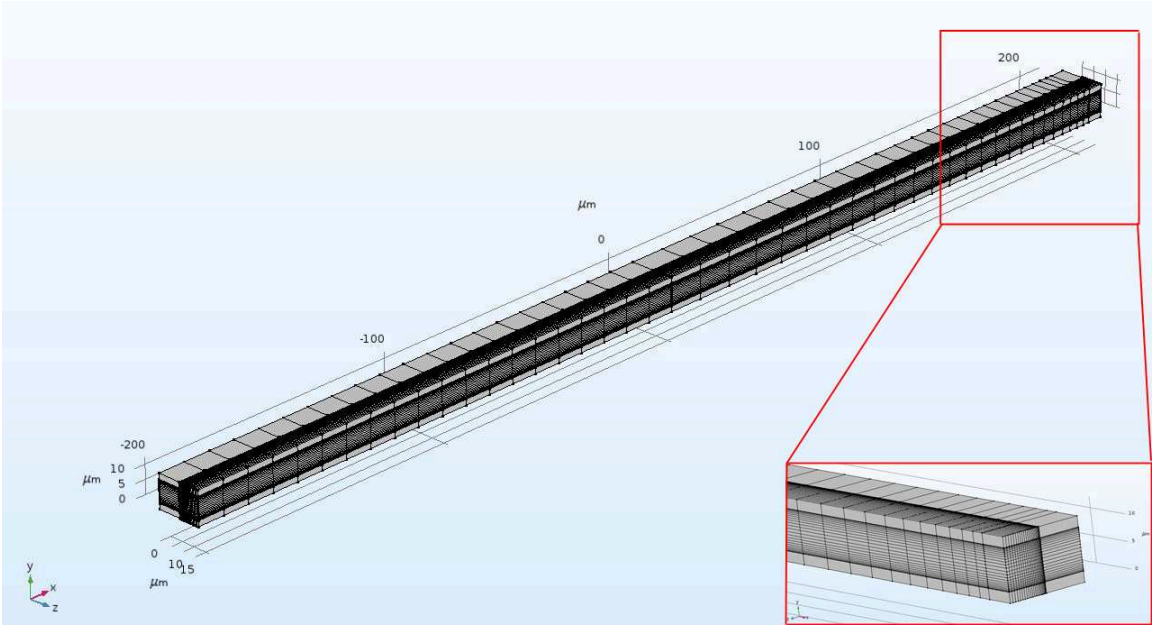

Figure 4.4.3: *Square Mesh (mesh quality = 1) for the 3D simplified geometry (without the wall separating the inlet and outlet channel); Inset: mesh refinement near the tip; the mesh density increases approaching the walls*

Importantly, Figure 4.4.3 shows how we exploited symmetry conditions, allowing for a big reduction of the number of degrees of freedom and the computational effort. Even though the geometry is symmetric with respect to two planes, only one symmetry condition was used because the eigenshapes are symmetric with respect to only one plane, with out-of-plane deformations. In all cases, thanks to the ease of the geometry, a minimum element quality of 1 was achieved: this is a very good condition and it avoids doubts on the reliability of the mesh. Table 4.2 shows different mesh settings: the third option has been used for all simulations as a good compromise between accuracy and computational effort, as discussed in Section 5.1. An element ratio of $\frac{1}{5}$ has been set to have

smaller elements close to the walls where the boundary layers develop.

N_x	$N_y = N_z$	N_{x_2}	Domain elements	Boundary elements	Edge elements	DOF
5	5	5	462	663	312	11448
10	10	10	2772	2208	572	38718
15	15	10	7803	5033	1014	70668
25	25	20	32292	11318	1292	199008

Table 4.2: *Number of elements and degrees of freedom for different mesh settings*

4.4.3 Boundary conditions and physics

The aforementioned physics of Solid Mechanics and Linearized Navier-Stokes were applied to the two different domains, as shown in Figure 4.4.4, where the darker blue highlights the selected domains.

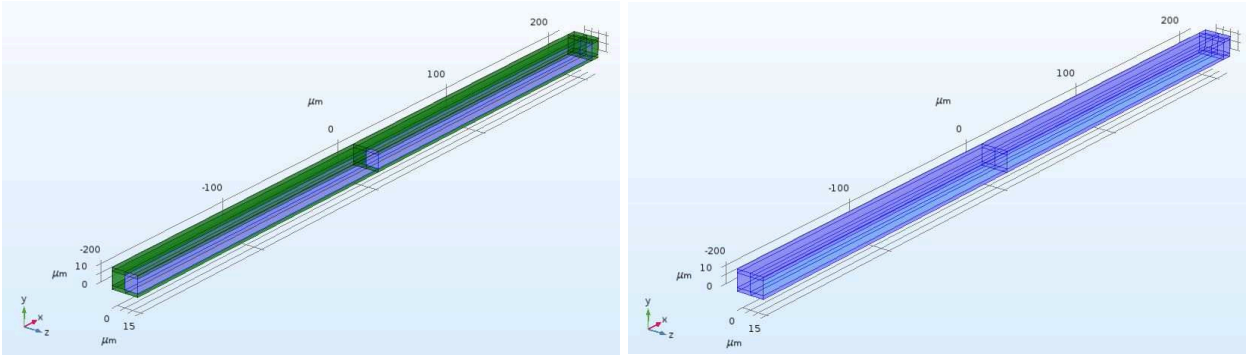

(a) *Navier-Stokes physics domain*

(b) *Linear elastic physics domain*

Figure 4.4.4: *Physical domains (darker blue highlights the domain of interest) in the 3D simplified geometry*

The boundary conditions are then set in agreement with the theoretical model and are here listed (darker blue shows the feature of interest):

Solid

- Fixed constraint $\mathbf{u}$, Figure 4.4.5b
- Boundary Load $S\mathbf{n} = \mathbf{F}_A$, Figure 4.4.5d
- Symmetry $\mathbf{n} \cdot \mathbf{u} = 0$, Figure 4.4.5a

Fluid

- Wall $\mathbf{u_t}$ and $T_t = 0$
- Prescribed Velocity $\mathbf{u_t} = \mathbf{u_p}$, Figure 4.4.5d
- Pressure (Adiabatic) $p_t = p_p$, $-\mathbf{n}(-k\nabla T_t) = 0$ and $\sigma\mathbf{n} = -p_p\mathbf{n}$, Figure 4.4.5e
- Symmetry $\mathbf{n} \cdot \mathbf{u} = 0$, Figure 4.4.5a

The two-way coupling has been modelled by means of stresses exerted by the fluid on the solid. The surfaces of contact between fluid and solid have been selected and a force per unit of surface has been applied on them, where:

$$\left[\frac{N}{m^2}\right] \mathbf{F}_A = \begin{cases} -T_{stress,x}\ \hat{\mathbf{x}} \\ -T_{stress,y}\ \hat{\mathbf{y}} \\ -T_{stress,z}\ \hat{\mathbf{z}} \end{cases} \tag{4.4.1}$$

with the components of the total fluid stress tensor defined in COMSOL as:

$$\begin{cases} T_{stress,x} = lnsf.T\_stress\_tensorxx * lnsf.nxmesh + lnsf.T\_stress\_tensoryx * lnsf.nymesh + lnsf.T\_stress\_tensorzx * lnsf.nzmesh \\ T_{stress,y} = lnsf.T\_stress\_tensorxy * lnsf.nxmesh + lnsf.T\_stress\_tensoryy * lnsf.nymesh + lnsf.T\_stress\_tensorzy * lnsf.nzmesh \\ T_{stress,z} = lnsf.T\_stress\_tensorxz * lnsf.nxmesh + lnsf.T\_stress\_tensoryz * lnsf.nymesh + lnsf.T\_stress\_tensorzz * lnsf.nzmesh \end{cases} \tag{4.4.2}$$

The Model Builder in Figure 4.4.7 contains all the information on the general set up of the simulations: the components, the physics, the studies and the results are easily accessible.

4.4.4 Structure properties

Table 4.3 shows the material properties of Devices A, B and C used in our numerical simulations for comparison with experimental results.

The resonance frequencies in the uncoupled case (in vacuum and with no fluid in the channel) are given in Tables 5.1, 5.2 and 5.3; experimental values are taken from [33], numerical values refer to the complete geometry with the wall separating the inlet and outlet channels. All these results are available in Chapter 5.

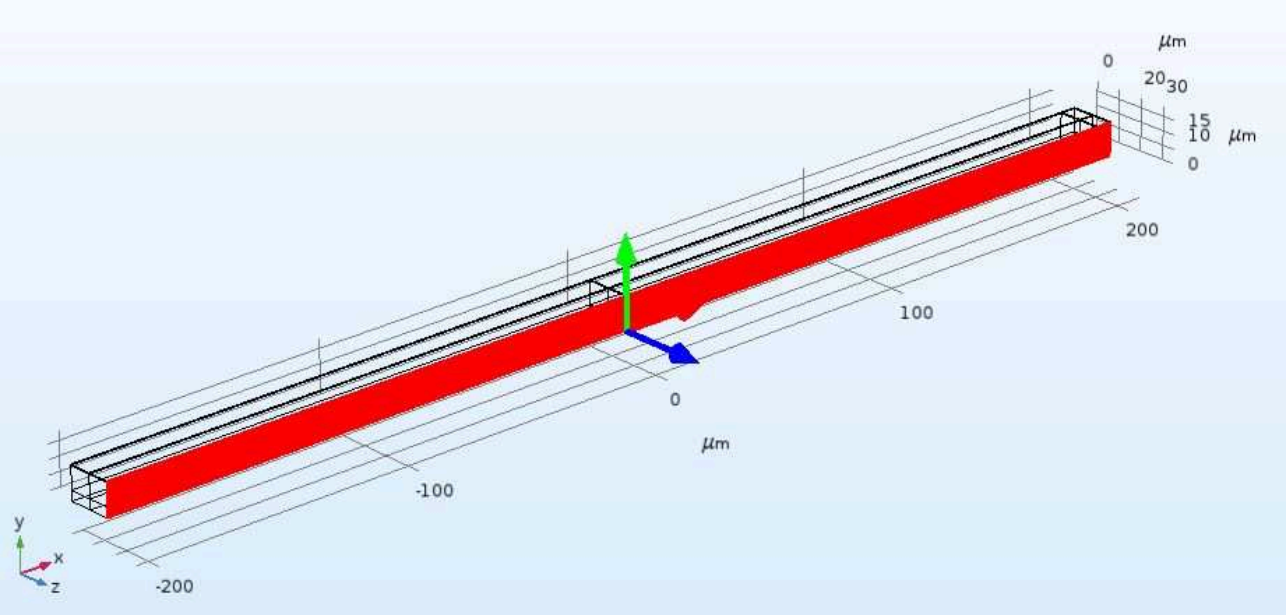

(a) *Symmetry plane boundary condition (red), applied to the 3D model to reduce the computational effort*

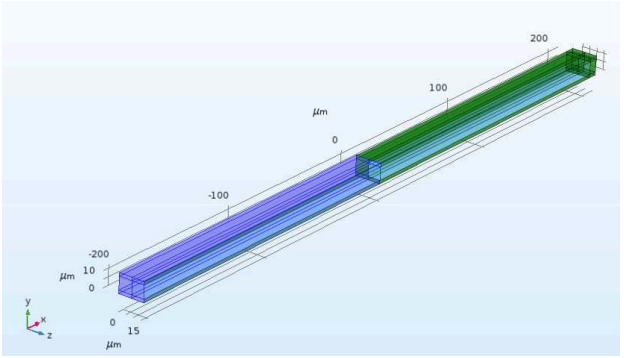

(b) *Fixed domain*

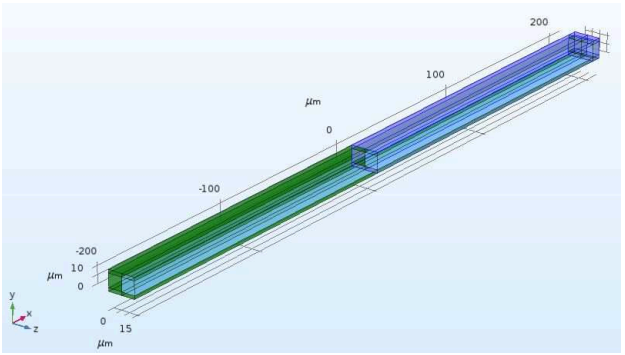

(c) *Free to vibrate domain*

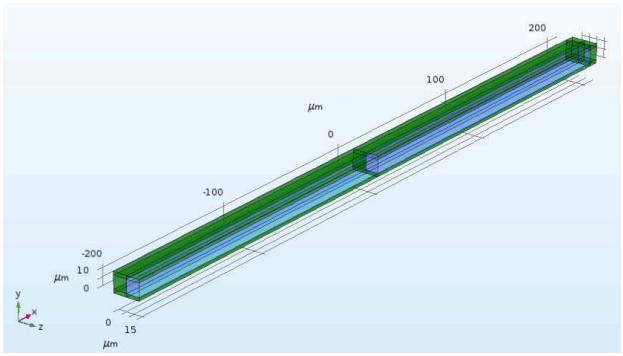

(d) *Fluid-Structure Interaction Boundaries*

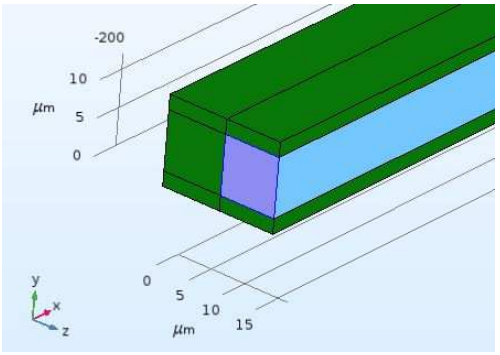

(e) *Adiabatic Pressure boundary condition at the channel inlet*

Figure 4.4.5: *Boundary conditions (darker blue) in the 3D simplified geometry; light blue stands for fluid, green stands for solid*

Description	Material parameter	Devices A, B, C
Young's Module [GPa]	E_c	170
Poisson's ratio	μ_c	0.25
Solid Density $[\frac{kg}{m^3}]$	ρ_c	2330

Table 4.3: *Material properties of the devices for the numerical simulations in COMSOL*

Glycerol %	Fluid Density $[\frac{g}{cm^3}]$	Viscosity [mPa·s]
0	0.99823	1.005
10	1.0221	1.31
20	1.0469	1.76
30	1.0727	2.5
50	1.1263	6
60	1.1538	10.8
70	1.1812	22.5
75	1.1948	35.5
80	1.2085	60.1
93	1.243	367
100	1.2611	1410

Table 4.4: *Density and viscosity values of the fluids used for the experiments: a water-glycerol mixture is used, with different percentages of glycerol affecting both density and viscosity*

4.4.5 Fluid properties

Experiments have been conducted changing the viscosity of a water/glycerol mixture by adding amounts of glycerol [33]. At first, when sweeping the viscosity we used the same fluid density, because this varies only slightly with different concentrations of glycerol. However, more precise results were obtained when sweeping both the viscosity and the density, as expectable: the values were taken from [5].

Compressibility Compressibility is supposed to be affecting the fluid motion in the complete case (Sections 3.3.2 and 3.2.1.2); in COMSOL, isothermal compressibility is defined as

$$\beta_T = -\frac{1}{V}\left(\frac{\partial V}{\partial p}\right)_T [Pa^{-1}] \tag{4.4.3}$$

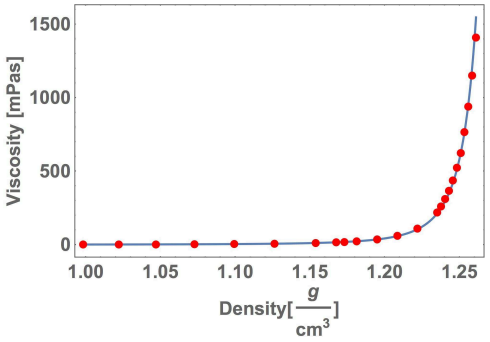

Figure 4.4.6: *Viscosity-density relationship; viscosity is changed using a water/glycerol mixture and adding amounts of glycerol to the water; density keeps almost constant while changing the viscosity, thus tuning β*

while isentropic compressibility

$$\beta_S = -\frac{1}{V}\left(\frac{\partial V}{\partial p}\right)_S = \frac{1}{\rho_0 c^2}[Pa^{-1}] \tag{4.4.4}$$

and the two are related by:

$$\beta_S = \beta_T - \frac{\alpha^2 T}{\rho c_p} \tag{4.4.5}$$

In our theoretical model $\gamma_\beta = \frac{\beta_T}{\beta_S} = 1$ and therefore $k = \beta_S = \beta_T$. To compare numerical results to theoretical results we simply derived the relationship to link these definitions to those given in [32]:

$$c = \sqrt{\frac{1}{\rho_0 k}} \tag{4.4.6}$$

$$\gamma = \omega^2 L^2 \rho_0 k \tag{4.4.7}$$

$$\alpha = \frac{\gamma}{\beta} = \frac{\omega L^2 \mu}{h_f^2} k \tag{4.4.8}$$

where $k[Pa^{-1}]$ is the parameter tuned in the parametric sweep in COMSOL. The values for k can be derived either from equation 4.4.6 or 4.4.7, assuming the knowledge of the speed of sound for any value of the density. We decided to find k for the three Devices after performing an eigenfrequency study with a starting guess value of $k_{guess} = 5.63E-10$: in this manner, the coupled study could be performed and the eigenfrequencies could be extracted and used in equation 4.4.7 (given γ) to obtain k (Table 4.5); no iteration was necessary because compressibility doesn't affect the eigenfrequencies much. Importantly, compressibility values do not change much for high changes of viscosity; however, to obtain more accurate results, compressibility has been changed while changing the viscosity.

	Device A, γ = 0.034	Device B, γ = 0.11	Device C, γ = 0.096
Fluid density $[\frac{g}{cm^3}]$	k $[Pa^{-1}]$	k $[Pa^{-1}]$	k $[Pa^{-1}]$
0.99823	4.34 E-10	4.71 E-10	4.21 E-10
1.0221	4.25 E-10	4.62 E-10	4.15 E-10
1.0469	4.16 E-10	4.52 E-10	4.09 E-10
1.0727	4.07 E-10	4.43 E-10	4.02 E-10
1.1263	3.89 E-10	4.25 E-10	3.89 E-10
1.1538	3.80 E-10	4.16 E-10	3.82 E-10
1.1812	3.72 E-10	4.08 E-10	3.77 E-10
1.1948	3.68 E-10	4.04 E-10	3.74 E-10
1.2085	3.64 E-10	4.00 E-10	3.71 E-10
1.243	3.55 E-10	3.91 E-10	3.64 E-10
1.2611	3.51 E-10	3.86 E-10	3.60 E-10

Table 4.5: *Values of compressibility for Devices A, B and C used in experiments and numerical simulations (first vibrational mode, complete geometries)*

4.4.6 Quantities for validation

In order to validate the model we will investigate the Quality factor trend with respect to the fluid viscosity, the fluid flow and the eigenfrequencies for the first two vibrational modes of the devices B and C, comparing numerical results with the theoretical and experimental ones. In the uncoupled structural analysis a comparison between the natural frequencies for the first two modes for Devices A, B and C is done, with little computational effort. In the coupled fluid-structure interaction problem the flow field, the energy dissipation, the quality factor and the natural frequencies are investigated to determine convergence of the mesh refinement and compare results with the theoretical and experimental ones. Often, to avoid useless waste of time, quantities for a single value of viscosity where discrepancies between theory and numerics are believed to be bigger have been compared.

	Device A, γ = 1.3	Device B, γ = 4.1	Device C, γ = 3.5
Fluid density [$\frac{g}{cm^3}$]	k [Pa^{-1}]	k [Pa^{-1}]	k [Pa^{-1}]
0.99823	4.32 E-10	4.27 E-10	4.16 E-10
1.0221	4.22 E-10	4.19 E-10	4.10 E-10
1.0469	4.12 E-10	4.10 E-10	4.03 E-10
1.0727	4.02 E-10	4.02 E-10	3.97 E-10
1.1263	3.83 E-10	3.85 E-10	3.84 E-10
1.1538	3.74 E-10	3.78 E-10	3.78 E-10
1.1812	3.65 E-10	3.70 E-10	3.72 E-10
1.1948	3.61 E-10	3.67 E-10	3.69 E-10
1.2085	3.57 E-10	3.63 E-10	3.67 E-10
1.243	3.47 E-10	3.55 E-10	3.61 E-10
1.2611	3.42 E-10	3.50 E-10	3.57 E-10

Table 4.6: *Values of compressibility for Devices A, B and C used in experiments and numerical simulations (second vibrational mode, complete geometries)*

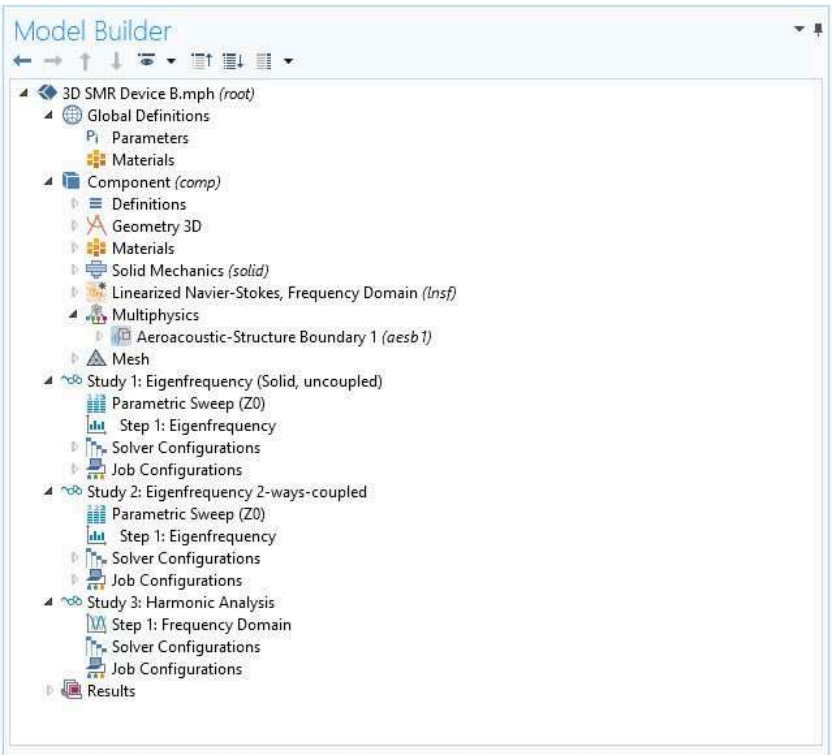

Figure 4.4.7: *Model builder for the 3D model simulations in COMSOL*

Chapter 5

Numerical results and discussion

Orandum est ut sit mens sana in corpore sano

Decimus Iunius Iuvenalis

In this chapter we report numerical results and discuss on the validity of the numerical model, highlighting the differences and similarities with the theoretical and experimental results. Most of the qualitative results (convergence analysis, effects of $\bar{z}_0$, Poisson's ratio, compressibility and fluid density, ...) are obtained running simulations on the simplified geometry of Device B (see Table 4.1) and working on the first vibrational mode.

Of course, viscosity is known to be a function of the temperature, which we assume to be $25°C$. For comparisons with the experimental results, in our simulations the viscosity spans from about 1-1400 [mPa·s], where 1 mPa·s = 1 cP; at $37°C$ blood viscosity is 3-4 cP. From figure 5.0.1 it is clear that in practical cases values much bigger than 1000 cP and much lower than 1 cP are unlikely to exist for bio-sensing. Corresponding values of β for the first mode of Device B are also shown.

However, some simulations on the simplified geometry were run with viscosity ranging 0.1-100000 [mPa·s] and β ranging in 0.001-1000, in order to investigate the behaviour out of the experimental range.

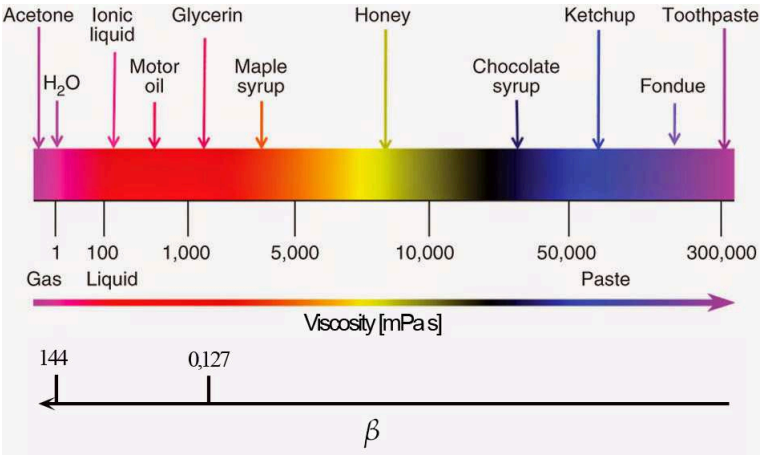

Figure 5.0.1: *Typical viscosity values and corresponding β values for Device B (simplified geometry) in the first vibrational mode (readapted from [4])*

5.1 Convergence analysis

To study the mesh convergence, the quality factor trend of Device B (simplified geometry) has been investigated while changing the mesh size in different directions. As shown in Figure 4.4.3 and explained in Section 4.4.2, the geometry has been divided in a certain number of elements, the amount of which depends on the number of divisions along each direction: x, y and z. Furthermore, the x-direction number of divisions is split in two: variable x_2 sets the number of divisions within the rigid lead channel, while variable x sets those in the cantilever.

From Figure 5.1.2 it appears that x_2 is not affecting the solution much, while the number of divisions in x, y and z strongly affects the results. It is also found out that slightly increasing the number of divisions in x, y and z at the same time gives a better convergence than strongly increasing one single parameter. It seems that 35/40 divisions are necessary along y and z to reach good convergence; for storage limitations, we choose a mesh with x=y=z=15 and x_2 = 10 number of divisions. This is found to give good enough results and not lose the correct qualitative behaviour; however, we underline that a finer mesh would give more accurate results.

Figure 5.1.1 shows the eigenvalue solver errors for the 2-way coupled analysis of Device B during the viscosity sweep. It expresses how fast the solver is to find a solution to the problem and how stable the procedure is; it is clearly affected by the mesh size and quality, but does not give any information on the reaching of a converged numerical solution.

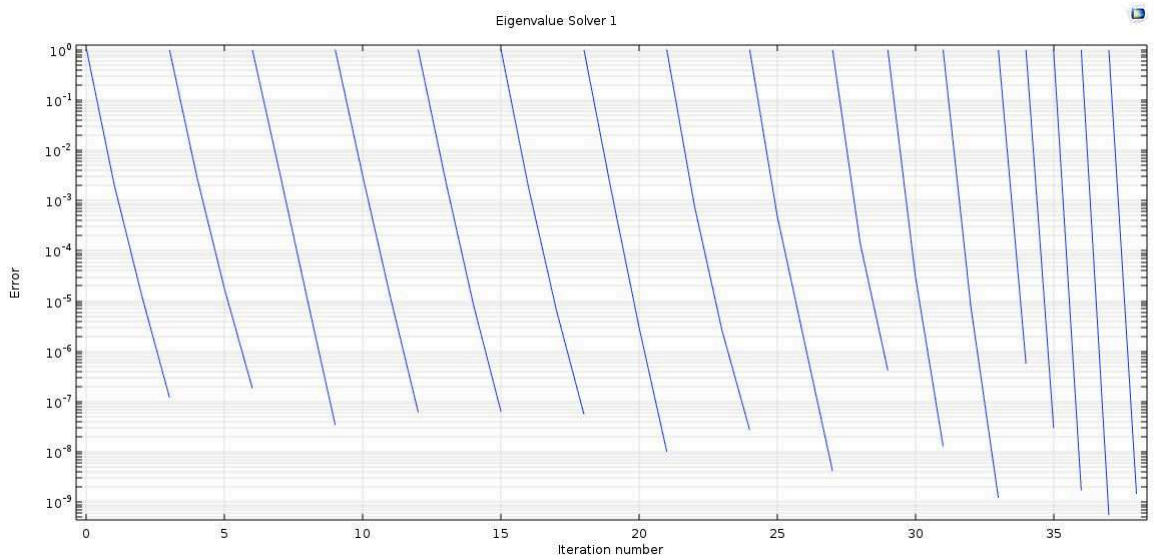

Figure 5.1.1: *Eigenvalue solver errors for the 2-way coupled analysis of Device B during the viscosity Parametric Sweep: convergence is quickly reached thanks to the good mesh quality*

We underline that values of parameters such as Si-N density, Young modulus and Poisson's ratios of the cantilevers experimented in [32] were not provided. Therefore, the first step has been reasonably tuning these values, together with the middle wall width, the tip dimensions and the channel U-bending dimensions and position, in order to achieve natural frequencies from our simulations as close as possible to the experimental ones.

5.2 Structural uncoupled analysis

Structural uncoupled results concern simulations run on the simplified geometry of Device B (Table 4.1), without any wall separating the inlet and outlet channels. We firstly performed a Parametric Sweep on the off-axis placement $\bar{z}_0$ and then on Poisson's ratios, as the theoretical model in [33], [31] and structures theory tell us how these parameters affect the eigenfrequencies of a structure. The first requirement was obtaining the correct eigenshapes and eigenfrequencies: values around hundreds of kHz for the first mode and some MHz for the second mode are coherent with the available devices. Figure 4.3.3 shows the first and second modes for Device B with $\bar{z}_0 = 0$ (simplified geometry); similar shapes have been correctly obtained for the complete geometries.

Effect of $\bar{z}_0$ A Parametric Sweep of $\bar{z}_0$ was run to investigate its influence on the eigenfrequencies. Figure 5.2.2 shows that increasing $\bar{z}_0$ brings about a decrease in the natural frequency of the first

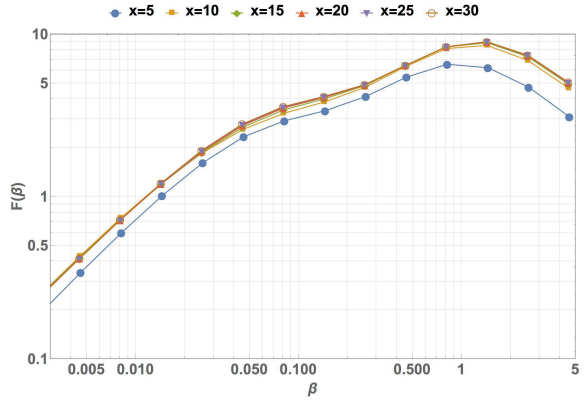

(a) *Effect of x-divisions of the mesh on the Quality Factor; other divisions: y=z=5, x_2=5*

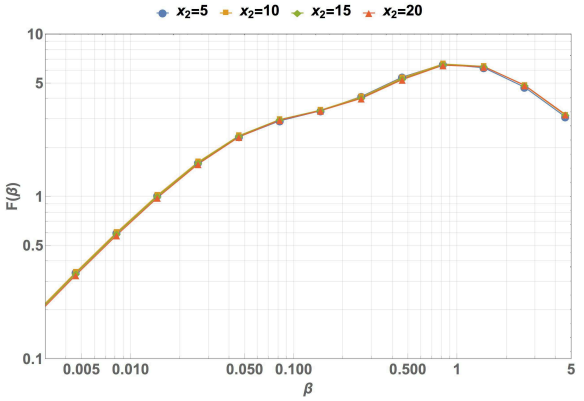

(b) *Effect of x_2-divisions of the mesh on the Quality Factor; other divisions: x=5, y=z=5*

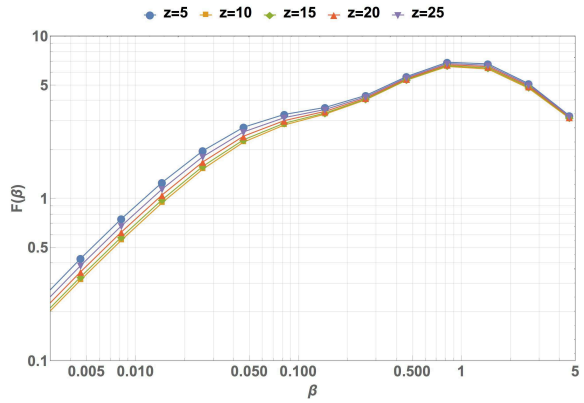

(c) *Effect of z-divisions of the mesh on the Quality Factor; other divisions: x_2=5, y=5, x=5*

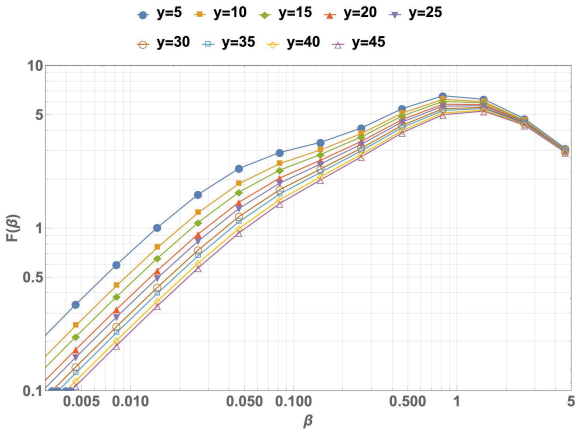

(d) *Effect of y-divisions of the mesh on the Quality Factor; other divisions: x_2=5, z=5, x=5*

Figure 5.1.2: *Mesh-convergence analysis on Device B (simplified geometry), with Poisson's ratio $\nu = 0.25$, $\bar{z}_0 = 0.1$ and two-way coupling analysis in the incompressible case (first vibrational mode)*

vibrational mode.

Effect of Poisson's ratio In the same manner as for $\bar{z}_0$, the influence of Poisson's ratio has been studied for $\bar{z}_0 = 0$, $\bar{z}_0 = 0.06$ and $\bar{z}_0 = 0.2$. Figure 5.2.3 shows that regardless the off-placement of the channel axis the trend of f_n with respect to ν is the same: increasing ν causes the resonance frequency to go up non-linearly. This qualitative result does not depend on the fact that the simulations were run on the simplified geometry and it is in agreement with intuition: in a 1D structure Poisson's ratio is known not to affect much the eigenfrequency. When moving to wide structures (plates and even more membranes) this parameter starts strongly affecting the eigenfrequencies, with the stiffness being proportional to the Poisson's ratio.

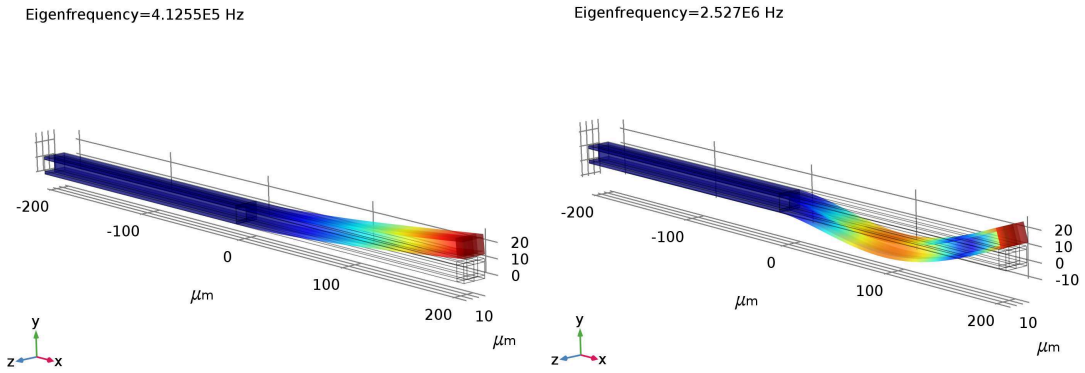

Figure 5.2.1: *First (left) and second (right) uncoupled mode shapes for Device B with* $\bar{z}_0 = 0$

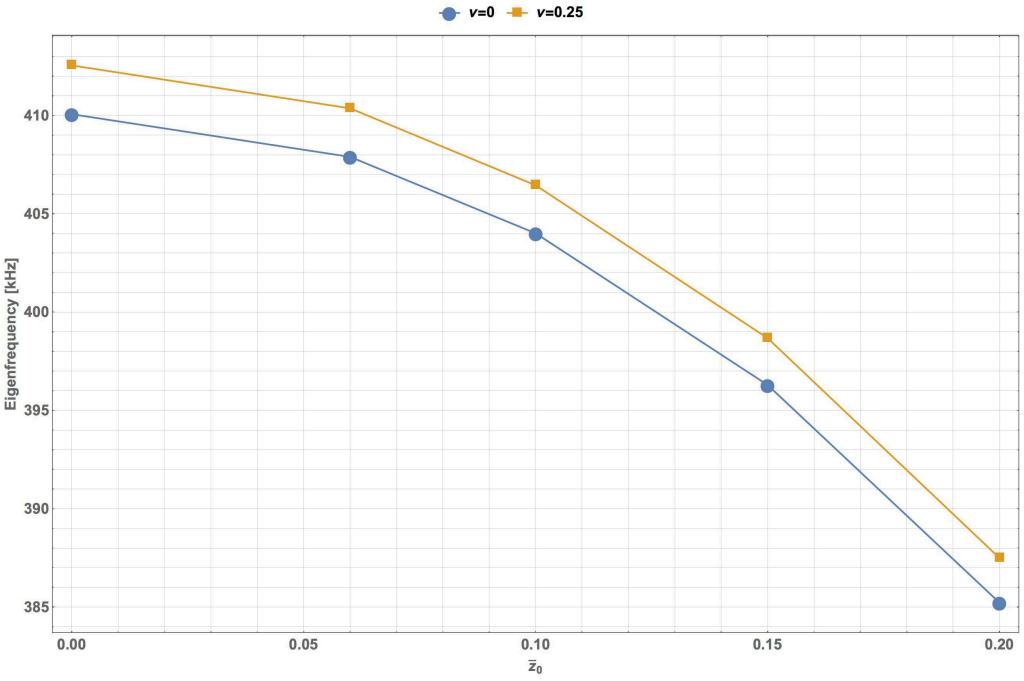

Figure 5.2.2: *Effect of* $\bar{z}_0$ *on the natural frequency of Device B (simplified geometry) in the uncoupled case for different Poisson's ratios (first vibrational mode)*

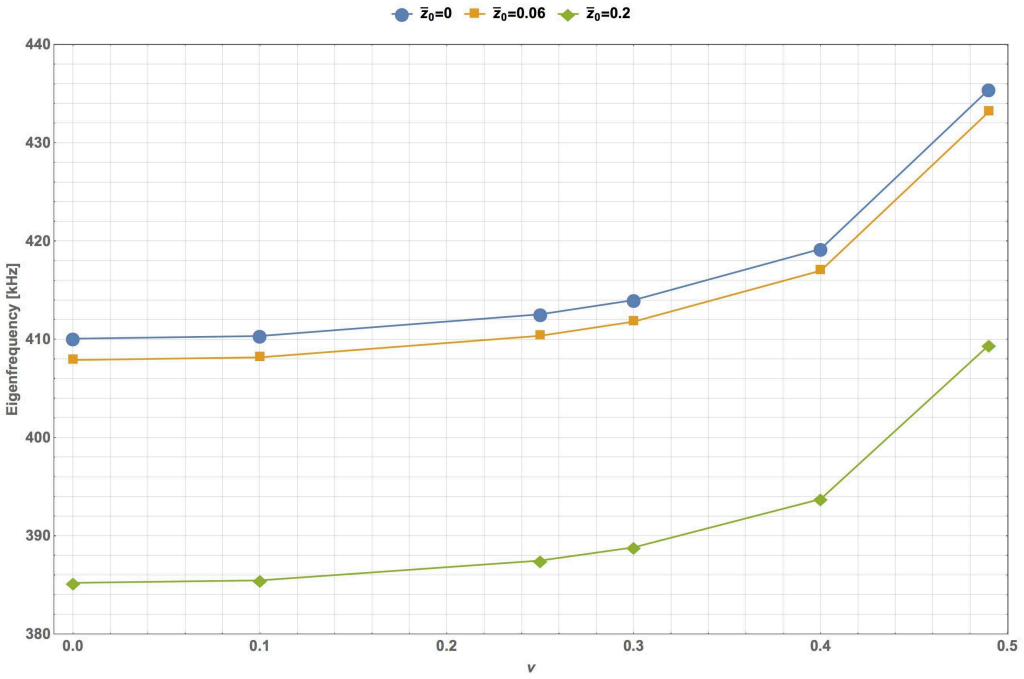

Figure 5.2.3: *Effect of Poisson's ratio ν on the natural frequency of Device B (simplified geometry) for several $\bar{z}_0$ in the uncoupled case (first vibrational mode)*

5.3 Coupled analysis

When turning on the fluid-structure interaction and solving for the eigenfrequency of the coupled system, we realize that the structural eigenshapes are not strongly affected; a literature survey [22] reveals that the eigenshapes of structures such as underwater structures, shore and off shore structures, moving tanks, dam reservoirs or big ship hulls containing fuel can be affected by the fluid loading; however, in this case, due to the fluid confinement in a small volume the loading seems to be not affecting the shapes.

5.3.1 On-axis solution

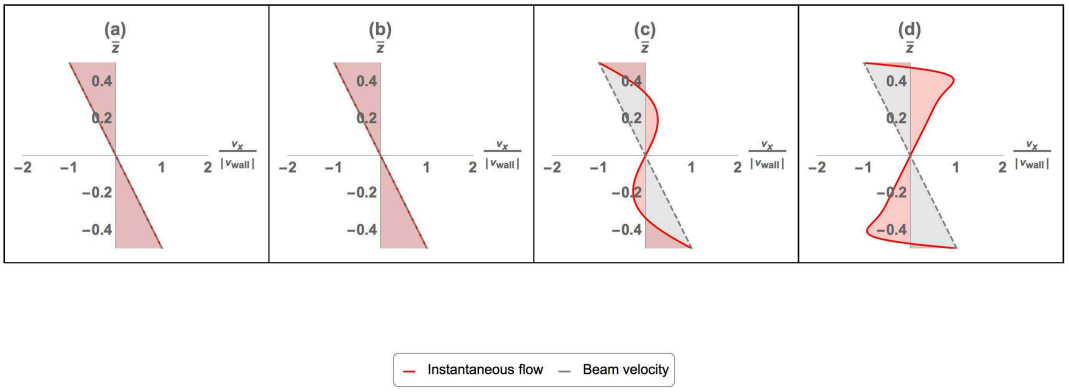

Figure 5.3.1: *On-axis fluid flow for different values of β: a) β = 0.001, b) β = 0.5, c) β = 46, d) β = 1000*

The on-axis solution ($\bar{z}_0 = 0$) is known to be unaffected by fluid compressibility and Poisson's ratio, which are therefore ignored at this stage. Figure 5.3.2 shows comparison between numerical and theoretical results for Device B (simplified geometry) in the incompressible case.

This simple case contains probably the most important result of this thesis, as it affects the complete solution and constitutes a mismatch with the theoretical model. Surprisingly, at low Reynolds numbers β (high viscosities) we numerically obtain a qualitative result opposite to the theoretical expectations. Whereas the theory predicts a counter-intuitive increase in the quality factor for increasing viscosities after the minimum in $\beta \simeq 46$, our simulations still show a non-monotonic trend but with the presence of two interesting points: a minimum in $\beta \simeq 46$ as in the theory and a maximum in $\beta \simeq 0.55$. Our physical intuition brings us to believe that our model is overestimating the dissipation or some dissipating phenomenon is missing in the theoretical model. One reason could be the fact that a more and more viscous fluid, even though commonly thought as almost a solid, cannot store more and more elastic or kinetic energy, then returning it during the vibrations. The system is not getting stiffer while the viscosity is increasing, and any shear, for as small as it is, between layers of fluid (which is kinetically behaving as the solid, but not dynamically) will bring about dissipation. In fact, no elasticity model is assigned to the fluid domain. So, there will be a point in the viscosity range where the fact that the fluid is moving as if it were a solid domain (almost linearly in x in the Euler-Bernoulli theory, but not perfectly in the numerical model) is being "damaged" by the fact that the dissipation is being enhanced by the viscosity increase: the very

viscous fluid simply acts as a load on the structure. We underline that:

- for inviscid fluid (very high β) the quality factor is very high because the fluid motion is almost linear and in counter-phase with respect to the beam everywhere but in a small boundary layer close to the walls; the very low viscosity term dominates imposing small dissipation;
- increasing viscosity (decreasing β) the quality factor coherently drops and reaches a minimum in $\beta = 46$, as the increase in viscosity makes the relative motion of the fluid with respect to the beam decrease and the boundary layers become thicker until merging in the channel;
- between the minimum and the maximum the fluid motion is tending to be almost linear in x and in-phase with the beam while the viscosity is increasing; this brings up the quality factor because the very small relative motion dominates on the increasing viscosity;
- a maximum is reached at $\beta \simeq 0.6$ when the fluid flow is not being affected from a further increase in viscosity; this brings up dissipation as the fluid flow is not perfectly linear in a numerical simulation.

Another source of discrepancy and error could be the absence of the wall at the end of the channel in the on-axis case in the theoretical model, which is coherently believed to affect the fluid motion, especially in proximity of the wall itself. This might lead to introduce back non-linear terms in the Navier-Stokes equations and the solution might be sufficiently more complex to describe this missing dissipation mechanism at low β even in the on-axis case. On the contrary, the theoretical model states that the matching between the movements of the fluid and solid parts is positive in terms of quality factor; it can be argued that including elasticity in the fluid and allowing for stiffening while increasing viscosity (as the very-viscous/solid analogy would push to do) might give back an indefinite increase in the quality factor. The fact that theoretical results with $\bar{z}_0 = 0.01$ almost perfectly match with numerical results with $\bar{z}_0 = 0$ is relieving. It is worth noting that it is not even possible to investigate this conceptually simple and fundamental case experimentally: technological issues and well-known imperfections that reality operates on ideally smooth mathematical surfaces will cause the fabrication to always be off-axis, even if just slightly. In this mismatch between theory and numerics, we are somehow also relieved as in practical cases no on-axis placement of the channel can ever exist and too deep investigation is not strictly necessary at unrealistic high viscosities.

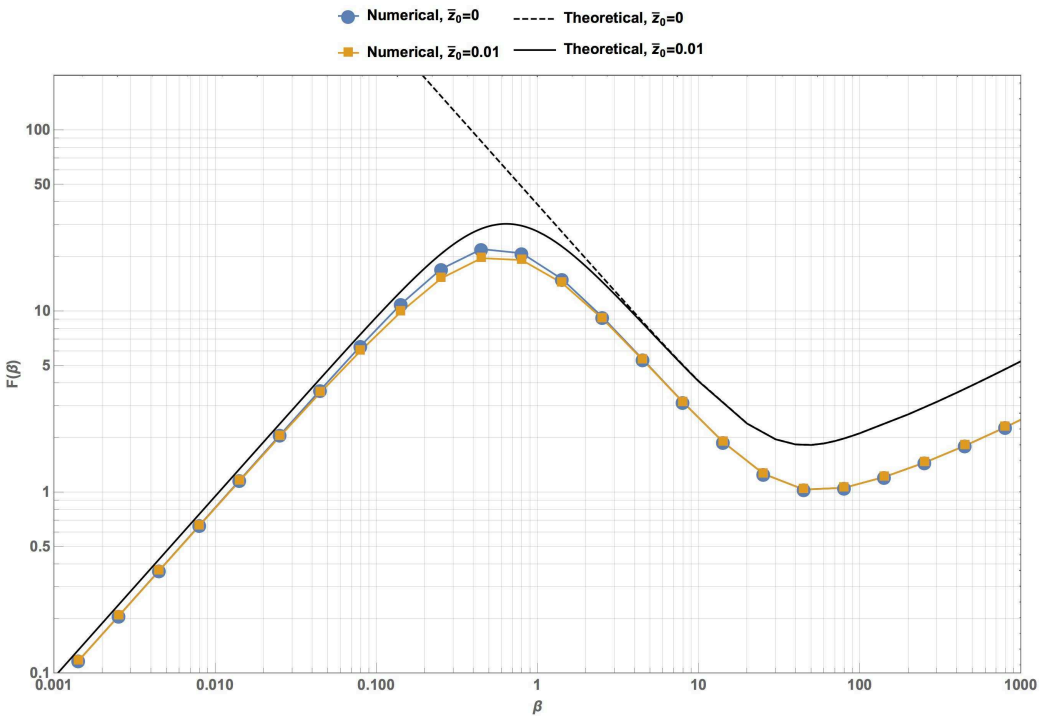

Figure 5.3.2: *Quality factor comparison in the on-axis case for Device B (simplified geometry) in the first vibrational mode, with Poisson's ratio $\nu = 0$, $\rho_f = 1000\ \frac{kg}{m^3}$ and two-way coupling; when $\bar{z}_0 = 0$, the theoretical model predicts a counter-intuitive behaviour, with the quality factor increasing for increasing viscosities (decreasing β); on the contrary, numerical results show that the quality factor reaches a maximum and then drops down; however, when $\bar{z}_0 = 0.01$ numerical and theoretical results agree quite well. This surprising result makes us think that the theoretical model in [32] is lacking of some dissipating phenomenon at high viscosities in the on-axis case*

Effect of fluid viscosity on eigenfrequency This is known not to affect the real part of the eigenfrequency of the system, but the dissipation through the imaginary part. However, a negligible dependence of the eigenfrequencies with viscosity is observed, probably due to what happens in the fluid while changing the viscosity: merging of boundary layers, linear or parabolic flow, in phase or in counter-phase flow.

Effect of rigid channel length The rigid channel length has no effect on the quality factor nor on the eigenfrequency, as expected, because no pumping is taking place in the on-axis case ($\bar{z}_0 = 0$).

5.3.2 Complete solution

It is clear that the off-axis case cannot be analysed individually, as it consists of a sub-solution to be linearly added to the on-axis case in the theoretical model; when running a simulation with a certain

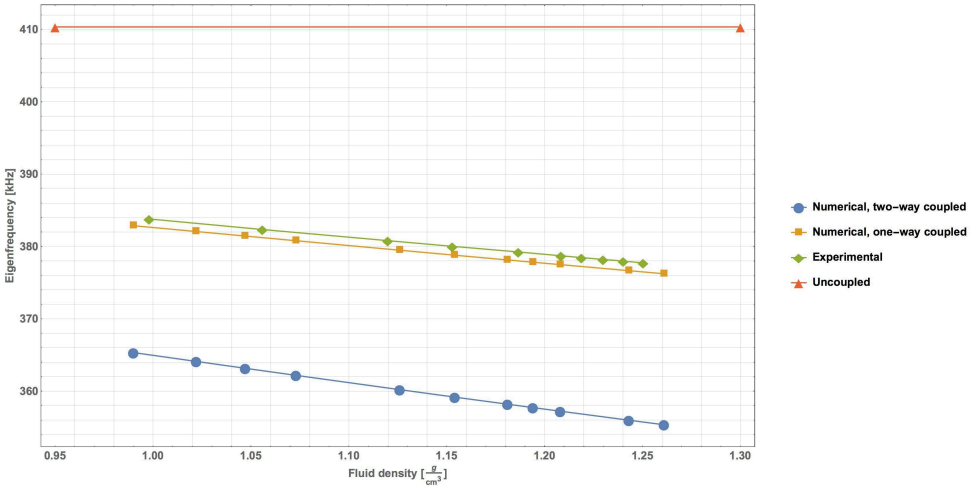

Figure 5.3.3: *Effect of ρ_f on the natural frequency of Device B (complete geometry) in the incompressible fluid case, with $\sigma = 0.25$, $\bar{z}_0 = 0.06$ and $\mu = 10$ $mPa{\cdot}s$; both the one-way and the two-way coupling are investigated (first vibrational mode)*

$\bar{z}_0 \neq 0$, the complete solution will obviously take place. We remind to the reader that, according to theoretical model, compressibility will affect the flow field in the channel and, consequently, the energy dissipation. For this reason, both the incompressible and compressible cases are simulated.

5.3.2.1 Incompressible fluid

At first, the case of incompressible fluid was analysed to learn if the model was capturing the main physical phenomena: in fact, compressibility will only affect results at low Reynolds numbers, as known from the theoretical model; thus, looking at the easier case of incompressible fluid is a good starting point of comparison with the experiments and theory and the quality factor is expected to be well captured at least at high Reynolds numbers. Therefore, we expected the minimum to occur at $\beta \simeq 46$, with $F(\beta) \simeq 1.58$.

Sensitivity of Eigenfrequency with fluid density As known, the fluid represents an added mass for the solid, therefore its density is expected to influence the eigenfrequency of the system: Figure 5.3.3 shows that higher values of fluid density return lower values of natural frequency, as expected. This analysis could be conducted without considering compressibility and with values of Poisson's ratio $\nu = 0.25$, $\bar{z}_0 = 0.06$ and $\mu = 10$ $mPa \cdot s$. Importantly, we note that the one-way coupling results are closer to the experiments than the two-way coupling ones.

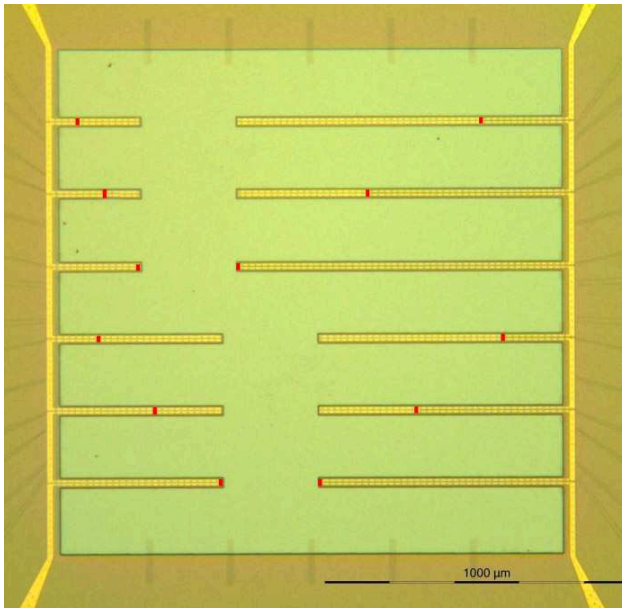

(a)

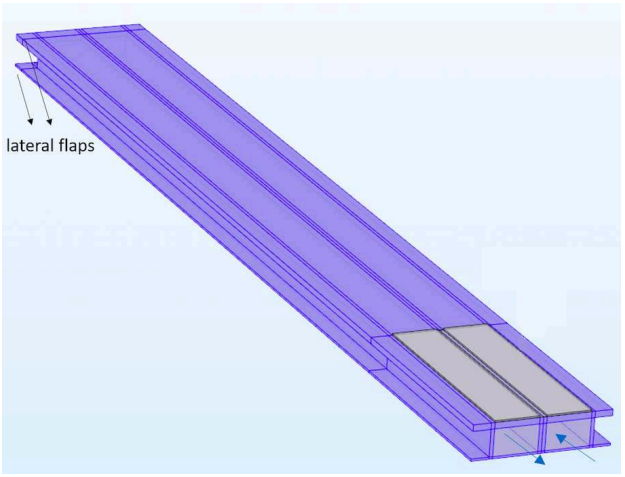

(b)

Figure 5.3.4: *(a) Chip image taken with Optishot microscope with a magnification of 5x (with courtesy of Mauricio Loucena Couto), showing an array of 12 SMRs with different tip lengths; red lines show the different positions of the channel end-walls; (b) ANEMS SMR geometry; ANEMS SMRs are fabricated in low stress silicon nitride ($ls - SiN_x$) via LPCVD (Low Pressure Chemical Vapour Deposition) to prevent residual stresses and buckling in the resonators*

Effect of tip length A parametric sweep of the tip length is available in the COMSOL model in prevision of a numerical analysis of Suspended Microchannel Resonators fabricated by the ANEMS group in EPFL, but the analysis has not been performed. Such a study would require some small changes to the geometry to reproduce the devices accurately and capture all the energy storing and dissipation. The effect of increasing the tip length is expected to be an increase in the stored energy with respect to the dissipated one, with a decrease in the natural frequencies.

Effect of rigid channel length Importantly, our simulations predict that the rigid channel length has not a big effect on the quality factor, oppositely to the theoretical expectations: this seems to be due to the small strength of the parabolic and plug flows within the rigid part of the device, due to the pumping mechanism, compared to the flow developed in the movable part.

Effect of Poisson's ratio Poisson's ratio has been found not to influence the Quality factor in the on-axis case, in agreement with the theory. However, when the channel is placed off-axis the theoretical model gives big importance to the value of ν, which brings up the quality factor at low

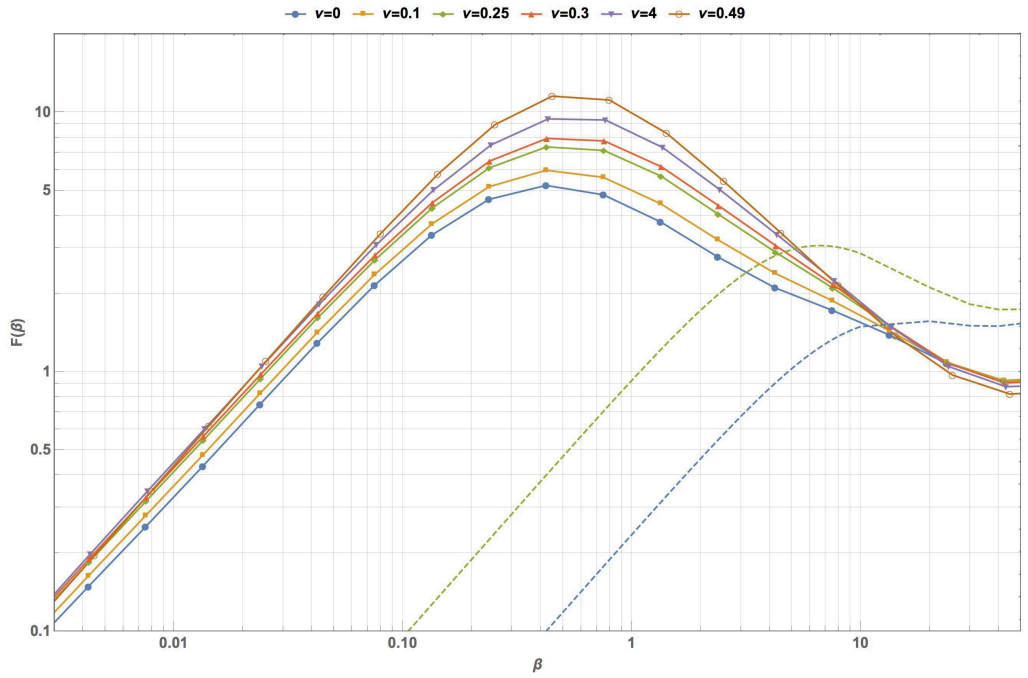

Figure 5.3.5: *Effect of Poisson's ratio ν on the Quality Factor of Device B (simplified geometry) in the incompressible fluid case, with* $\bar{z}_0 = 0.2$, $\rho_f = 1000\ \frac{kg}{m^3}$ *and two-way coupling: the theoretical model seems to overestimate the influence of Poisson's ratio on Q at low β, while the numerical results suggest that high ν give very small benefits in terms of energy dissipation; dashed lines stand for theoretical model, solid lines with markers for simulations*

β uniformly. On the contrary, our numerical simulations state that the benefits in terms of energy dissipation are reduced: high Poisson's ratios still increase Q at intermediate-low β, but for very low β Q values tend to merge on a line.

Effect of $\bar{z}_0$ Figures 5.3.6 and 5.3.7 show that the behaviour for intermediate β is more complex than the one predicted by the theoretical model in [32] and the drop is less strong with respect to an increase in $\bar{z}_0$.

Effect of bulk viscosity Bulk viscosity is believed not to affect the quality factor that much, according to [32]. Figure 5.3.8 shows that numerical results agree with this assumption.

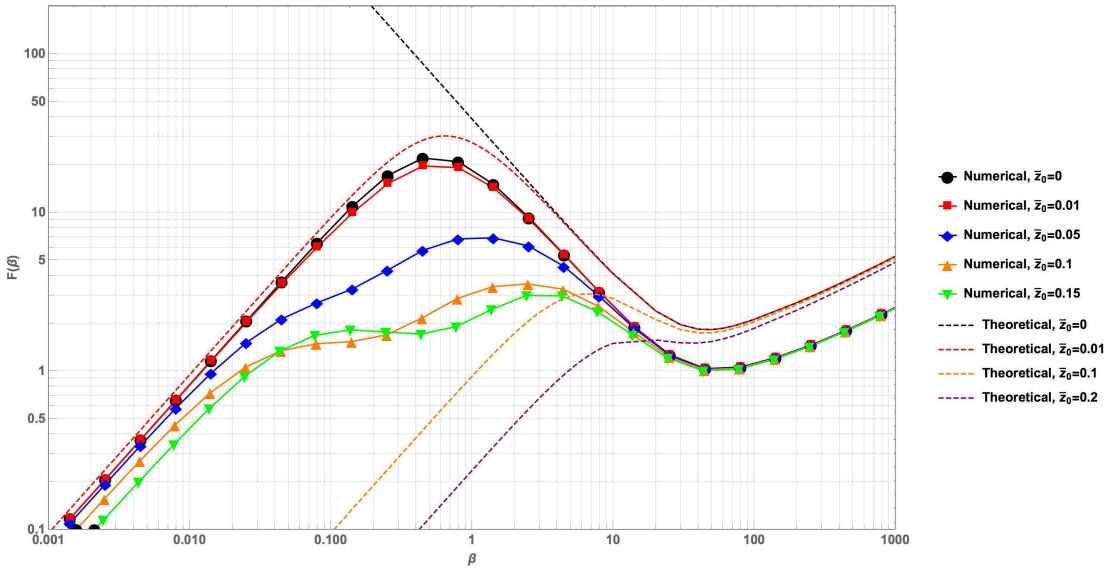

Figure 5.3.6: *Effect of $\bar{z}_0$ on the Quality Factor of Device B (simplified geometry) in the incompressible fluid case, with Poisson's ratio $\nu = 0$, $\rho_f = 1000\ \frac{kg}{m^3}$ and two-way coupling: the theoretical model seems to underestimate the quality factor at low Reynolds numbers β and slightly overestimate it at high Reynolds numbers β; dashed lines stand for theoretical results, solid lines for simulations*

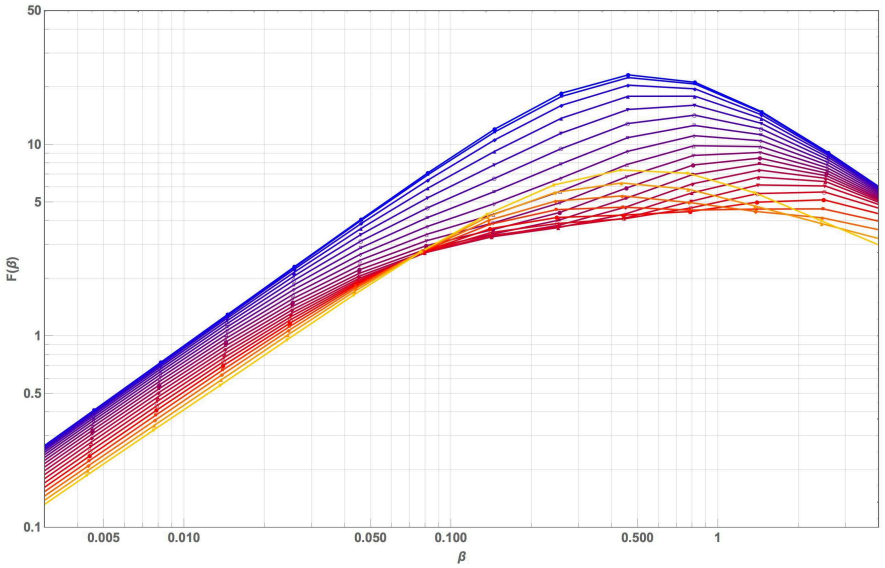

Figure 5.3.7: *Effect of $\bar{z}_0$ on the Quality Factor of Device B (simplified geometry) in the incompressible fluid case, with Poisson's ratio $\nu = 0$, $\rho_f = 1000\ \frac{kg}{m^3}$ and two-way coupling: colour gradient from blue to yellow passing through red shows the effect of increasing $\bar{z}_0$ from $\bar{z}_0 = 0$ to $\bar{z}_0 = 0.2$ with steps of $\Delta\bar{z} = 0.01$; the range β is reduced to where the effects occur*

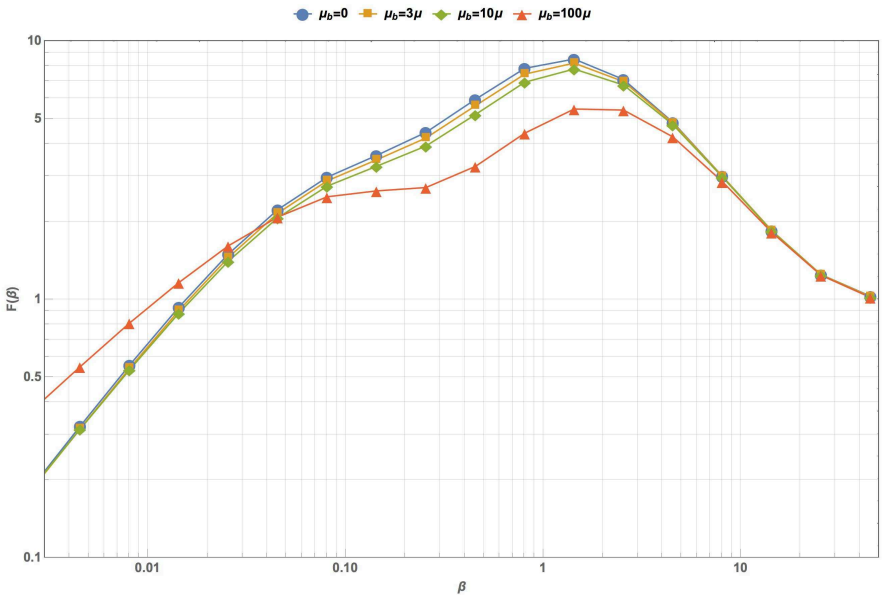

Figure 5.3.8: *Effect of bulk viscosity for Device B (simplified geometry) in the incompressible fluid case, with Poisson's ratio* $\nu = 0.25$, $\bar{z}_0 = 0.1$, $\rho_f = 1000\ \frac{kg}{m^3}$ *and two-way coupling: as predicted by the theoretical model, the bulk viscosity doesn't have a big effect on the dynamics of the fluid and therefore on the energy dissipation; a solution with an unrealistic value of* $\mu_b = 100\mu$ *has been found to give an idea of the strength of its effects*

5.3.2.2 Compressible fluid

Surprisingly oppositely to what predicted by the theoretical model, compressibility values do not seem to have a big influence on the quality factor. However, as stated in Section 4.4.5 we found k from equation 4.4.7, with γ taken from [33], and when comparing numerical and experimental results we used values of compressibility as in Tables 4.5 and 4.6.

5.4 Theoretical, numerical and experimental comparison

This section contains the comparison between numerical results of Devices B and C (see Tables 4.1, 5.2 and 5.3) with their experimental counterparts [33] and [32].

All simulations discussed in this section have been run on the complete geometries for the first and second vibrational mode. The geometries have been built in such a way to reproduce as precisely as possible the experimented ones. Fluid properties (compressibility, viscosity) and solid properties (Young Modulus, Poisson's ratios) have also been chosen coherently to match the experimental conditions.

Description	COMSOL	Experiment
Eigenfrequency (Mode 1) [kHz]	220	218.9
Eigenfrequency (Mode 2) [kHz]	1372	1354.1

Table 5.1: *First two modes eigenfrequencies for Device A (complete geometry) in vacuum*

Description	COMSOL	Experiment
Eigenfrequency (Mode 1) [kHz]	427	426.8
Eigenfrequency (Mode 2) [kHz]	2400	2476

Table 5.2: *First two modes eigenfrequencies for Device B (complete geometry) in vacuum*

After reaching convergence with a mesh convergence study (Section 5.1), we performed an Eigenfrequency analysis and obtained the eigenfrequencies for Devices A, B and C for the first two vibrational modes. Results are summed up in Tables 5.1, 5.2 and 5.3 and show good matching with the experimental results.

As far as the quality factor is concerned, the results match quite well, especially in the first mode case and at intermediate β (Figure 5.4.1) of Devices B and C. Simulations for Device A are to be still performed. Experiments at very high and low β are not available and an experimental evidence of our belief on the behaviour at low β of the Quality Factor is not possible (section 5.3.1). However, such a good matching lets us believe that our nuemrical model and simulations are reliable and valid; the linearized Navier-Stokes equations and Euler-Bernoulli beam theory combined and the eigenvalue study are able to capture the energy dissipation in Suspended Microchannel Resonators; we also claim that when simulations are extended to very low β they reveal a surprising different behaviour than that stated in [32], and more investigation is needed.

We mention the fact that when we turned on the 2-way coupling, the eigenfrequencies were shifted down (5.3.3) and Q dropped of some units. Therefore, to obtain a good matching between the experiments and the numerical results in this case too, the width of the wall between inlet and outlet channel had to be changed: we remind that this parameter is not defined in [33], therefore it is assumed reasonably. We underline that the best results were obtained with the 1-way coupling: such a numerical model seems to be sufficiently good to obtain Q as close as possible to the experimental ones; 2-way coupling makes things more difficult and is likely to be not even necessary in the model: due to the small fluid density and small channel volume, the forces exerted by the fluid on the solid

Description	COMSOL	Experiment
Eigenfrequency (Mode 1) [kHz]	281	275.1
Eigenfrequency (Mode 2) [kHz]	1710	1663.9

Table 5.3: *First two modes eigenfrequencies for Device C (complete geometry) in vacuum*

are small and could be neglected. This is done also in [29], where experiments, numerics and theory match well.

Many reasons of discrepancy between theoretical, experimental and numerical results are here discussed. Importantly, all the dimensions in the real devices are affected by a certain fabrication tolerance: as these dimensions enter the eigenfrequencies and the normalizing factors and affect the energy dissipation mechanism at this small scale, experimental results are to be taken carefully; for instance, β values depend on eigenfrequencies and small changes in them affect the β range; for instance, the channel thickness h_fluid strongly affects the normalizing factor, which goes as $\frac{1}{h_f^3}$; secondly, due to the uncertainty in the normalized off-axis placement $\bar{z}_0$ in the devices for fabrication tolerances, Sader [32] used it as a fitting parameter in the theoretical/experimental comparison. Other reasons of discrepancy shall be found in the fact that some damping might have affected experiments if the environment was not perfectly vacuum or because of other unseen phenomena. Furthermore, extraction of Q_{fluid} from the total Q requires additional experiments which tend to accumulate the error. Another source of difference between experiments and numerical results can be found in the fact that experiments were conducted applying an external pressure and thus developing a stream within the channel. Thus, in the inlet and outlet channel the flows would be different and it cannot be stated that a lower dissipation in one channel is compensated by the increase of dissipation in the other channel. For all these reasons, experimental values are to be considered valid for comparison within a certain range of tolerance (measurements error bars are not shown in Figure 5.4.1).

As far as the comparison with the theoretical model is concerned, we recall that Euler-Bernoulli theory makes use of strong assumptions, whose validity depends on the final scope. It might be possible that these assumptions strongly reduce the accuracy to model a complex phenomenon such as Fluid-Structure Interaction at the small scale. For instance, a 2D theoretical model might not be sufficient to predict all the 3D deformative mechanisms, while a 3D numerical model with a big number of elements will be able to describe fluidic and solid deformations closer to reality.

As a matter of fact, a strong assumption has been the linearization of the fluid motion. It could be possible that small second order terms enter the vectorial laplacian in Navier-Stokes equations and become important at high viscosity.

Furthermore, stating that the fluid is experiencing rigid motion when very viscous is not completely coherent. If that were the case, such a statement would apply to the solid domain too, thus storing no elastic energy through deformation. On the contrary, the solid elements must be slightly deformed in order to store elastic energy, as well as the fluid elements which in turn will be deformed and dissipate energy through viscosity (see Section 5.3.1 for more details).

We finally recall that the quality factor is typically defined by means of a decaying factor in a harmonic analysis, while the theoretical model defines $Q = \frac{Solid\ Kinetic\ Energy}{Fluid\ Dissipation}$, neglecting, for instance, fluid Kinetic Energy.

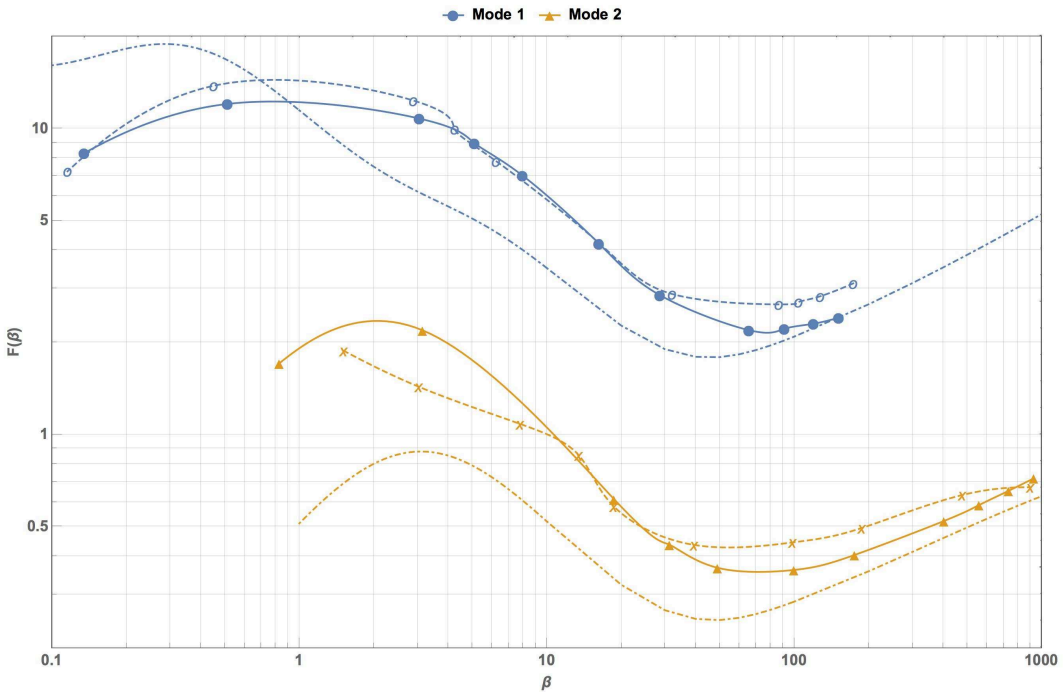

(a)

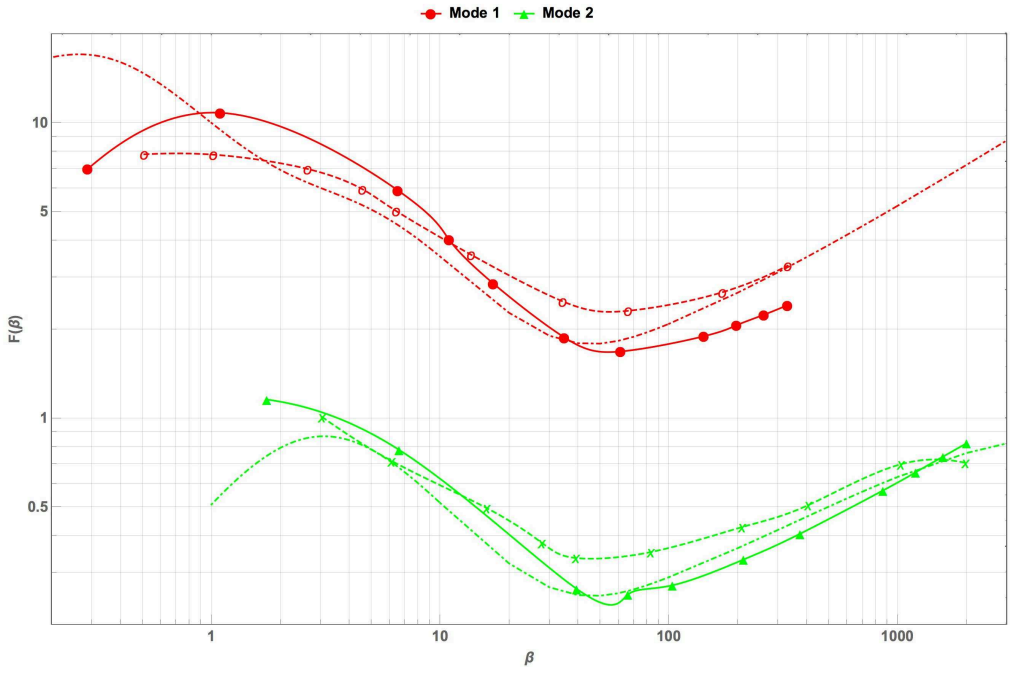

(b)

Figure 5.4.1: *Experimental and numerical comparison of the Quality factor for the first two vibrational modes of a Suspended Microchannel Resonator (SMR), one-way coupled: experiments (dashed lines) match quite well with numerical results (solid lines) and theoretical predictions (dot-dashed lines). Markers are placed where experimental and numerical values were obtained; third order interpolation of the data has been performed; density, viscosity and compressibility are changed according to Tables 4.4 and 4.5; a) Device B:* $\bar{z}_0 = 0.05$, $\gamma_1 = 0.11$, $\gamma_2 = 4.1$ *and* $\nu = 0.25$*; b) Device C:* $\bar{z}_0 = 0.05$, $\gamma_1 = 0.096$, $\gamma_2 = 3.5$ *and* $\nu = 0.25$*; experimental results are taken from [33]*

Chapter 6

Conclusions and future work

> L'illuminismo è l'uscita dell'uomo dallo stato di minorità di cui egli stesso è colpevole. Minorità è l'incapacità di servirsi della propria intelligenza senza la guida di un altro. Colpevole è questa minorità, se la sua causa non dipende da un difetto di intelligenza, ma dalla mancanza di decisione e del coraggio di servirsi di essa senza essere guidati da un altro. "Sapere aude!" Abbi il coraggio di servirti della tua propria intelligenza! Questo dunque è il motto dell'illuminismo.
>
> *Immanuel Kant*

To validate the numerical model, we compared results of the Quality Factor from the theory and the experiments provided in [32] and [33]. Our numerical model seems to work fine where the experimental data are provided but it is in contrast with the theoretical model at low Reynolds number. We consider it valid in the region of interest and send to further investigation the difference at low β between theory and numerics.

Some parameters were not provided in the reference paper [33] and had to be properly tuned to match the eigenfrequencies. More reliable results would be obtained if simulations and experiments were performed on own devices, of which all dimensions and material properties would be known; filtering out the Quality Factor due to the structural energy dissipation is also a major issue.

Our numerical model has proved to capture well enough the energy dissipation in Suspended Microchannel Resonator: it can therefore be used to perform simulations while sweeping material

and geometrical parameters to design an optimized Suspended Microchannel Resonator, to achieve as high as possible Quality Factors. To do so, it seems wise to reduce the off-axis placement of the channel $\bar{z}_0$, to use materials with as big as possible Poisson's ratios (compatibly with fabrication requirements and bio-sensing performances) and to drive the device at its first vibrational mode.

Future work requires investigation on Device A to validate our numerical model at very low β too, confirming our believes on the theoretical model limitations and sweeping geometrical properties for a fixed viscosity value to learn how to decrease energy dissipation by optimal design; a numerical analysis on the effects of the longitudinal in-plane eigenmodes of the cantilever is suggested; in such a way, the pumping mechanism can be isolated and studied; investigation on why compressibility and rigid channel length do not to affect the Quality Factor and the fluid motion (as theoretically expected) is necessary, especially when comparison with experimental results is good anyhow; we finally recommend deeper investigation on the validity of the 2-way coupling defined in our model, suggesting for more comparison between 1-way and 2-way coupled results and questioning the need of the 2-way coupling at a small scale such that of Suspended Microchannel Resonators.

Appendices

Appendix A

Conference Abstract and Poster

In this appendix we attach the abstract and poster that have been submitted to the 1st International Workshop on Nanofluidics and Nanomechanics, held in Turin on 14th-15th September 2017.

They sum up the most relevant results of this Master of Science Thesis when comparing numerics, theory and experiments.

We had the chance to meet some of the authors of the reference paper [32], [33] and discuss about the main discoveries obtained in these six months of work at the École polytechnique fédérale de Lausanne from February to August 2017.

Energy Dissipation in hollow beams resonators: COMSOL model comparison with theoretical and experimental results

A. Gerbino[1,2*], A. De Pastina[1], F. Gallaire[3], C. Meinhart[4], L.G. Villanueva[1]

[1] *Advanced Nano-electromechanical Systems Laboratory, EPFL, 1015 Lausanne, Switzerland*
[2] *Dipartimento di Ingegneria Meccanica e Aerospaziale, Sapienza Università di Roma, 00184, Italy*
[3] *Laboratory of fluid mechanics and instabilities, EPFL, 1015 Lausanne, Switzerland*
[4] *Department of Mechanical Engineering, University of California Santa Barbara, Santa Barbara, California 93106, USA*
* *Email: andreagerbino@gmail.com*

Suspended Microchannel Resonators (SMRs) are hollow resonant structures containing an embedded U-shaped microfluidic channel. This configuration reduces the losses due to the damping caused by the fluid, which are deleterious for the quality factor in traditional solid resonators immersed in fluid. As bio-sensors, SMRs enable real time detection of liquid compounds, by added mass resonance frequency shift, with very high quality factors [1], and weighing of nanoparticles, bacterial cells and more[2].
Theoretical and experimental results have proved that in these devices the energy dissipation is a non-monotonic function of the fluid viscosity (or Reynolds number), while in conventional cantilevers it always increases with the viscosity as the damping from the fluid on the solid structure increases. Furthermore, a variation in the device quality factor by several orders of magnitude was discovered when the microfluidic channel axis was placed away from the beam neutral axis, which is expected to happen always for fabrication limits, and a change in the behavior of Q at high viscosities was noticed when varying fluid compressibility [3].
In this work, both a Mathematica (V10.4) code and a 3D COMSOL (V5.3) models are produced to validate the theoretical and experimental results on the energy dissipation in these devices (Device A) [3]. To reduce the computational effort an eigenvalue study is performed. The incompressible and compressible cases are investigated while changing the fluid and device characteristics. The effects of the rigid lead channel length have been studied and some differences have been found with respect to the reference paper [3]. Importantly, numerical results seem to match quite well with the theoretical results everywhere but at high viscosities, while a slightly bigger difference exists between numerical and experimental results at this stage.

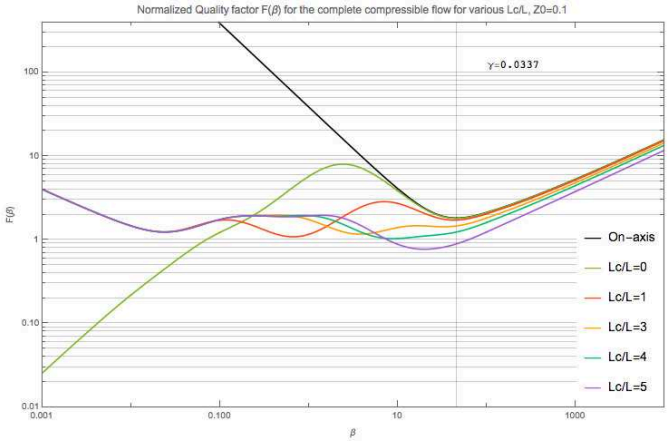

Figure 1: Effect of the Rigid Lead Channel length on the normalized quality factor as a function of Reynolds number, with Z_0=0.1 and acoustic wavenumber γ=0.337.

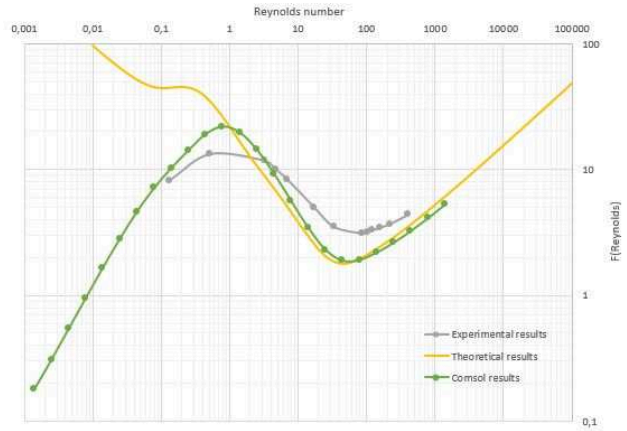

Figure 2: Comparison between numerical, experimental (Device A, [3]) and theoretical results. Z_0=0.06, h_f=8 μm, γ=0.12.

References

[1] T. P. Burg and S. R. Manalis, *Appl. Phys. Lett.* **83**(13), 2698, 2003
[2] T. P. Burg et al., *Nature,* **446**, 1066, 2007
[3] J. E. Sader et al., *J. Fluid Mech.,* **650**, 215, 2010

FEM modeling of energy dissipation in SMRs

Andrea Gerbino[1,2], A. De Pastina[1], F. Gallaire[3], C. Meinhart[4], and Luis Guillermo Villanueva[1]

1. EPFL - School of Engineering – Mechanical Engineering– Advanced NEMS Lab
2. Sapienza Università di Roma, Dipartimento di Ingegneria Meccanica e Aerospaziale
3. EPFL - School of Engineering – Laboratory of fluid mechanics and instabilities
4. University of California Santa Barbara, Department of Mechanical Engineering

Abstract

- Suspended Microchannel Resonator [1], [2], [3]
- Development of a 3D coupled fluid-structure interaction model to extract Quality Factor as function of fluid dynamic viscosity
- Comparison between numerical, theoretical [1] and experimental [2] results
- **Good match between experimental and numerical Q for first two modes**
- **Decreasing Q for increasing viscosity in contrast with theory**

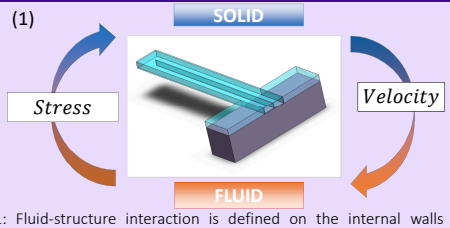

Fig. 1: Fluid-structure interaction is defined on the internal walls of the channel; a fixed constraint is imposed to the rigid channel (x<0). The cantilever is let free to vibrate (x>0). Linearized Navier-Stokes and Solid Mechanics equations are solved in COMSOL. The solid transfers momentum to the fluid, which sends back stresses to the cantilever, affecting its motion.

FEM model

- 3D eigenfrequency study in COMSOL Multiphysics®
- Device symmetry is exploited (fig.2a)
- Both 1-way-coupling and 2-way-coupling simulations are performed
- The quality factor is extracted as:

$$Q_{Comsol} = \frac{Im[\lambda]}{2Re[\lambda]}$$

where λ is the complex eigenvalue.

- The quality factor is scaled according to the analytical model proposed by Sader in [1], in function of the Reynolds number β:

$$Q = F(\beta)\frac{\rho_c}{\rho_f}\left(\frac{h_c}{h_f}\right)\left(\frac{b_c}{b_f}\right)\left(\frac{L}{h_f}\right)^2, \qquad \beta = \frac{\rho_f \omega h_f^2}{\mu}$$

- Parameters studied: compressibility ($\gamma = \left(\frac{\omega L}{c}\right)^2$ is the normalized acoustic wavenumber), dynamic viscosity, off-axis placement Z_0, Poisson ratio, mode number.

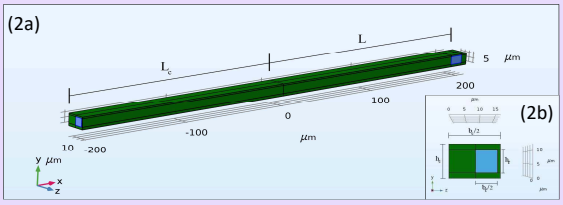

Fig.2a: COMSOL Model (half geometry) of Device A [1]: h_f=8 μm, h_c=12 μm, b_f=16 μm, b_c=33 μm, L=204 μm, L_c=210 μm, cantilever length= 210 μm, Z_0=0.06.
In green the elastic domain, in blue the fluid domain. Z_0 is the off-axis placement of the fluidic channel with respect to the beam neutral axis.
Fig.2b: Cross-section of half geometry of Device A [1] (symmetry boundary condition is exploited)

Theoretical model [1]

- 2D theoretical model is only due to fluid motion and viscous forces, through the rate-of-strain tensor **e**, defined as: $E_{ij} = \frac{1}{2}(\partial_j v_i + \partial_i v_j)$
- Quality factor is computed as:

$$Q = 2\pi \left.\frac{E_{stored}}{E_{diss/cycle}}\right|_{\omega_R}$$

- Strong effect of:
  - compressibility [1]
  - channel off-placement Z_0 [1]
  - Poisson's ratio [3]
  - mode number [2]

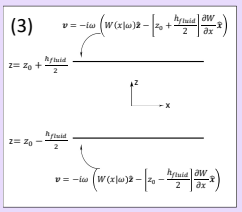

Fig. 3:
2D theoretical model; Euler-Bernoulli beam equations imposed as boundary conditions on the top and bottom wall; x is the coordinate along the length of the beam, z_0 is the off-placement of the channel with respect to the beam neutral axis [1].

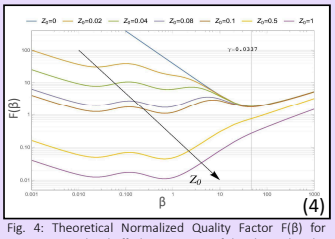

Fig. 4: Theoretical Normalized Quality Factor F(β) for various normalized off-placements Z_0 of the channel in the compressible case (γ=0.0337) for L_c=L; the theoretical model predicts an increasing F(β) for increasing viscosity (decreasing β) and lower F(β) for higher off-placements of the channel with respect to the beam neutral axis. For Z_0<0.2 this effect is stronger for β<10.

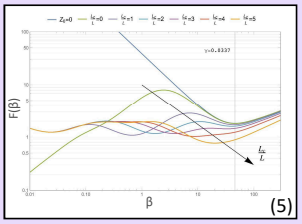

Fig. 5: Theoretical Normalized Quality Factor F(β) for various rigid lead channel lengths L_c in the compressible case (γ=0.0337) and Z_0=0.1; the theoretical model predicts a surprisingly different behavior when L_c=0. The local maxima and minima of F(β) are strongly affected by L_c.

Results

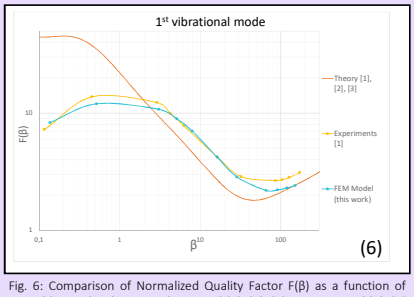

Fig. 6: Comparison of Normalized Quality Factor F(β) as a function of Reynolds Number between theoretical [1], [2], [3], experimental [1], [2] and numerical results for Device A (h_f=8 μm, h_c=12 μm, b_f=16 μm, b_c=33 μm, L=204 μm, L_c=210 μm, cantilever length=210 μm, Z_0=0.06, normalized wavenumber γ=0.12, Poisson's ratio=0.25) for Mode 1. Viscosity spans from to 1 mPa·s to 1000 mPa·s and is inversely proportional to Reynolds Number.

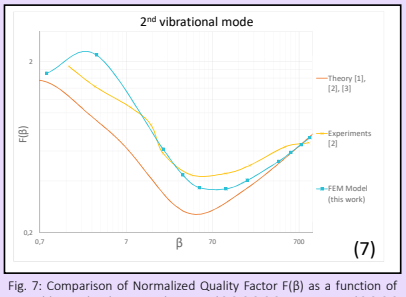

Fig. 7: Comparison of Normalized Quality Factor F(β) as a function of Reynolds Number between theoretical [1], [2], [3], experimental [1], [2] and numerical results for Device A (h_f=8 μm, h_c=12 μm, b_f= 16 μm, b_c=33 μm, L=204 μm, L_c=210 μm, cantilever length=210 μm, Z_0=0.06, normalized wavenumber γ=0.12, Poisson's ratio=0.25) for Mode 2. Viscosity spans from to 1 mPa·s to 1000 mPa·s and is inversely proportional to Reynolds Number.

Conclusions

- Good agreement between experimental and numerical results for β∈(1,1000) for first two modes
- Contrasting behavior at high viscosities between theoretical and numerical results (β<1)
- Dependence of Q on Z_0, L_c, compressibility, Poisson's ratio and mode number for β<1.
- Need of improvement of 2-way-coupling modelling

References
[1] E. Sader et al., "Energy dissipation in microfluidic beam resonators", J. Fluid Mech., 650, 215, 2010
[2] E. Sader et al., "Energy dissipation in microfluidic beam resonators: Dependence on mode number", J. Fluid Mech., 108, 114507, 2010
[3] E. Sader et al., "Energy dissipation in microfluidic beam resonators: Effect of Poisson's ratio", Physical Review, E 84, 026304, 2011

Andrea Gerbino
Advanced NEMS Lab
andreagerbino@gmail.com

The authors would like to thank SNSF for the funding provided via the project PP00P2 144695 .

Appendix B

Mathematica code

In this section the most relevant codes written in Mathematica (release 10.4) are collected: these codes are meant to serve any user to solve the theoretical model and verify the discussed results.

Appendix B.1. Coefficients for the on-axis case

Coefficient research for the general β solution for the Quality factor of the on – axis case

The beam is believed to vibrate at its fundamental mode, the coefficient of which is B and the lenght is L (eq. 17 from Sader)

```
B = 1.8751 / L; (*for the first mode shape*)
c = (Cos[B * L] + Cosh[B * L]) / (Sin[B * L] + Sinh[B * L]);

coefficientGeneral = 1 / 4 *
    Integrate[(Cos[B * x] - Cosh[B * x] - c * (Sin[B * x] - Sinh[B * x])) ^ 2, {x, 0, L}] /
     Integrate[D[(Cos[B * x] - Cosh[B * x] - c * (Sin[B * x] - Sinh[B * x])), x] ^ 2,
      {x, 0, L}] // FullSimplify
```

$$0. + 0.0537891\, L^2$$

```
(*Please notice that the mode functions W[x]^2=W[x]*W[x] are orthonormal,
therefore we simply obtain 1*L^2. The factor
 L^2 will then enter the normalization factor*)
```

Coefficient research for the small β solution for the Quality factor of the on – axis case

```
coefficientSmall =
 0.053789097181435507 * 4 / Integrate[(z ^ 2 - 1 / 12) ^ 2, {z, -0.5, 0.5}]
```

$$38.7281$$

Coefficient research for the large β solution for the Quality factor of the on – axis case

Here we solve for the large β, looking for the coefficient. Notice that we neglect only the small terms in β for β->Infinity, but not those that are a function of z because this is not allowed before integration. We use equations (14) and (17) from Sader.

```
absE = FullSimplify[
    Abs[1 - (1 - I) * (beta / 2) ^ (1 / 2) * Exp[- (1 - I) / 2 * (beta / 2) ^ (1 / 2)] *
         Cosh[(1 - I) Sqrt[beta / 2] z]] // ComplexExpand, beta > 0];
W = Cos[B * x] - Cosh[B * x] - c * (Sin[B * x] - Sinh[B * x]);
RatioIntegrals = TrigToExp[FullSimplify[1 / 4 * Integrate[(W) ^ 2, {x, 0, L}] /
       (Integrate[D[(W), x] ^ 2, {x, 0, L}] * Integrate[absE ^ 2, {z, -1 / 2, 1 / 2}])]]
```

$$\left(0.215156\, e^{\sqrt{2}\,\sqrt{\text{beta}}}\, L^2\right) \Big/ \left(-1.41421\,\sqrt{\text{beta}} + \left(-4. + 1.41421\,\sqrt{\text{beta}}\right) e^{\sqrt{2}\,\sqrt{\text{beta}}} + e^{\frac{\sqrt{\text{beta}}}{\sqrt{2}}} \left(\left(0. + 1.41421\, i\right) \sqrt{\text{beta}} \left(e^{-\frac{i\sqrt{\text{beta}}}{\sqrt{2}}} - e^{\frac{i\sqrt{\text{beta}}}{\sqrt{2}}} \right) + 4. \left(e^{-\frac{i\sqrt{\text{beta}}}{\sqrt{2}}} + e^{\frac{i\sqrt{\text{beta}}}{\sqrt{2}}} \right) \right) \right)$$

Now we neglect (this step has been done by hand) the small terms for large Beta in the previous result and compute the coefficient:

```
coefficientLarge1 =
 (0.21515638872574203` e^(Sqrt[2] Sqrt[beta]) L^2) / (1.4142135623730951` Sqrt[beta] e^(Sqrt[2] Sqrt[beta]))
```

$$\frac{0.152139\,L^2}{\sqrt{\text{beta}}}$$

Appendix B.2. On-axis flow solution and F(β)

We now copy the results from the previous notebook and plot all the functions (eq. 17, 20, 24):

```
small = 38.73 / beta;
large = 0.1521 * (beta) ^ (1 / 2);
exact = 0.05379 * beta / IntegralExact;

IntegrandON =
  Simplify[Abs[1 - (1 - I) / 2 * Sqrt[(beta / 2)] * Cosh[(1 - I) * z * Sqrt[(beta / 2)]] /
         (Sinh[(1 - I) / 2 * Sqrt[(beta / 2)]])] // ComplexExpand, beta > 0] ^ 2;
IntegralExact = FullSimplify[Integrate[IntegrandON, {z, -1 / 2, 1 / 2}]];

LogLogPlot[{small, large, exact},
 {beta, 1, 100 000}, PlotLegends → {"Small", "Large", "Exact"},
 PlotLabel → "Quality factor", AxesLabel → {β, F[β]}, ImageSize → Large]
FindMinimum[exact, {beta, 2}]
```

```
{1.81751, {beta → 46.4348}}
```

The minimum in the Normalized quality factor in the On-axis case (only incompressible; no compressibility effect) occurs at β=46.435 and is F_{max}=1.81751.
In this case, the whole dissipation is taking place in the cantilever proper, as the on-axis problem model doesn't include any rigid lead channel: this is trustworthy because the flow is developed only after the entrance of the fluid in the cantilever, as no change in volume occurs and no flow can be developed before the cantilever proper, the vibrations of which are causing the antisymmetric flow field.

Parameters and Definitions

```
(*function to flip the axis*)
axisFlip = # /. {x_Line | x_GraphicsComplex :> MapAt[# ~ Reverse ~ 2 &, x, 1],
      x : (PlotRange → _) :> x ~ Reverse ~ 2} &;

maxz[beta_] := z /. Last[FindMaximum[{Abs[vx[x, z, beta] - vxbeam[x, z]],
       0 ≤ x ≤ Lnum / h && -1 / 2 ≤ z ≤ 1 / 2}, {x, 0}, {z, 0}]];
h = 5 * 10^-6;
f = 173 * 10^3;
omega = 2 * N[Pi, 5] * f;
Lnum = N[250 * 10^-6];
Lc = Lnum / h;
rho = 1000;
patm = 101 325;
(*I mode shape*)
B1 = 1.8751;
c = (Cos[B1 ] + Cosh[B1 ]) / (Sin[B1 ] + Sinh[B1 ]);
W[x_] = Cos[B1 * x * h] - Cosh[B1 * x * h] - c * (Sin[B1 * x * h] - Sinh[B1 * x * h]);
dW[x1_] = -c (B1 * h Cos[B1 x1 h] - B1 * h Cosh[B1 x1 h]) -
    B1 * h Sin[B1 x1 h] - B1 * h Sinh[B1 x1 h];

(*Beam displacement (u) and velocity (v)*)
A[x_] = -I omega dW[x]; (*eq 6*)
uxbeam[x_, z_] = - z dW[x]; (*Euler-Bernoulli*)
uzbeam[x_] = (W[x ]); (*Euler-Bernoulli*)
vxbeam[x_, z_] = - I omega uxbeam[x, z]; (*beam velocity, x component, eq 3*)
vzbeam[x_] = -I omega uzbeam[x]; (*beam velocity, z component, eq 3*)

(*Fluid displacement and velocity*)
M[z_, x_, beta_] =
  -A[x] Sinh[(1 - I) Sqrt[beta / 2] z] / (Sinh[(1 - I) / 2 Sqrt[beta / 2]]);
(*corrective term, eq 12*)
vx[x_, z_, beta_] = A[x] z + M[z, x, beta];
(*fluid velocity, x component, eq 13*)
vz[x_] = -I omega (W[x]); (*fluid velocity, z component, eq 13*)
ux[x_, z_, beta_] = vx[x, z, beta] / (-I omega);
(*fluid displacement, x component*)

P[x_, z_] = I rho omega h (-I omega  W[x] ) z; (*pressure, eq 9*)

(*plot setting*)
ticks =
  Charting`FindTicks[{0, 1}, {0, 1}] @@ PlotRange[Plot[x, {x, -20, 20}]][[1]];
newticks = {{Pi, Pi}, {Pi 3 / 2, Pi 3 / 2}, {Pi 3 / 4, Pi 3 / 4}, {Pi / 2, Pi / 2},
    {-Pi, -Pi}, {-Pi 3 / 2, -Pi 3 / 2}, {-Pi / 2, -Pi / 2}} ~ Join ~ ticks;
Show[Plot[x, {x, -2 Pi, 2 Pi}], Ticks → {newticks, Automatic}];
```

Beam displacement function and derivative

```
Manipulate[Plot[Im[Exp[ -I omega t] * W[x]], {x, 0, Lnum / h},
  PlotLabel → "Beam fundamental mode (displacement of beam)",
  AxesLabel → {"x[x/h]", "W(x) [m]"},
  PlotRange → {{0, Lnum / h}, {-Abs[W[Lnum / h]], Abs[W[Lnum / h]]}}] ,
 {t, 0, 5 / f, Appearance → "Labeled"}]
```

```
Manipulate[Plot[Im[Exp[- I omega t] dW[x]],
  {x, 0, Lnum / h}, PlotLabel → "Derivative of beam fundamental mode",
  AxesLabel → {"x[x/h]", "W'(x)"},
  PlotRange → {{0, Lnum / h}, {-Abs[dW[Lnum / h]], Abs[dW[Lnum / h]]}}] ,
 {t, 0, 5 / f, Appearance → "Labeled"}]
```

```
Manipulate[Plot[{Im[omega Exp[- I omega t] uxbeam[x, z]],
   Im[ Exp[- I omega t] vxbeam[x, z]]}, {t, 0, 5 / f}, PlotLabel →
   "Out-of-phase velocity and displacement for a certain x and z of beam",
  ImageSize → Large, PlotLegends → {"beam displacement", "beam velocity"}],
 {x, 0, Lnum / h}, {z, -1 / 2, 1 / 2}]
```

```
Manipulate[Plot[{Im[ Exp[- I omega t] uxbeam[x, z]],
    Im[ Exp[- I omega t] vxbeam[x, z] / omega]}, {z, -1 / 2, 1 / 2},
   PlotLabel → "Beam linear x-component of displacement and velocity",
   AxesLabel → {"a.u.", "z"}, PlotLegends → {"u_x,beam", "v_x,beam"}, PlotRange →
    {{-1 / 2, 1 / 2}, {-Abs[uxbeam[Lnum / h, 1 / 2]], Abs[uxbeam[Lnum / h, 1 / 2]]}}] //
  axisFlip, {x, 0, Lnum / h, Appearance → "Labeled"},
 {t, 0, 5 / f, Appearance → "Labeled"}]
```

```
Manipulate[Plot[{Im[Exp[-I omega t] uxbeam[x, z]] + (-1 + 2 x (h / Lnum))
      Abs[uxbeam[Lnum / h, 1 / 2]], Im[Exp[-I omega t] vxbeam[x, z] / omega] +
     (-1 + 2 x (h / Lnum)) Abs[vxbeam[Lnum / h, 1 / 2] / omega]}, {z, -1 / 2, 1 / 2},
   PlotLabel → "Beam linear x-components", AxesLabel → {"m/s", "z"},
   PlotLegends → {"u_x,beam", "v_x,beam"}, PlotRange →
    {{-1 / 2, 1 / 2}, {-Abs[uxbeam[Lnum / h, 1 / 2]], Abs[uxbeam[Lnum / h, 1 / 2]]}},
   Frame → True, AspectRatio → 1 / 5, Axes → False,
   ImagePadding → {{1, 1}, {1, Automatic}}] // axisFlip,
 {x, 0, Lnum / h, Appearance → "Labeled"},
 {t, 0, 5 / f, Appearance → "Labeled"}]
```

```
Manipulate[Plot[{Im[Exp[-I omega t] uxbeam[x, z]] + (-1 + 2 x (h / Lnum))
      Abs[uxbeam[Lnum / h, 1 / 2]], Im[Exp[-I omega t] vxbeam[x, z] / omega] +
     (-1 + 2 x (h / Lnum)) Abs[vxbeam[Lnum / h, 1 / 2] / omega]}, {z, -1 / 2, 1 / 2},
   PlotLabel → "Beam linear x-components", AxesLabel → {"m/s", "z"},
   PlotLegends → {"u_x,beam", "v_x,beam"}, PlotRange →
    {{-1 / 2, 1 / 2}, {-Abs[uxbeam[Lnum / h, 1 / 2]], Abs[uxbeam[Lnum / h, 1 / 2]]}},
   Frame → True, AspectRatio → 1 / 5, Axes → False,
   ImagePadding → {{1, 1}, {1, Automatic}}] // axisFlip,
 {x, 0, Lnum / h, Appearance → "Labeled"},
 {t, 0, 5 / f, Appearance → "Labeled"}]
```

```
Manipulate[Row[
  # & /@ {Show[Table[Plot[{i, (Im[Exp[-I omega t] * uxbeam[i, z] * 1 000 000 000] + i)},
        {z, -1 / 2, 1 / 2}, ImageSize → Medium, FrameLabel → {"x/h", "z"}] //
      axisFlip, {i, 0, Lnum / h, 10}], PlotRange →
     {{0, Lnum / h}, {-1 / 2, 1 / 2}}, Frame -> True, AspectRatio → 1 / 3],
   Show[Table[Plot[{i, (Im[Exp[- I omega t] * (ux[i, z, beta]) * 1 000 000 000] + i),
        Im[Exp[-I omega t]] * Re[(ux[i, z, beta]) * 1 000 000 000] + i,
        Re[Exp[-I omega t]] * Im[(ux[i, z, beta]) * 1 000 000 000] + i},
       {z, -1 / 2, 1 / 2}, ImageSize → Medium, Background → None, PlotRange → All] //
      axisFlip, {i, 0, Lnum / h, 10}], PlotRange → {{0, Lnum / h}, {-1 / 2, 1 / 2}},
    Frame -> True, FrameLabel → {"x/h", "z"}, AspectRatio → 1 / 3]}],
 {beta, 0.001, 100, Appearance → "Labeled"},
 {t,
  0,
  5 / f,
  AnimationRate → 1 / (50),
  RefreshRate → 0.1,
  Appearance → "Labeled"}]
```

Corrective term M(z) for the X-component of fluid velocity

```
Manipulate[Plot[{Im[Exp[- I omega t]] Re[M[z, x, beta] / Abs[vxbeam[x, -1 / 2]]],
    Re[Exp[-I omega t]] Im[M[z, x, beta] / Abs[vxbeam[x, -1 / 2]]]}, {z, -1 / 2, 1 / 2},
   AxesLabel → {"m/s", "z"}, PlotLegends → {"Re[M(z)]", "Im[M(z)]"}, PlotRange →
    {{-1 / 2, 1 / 2}, {-Abs[M[1 / 2, Lnum / h, beta] / Abs[vxbeam[x, -1 / 2]]],
      Abs[M[1 / 2, Lnum / h, beta] / Abs[vxbeam[x, -1 / 2]]]}}, PlotLabel →
    "Normalized Corrective term M(z) for the X-component of fluid velocity"] //
  axisFlip, {x, 0.0001, Lnum / h, Appearance → "Labeled"},
 {beta, 0.0001, 1000, Appearance → "Labeled"},
 {t, 0, 2 / f, Appearance → "Labeled"}]
```

X and Z-Component of fluid velocity relative to beam

```
Manipulate[Plot[
   {Im[Exp[-I omega t]] Re[(vx[x, z, beta] - vxbeam[x, z]) / Abs[vxbeam[x, -1 / 2]]],
    Re[Exp[-I omega t]] Im[(vx[x, z, beta] - vxbeam[x, z]) / Abs[vxbeam[x, -1 / 2]]],
    Im[Exp[-I omega t] (vx[x, z, beta] - vxbeam[x, z]) / Abs[vxbeam[x, -1 / 2]]],
    Re[Exp[-I omega t] vxbeam[x, z] / Abs[vxbeam[x, -1 / 2]]] +
     (-1 + 2 x (h / Lnum)) Abs[vxbeam[Lnum / h, 1 / 2] / omega]}, {z, -1 / 2, 1 / 2},
   PlotLegends → {"Real part", "Imaginary part", "Combination"},
   PlotLabel → "X-component of fluid velocity
      relative to beam velocity, normalized to wall",
   AxesLabel → {"(v_x - v_beam) / |v_wall|", "z"}, PlotRange → {{-1 / 2, 1 / 2},
     {-Abs[vx[x, maxz[1000], 1000] - vxbeam[x, maxz[1000]]] / Abs[vxbeam[x,
         maxz[1000]]], Abs[vx[x, maxz[1000], 1000] - vxbeam[x, maxz[1000]]] /
       Abs[vxbeam[x, maxz[1000]]]}}, ImageSize → Large] // axisFlip,
 {beta, 0.001, 1000, Appearance → "Labeled"}, {x, 0.0001, Lnum / h,
  Appearance → "Labeled"},
 {t, 0, 5 / f, Appearance → "Labeled"}]
```

```
Manipulate[Plot[
  {Im[Exp[-I omega t]] Re[(vx[x, z, beta] - vxbeam[x, z]) / Abs[vxbeam[x, -1 / 2]]],
   Re[Exp[-I omega t]] Im[(vx[x, z, beta] - vxbeam[x, z]) / Abs[vxbeam[x, -1 / 2]]],
   Im[Exp[-I omega t] (vx[x, z, beta] - vxbeam[x, z]) / Abs[vxbeam[x, -1 / 2]]]},
  {t, 0, 5 / f}, PlotLabel → "Out-of-phase velocity components", ImageSize → Large,
  PlotLegends → {"Re[Δ]", "Im[Δ]", "Δ"}, AxesLabel → {"time", "(vx - vbeam)/|vwall|"}],
 {x, 0.0001, Lnum / h}, {z, -1 / 2, 1 / 2}, {beta, 0.01, 1000}]

Manipulate[Row[# & /@ {VectorPlot[{Im[Exp[-I omega t]]
       Re[(vx[x, z, beta] - vxbeam[x, z]) / Abs[vxbeam[x, -1 / 2]]], 0},
     {x, 0.001, Lnum / h}, {z, -1 / 2, 1 / 2}, AspectRatio → 1 / 3, ImageSize → Large,
     Ticks → Automatic, PlotRange → {{0, Lnum / h}, {-0.5, 0.5}},
     PlotLabel → "Vector field of Real Part of fluid velocity relative
        to the beam velocity", FrameLabel → {"x/h", "z"}],
    Plot[{Im[Exp[-I omega t]] Re[(vx[x, z, beta] - vxbeam[x, z]) /
          Abs[vxbeam[x, -1 / 2]]], Re[Exp[-I omega t]]
        Im[(vx[x, z, beta] - vxbeam[x, z]) / Abs[vxbeam[x, -1 / 2]]],
       Im[Exp[-I omega t] (vx[x, z, beta] - vxbeam[x, z]) / Abs[vxbeam[x, -1 / 2]]]},
      {z, -1 / 2, 1 / 2}, PlotLegends → {"Real part", "Imaginary part",
        "Combination"}, PlotLabel → "X-component of fluid velocity
         relative to beam velocity, normalized to wall",
      AxesLabel → {"(vx - vbeam)/|vwall|", "z"}, PlotRange → {{-1 / 2, 1 / 2},
        {-Abs[vx[x, maxz[1000], 1000] - vxbeam[x, maxz[1000]]] / Abs[vxbeam[x,
            maxz[1000]]], Abs[vx[x, maxz[1000], 1000] - vxbeam[x, maxz[1000]]] /
          Abs[vxbeam[x, maxz[1000]]]}}, ImageSize → Large] // axisFlip}],
 {beta, 0.001, 1000, Appearance → "Labeled"},
 {x,
  0.0001,
  Lnum /
   h, Appearance →
   "Labeled"}, {t, 0, 5 /
   f, Appearance →
   "Labeled"}]
```

```
Manipulate[Row[# & /@ {VectorPlot[{Re[Exp[-I omega t]]
        Im[(vx[x, z, beta] - vxbeam[x, z]) / Abs[vxbeam[x, -1 / 2]]], 0},
      {x, 0.001, Lnum / h}, {z, -1 / 2, 1 / 2}, AspectRatio → 1 / 3, ImageSize → Large,
      Ticks → Automatic, PlotRange → {{0, Lnum / h}, {-0.5, 0.5}},
      PlotLabel → "Vector field of Imaginary Part of fluid velocity
         relative to the beam velocity", FrameLabel → {"x/h", "z"}],
     Plot[{Im[Exp[-I omega t]] Re[(vx[x, z, beta] - vxbeam[x, z]) /
           Abs[vxbeam[x, -1 / 2]]], Re[Exp[-I omega t]]
         Im[(vx[x, z, beta] - vxbeam[x, z]) / Abs[vxbeam[x, -1 / 2]]],
        Im[Exp[-I omega t] (vx[x, z, beta] - vxbeam[x, z]) / Abs[vxbeam[x, -1 / 2]]]},
       {z, -1 / 2, 1 / 2}, PlotLegends → {"Real part", "Imaginary part",
         "Combination"}, PlotLabel → "X-component of fluid velocity
          relative to beam velocity, normalized to wall",
       AxesLabel → {"(vx - vbeam) / |vwall|", "z"}, PlotRange → {{-1 / 2, 1 / 2},
         {-Abs[vx[x, maxz[1000], 1000] - vxbeam[x, maxz[1000]]] / Abs[vxbeam[x,
             maxz[1000]]], Abs[vx[x, maxz[1000], 1000] - vxbeam[x, maxz[1000]]] /
           Abs[vxbeam[x, maxz[1000]]]}}, ImageSize → Large] // axisFlip}],
 {beta, 0.001, 1000, Appearance → "Labeled"},
 {x,
  0.0001,
  Lnum /
   h, Appearance →
   "Labeled"}, {t, 0, 5 /
   f, Appearance →
   "Labeled"}]

Manipulate[
 Row[# & /@ {VectorPlot[{Im[Exp[-I omega t] (vx[x, z, beta] - vxbeam[x, z]) /
          Abs[vxbeam[x, -1 / 2]]], 0}, {x, 0.001, Lnum / h}, {z, -1 / 2, 1 / 2},
     AspectRatio → 1 / 3, ImageSize → Large, Ticks → Automatic,
     FrameLabel → {"x/h", "z"}, PlotRange → {{0, Lnum / h}, {-0.5, 0.5}},
     PlotLabel → "Vector field of Global fluid velocity relative
        to the beam velocity, normalized to wall velocity"],
    Plot[{Im[Exp[-I omega t]] Re[(vx[x, z, beta] - vxbeam[x, z]) /
           Abs[vxbeam[x, -1 / 2]]], Re[Exp[-I omega t]]
         Im[(vx[x, z, beta] - vxbeam[x, z]) / Abs[vxbeam[x, -1 / 2]]],
        Im[Exp[-I omega t] (vx[x, z, beta] - vxbeam[x, z]) / Abs[vxbeam[x, -1 / 2]]]},
       {z, -1 / 2, 1 / 2}, PlotLegends → {"Real part", "Imaginary part",
         "Combination"}, PlotLabel → "X-component of fluid velocity
          relative to beam velocity, normalized to wall velocity",
       AxesLabel → {"(vx - vbeam) / |vwall|", "z"}, GridLines → All, PlotRange →
        {{-1 / 2, 1 / 2}, {-Abs[vx[x, maxz[1000], 1000] - vxbeam[x, maxz[1000]]] /
           Abs[vxbeam[x, maxz[1000]]],
         Abs[vx[x, maxz[1000], 1000] - vxbeam[x, maxz[1000]]] /
          Abs[vxbeam[x, maxz[1000]]]}}, ImageSize → Large] // axisFlip}],
 {beta, 0.001, 1000, Appearance → "Labeled"},
 {x,
  0.0001,
  Lnum /
   h, Appearance →
   "Labeled"},
 {t, 0, 1 / f, Appearance → "Labeled"}
]
```

Velocity field of fluid in the beam

```
Manipulate[
 Row[# & /@ {Show[Table[Plot[{i, (Im[Exp[-I omega t] * vxbeam[i, z] * 1000] + i)}, {z,
          -1 / 2, 1 / 2}, ImageSize → Medium, FrameLabel → {"x/h", "z"}] // axisFlip,
       {i, 0, Lnum / h, 10}], PlotRange → {{0, Lnum / h}, {-1 / 2, 1 / 2}},
     Frame -> True, AspectRatio → 1 / 3],
    Show[Table[Plot[{i, (Im[Exp[- I omega t] * (vx[i, z, beta]) * 1000] + i),
         Im[Exp[-I omega t]] * Re[(vx[i, z, beta]) * 1000] + i,
         Re[Exp[-I omega t]] * Im[(vx[i, z, beta]) * 1000] + i}, {z, -1 / 2, 1 / 2},
        ImageSize → Medium, Background → None, PlotRange → All] // axisFlip,
       {i, 0, Lnum / h, 10}], PlotRange → {{0, Lnum / h}, {-1 / 2, 1 / 2}},
     Frame -> True, FrameLabel → {"x/h", "z"}, AspectRatio → 1 / 3]}],
 {beta, 0.001, 100, Appearance → "Labeled"},
 {t,
  0,
  3 / f,
  AnimationRate → 1 / (50),
  RefreshRate → 0.1,
  Appearance → "Labeled"}]

Manipulate[Plot[{Re[Exp[-I omega t] (vx[x, z, beta]) / Abs[vxbeam[x, -1 / 2]]],
    Re[Exp[-I omega t] vxbeam[x, z] / Abs[vxbeam[x, -1 / 2]]] +
     (-1 + 2 x (h / Lnum)) Abs[vxbeam[Lnum / h, 1 / 2] / omega]},
   {z, -1 / 2, 1 / 2}, PlotLegends → {"v_x(x,z)"},
   PlotLabel → "X-component of fluid velocity, normalized to wall velocity",
   AxesLabel → {"v_x / |v_wall|", "z"}, PlotRange →
    {{-1 / 2, 1 / 2}, {-Abs[vx[x, maxz[1000], 1000] - vxbeam[x, maxz[1000]]] /
       Abs[vxbeam[x, maxz[1000]]], Abs[vx[x, maxz[1000], 1000] -
         vxbeam[x, maxz[1000]]] / Abs[vxbeam[x, maxz[1000]]]}}] // axisFlip,
 {beta, 1, 100, Appearance → "Labeled"}, {x, 0.0001, Lnum / h,
  Appearance → "Labeled"},
 {t, 0, 5 / f, Appearance → "Labeled"}]
```

Normalized On-axis Dissipated Energy

```
ClearAll[dW];
dW[x_] =
  (Piecewise[{{-c * (B1 Cos[B1 x] - B1 Cosh[B1 x]) - B1 Sin[B1 x] - B1 Sinh[B1 x],
      0 <= x ≤ 1}}]);
dW1 = (-c (B1 Cos[B1 ] - B1 Cosh[B1 ]) - B1 Sin[B1 ] - B1 Sinh[B1 ]);
(*with the exact solution*)
(*Normalized Energy dissipation, integral of eq.15 *)
Edissexact = FullSimplify[Integrate[Simplify[
       Abs[1 - (1 - I) / 2 * (beta / 2) ^ (0.5) * Cosh[(1 - I) * z * (beta / 2) ^ (0.5)] /
           (Sinh[(1 - I) / 2 * (beta / 2) ^ (0.5)])] // ComplexExpand, beta > 0] ^ 2,
     {z, -0.5, 0.5}] * Integrate[(dW[x] / dW1) ^ 2, {x, 0, 1}] / beta];
(*Normalized Energy dissipation distribution, from eq.15*)
Edistrexact[x_, z_, beta_] =
  Simplify[1 / beta Abs[(1 - (1 - I) / 2 Sqrt[beta / 2] Cosh[(1 - I) Sqrt[beta / 2] z] /
         Sinh[(1 - I) / 2 Sqrt[beta / 2]])] ^ 2 (dW[x] / dW1) ^ 2];
(*values of β of which we want to plot the energy dissipation distribution*)
vecbeta = {0.01, 0.1, 1, 10, 46, 100, 1000};

Manipulate[Plot3D[Edistrexact[x, z, beta], {x, -1, 1}, {z, -1 / 2, 1 / 2},
  PlotRange → All, PlotLegends → {"Dissipated energy distribution"},
  ImageSize → Large, AxesLabel → {"x̄", "z̄"}, PlotLabel →
   "Normalized distribution of energy dissipation W_diss in the on-axis case",
  AspectRatio → 1 / 2], {beta, 0.001, 1000, Appearance → "Labeled"}]

Plot3D[Evaluate[
  Table[Edistrexact[x, z, beta], {beta, {0.01, 0.1, 1, 10, 46, 100, 1000}}]],
 {x, -1, 1}, {z, -1 / 2, 1 / 2}, Evaluated → True,
 PlotLegends → {Table["β=" <> ToString[i], {i, vecbeta}]},
 PlotRange → All, ImageSize → Large, AxesLabel → {"x̄", "z̄"},
 PlotLabel → "Normalized distribution of rate of energy
    dissipation W_diss in the on-axis case", AspectRatio → 1 / 2]

Manipulate[Plot[Edistrexact[1, z, beta], {z, -1 / 2, 1 / 2},
  PlotRange → Automatic, PlotLegends → {"Dissipated energy distribution"},
  ImageSize → Large, AxesLabel → {"z̄", "W_diss"},
  PlotLabel → "Normalized distribution of rate of energy
     dissipation W_diss in the on-axis case, at x̄=1",
  AspectRatio → 1 / 2], {beta, 0.001, 1000, Appearance → "Labeled"}]

LogPlot[Evaluate[Table[Edistrexact[1, z, beta], {beta, vecbeta}]],
 {z, -1 / 2, 1 / 2}, PlotRange → All,
 PlotLegends → {Table["β=" <> ToString[i], {i, vecbeta}]},
 ImageSize → Large, AxesLabel → {"z̄", "W_diss "},
 PlotLabel → "Normalized distribution of rate of energy dissipation
    W_diss in the on-axis case, at x̄=1 ", AspectRatio → 1 / 2]
```

Appendix B.3. Off-axis flow solution and F(β)

Parameters and Definitions

```
$Assumptions = x ∈ Reals && -LcBar ≤ x ≤ 1 &&
    LcBar > 0 && beta > 0 && alpha > 0 && L > 0 && Lc > 0 && beta ∈ Reals;
hFluidNum = 5 * 10^-6;
f = 173 * 10^3;
omega = 2 * N[Pi, 5] * f;
rho = 1000;
mu = 1 * 10^-3;

(*Scaling factors*)
us = I omega z0 dW[1] / L;
ws = (hFluid / L) us;
xs = L;
Ps = mu us L / (hFluid^2);
zs = hFluid;

(*Main Scaled functions*)
dW[x1_] = Piecewise[{{-c (B1 L Cos[B1 L x1] - B1 L Cosh[B1 L x1]) -
       B1 L Sin[B1 L x1] - B1 L Sinh[B1 L x1], 0 <= x1 ≤ 1}}];
S[x1_] = Piecewise[{{-1 + dW[x1] / dW1, 0 <= x1 ≤ 1}, {-1, -LcBar <= x1 < 0}}];
Integral1[x_] = Integrate[(I * B * S[x1] - beta) * Cos[M * (x1 + LcBar)],
    {x1, -LcBar, x}, Assumptions → x ∈ Reals && -LcBar ≤ x ≤ 1 && LcBar > 0];
Integral2[x_] = Integrate[(I * B * S[x1] - beta) * Sin[M * (1 - x1)],
    {x1, x, 1}, Assumptions → x ∈ Reals && -LcBar ≤ x ≤ 1 && LcBar > 0];
c = (Cos[B1 * L] + Cosh[B1 * L]) / (Sin[B1 * L] + Sinh[B1 * L]);
dW1 = -c (B1 L Cos[B1 L] - B1 L Cosh[B1 L]) - B1 L Sin[B1 L] - B1 L Sinh[B1 L];
B1 = 1.8751 / L;
M = Sqrt[alpha * (beta + I B)];
B = (-2 I beta Sinh[((1 - I) / 2) * Sqrt[beta / 2]]) /
    ((1 - I) * Sqrt[beta / 2] * Cosh[((1 - I) / 2) * Sqrt[beta / 2]] -
      2 Sinh[((1 - I) / 2) * Sqrt[beta / 2]]);

(*Giving some values of alpha, beta, L, Lc according to our cantilever*)
LNum = N[250 * 10^-6];
LcNum = LNum;
LcBar = Lc / L;
LcBarNum = LcNum / LNum;
cFluid = 1481;
gamaNum[L_] = (omega L / cFluid)^2;
betaNum = (rho omega hFluidNum^2) / mu + 20;
(*Notice that we can change β changing,
for instance, ρ or μ, withouth changing hFluid*)
alphaNum[L_] = gamaNum[L] / betaNum; (*α changes if β changes*)
z0Num = 0.1;
```

S(x) and B(β)

```
Plot[S[x] /. {L → LNum, Lc → LcNum}, {x, -LcBarNum, 1},
 PlotLegends → {"S(x)"}, AxesLabel → {x [adim], "S(x)"},
 PlotLabel → "S(x) for both the components of fluid velocity"]
Plot[{Norm[B], Re[B], Im[B]}, {beta, 0.01, 10000}, AxesLabel → {"β", "B(β)"},
 PlotLegends → {"|B(β)|", "Re[B(β)]", "Im[B(β)]"}, PlotLabel → "B(β) for k(z)"]
```

Compressible flow - general solution (gas)

h(x) for the Z-Component of fluid velocity

```
Part1 = -(alpha / (M * (Cos[M (1 + LcBar)]))) * Integral1[x] * Sin[M * (1 - x)];
Part2 = -(alpha / (M * (Cos[M (1 + LcBar)]))) * Integral2[x] * Cos[M * (x + LcBar)];
h = (Part1 + Part2);
```

```
(*checking the limit of h(x) for α→0(Paragraph 2.2.1)*)
hLimit = h /. {L → LNum, Lc → LcNum, beta → betaNum};
Limit[hLimit, alpha → 0, Assumptions → alpha ∈ Reals && -LcNum ≤ x ≤ 1] //
 TraditionalForm
```

$0. + 0. i$

```
Plot[{Abs[h] /. {L → LNum, Lc → LcNum, alpha → alphaNum[LNum], beta → betaNum},
  Re[h] /. {L → LNum, Lc → LcNum, alpha → alphaNum[LNum], beta → betaNum},
  Im[h] /. {L → LNum, Lc → LcNum, alpha → alphaNum[LNum], beta → betaNum}},
 {x, -LcBarNum, 1}, PlotLegends → {{"|h(x)|", "Re[h(x)]", "Im[h(x)]"},
   Placed[Grid[{{StringForm["L=`` m", LNum]},
       {StringForm["Lc=`` m", LcNum]}, {StringForm["α=``", alphaNum[LNum]]},
       {StringForm["γ=``", alphaNum[LNum] * betaNum]},
       {StringForm["β=``", betaNum]}}], {{1.05, 0.5}, {0, 0.5}}]},
 PlotLabel → "h(x) for the X-component of fluid velocity",
 AxesLabel → {x [adim], "Normalized Magnitude"},
 PlotRange → All]
```

Pressure along the channel

```
P = D[h, x] / (I * alpha); (*pressure, eq. 45*)
P2[x_, alpha_, beta_, Lc_] = P /. {L → LNum};
```

```
Plot[{Abs[P] /. {L → LNum, Lc → LcNum, alpha → alphaNum[LNum], beta → betaNum},
  Re[P] /. {L → LNum, Lc → LcNum, alpha → alphaNum[LNum], beta → betaNum},
  Im[P] /. {L → LNum, Lc → LcNum, alpha → alphaNum[LNum], beta → betaNum}},
 {x, -LcBarNum, 1}, PlotLegends → {{"|P(x)|", "Re[P(x)]", "Im[P(x)]"},
   Placed[Grid[{{StringForm["L=`` m", LNum]}, {StringForm["Lc=`` m", LcNum]},
       {StringForm["α=``", alphaNum[LNum]]}, {StringForm["γ=``", gamaNum[LNum]]},
       {StringForm["β=``", betaNum]}}], {{1.05, 0.5}, {0, 0.5}}]},
 PlotLabel → "Pressure profile along the channel",
 AxesLabel → {x [adim], "Normalized Magnitude"}]
```

f(x) for the X-Component of fluid velocity

```
f = S[x] - h;
```

f ’(x) for the Z-component of fluid velocity

```
df = D[f, x];
```

k(z) for the Z-component of fluid velocity

```
k[z_, beta_] =
  (Sinh[(1 - I) * Sqrt[beta / 2] * z] - 2 z Sinh[((1 - I) / 2) * Sqrt[beta / 2]]) /
   ((1 - I) * Sqrt[beta / 2] Cosh[((1 - I) / 2) * Sqrt[beta / 2]] -
     2 Sinh[((1 - I) / 2) Sqrt[beta / 2]]);
```

```
Plot[{Abs[k[z, beta]] /. beta → betaNum, Re[k[z, beta]] /. beta → betaNum,
  Im[k[z, beta]] /. beta → betaNum}, {z, -1 / 2, 1 / 2},
 PlotLegends → {{"|k(z)|", "Re[k(z)]", "Im[k(z)]"}, Placed[Grid[
     {{StringForm["γ=``", gamaNum[LNum]]}, {StringForm["α=``", alphaNum[LNum]]},
      {StringForm["β=``", betaNum]}}], {{1.05, 0.5}, {0, 0.5}}]},
 PlotLabel → "Function k(z) for the Z-Component of fluid velocity",
 AxesLabel → {z [adim], "Normalized Magnitude"}]
```

```
Manipulate[Plot[{Abs[k[z, beta]], Re[k[z, beta]], Im[k[z, beta]]},
  {z, -1 / 2, 1 / 2}, PlotLegends → {{"|k(z)|", "Re[k(z)]", "Im[k(z)]"},
    Placed[Grid[{{StringForm["γ=``", gamaNum[LNum]]},
       {StringForm["α=``", gamaNum[LNum] / beta]}, {StringForm["β=``", beta]}}],
     {{1.05, 0.5}, {0, 0.5}}]}, PlotLabel →
   "Function k(z) for the Z-Component of fluid velocity for several β",
  AxesLabel → {z [adim], "Normalized Magnitude"}, PlotRange → All],
 {beta, 0.0001, 1 000 000, Appearance → "Labeled"}]
```

k’(z) for the X-component of fluid velocity

```
dk[z_, beta_] = D[k[z, beta], z];
```

Incompressible flow (liquid)

General equations and Pressure plots

```
dPInc[x1_, beta_] = B * S[x1] + I beta; (*eq. 48*)
PInc[beta_, x_] = Integrate[dPInc[x1, beta], {x1, -LcBar, x},
   Assumptions → x ∈ Reals && -LcBar ≤ x ≤ 1 && LcBar > 0 && beta > 0 && beta ∈ Reals];
(* Independent of alpha, and needs to be done definite
  integral and knowing that P(-LcBar)=0 *)
```

```
Plot[{Abs[dPInc[x, beta]] /. {L → LNum, Lc → LcNum, beta → 0.0001},
  Re[dPInc[x]] /. {L → LNum, Lc → LcNum, beta → 0.0001},
  Im[dPInc[x, beta]] /. {L → LNum, Lc → LcNum, beta → 0.0001}}, {x, -LcBarNum, 1},
 PlotLegends → {{"|dPInc(x)|", "Re[dPInc(x)]", "Im[dPInc(x)]"},
   Placed[Grid[{{StringForm["L=`` m", LNum]}, {StringForm["Lc=`` m", LcNum]},
      {StringForm["α=``", alphaNum[LNum]]}, {StringForm["β=``", 0.0001]}}],
    {{1.05, 0.5}, {0, 0.5}}]}, PlotLabel →
  "Pressure Gradient along the channel for the incompressible case",
 AxesLabel → {x [adim], "Normalized Magnitude"}]
```

Asymptotic behaviour for small and large β

```
Limit[k[z, beta], beta → 0]
```

$$-\frac{z}{2}+2\,z^3$$

```
seriedk = Series[dk[z, beta], {beta, 0, 1}] // Normal
```

$$-\frac{1}{2}+6\,z^2-\frac{1}{160}\,\mathbb{i}\,\text{beta}\left(1-24\,z^2+80\,z^4\right)$$

```
Limit[dk[z, beta], beta → Infinity, Assumptions → -1 / 2 < z < 0]
Limit[dk[z, beta], beta → Infinity, Assumptions → 0 < z < 1 / 2]
```

```
0

0
```

```
f[z_] := Limit[k[z, beta], beta → Infinity]
{#, f[#]} & /@ Range[-1, 1, 1 / 10]
```

$$\left\{\{-1,\text{ComplexInfinity}\},\left\{-\frac{9}{10},\text{ComplexInfinity}\right\},\left\{-\frac{4}{5},\text{ComplexInfinity}\right\},\left\{-\frac{7}{10},\text{ComplexInfinity}\right\},\left\{-\frac{3}{5},\text{ComplexInfinity}\right\},\left\{-\frac{1}{2},0\right\},\left\{-\frac{2}{5},0\right\},\left\{-\frac{3}{10},0\right\},\left\{-\frac{1}{5},0\right\},\left\{-\frac{1}{10},0\right\},\{0,0\},\left\{\frac{1}{10},0\right\},\left\{\frac{1}{5},0\right\},\left\{\frac{3}{10},0\right\},\left\{\frac{2}{5},0\right\},\left\{\frac{1}{2},0\right\},\left\{\frac{3}{5},\text{ComplexInfinity}\right\},\left\{\frac{7}{10},\text{ComplexInfinity}\right\},\left\{\frac{4}{5},\text{ComplexInfinity}\right\},\left\{\frac{9}{10},\text{ComplexInfinity}\right\},\{1,\text{ComplexInfinity}\}\right\}$$

```
g[z_] := Limit[dk[z, beta], beta → Infinity]
{#, g[#]} & /@ Range[-1, 1, 1 / 10]
```

$$\left\{\{-1,\text{ComplexInfinity}\},\left\{-\frac{9}{10},\text{ComplexInfinity}\right\},\left\{-\frac{4}{5},\text{ComplexInfinity}\right\},\left\{-\frac{7}{10},\text{ComplexInfinity}\right\},\left\{-\frac{3}{5},\text{ComplexInfinity}\right\},\left\{-\frac{1}{2},1\right\},\left\{-\frac{2}{5},0\right\},\left\{-\frac{3}{10},0\right\},\left\{-\frac{1}{5},0\right\},\left\{-\frac{1}{10},0\right\},\{0,0\},\left\{\frac{1}{10},0\right\},\left\{\frac{1}{5},0\right\},\left\{\frac{3}{10},0\right\},\left\{\frac{2}{5},0\right\},\left\{\frac{1}{2},1\right\},\left\{\frac{3}{5},\text{ComplexInfinity}\right\},\left\{\frac{7}{10},\text{ComplexInfinity}\right\},\left\{\frac{4}{5},\text{ComplexInfinity}\right\},\left\{\frac{9}{10},\text{ComplexInfinity}\right\},\{1,\text{ComplexInfinity}\}\right\}$$

```
l[z_] := Limit[ddk[z, beta], beta → Infinity]
{#, l[#]} & /@ Range[-1, 1, 1 / 10]
```

$$\left\{\{-1, \text{ComplexInfinity}\}, \left\{-\frac{9}{10}, \text{ComplexInfinity}\right\}, \left\{-\frac{4}{5}, \text{ComplexInfinity}\right\}, \left\{-\frac{7}{10}, \text{ComplexInfinity}\right\}, \left\{-\frac{3}{5}, \text{ComplexInfinity}\right\}, \left\{-\frac{1}{2}, \left(-\frac{1-i}{\sqrt{2}}\right)\infty\right\}, \left\{-\frac{2}{5}, 0\right\}, \left\{-\frac{3}{10}, 0\right\}, \left\{-\frac{1}{5}, 0\right\}, \left\{-\frac{1}{10}, 0\right\}, \{0, 0\}, \left\{\frac{1}{10}, 0\right\}, \left\{\frac{1}{5}, 0\right\}, \left\{\frac{3}{10}, 0\right\}, \left\{\frac{2}{5}, 0\right\}, \left\{\frac{1}{2}, \frac{1-i}{\sqrt{2}}\infty\right\}, \left\{\frac{3}{5}, \text{ComplexInfinity}\right\}, \left\{\frac{7}{10}, \text{ComplexInfinity}\right\}, \left\{\frac{4}{5}, \text{ComplexInfinity}\right\}, \left\{\frac{9}{10}, \text{ComplexInfinity}\right\}, \{1, \text{ComplexInfinity}\}\right\}$$

Volumetric flux

```
q[beta_, gama_] =
  (1 + h) /. {x → -LcBarNum, Lc → LcNum, L → LNum, alpha → (gama / beta)};

GraphicsGrid[
 {{LogLogPlot[Abs[q[1, gama]], {gama, 0.01, 500}, PlotRange → Full, Frame → True,
    FrameLabel → {"γ", "Normalized volumetric flux"},
    RotateLabel → True, PlotLegends →
     {Placed[Grid[{{StringForm["β=``", 1]}}], {{0.7, 0.7}, {0, 0.5}}]}],
   LogLogPlot[Abs[q[10, gama]], {gama, 0.01, 500},
    PlotRange → Full, Frame → True, PlotLegends →
     {Placed[Grid[{{StringForm["β=``", 10]}}], {{0.7, 0.7}, {0, 0.5}}]}],
  {LogLogPlot[Abs[q[100, gama]], {gama, 0.01, 500},
    FrameLabel → {"γ", "Normalized volumetric flux"},
    PlotRange → Full, Frame → True, PlotLegends →
     {Placed[Grid[{{StringForm["β=``", 100]}}], {{0.7, 0.7}, {0, 0.5}}]}],
   LogLogPlot[Abs[q[1000, gama]], {gama, 0.01, 500}, PlotRange → Full,
    Frame → True, PlotLegends → {Placed[Grid[{{StringForm["β=``", 1000]}}],
       {{0.7, 0.7}, {0, 0.5}}]}]}}, ImageSize → Full]

Show[LogLogPlot[{Abs[q[0.001, gama]], Abs[q[0.01, gama]], Abs[q[0.1, gama]],
   Abs[q[1, gama]], Abs[q[10, gama]], Abs[q[100, gama]], Abs[q[1000, gama]]},
  {gama, 0.001, 100}, PlotRange → Full, Frame → True,
  FrameLabel → {"γ", "Normalized volumetric flux"},
  RotateLabel → True, ImageSize → Large, GridLines → All,
  PlotLegends → {"β=0.001", "β=0.01", "β=0.1", "β=1", "β=10", "β=100", "β=1000"}],
 Graphics[{Arrow[Log@{{0.01, 10^-9}, {100, 10^-(1 / 2)}}], Text["β",
    Log@{100, 10^-(1 / 2)}, BaseStyle → {Large, FontFamily → "Times", Italic}]}]]


FindMaximum[Abs[q[1000, gama]], {gama, 0.2}]
```

```
{27.0179, {gama → 0.589577}}
```

Off-axis dissipated Energy

Functions and variables

```
ClearAll[dW, S, h, dkk, c, dW1, B1, gamaNum];
h[x_, alpha_, beta_] = (Part1 + Part2);
k[z_, beta_] =
  (Sinh[(1 - I) * Sqrt[beta / 2] * z] - 2 z Sinh[((1 - I) / 2) * Sqrt[beta / 2]]) /
   ((1 - I) * Sqrt[beta / 2] Cosh[((1 - I) / 2) * Sqrt[beta / 2]] -
     2 Sinh[((1 - I) / 2) Sqrt[beta / 2]]);
dk[z_, beta_] = D[k[z, beta], z];
dkk[z_, beta_] = D[dk[z, beta], z];
gamaNum2 = 0.01;
B1 = 1.8751;
c = (Cos[B1] + Cosh[B1]) / (Sin[B1] + Sinh[B1]);
dW[x_] =
  (Piecewise[{{-c * (B1 Cos[B1 x] - B1 Cosh[B1 x]) - B1 Sin[B1 x] - B1 Sinh[B1 x],
      0 <= x ≤ 1}}]);
dW1 = (-c (B1 Cos[B1 ] - B1 Cosh[B1 ]) - B1 Sin[B1 ] - B1 Sinh[B1 ]);
S[x_] = Piecewise[{{-1 + (dW[x] / dW1), 0 <= x ≤ 1}, {-1, -1 <= x < 0}}];

firstk = -1;
lastk = 3;
vectork = Table[k, {k, firstk, lastk}];
vectorLcL = Table[j, {j, {0.01, 0.1, 0.2, 0.35, 0.5, 0.6, 1, 2, 3, 4, 5}}];
vectorj = List[0.001, 0.01, 0.1, 1, 10]; (*values of γ*)
vector = Table[Table[Table[i, {i, 10^k, 10^(k + 1), If[k ≥ 2, 10^k, 10^(k - 1)]}],
    {k, firstk, lastk, 1}], {j, vectorj}];
vector2 = Table[Table[i, {i, 10^k, 10^(k + 1), If[k ≥ 2, 10^k, 10^(k - 1)]}],
   {k, firstk, lastk, 1}];

vectorbeta = {0.001, 0.01, 0.25, 1, 10, 100, 1000}; (*values of β*)
vectorγ =
  Table[Table[Table[i, {i, 10^k, 10^(k + 1), If[k ≥ 3, 10^k, 10^(k - 1)]}],
    {k, firstk, lastk - 2, 1}], {j, vectorbeta}];
h2[x_, alpha_, beta_] = Table[h[x, alpha, beta] /. LcBar → j, {j, {j, vectorLcL}}];
S2[x_] = Table[Piecewise[{{-1 + dW[x] / dW1, 0 <= x ≤ 1}, {-1, -j <= x < 0}}],
   {j, {j, vectorLcL}}];
```

Incompressible flow

In the incompressible off-axis case the rate-of-strain tensor reduces to:

$$\mathbf{e} = \frac{i\omega z_0}{2h_{fluid}} \left.\frac{dW}{dx}\right|_{x=L} [S(\bar{x}) - h(\bar{x})]k''(\bar{z})(\hat{\mathbf{x}}\hat{\mathbf{z}} + \hat{\mathbf{z}}\hat{\mathbf{x}}) + O\left(\frac{h_{fluid}}{L}\right)$$

with h(x)=0 (in this case there are no several *γ*)!

```
EdissInc = Table[
   Table[NIntegrate[Abs[(S[x]) dkk[z, i]]^2, {x, -1, 1}, {z, -1 / 2, 1 / 2}] / (4 i),
    {i, 10^k, 10^(k + 1), If[k ≥ 2, 10^k, 10^(k - 1)]}], {k, firstk, lastk, 1}];

EdissIncRigid = Table[
   Table[NIntegrate[Abs[(S[x]) dkk[z, i]]^2, {x, -1, 0}, {z, -1 / 2, 1 / 2}] / (4 i),
    {i, 10^k, 10^(k + 1), If[k ≥ 2, 10^k, 10^(k - 1)]}], {k, firstk, lastk, 1}];
```

```
EdissIncCantilever = Table[
   Table[NIntegrate[Abs[(S[x]) dkk[z, i]]^2, {x, 0, 1}, {z, -1 / 2, 1 / 2}] / (4 i),
    {i, 10^k, 10^(k + 1), If[k ≥ 2, 10^k, 10^(k - 1)]}], {k, firstk, lastk, 1}];

EdistrInc = Table[1 / (4 i) Abs[(S[x]) dkk[z, i]]^2, {i, vectorbeta}];
```

Compressible flow

The rate-of-strain tensor (which must be integrated over the channel volume) for the off-axis compressible case is:

$$\mathbf{e} = \frac{\mathrm{i}\omega z_0}{2h_{fluid}} \left.\frac{\mathrm{d}W}{\mathrm{d}x}\right|_{x=L} [S(\bar{x}) - h(\bar{x})]k''(\bar{z})(\hat{\boldsymbol{x}}\hat{\boldsymbol{z}} + \hat{\boldsymbol{z}}\hat{\boldsymbol{x}}) + O\left(\frac{h_{fluid}}{L}\right)$$

```
EdissComp = Table[Table[Table[
      NIntegrate[Abs[(S[x] - h[x, j / i, i] /. {Lc → LcNum, L → LNum}) dkk[z, i]]^2,
        {x, -1, 1}, {z, -1 / 2, 1 / 2}] / (4 i), {i, 10^k, 10^(k + 1),
       If[k ≥ 2, 10^k, 10^(k - 1)]}], {k, firstk, lastk, 1}], {j, vectorj}];

EdissCompRigid = Table[Table[Table[
      NIntegrate[Abs[(S[x] - h[x, j / i, i] /. {Lc → LcNum, L → LNum}) dkk[z, i]]^2,
        {x, -1, 0}, {z, -1 / 2, 1 / 2}] / (4 i), {i, 10^k, 10^(k + 1),
       If[k ≥ 2, 10^k, 10^(k - 1)]}], {k, firstk, lastk, 1}], {j, vectorj}];

EdissCompCantilever = Table[Table[Table[
      NIntegrate[Abs[(S[x] - h[x, j / i, i] /. {Lc → LcNum, L → LNum}) dkk[z, i]]^2,
        {x, 0, 1}, {z, -1 / 2, 1 / 2}] / (4 i), {i, 10^k, 10^(k + 1),
       If[k ≥ 2, 10^k, 10^(k - 1)]}], {k, firstk, lastk, 1}], {j, vectorj}];

EdistrComp = Table[
   1 / (4 i) Abs[(S[x] - h[x, gamaNum2 / i, i] /. {Lc → LcNum, L → LNum}) dkk[z, i]]^2,
   {i, vectorbeta}];

EdistrCompLcL = Table[1 / (4 vectorbeta[[2]])
     Abs[(S2[x][[i]] - h2[x, gamaNum2 / vectorbeta[[2]], vectorbeta[[2]]][[i]])
        dkk[z, vectorbeta[[2]]]]^2 /.
    {LcBar → vectorLcL[[i]], L → LNum}, {i, 1, Length[vectorLcL]}];

EdistrCompLcL2 = Table[1 / (4 vectorbeta[[3]])
     Abs[(S2[x][[i]] - h2[x, gamaNum2 / vectorbeta[[3]], vectorbeta[[3]]][[i]])
        dkk[z, vectorbeta[[3]]]]^2 /.
    {LcBar → vectorLcL[[i]], L → LNum}, {i, 1, Length[vectorLcL]}];
```

Plots

Complete channel

- Distribution of energy dissipation at the walls

```
Row[# & /@ {Show[Flatten[
      {Table[Plot3D[EdistrInc[[i]], {x, -1, 1}, {z, -1 / 2, 1 / 2}, PlotRange → All,
         PlotStyle → ColorData[97][i]], {i, 1, Length[EdistrInc]}]}],
     ImageSize → Medium, AxesLabel → {"x̄", "z̄"}],
    Show[Flatten[{Table[Plot[EdistrInc[[i]] /. z → 1 / 2, {x, -1, 1}, Frame → True,
         PlotRange → All, PlotStyle → ColorData[97][i], PlotLegends →
          {Row[{"β=", ToString[If[Element[vectorbeta[[i]], Integers] == True,
               Rationalize[vectorbeta[[i]]], N[vectorbeta[[i]], 3]]]}]}],
        {i, 1, Length[EdistrInc]}]}], ImageSize → Medium, FrameLabel →
      {"x̄", "Energy"}, PlotLabel → "Normalized distribution of rate of
        energy dissipation W_diss in the off-axis incompressible case"]}]
```

Quality factor

Functions and variables

```
firstk = -1;
lastk = 3;
vectork = Table[k, {k, firstk, lastk}];
vectorLcL = Table[j, {j, {0.01, 0.1, 0.2, 0.35, 0.5, 0.6, 1, 2, 3, 4, 5}}];
vectorj = List[0.001, 0.01, 0.1, 1, 10]; (*values of γ*)
vector = Table[Table[Table[i, {i, 10^k, 10^(k + 1), If[k ≥ 2, 10^k, 10^(k - 1)]}],
    {k, firstk, lastk, 1}], {j, vectorj}];
vector2 = Table[Table[i, {i, 10^k, 10^(k + 1), If[k ≥ 2, 10^k, 10^(k - 1)]}],
   {k, firstk, lastk, 1}];

foff =
  Table[Table[Table[i / (z0Num^2 * dW1^2 * NIntegrate[Abs[(S[x] - h[x, j / i, i] /.
                {Lc → LcNum, L → LNum}) dkk[z, i]]^2, {x, -1, 1}, {z, -1 / 2, 1 / 2}]),
     {i, 10^k, 10^(k + 1), If[k ≥ 2, 10^k, 10^(k - 1)]}], {k, firstk,
     lastk, 1}], {j, vectorj}];

foffInc = Table[Table[i / (z0Num^2 dW1^2 *
       NIntegrate[Abs[(S[x]) dkk[z, i]]^2, {x, -1, 1}, {z, -1 / 2, 1 / 2}]),
    {i, 10^k, 10^(k + 1), If[k ≥ 2, 10^k, 10^(k - 1)]}], {k, firstk, lastk, 1}];

foffinfinity =
  Table[Table[i / (z0Num^2 * dW1^2 * NIntegrate[Abs[(S[x] - h[x, 1000 / i, i] /.
              {Lc → LcNum, L → LNum}) dkk[z, i]]^2, {x, -1, 1}, {z, -1 / 2, 1 / 2}]),
    {i, 10^k, 10^(k + 1), If[k ≥ 2, 10^k, 10^(k - 1)]}], {k, firstk, lastk, 1}];
```

Quality factor for same β as a function of γ at some Z0: F(γ;β)

```
h[x_, alpha_, beta_] = (Part1 + Part2);
q[beta_, gama_] = (1 + h[x, alpha, beta]) /.
    {x → -LcBarNum, Lc → LcNum, L → LNum, alpha → (gama / beta)};

firstk = -4;
lastk = 4;
vectork = Table[k, {k, firstk, lastk}];
vectorbeta = {0.001, 0.01, 0.1, 1, 10, 100, 1000};
vectorγ = Table[Table[Table[i, {i, 10^k, 10^(k + 1), If[k ≥ 3, 10^k, 10^(k - 1)]}],
    {k, firstk, lastk - 2, 1}], {j, vectorbeta}]

foffγ =
  Table[Table[Table[i / (z0Num^2 * dW1^2 * NIntegrate[Abs[(S[x] - h[x, j / i, i] /.
              {Lc → LcNum, L → LNum}) dkk[z, i]]^2, {x, -1, 1}, {z, -1 / 2, 1 / 2}]),
     {j, 10^k, 10^(k + 1), If[k ≥ 3, 10^k, 10^(k - 1)]}], {k, firstk,
     lastk, 1}], {i, vectorbeta}];

Show[Flatten[{LogLogPlot[0, {x, 0.01, 10^3}, PlotRange →
     {{10^(firstk), 10^(lastk)}, {10^-1, 10^6}}, GridLines → All], Table[Table[
     ListLogLogPlot[Transpose[{Transpose[{vectorγ[[j]], foffγ[[j]]}][[k]][[1]],
        Transpose[{vectorγ[[j]], foffγ[[j]]}][[k]][[2]]}],
      PlotStyle → ColorData[97][j], If[k == 1, PlotLegends →
        {Row[{"β=", ToString[If[Element[vectorbeta[[j]], Integers] == True,
             Rationalize[vectorbeta[[j]]], N[vectorbeta[[j]], 1]]]}]},
       Unevaluated[Sequence[]]], Joined → True], {k, 1, Length[vectork], 1}],
    {j, 1, Length[vectorbeta], 1}]}], ImageSize → Large,
 PlotLabel → "Quality factor for various β in the off-axis
     compressible case as a function of γ, Z0=" <>
   ToString[z0Num], FrameLabel → {"γ", "F(γ)"}, Frame -> True]
```

Comparison: Cantilever + Rigid + Complete for various Lc/L, changing Lc

```
ClearAll[dW, S, h, dkk, c, dW1, B1, gamaNum];
h[x_, alpha_, beta_] = (Part1 + Part2);
k[z_, beta_] =
  (Sinh[(1 - I) * Sqrt[beta / 2] * z] - 2 z Sinh[((1 - I) / 2) * Sqrt[beta / 2]]) /
   ((1 - I) * Sqrt[beta / 2] Cosh[((1 - I) / 2) * Sqrt[beta / 2]] -
     2 Sinh[((1 - I) / 2) Sqrt[beta / 2]]);
dk[z_, beta_] = D[k[z, beta], z];
dkk[z_, beta_] = D[dk[z, beta], z];
gamaNum2 = 0.01;
B1 = 1.8751;
c = (Cos[B1] + Cosh[B1]) / (Sin[B1] + Sinh[B1]);
dW[x_] =
  (Piecewise[{{-c * (B1 Cos[B1 x] - B1 Cosh[B1 x]) - B1 Sin[B1 x] - B1 Sinh[B1 x],
      0 <= x ≤ 1}}]);
dW1 = (-c (B1 Cos[B1] - B1 Cosh[B1]) - B1 Sin[B1] - B1 Sinh[B1]);

firstk = -3;
lastk = 3;
vectork = Table[k, {k, firstk, lastk}];
vectorLcL = Table[j, {j, {0.01, 0.1, 0.2, 0.35, 0.5, 0.6, 1, 4}}];
vector4 =
  Table[Table[Table[i, {i, 10^k, 10^(k + 1), If[k ≥ 2, 10^k, 10^(k - 1)]}],
    {k, firstk, lastk, 1}], {j, vectorLcL}];
```

```
h2[x_, alpha_, beta_] = Table[h[x, alpha, beta] /. LcBar → j, {j, vectorLcL}];
S2[x_] = Table[
   Piecewise[{{-1 + dW[x] / dW1, 0 <= x ≤ 1}, {-1, -j <= x < 0}}], {j, vectorLcL}];

EdissCompLcL =
  Table[Table[Table[NIntegrate[Abs[(S2[x][[j]] - h2[x, gamaNum2 / i, i][[j]] /.
            {LcBar → vectorLcL[[j]], L → LNum}) dkk[z, i]]^2,
       {x, -vectorLcL[[j]], 1}, {z, -1 / 2, 1 / 2}] / (4 i),
     {i, 10^k, 10^(k + 1), If[k ≥ 2, 10^k, 10^(k - 1)]}],
    {k, firstk, lastk, 1}], {j, 1, Length[vectorLcL]}];

EdissCompRigidLcL =
  Table[Table[Table[NIntegrate[Abs[(S2[x][[j]] - h2[x, gamaNum2 / i, i][[j]] /.
            {LcBar → vectorLcL[[j]], L → LNum}) dkk[z, i]]^2,
       {x, -vectorLcL[[j]], 0}, {z, -1 / 2, 1 / 2}] / (4 i),
     {i, 10^k, 10^(k + 1), If[k ≥ 2, 10^k, 10^(k - 1)]}],
    {k, firstk, lastk, 1}], {j, 1, Length[vectorLcL]}];

EdissCompCantileverLcL =
  Table[Table[Table[NIntegrate[Abs[(S2[x][[j]] - h2[x, gamaNum2 / i, i][[j]] /.
            {LcBar → vectorLcL[[j]], L → LNum}) dkk[z, i]]^2, {x, 0, 1},
       {z, -1 / 2, 1 / 2}] / (4 i), {i, 10^k, 10^(k + 1), If[k ≥ 2, 10^k, 10^(k - 1)]}],
    {k, firstk, lastk, 1}], {j, 1, Length[vectorLcL]}];

EdissIncLcL = Table[Table[
    Table[NIntegrate[Abs[(S2[x][[j]]) dkk[z, i]]^2, {x, -vectorLcL[[j]], 1},
       {z, -1 / 2, 1 / 2}] / (4 i), {i, 10^k, 10^(k + 1), If[k ≥ 2, 10^k, 10^(k - 1)]}],
    {k, firstk, lastk, 1}], {j, 1, Length[vectorLcL]}];

EdissIncRigidLcL = Table[Table[
    Table[NIntegrate[Abs[(S2[x][[j]]) dkk[z, i]]^2, {x, -vectorLcL[[j]], 0},
       {z, -1 / 2, 1 / 2}] / (4 i), {i, 10^k, 10^(k + 1), If[k ≥ 2, 10^k, 10^(k - 1)]}],
    {k, firstk, lastk, 1}], {j, 1, Length[vectorLcL]}];

EdissIncCantileverLcL =
  Table[Table[Table[NIntegrate[Abs[(S2[x][[j]]) dkk[z, i]]^2, {x, 0, 1},
       {z, -1 / 2, 1 / 2}] / (4 i), {i, 10^k, 10^(k + 1), If[k ≥ 2, 10^k, 10^(k - 1)]}],
    {k, firstk, lastk, 1}], {j, 1, Length[vectorLcL]}];
```

```
Show[Flatten[
  {LogLogPlot[0, {x, 0.001, 10^4}, PlotRange → {{10^firstk, 100}, {0.001, 100}},
    GridLines → All], Table[ListLogLogPlot[Transpose[
      {Transpose[{vector4[[1]], EdissIncCantileverLcL[[1]]}][[k]][[1]],
       Transpose[{vector4[[1]], EdissIncCantileverLcL[[1]]}][[k]][[2]]}],
     PlotStyle → {Dashing → Tiny, ColorData[97][1]},
     If[k == 1, PlotLegends → {Row[{"Incompressible Cantilever proper"}]},
      Unevaluated[Sequence[]]], Joined → True],
    {k, 1, Length[vectork], 1}], Table[ListLogLogPlot[
     Transpose[{Transpose[{vector4[[1]], EdissIncRigidLcL[[1]]}][[k]][[1]],
       Transpose[{vector4[[1]], EdissIncRigidLcL[[1]]}][[k]][[2]]}],
     PlotStyle → ColorData[97][2], If[k == 1, PlotLegends →
       {Row[{"Incompressible Rigid lead channel"}]}, Unevaluated[Sequence[]]],
     Joined → True], {k, 1, Length[vectork], 1}], Table[ListLogLogPlot[
     Transpose[{Transpose[{vector4[[1]], EdissCompRigidLcL[[1]]}][[k]][[1]],
       Transpose[{vector4[[1]], EdissCompRigidLcL[[1]]}][[k]][[2]]}],
     PlotStyle → ColorData[97][3], If[k == 1, PlotLegends →
       {Row[{"Compressible Rigid lead channel"}]}, Unevaluated[Sequence[]]],
     Joined → True], {k, 1, Length[vectork], 1}], Table[ListLogLogPlot[Transpose[
      {Transpose[{vector4[[1]], EdissCompCantileverLcL[[1]]}][[k]][[1]],
       Transpose[{vector4[[1]], EdissCompCantileverLcL[[1]]}][[k]][[2]]}],
     PlotStyle → {Dashing → Tiny, ColorData[97][4]},
     If[k == 1, PlotLegends → {Row[{"Compressible Cantilever proper"}]},
      Unevaluated[Sequence[]]], Joined → True],
    {k, 1, Length[vectork], 1}], Table[ListLogLogPlot[
     Transpose[{Transpose[{vector4[[1]], EdissIncLcL[[1]]}][[k]][[1]],
       Transpose[{vector4[[1]], EdissIncLcL[[1]]}][[k]][[2]]}], PlotStyle →
      Gray, If[k == 1, PlotLegends → {Row[{"Incompressible complete channel"}]},
      Unevaluated[Sequence[]]], Joined → True],
    {k, 1, Length[vectork], 1}], Table[ListLogLogPlot[
     Transpose[{Transpose[{vector4[[1]], EdissCompLcL[[1]]}][[k]][[1]],
       Transpose[{vector4[[1]], EdissCompLcL[[1]]}][[k]][[2]]}], PlotStyle →
      Black, If[k == 1, PlotLegends → {Row[{"Compressible complete channel"}]},
      Unevaluated[Sequence[]]], Joined → True],
    {k, 1, Length[vectork], 1}]}], ImageSize → Large, PlotLabel →
  "Normalized dissipated energy per unit cycle in the off-axis case, γ=" <>
   ToString[gamaNum2] <> ", L_c/L =" <>
   ToString[vectorLcL[[1]]],
 FrameLabel → {"β", "E_diss(β)"},
 Frame ->
  True]
```

Appendix B.4. Complete incompressible case

Small β limit

```
absE = FullSimplify[
    Abs[1 - (1 - I) * (beta / 2) ^ (1 / 2) * Exp[- (1 - I) / 2 * (beta / 2) ^ (1 / 2)] *
        Cosh[(1 - I) Sqrt[beta / 2] z] * (dWNorm[x]) + (Z0 I beta dWNorm1 / 2) *
        ((Sinh[(1 - I) Sqrt[beta / 2] z] / (Exp[(1 - I) / 2 * (beta / 2) ^ (1 / 2)] *
              ((1 - I) / 2 Sqrt[beta / 2]))) * S[x])] // ComplexExpand, beta > 0];
B1 = 1.8751;
c = (Cos[B1] + Cosh[B1]) / (Sin[B1] + Sinh[B1]);
dW[x_] =
  (Piecewise[{{-c * (B1 Cos[B1 x] - B1 Cosh[B1 x]) - B1 Sin[B1 x] - B1 Sinh[B1 x],
      0 <= x ≤ 1}}]);
dW1 = (-c (B1 Cos[B1 ] - B1 Cosh[B1 ]) - B1 Sin[B1 ] - B1 Sinh[B1 ]);
dWNorm[x_] = 1 / 2
   (Piecewise[{{(-c * (B1 Cos[B1 x] - B1 Cosh[B1 x]) - B1 Sin[B1 x] - B1 Sinh[B1 x]),
      0 <= x ≤ 1}}]);
dWNorm1 = 1 / 2 ((-c (B1 Cos[B1 ] - B1 Cosh[B1 ]) - B1 Sin[B1 ] - B1 Sinh[B1 ]));
S[x_] = Piecewise[{{-1 + (dW[x] / dW1), 0 <= x ≤ 1}, {-1, -1 <= x < 0}}];
largebeta = TrigToExp[
  FullSimplify[(beta / 16) / (Integrate[absE^2, {x, -1, 1}, {z, -1 / 2, 1 / 2}])]]
```

$$\left(1.11092\times 10^{46}\ \text{beta}\ e^{(1.41421+0.707107\,i)\sqrt{\text{beta}}}\right)\Big/$$
$$\Big(-1.77747\times 10^{47}\ e^{0.707107\sqrt{\text{beta}}}-1.77747\times 10^{47}\ e^{(0.707107+1.41421\,i)\sqrt{\text{beta}}}+$$
$$7.10988\times 10^{47}\ e^{(1.41421+0.707107\,i)\sqrt{\text{beta}}}+$$
$$\frac{1}{2}\,i\sqrt{\text{beta}}\ e^{(0.707107+0.707107\,i)\sqrt{\text{beta}}}\left(e^{(0.-0.707107\,i)\sqrt{\text{beta}}}-e^{(0.+0.707107\,i)\sqrt{\text{beta}}}\right)$$
$$\left(1.4604\times 10^{47}-2.76316\times 10^{47}\ Z0^2\right)+\frac{1}{2}\sqrt{\text{beta}}\ e^{(0.707107+0.707107\,i)\sqrt{\text{beta}}}$$
$$\left(-e^{-0.707107\sqrt{\text{beta}}}+e^{0.707107\sqrt{\text{beta}}}\right)\left(1.4604\times 10^{47}+2.76316\times 10^{47}\ Z0^2\right)\Big)$$

```
(*We now neglect the small terms for β going to
 Infinity (sines and cosines when imaginary unit appears)*)

flarge = (1.1109207546867656`*^46 beta e^((1.4142135623730951`+0.7071067811865476` i) Sqrt[beta])) /
    ((1 / 2) Sqrt[beta] e^((0.7071067811865476`+0.7071067811865476` i) Sqrt[beta])
      (+e^(0.7071067811865476` Sqrt[beta]))
       (1.460397230359204`*^47 + 2.7631630989866252`*^47 Z0^2)) // Chop
```

$$\frac{2.22184\times 10^{46}\sqrt{\text{beta}}}{1.4604\times 10^{47}+2.76316\times 10^{47}\ Z0^2}$$

```
(*in the case Z0=0 I get the On-Axis solution*)

FullSimplify[flarge /. Z0 → 0]
```

$$0.15214\sqrt{\text{beta}}$$

```
(*My expansion at high β*)

Numerator[flarge] / flarge[[1]] /
  Collect[Simplify[Denominator[flarge] / flarge[[1]]], Z0] // Chop
```

$$\frac{1.\sqrt{\text{beta}}}{6.57291 + 12.4364\ Z0^2}$$

Plots

Various Z0

```
(*First mode of vibration*)
B1 = 1.8751;
c = (Cos[B1] + Cosh[B1]) / (Sin[B1] + Sinh[B1]);
dW[x_] =
  (Piecewise[{{-c * (B1 Cos[B1 x] - B1 Cosh[B1 x]) - B1 Sin[B1 x] - B1 Sinh[B1 x],
      0 <= x ≤ 1}}]);
dW1 = (-c (B1 Cos[B1 ] - B1 Cosh[B1 ]) - B1 Sin[B1 ] - B1 Sinh[B1 ]);
dWNorm[x_] = 1 / 2
   (Piecewise[{{(-c * (B1 Cos[B1 x] - B1 Cosh[B1 x]) - B1 Sin[B1 x] - B1 Sinh[B1 x]),
       0 <= x ≤ 1}}]);
dWNorm1 = 1 / 2 ((-c (B1 Cos[B1 ] - B1 Cosh[B1 ]) - B1 Sin[B1 ] - B1 Sinh[B1 ]));

(*On-axis solution*)
fon = 0.05379 * beta / IntegralExact;
IntegrandON =
  Simplify[Abs[1 - (1 - I) / 2 * Sqrt[(beta / 2)] * Cosh[(1 - I) * z * Sqrt[(beta / 2)]] /
        (Sinh[(1 - I) / 2 * Sqrt[(beta / 2)]])] // ComplexExpand, beta > 0] ^ 2;
IntegralExact = FullSimplify[Integrate[IntegrandON, {z, -1 / 2, 1 / 2}]];

(*Beta range and vector for various Z0*)
z0Num = 0.1;
vectorj = Table[j, {j, {0.01, 0.1, 0.2}}];
firstk = -3;
lastk = 4;
vectork = Table[k, {k, firstk, lastk}];
vector =
  Table[Table[Table[i, {i, 10^k, 10^(k + 1), If[k >= 1, 10^k, 10^(k - 1)]}],
    {k, firstk, lastk, 1}], {j, vectorj}];
vector2 = Table[Table[i, {i, 10^k, 10^(k + 1), If[k ≥ 2, 10^k, 10^(k - 1)]}],
   {k, firstk, lastk, 1}];
```

```
(*Equations for the Incompressible solution of F(β)*)
k[z_, beta_] =
  (Sinh[(1 - I) * Sqrt[beta / 2] * z] - 2 z Sinh[((1 - I) / 2) * Sqrt[beta / 2]]) /
   ((1 - I) * Sqrt[beta / 2] Cosh[((1 - I) / 2) * Sqrt[beta / 2]] -
     2 Sinh[((1 - I) / 2) Sqrt[beta / 2]]);
dkk[z_, beta_] = D[k[z, beta], {z, 2}]; (*Second derivative of eq. 38a*)
(*Term in integral in eq. 56, Incompressible*)
IntegrandOFF[beta_] = Abs[(1 - (1 - I) / 2 * Sqrt[beta / 2] *
         Cosh[(1 - I) * z * Sqrt[beta / 2]] / (Sinh[(1 - I) / 2 * Sqrt[ beta / 2]])) *
       (dWNorm[x]) + (Z0 I beta dWNorm1 / 2) * (Sinh[(1 - I) Sqrt[beta / 2] z] /
         ((1 - I) Sqrt[beta / 2] Cosh[(Sqrt[beta / 2] (1 - I) / 2)] -
           2 Sinh[Sqrt[beta / 2] (1 - I) / 2])) * (S[x])]^2;
S[x_] = Piecewise[{{-1 + (dW[x] / dW1), 0 <= x ≤ 1}, {-1, -1 <= x < 0}}];

(*Off-axis term in eq.56, Incompressible*)
foffInc = Table[Table[i / (z0Num^2 dW1^2 *
        NIntegrate[Abs[(S[x]) dkk[z, i]]^2, {x, -1, 1}, {z, -1 / 2, 1 / 2}]),
    {i, 10^k, 10^(k + 1), If[k ≥ 2, 10^k, 10^(k - 1)]}], {k, firstk, lastk, 1}];

(*F(β) eq.56, Incompressible*)
fExact = Table[Table[Table[i / (16 *
         (NIntegrate[IntegrandOFF[i] /. {Z0 → j}, {x, -1, 1}, {z, -1 / 2, 1 / 2}])),
     {i, 10^k, 10^(k + 1), If[k >= 1, 10^k, 10^(k - 1)]}], {k,
     firstk, lastk, 1}], {j, vectorj}];

Show[Flatten[
  {LogLogPlot[{fon}, {beta, 10^firstk, 10^lastk}, PlotLegends → {"On-axis"},
    PlotStyle → Black, PlotRange → {{10^firstk, 10^lastk},
      {10^firstk, 10^(lastk + 2)}}, GridLines → {{46}, All}],
   Table[ListLogLogPlot[Transpose[{Transpose[{vector2, foffInc}][[k]][[1]],
       Transpose[{vector2, foffInc}][[k]][[2]]}],
     PlotStyle → {ColorData[97][3], Dashing → Tiny}, Joined → True, If[k == 1,
      PlotLegends → {"Off-axis (incompressible, Z0=" <> ToString[z0Num] <> ")"},
      Unevaluated[Sequence[]]]], {k, 1, Length[vectork], 1}], Table[Table[
     ListLogLogPlot[Transpose[{Transpose[{vector[[j]], fExact[[j]]}][[k]][[1]],
        Transpose[{vector[[j]], fExact[[j]]}][[k]][[2]]}],
      PlotStyle → ColorData[97][j], If[k == 1, PlotLegends →
        {Row[{"Z0=", ToString[If[Element[vectorj[[j]], Integers] == True,
            Rationalize[vectorj[[j]]], N[vectorj[[j]], 1]]]}]},
      Unevaluated[Sequence[]]], Joined → True], {k, 1, Length[vectork], 1}],
    {j, 1, Length[vectorj], 1}]}], ImageSize → Large,
 PlotLabel → "Normalized Quality factor F(β) for the
    complete incompressible flow for various Z0",
 FrameLabel → {"β", "F(β)"}, Frame -> True]
```

Various Lc/L

```
fon = 0.05379 * beta / IntegralExact;
IntegrandON =
  Simplify[Abs[1 - (1 - I) / 2 * Sqrt[(beta / 2)] * Cosh[(1 - I) * z * Sqrt[(beta / 2)]] /
        (Sinh[(1 - I) / 2 * Sqrt[(beta / 2)]])] // ComplexExpand, beta > 0] ^ 2;
IntegralExact = FullSimplify[Integrate[IntegrandON, {z, -1 / 2, 1 / 2}]];

B1 = 1.8751;
c = (Cos[B1] + Cosh[B1]) / (Sin[B1] + Sinh[B1]);
dW[x_] =
  (Piecewise[{{-c * (B1 Cos[B1 x] - B1 Cosh[B1 x]) - B1 Sin[B1 x] - B1 Sinh[B1 x],
      0 <= x ≤ 1}}]);
dW1 = (-c (B1 Cos[B1 ] - B1 Cosh[B1 ]) - B1 Sin[B1 ] - B1 Sinh[B1 ]);
dWNorm[x_] = 1 / 2
   (Piecewise[{{(-c * (B1 Cos[B1 x] - B1 Cosh[B1 x]) - B1 Sin[B1 x] - B1 Sinh[B1 x]),
      0 <= x ≤ 1}}]);
dWNorm1 = 1 / 2 ((-c (B1 Cos[B1 ] - B1 Cosh[B1 ]) - B1 Sin[B1 ] - B1 Sinh[B1 ]));
S[x_] = Table[
   Piecewise[{{-1 + (dW[x] / dW1), 0 <= x ≤ 1}, {-1, -1 <= x < 0}}], {l, vectorLcL}];
IntegrandOFFLcL[beta_] = Table[
   Abs[(1 - (1 - I) / 2 * Sqrt[beta / 2] * Cosh[(1 - I) * z * Sqrt[beta / 2]] /
         (Sinh[(1 - I) / 2 * Sqrt[ beta / 2]])) * (dWNorm[x]) +
     (Z0 I beta dWNorm1 / 2) * (Sinh[(1 - I) Sqrt[beta / 2] z] / ((1 - I) Sqrt[beta / 2]
          Cosh[(Sqrt[beta / 2] (1 - I) / 2)] - 2 Sinh[Sqrt[beta / 2] (1 - I) / 2])) *
      (S[x][[j]])] ^ 2, {j, 1, Length[vectorLcL]}];

z0Num = 0.01;
fExactLcL =
  Table[Table[Table[i / (16 * (NIntegrate[IntegrandOFFLcL[i][[j]] /. {Z0 → z0Num},
          {x, -vectorLcL[[j]], 1}, {z, -1 / 2, 1 / 2}])),
     {i, 10 ^ k, 10 ^ (k + 1), If[k ≥ 2, 10 ^ k, 10 ^ (k - 1)]}],
    {k, firstk, lastk, 1}], {j, 1, Length[vectorLcL]}];

Show[Flatten[{LogLogPlot[{fon}, {beta, 10 ^ firstk, 10 ^ lastk}, PlotStyle → Black,
    PlotRange → {{10 ^ firstk, 10 ^ lastk}, {10 ^ firstk, 10 ^ (lastk + 4)}},
    PlotLegends → {"On-axis"}, GridLines → {{46}, All}], Table[Table[
     ListLogLogPlot[Transpose[{Transpose[{vector3[[j]], fExactLcL[[j]]}][[k]][[
         1]], Transpose[{vector3[[j]], fExactLcL[[j]]}][[k]][[2]]}],
      PlotStyle → ColorData[97][j], If[k == 1, PlotLegends →
        {Row[{"Lc/L=", ToString[If[Element[vectorLcL[[j]], Integers] == True,
             Rationalize[vectorLcL[[j]]], N[vectorLcL[[j]], 1]]]}]},
       Unevaluated[Sequence[]]], Joined → True], {k, 1, Length[vectork], 1}],
    {j, 1, Length[vectorLcL], 1}], Graphics[
    {Arrow[Log@{{0.005, 100}, {0.1, 0.1}}], Text["Lc/L", Log@{0.4, 0.5},
      BaseStyle → {Large, FontFamily → "Times", Italic}]}]}],
 ImageSize → Large, PlotLabel → "Normalized Quality factor F(β) for
    the complete incompressible flow for various Lc/L, Z0=" <>
   ToString[z0Num], FrameLabel → {"β", "F(β)"}, Frame -> True]
```

Various Poisson

```
B1 = 1.8751;
c = (Cos[B1] + Cosh[B1]) / (Sin[B1] + Sinh[B1]);
dW[x_] =
  (Piecewise[{{-c * (B1 Cos[B1 x] - B1 Cosh[B1 x]) - B1 Sin[B1 x] - B1 Sinh[B1 x],
      0 <= x ≤ 1}}]);
dW1 = (-c (B1 Cos[B1 ] - B1 Cosh[B1 ]) - B1 Sin[B1 ] - B1 Sinh[B1 ]);
dWNorm[x_] = 1 / 2
   (Piecewise[{{(-c * (B1 Cos[B1 x] - B1 Cosh[B1 x]) - B1 Sin[B1 x] - B1 Sinh[B1 x]),
      0 <= x ≤ 1}}]);
dWNorm1 = 1 / 2 ((-c (B1 Cos[B1 ] - B1 Cosh[B1 ]) - B1 Sin[B1 ] - B1 Sinh[B1 ]));

fon = 0.05379 * beta / IntegralExact;
IntegrandON =
  Simplify[Abs[1 - (1 - I) / 2 * Sqrt[(beta / 2)] * Cosh[(1 - I) * z * Sqrt[(beta / 2)]] /
       (Sinh[(1 - I) / 2 * Sqrt[(beta / 2)]])] // ComplexExpand, beta > 0] ^ 2;
IntegralExact = FullSimplify[Integrate[IntegrandON, {z, -1 / 2, 1 / 2}]];

z0Num = 0.2;
vectorj = Table[j, {j, {0, 0.1, 0.25, 0.3, 0.4, 0.49}}];
firstk = -3;
lastk = 4;
vectork = Table[k, {k, firstk, lastk}];
vector =
  Table[Table[Table[i, {i, 10^k, 10^(k + 1), If[k >= 1, 10^k, 10^(k - 1)]}],
    {k, firstk, lastk, 1}], {j, vectorj}];
vector2 = Table[Table[i, {i, 10^k, 10^(k + 1), If[k ≥ 2, 10^k, 10^(k - 1)]}],
   {k, firstk, lastk, 1}];

Clear[IntegrandOFF]

k[z_, beta_] =
  (Sinh[(1 - I) * Sqrt[beta / 2] * z] - 2 z Sinh[((1 - I) / 2) * Sqrt[beta / 2]]) /
   ((1 - I) * Sqrt[beta / 2] Cosh[((1 - I) / 2) * Sqrt[beta / 2]] -
     2 Sinh[((1 - I) / 2) Sqrt[beta / 2]]);
dkk[z_, beta_] = D[k[z, beta], {z, 2}];
IntegrandOFF[beta_] =
  Abs[(1 - (1 - I) / 2 * Sqrt[beta / 2] * Cosh[(1 - I) * z * Sqrt[beta / 2]] /
        (Sinh[(1 - I) / 2 * Sqrt[ beta / 2]])) * (dWNorm[x]) +
     (z0Num I beta dWNorm1 / 2) * (Sinh[(1 - I) Sqrt[beta / 2] z] /
        ((1 - I) Sqrt[beta / 2] Cosh[(Sqrt[beta / 2] (1 - I) / 2)] -
          2 Sinh[Sqrt[beta / 2] (1 - I) / 2])) * (1 - 2 * nu) * (S[x])] ^ 2;
S[x_] = Piecewise[{{-1 + (dW[x] / dW1), 0 <= x ≤ 1}, {-1, -1 <= x < 0}}];

fExact = Table[Table[Table[i / (16 *
        (NIntegrate[IntegrandOFF[i] /. {nu → j}, {x, -1, 1}, {z, -1 / 2, 1 / 2}])),
     {i, 10^k, 10^(k + 1), If[k >= 1, 10^k, 10^(k - 1)]}], {k,
     firstk, lastk, 1}], {j, vectorj}];
```

```
Show[Flatten[{LogLogPlot[{fon}, {beta, 10^firstk, 10^lastk},
    PlotLegends → {"On-axis"}, PlotStyle → Black,
    PlotRange → {{10^firstk, 10^lastk}, {10^firstk, 10^(lastk + 2)}},
    GridLines → {{46}, All}], Table[Table[
     ListLogLogPlot[Transpose[{Transpose[{vector[[j]], fExact[[j]]}][[k]][[1]],
        Transpose[{vector[[j]], fExact[[j]]}][[k]][[2]]}],
      PlotStyle → ColorData[97][j], If[k == 1, PlotLegends →
        {Row[{"mu_c=", ToString[If[Element[vectorj[[j]], Integers] == True,
             Rationalize[vectorj[[j]]], N[vectorj[[j]], 1]]]}]},
       Unevaluated[Sequence[]]], Joined → True], {k, 1, Length[vectork], 1}],
    {j, 1, Length[vectorj], 1}]}], ImageSize → Large,
 PlotLabel → "Normalized Quality factor F(β) for the complete
    incompressible flow for various muc, Z0=0.2",
 FrameLabel → {"β", "F(β)"}, Frame -> True]
```

Appendix B.5. Complete compressible case

Variables

```
$Assumptions = x ∈ Reals && -LcBar ≤ x ≤ 1 &&
    LcBar > 0 && beta > 0 && alpha > 0 && L > 0 && Lc > 0 && beta ∈ Reals;
hFluidNum = 5 * 10^-6; (*m*)
fn = 173 * 10^3; (*Hz*)
omega = 2 * N[Pi, 5] * fn;
rho = 1000; (*kg/m^3*)
mu = 1 * 10^-3;(*Pa*s*)
```

$$x_s = L, \quad z_s = h_{fluid}, \quad u_s = \mathrm{i}\omega z_0 \left.\frac{\mathrm{d}W}{\mathrm{d}x}\right|_{x=L}, \quad w_s = \frac{h_{fluid}}{L} u_s, \quad P_s = \frac{\mu u_s L}{h_{fluid}^2}, \qquad (31)$$

```
(*Scaling factors, from equation 31*)
us = I omega z0 dW[1] / L;
ws = (hFluid / L) us;
xs = L;
Ps = mu us L / (hFluid^2);
zs = hFluid;

(*Giving some values of alpha, beta, L, Lc according to our cantilever*)
LNum = N[250 * 10^-6]; (*m*)
LcNum = LNum;
LcBar = Lc / L;
LcBarNum = LcNum / LNum;
cFluid = 1481; (*m/s*)
gamaNum[L_] = (omega L / cFluid) ^2;
betaNum = (rho omega hFluidNum^2) / mu;
alphaNum[L_] = gamaNum[L] / betaNum;(*alpha changes if beta changes*)
```

Functions

```
(*Solutions from Sader eq. 60*)
fSmallBook[beta_, Z0_] = 38.73 beta / (beta^2 + 564.6 Z0^2 (1 + (beta^2) / 8400));
fLargeBook[beta_, Z0_] = Sqrt[beta] / (6.573 + 1.718 Z0^2);
```

```
dW[x1_] = -c (B1 L Cos[B1 L x1] - B1 L Cosh[B1 L x1]) -
    B1 L Sin[B1 L x1] - B1 L Sinh[B1 L x1]; (*derivative of mode shape*)
S[x1_] = Piecewise[{{-1 + dW[x1] / dW1, 0 <= x1 ≤ 1}, {-1, -LcBar <= x1 < 0}}];
(*equation 37*)

(*Green's Method, eq 43*)
Integral1[x_] = Integrate[(I * B * S[x1] - beta) * Cos[M * (x1 + LcBar)],
    {x1, -LcBar, x}, Assumptions → x ∈ Reals && -LcBar ≤ x ≤ 1 && LcBar > 0];
Integral2[x_] = Integrate[(I * B * S[x1] - beta) * Sin[M * (1 - x1)],
    {x1, x, 1}, Assumptions → x ∈ Reals && -LcBar ≤ x ≤ 1 && LcBar > 0];

(*First mode defintions*)
c = (Cos[B1 * L] + Cosh[B1 * L]) / (Sin[B1 * L] + Sinh[B1 * L]);
dW1 = -c (B1 L Cos[B1 L] - B1 L Cosh[B1 L]) - B1 L Sin[B1 L] - B1 L Sinh[B1 L];
(*First mode derivative calculated at the tip, in x=L*)
B1 = 1.8751 / L;

M = Sqrt[alpha * (beta + I B)]; (*eq 44*)
B = (-2 I beta Sinh[((1 - I) / 2) * Sqrt[beta / 2]]) /
    ((1 - I) * Sqrt[beta / 2] * Cosh[((1 - I) / 2) * Sqrt[beta / 2]] -
      2 Sinh[((1 - I) / 2) * Sqrt[beta / 2]]); (*eq. 38b*)

(*I split eq.43 in two parts*)
Part1 = -(alpha / (M * (Cos[M (1 + LcBar)]))) * Integral1[x] * Sin[M * (1 - x)];
Part2 = -(alpha / (M * (Cos[M (1 + LcBar)]))) * Integral2[x] * Cos[M * (x + LcBar)];
h[x_, alpha_] = (Part1 + Part2);
ClearAll[dW, S, c, dW1, dW, B1];

(*First mode defintions*)
B1 = 1.8751;
c = (Cos[B1] + Cosh[B1]) / (Sin[B1] + Sinh[B1]);
dW[x_] =
  (Piecewise[{{-c * (B1 Cos[B1 x] - B1 Cosh[B1 x]) - B1 Sin[B1 x] - B1 Sinh[B1 x],
      0 <= x ≤ 1}}]); (*First mode derivative*)
dW1 = (-c (B1 Cos[B1 ] - B1 Cosh[B1 ]) - B1 Sin[B1 ] - B1 Sinh[B1 ]);
(*First mode derivative calculated at the tip, in x=L*)

dWNorm[x_] = 1 / 2
    (Piecewise[{{(-c * (B1 Cos[B1 x] - B1 Cosh[B1 x]) - B1 Sin[B1 x] - B1 Sinh[B1 x]),
      0 <= x ≤ 1}}]); (*First mode derivative, normalized*)
dWNorm1 = 1 / 2 ((-c (B1 Cos[B1 ] - B1 Cosh[B1 ]) - B1 Sin[B1 ] - B1 Sinh[B1 ]));
S[x_] = Piecewise[{{-1 + (dW[x] / dW1), 0 <= x ≤ 1}, {-1, -1 <= x < 0}}];
(*equation 37*)

(*Term in the integral of denominator of eq.56a*)
IntegrandOFF[beta_] =
  Abs[-I (1 - (1 - I) / 2 * Sqrt[beta / 2] * Cosh[(1 - I) * z * Sqrt[beta / 2]] /
          (Sinh[(1 - I) / 2 * Sqrt[ beta / 2]])) * (dWNorm[x]) +
      (Z0 I beta dWNorm1 / 2) * (Sinh[(1 - I) Sqrt[beta / 2] z] /
          ((1 - I) Sqrt[beta / 2] Cosh[(Sqrt[beta / 2] (1 - I) / 2)] -
            2 Sinh[Sqrt[beta / 2] (1 - I) / 2])) * (S[x] - h[x, alpha])]^2;

(*vectorj is used to compute solutions for several Z0, or Lc/L.
   vector defines the beta range*)
vectorj = Flatten[List[0, 0.01, 0.1, 0.2]];
vector =
  Table[Table[Table[i, {i, 10^k, 10^(k + 1), If[k >= 1, 10^k, 10^(k - 1)]}],
    {k, -3, 4, 1}], {j, vectorj}];
```

```
(*Solution in the compressible case, for various Z0, Lc/L=1*)
fExact =
  Table[Table[Table[i / (16 * ( NIntegrate[IntegrandOFF[i] /. {Lc → LcNum, L → LNum,
            Z0 → j, alpha → (gamaNum[LNum] / i)}, {x, -1, 1}, {z, -1 / 2, 1 / 2}])),
     {i, 10^k, 10^(k + 1), If[k >= 1, 10^k, 10^(k - 1)]}], {k, -3,
     4, 1}], {j, vectorj}];

(*Solution in the compressible case, for various Z0, Lc=0*)

fExactLc0 =
  Table[Table[Table[i / (16 * ( NIntegrate[IntegrandOFF[i] /. {Lc → 0, L → LNum,
            Z0 → j, alpha → (gamaNum[LNum] / i)}, {x, -1, 1}, {z, -1 / 2, 1 / 2}])),
     {i, 10^k, 10^(k + 1), If[k >= 1, 10^k, 10^(k - 1)]}], {k, -3,
     4, 1}], {j, vectorj}];
```

Plots

Various Z0

```
plot = Show[Flatten[
    {LogLogPlot[0, {x, 0.001, 10^4}, PlotRange → {{0.001, 10^3}, {0.0001, 400}},
      GridLines → {{46}, All}, PlotLegends →
       {Placed[Grid[{{StringForm["γ=``", NumberForm[gamaNum[LNum], 3]]}}],
         {{0.8, 0.9}, {1, 1}}]}], Table[Table[ListLogLogPlot[
       Transpose[{Transpose[{vector[[j]], fExact[[j]]}][[k]][[1]],
         Transpose[{vector[[j]], fExact[[j]]}][[k]][[2]]}],
       PlotStyle → ColorData[97][j], If[k == 1, PlotLegends → {Row[{"Z0=",
            ToString[If[Element[vectorj[[j]], Integers] == True || vectorj[[j]] ==
                0, Rationalize[vectorj[[j]]], N[vectorj[[j]], 1]]]}]},
        Unevaluated[Sequence[]]], Joined → True], {k, 1, 8, 1}],
     {j, 1, Length[vectorj], 1}], Graphics[
     {Arrow[Log@{{0.01, 100}, {10, 0.001}}], Text["Z0", Log@{3, 0.001},
       BaseStyle → {Large, FontFamily → "Times", Italic}]}]}],
  ImageSize → Large, PlotLabel → "Normalized Quality factor F(β)
     for the complete compressible flow, Lc=L",
  FrameLabel → {"β", "F(β)"}, Frame -> True]
```

Various Lc/L

```
(*on-axis solution*)
fon = 0.05379 * beta / IntegralExact;
IntegrandON =
  Simplify[Abs[1 - (1 - I) / 2 * Sqrt[(beta / 2)] * Cosh[(1 - I) * z * Sqrt[(beta / 2)]] /
        (Sinh[(1 - I) / 2 * Sqrt[(beta / 2)]])] // ComplexExpand, beta > 0] ^ 2;
IntegralExact = FullSimplify[Integrate[IntegrandON, {z, -1 / 2, 1 / 2}]];

z0Num = 0.1;

(*Definition of beta range*)
firstk = -3;
lastk = 4;
vectork = Table[k, {k, firstk, lastk}];
vectorLcL = Table[j, {j, {0, 0.001, 0.01, 0.5, 1, 3, 4, 5, 10, 50}}];
(*Vector of various Lc/L*)
vector3 = Table[Table[Table[i, {i, 10^k, 10^(k + 1), If[k ≥ 2, 10^k, 10^(k - 1)]}],
    {k, firstk, lastk, 1}], {j, vectorLcL}];

(*Functions to compute for various Lc/L*)
h2[x_, alpha_, beta_] = Table[h[x, alpha] /. LcBar → j, {j, vectorLcL}];
dW[x_] =
  (Piecewise[{{-c * (B1 Cos[B1 x] - B1 Cosh[B1 x]) - B1 Sin[B1 x] - B1 Sinh[B1 x],
      0 <= x ≤ 1}}]);
dW1 = (-c (B1 Cos[B1 ] - B1 Cosh[B1 ]) - B1 Sin[B1 ] - B1 Sinh[B1 ]);
B1 = 1.8751;
c = (Cos[B1] + Cosh[B1]) / (Sin[B1] + Sinh[B1]);
S2[x_] = Table[Piecewise[{{-1 + dW[x] / dW1, 0 <= x ≤ 1}, {-1, -LcBar <= x < 0}}] /.
    LcBar → j, {j, vectorLcL}];
dWNorm[x_] = 1 / 2 (Piecewise[{{(-c * (B1 Cos[B1 x] - B1 Cosh[B1 x]) -
        B1 Sin[B1 x] - B1 Sinh[B1 x]), 0 <= x ≤ 1}}]);
dWNorm1 = 1 / 2 ((-c (B1 Cos[B1 ] - B1 Cosh[B1 ]) - B1 Sin[B1 ] - B1 Sinh[B1 ]));

(*Term in the integral of denominator of eq.56a, compressible*)
IntegrandLcL[beta_] =
  Table[Abs[(1 - (1 - I) / 2 * Sqrt[beta / 2] * Cosh[(1 - I) * z * Sqrt[beta / 2]] /
          (Sinh[(1 - I) / 2 * Sqrt[ beta / 2]])) * (dWNorm[x]) +
      (Z0 I beta dWNorm1 / 2) * (Sinh[(1 - I) Sqrt[beta / 2] z] / ((1 - I) Sqrt[beta / 2]
          Cosh[(Sqrt[beta / 2] (1 - I) / 2)] - 2 Sinh[Sqrt[beta / 2] (1 - I) / 2])) *
       (S2[x][[j]] - h2[x, alpha, beta][[j]])] ^ 2, {j, 1, Length[vectorLcL]}];

(*Term in the integral of denominator of eq.56a, incompressible*)
IntegrandLcLOFF[beta_] =
  Table[Abs[(1 - (1 - I) / 2 * Sqrt[beta / 2] * Cosh[(1 - I) * z * Sqrt[beta / 2]] /
          (Sinh[(1 - I) / 2 * Sqrt[ beta / 2]])) * (dWNorm[x]) +
      (Z0 I beta dWNorm1 / 2) * (Sinh[(1 - I) Sqrt[beta / 2] z] / ((1 - I) Sqrt[beta / 2]
          Cosh[(Sqrt[beta / 2] (1 - I) / 2)] - 2 Sinh[Sqrt[beta / 2] (1 - I) / 2])) *
       (S2[x][[j]])] ^ 2, {j, 1, Length[vectorLcL]}];

(*Solution in the compressible case, for various Lc/L*)
fExactLcL = Table[Table[Table[
      i / (16 * (NIntegrate[IntegrandLcL[i][[j]] /. {L → LNum, Z0 → z0Num, alpha →
            (gamaNum[LNum] / i)}, {x, -vectorLcL[[j]], 1}, {z, -1 / 2, 1 / 2}])),
      {i, 10^k, 10^(k + 1), If[k ≥ 2, 10^k, 10^(k - 1)]}], {k, firstk,
      lastk, 1}], {j, 1, Length[vectorLcL]}];
```

```
(*Solution in the incompressible case, for various Lc/L*)
fExactLcLOFF = Table[Table[Table[
      i / (16 * (NIntegrate[IntegrandLcLOFF[i][[j]] /. {L → LNum, Z0 → z0Num, alpha →
                (gamaNum[LNum] / i)}, {x, -vectorLcL[[j]], 1}, {z, -1 / 2, 1 / 2}])),
      {i, 10^k, 10^(k + 1), If[k ≥ 2, 10^k, 10^(k - 1)]}], {k, firstk,
      lastk, 1}], {j, 1, Length[vectorLcL]}];

Show[Flatten[{LogLogPlot[0, {x, 0.001, 10^6},
     PlotRange → {{10^firstk, 10^lastk}, {10^-2, 400}},
     GridLines → {{46}, All}, PlotLegends →
      {Placed[Grid[{{StringForm["γ=``", NumberForm[gamaNum[LNum], 3]]}}],
        {{0.8, 0.9}, {1, 1}}]}], LogLogPlot[{fon}, {beta, 10^firstk, 10^lastk},
     PlotLegends → {"On-axis"}, PlotStyle → {Black, Dashing[Large]},
     PlotRange → {{10^firstk, 10^lastk}, {10^-2, 400}},
     GridLines → {{46}, All}], Table[Table[ListLogLogPlot[
       Transpose[{Transpose[{vector3[[j]], fExactLcL[[j]]}][[k]][[1]],
         Transpose[{vector3[[j]], fExactLcL[[j]]}][[k]][[2]]}],
       PlotStyle → ColorData[97][2 j + 1], If[k == 1, PlotLegends →
         {Row[{"Lc/L=", ToString[If[Element[vectorLcL[[j]], Integers] == True,
              Rationalize[vectorLcL[[j]]], N[vectorLcL[[j]], 1]]]}]},
        Unevaluated[Sequence[]]], Joined → True], {k, 1, Length[vectork], 1}],
    {j, {1, 5, 6, 7, 8}}]}], ImageSize → Large, PlotLabel →
  "Normalized Quality factor F(β) for the complete
     compressible flow for various Lc/L, Z0=" <>
   ToString[z0Num], FrameLabel → {"β", "F(β)"}, Frame -> True]
```

Appendix B.6. COMSOL shape fitting

Mode shape functions

```
(*coefficients for the various mode numbers*)
```

$\lambda_n = \beta_n L = 1.8751, 4.6941, 7.8548, (2n-1)\pi/2.$

```
Bn[n_] = (2 n - 1) Pi / 2; (*good for n≥4,
excellent for n→Infinity, Villanueva's Book*)
N[Bn[3]]
```

```
7.85398
```

```
solidrho = 2329;
fluidrho = 1000;
hcant = 12 * 10^-6;
hfluid = 8 * 10^-6;
bcant = 33 * 10^-6;
bfluid = 16 * 10^-6;
Lcant = 204 * 10^-6;
factor =
 N[(solidrho / fluidrho) (hcant / hfluid) (bcant / bfluid) (Lcant / hfluid)^2]
```

```
4685.27
```

```
B1 = 1.8751;
c = (Cos[B1] + Cosh[B1]) / (Sin[B1] + Sinh[B1]);
W[x_] =
  Piecewise[{{Cos[B1 * x] - Cosh[B1 * x] - c * (Sin[B1 * x] - Sinh[B1 * x]), 0 ≤ x ≤ 1}}];
dW = D[W[x], x];
ddW[x_] = D[W[x], {x, 2}];
Plot[dW, {x, 0, 1}]
```

```
cn = (Cos[Bn[n]] + Cosh[Bn[n]]) / (Sin[Bn[n]] + Sinh[Bn[n]]);
Wn[x_, n_] = Piecewise[{{Cos[Bn[n] * x] -
       Cosh[Bn[n] * x] - cn * (Sin[Bn[n] * x] - Sinh[Bn[n] * x]), 0 ≤ x ≤ 1}}];
ddWn[x_, n_] = D[Wn[x, n], {x, 2}];
dWn[x_, n_] = D[Wn[x, n], x];
```

Change the number in Wn[x,n] and plot the mode shape for each mode number.

```
Plot[Wn[x, 1], {x, 0, 1}]
```

```
(*fitting*)
imported1 =
  {{{0.`, 0.`}, {0.233333333333348`, 6.75737430212296`*^-7}, {0.466666666666696`,
     1.34741167038904`*^-6}, {0.700000000000045`, 2.01575736350017`*^-6},
    {0.952380952381001`, 2.87365026625964`*^-6}, {1.20476190476195`,
     3.83994324543282`*^-6}, {1.45714285714291`, 4.93013338525173`*^-6},
    {1.72857142857147`, 6.25992617824391`*^-6}, {2.00000000000003`,
     7.76130951979302`*^-6}, {2.2714285714286`, 9.44285488683282`*^-6},
    {2.56190476190477`, 0.0000114483343499893`},
    {2.85238095238094`, 0.0000136709988171308`},
    {3.14285714285711`, 0.0000161144699220895`}, {3.45238095238092`,
     0.0000189629170293671`}, {3.76190476190473`, 0.0000220650458757644`},
    {4.07142857142855`, 0.0000254223739718898`}, {4.39999999999997`,
```

Appendix B.7. Fluid density and viscosity fitting

```
(*fit for density and viscosity of fluid)

data = {{0.99823, 1.005}, {1.0221, 1.31}, {1.0469, 1.76}, {1.0727, 2.5},
   {1.0993, 3.72}, {1.1263, 6.}, {1.1538, 10.8}, {1.1675, 15.2},
   {1.173, 17.7}, {1.18125, 22.5}, {1.19485, 35.5}, {1.2085, 60.1},
   {1.2218, 109.}, {1.2351, 219.}, {1.2377, 259.}, {1.24035, 310.},
   {1.243, 367.}, {1.2456, 437.}, {1.24825, 523.}, {1.2508, 624.},
   {1.25335, 765.}, {1.2559, 939.}, {1.2585, 1150.}, {1.26108, 1410.}};

f[x_] = Exp[FindFormula[{#[[1]], Log[#[[2]]]} & /@ data, x]]

(*E^(0.0182879-2.93441 Cot[4.68 x])*)

{xmin, xmax} = MinMax[data[[All, 1]]];

Plot[f[x], {x, xmin, xmax},
 Epilog → {Red, AbsolutePointSize[6], Point[data]}, Frame → True,
 FrameLabel → (Style[#, Bold, 14] & /@ {"Density [g/cm^3]", "Viscosity [mPas]"}),
 PlotRange → All]

viscosity = Table[f[i], {i, 0.99, 1.26, 0.0001}];
density = Table[i, {i, 0.99, 1.26, 0.0001}];
Transpose[{viscosity, density}];
```

List of Symbols

A_c Beam cross section area

α Fluid compressibility number (dimensionless)

λ, μ_b Bulk viscosity

B_1 First vibrational mode coefficient for a clamped beam

β Reynold's number (dimensionless)

b_c Cantilever beam width

b_f Channel width

$\frac{D}{Dt}$ Material derivative

δ Dissipation term in Q definition

$\partial\Omega^+$ Top channel boundary

E_s Dissipative energy scaling factor

E Internal energy per unit mass of a material element of fluid

$E_{diss/cycle/volume}$ Dissipated energy per unit volume per cycle in the resonator

E_{stored} Stored energy in the resonator

$\bar{\bar{e}}$ Fluid rate-of-strain tensor

$\bar{u}$ x-velocity

F_{on} On-axis normalized quality factor

$F(\beta)$ Normalized Quality Factor

$\tilde{f}$ Complex eigenfrequency in COMSOL

f Eigenfrequency in COMSOL

ϕ, $\mathbf{\Phi}$ Viscous dissipation function

∇ Nabla operator

γ Fluid normalized acoustic wavenumber (dimensionless)

h_c Cantilever beam thickness

h_f Channel thickness

i, j Imaginary unit

L_c Rigid lead channel length

L Vibrating channel length

M On-axis corrective flow term

ν Poisson's ratio

ν_f Kinematic viscosity

Ω Fluidic channel domain

P_s Pressure scaling factor

$\bar{P}$ Scaled fluid pressure

P Fluid pressure

Q_{off} Off-axis Quality Factor

Q_{on} On-axis Quality Factor

Q_{tot} Total Quality Factor

q_s Volumetric flux normalizing factor

q Volumetric flux

ρ_c Beam density

ρ_f Fluid density

σ_{ij} Fluid stress tensor

T Period of vibration

t Time variable

U Fourier transform of vertical beam velocity

μ Fluid dynamic viscosity

$\mathbf{u_b}$ Cantilever beam displacement vector

$\bar{u}$ Fluid scaled velocity x-component

u_s x-velocity scaling factor

$\mathbf{V}$ Reduced velocity

$\mathbf{v_b}$ Cantilever beam velocity vector

$\mathbf{v_{inv}}$ On-axis inviscid flow solution

W_{kin} Beam kinetic energy

W Cantilever beam displacement

ω_n Angular eigenfrequency of beam vibration of mode n

ω Angular frequency of vibration

$\bar{w}$ Fluid scaled velocity z-component

w_s z-velocity scaling factor

$\tilde{X}(x, z; \omega)$ Fourier Transform of the generic function X(x,z,t)

$\bar{x}$ Scaled x-coordinate

x_0 Local point of Taylor Series expansion

x_s x-coordinate scaling factor

$\bar{z}$ Scaled z-coordinate

z_0 Off-axis placement of the channel with respect to the beam neutral axis

z_s z-coordinate scaling factor

Bibliography

[1] Comsol documentation (online).

[2] Comsol multiphysics reference manual, version 5.3", comsol, inc, www.comsol.com.

[3] Comsol user's guide.

[4] Homogenizing viscous materials.

[5] G. P. Association. *Physical properties of glycerine and its solutions*. Glycerine Producers' Association, 1963.

[6] R. e. a. Bashir. Single virus particle mass detection using microresonators with nanoscale thickness. *Applied Physics Letters*, 84:1976–1978, 2004.

[7] G. K. Batchelor. *An Introduction to Fluid Dynamics*. Cambridge Mathematical Library. Cambridge University Press, 2000.

[8] O. A. Bauchau and J. I. Craig. *Euler-Bernoulli beam theory*, pages 173–221. Springer Netherlands, Dordrecht, 2009.

[9] T. Braun, V. Barwich, M. K. Ghatkesar, A. H. Bredekamp, C. Gerber, M. Hegner, and H. P. Lang. Micromechanical mass sensors for biomolecular detection in a physiological environment. *Phys. Rev. E*, 72:031907, Sep 2005.

[10] T. Burg and S. Manalis. Suspended microchannel resonators for biomolecular detection. *Applied Physics Letter*, 83:2698–2700, 2003.

[11] T. P. Burg, A. R. Mirza, N. Milovic, C. H. Tsau, G. A. Popescu, J. S. Foster, and S. R. Manalis. Vacuum-packaged suspended microchannel resonant mass sensor for biomolecular detection. *Journal of Microelectromechanical Systems*, 15(6):1466–1476, Dec 2006.

[12] T. P. Burg and others. Weighing of biomolecules, single cells and single nanoparticles in fluid. *Nature*, 446:1066–1069, 2007.

[13] S. Carrara. *Biochemistry of Targets and Probes*, pages 29–51. Springer New York, New York, NY, 2013.

[14] J. Chaste, A. Eichler, J. Moser, G. Ceballos, R. Rurali, and A. Bachtold. A nanomechanical mass sensor with yoctogram resolution. 7:301–4, 04 2012.

[15] P. G. e. a. Datskos. Cantilever transducers as a platform for chemical and biological sensors. *Review of Scientific Instruments*, 75:2229–2253, 2004.

[16] M. del Rey, R. A. da Silva, D. Meneses, D. F. Petri, J. Tamayo, M. Calleja, and P. M. Kosaka. Monitoring swelling and deswelling of thin polymer films by microcantilever sensors. *Sensors and Actuators B: Chemical*, 204:602 – 610, 2014.

[17] P. Enoksson, G. Stemme, and E. Stemme. Fluid density sensor based on resonance vibration. *Sensors and Actuators A: Physical*, 47(1):327 – 331, 1995.

[18] M. Evans. Methods of Mathematical Physics, 2005.

[19] R. M. Fratila, S. G. Mitchell, P. del Pino, V. Grazu, and J. M. de la Fuente. Strategies for the biofunctionalization of gold and iron oxide nanoparticles. *Langmuir*, 30(50):15057–15071, 2014. PMID: 24911468.

[20] C. P. Green and J. E. Sader. Torsional frequency response of cantilever beams immersed in viscous fluids with applications to the atomic force microscope. *Journal of Applied Physics*, 92(10):6262–6274, 2002.

[21] B. Ilic, H. G. Craighead, S. Krylov, W. Senaratne, C. Ober, and P. Neuzil. Attogram detection using nanoelectromechanical oscillators. *Journal of Applied Physics*, 95(7):3694–3703, 2004.

[22] A. Keivani and V. Lotfi. An effective method for eigen-problem solution of fluid-structure systems. *Computational Methods in Civil Engineering*, 3(2):1–14, 2012.

[23] N. V. Lavrik and P. G. Datskos. Femtogram mass detection using photothermally actuated nanomechanical resonators. *Applied Physics Letters*, 82(16):2697–2699, 2003.

[24] R. Lifshitz and M. L. Rouke. Thermoelastic damping in micro- and nanomechanical systems. *Phys. Rev. B*, 61:5600–5609, 2000.

[25] A. Manickam, C. A. Johnson, S. Kavusi, and A. Hassibi. Interface design for cmos-integrated electrochemical impedance spectroscopy (eis) biosensors. *Sensors*, 12(11):14467–14488, 2012.

[26] M. B. Panchal. Boron nitride nanotube as a nano-mechanical biosensor: A computational approach. *Biosensors Journal*, 0(0):–, 2015.

[27] F. Petronetto, A. Paiva, M. Lage, G. Tavares, H. Lopes, and T. Lewiner. Meshless helmholtz-hodge decomposition. *IEEE Transactions on Visualization and Computer Graphics*, 16(2):338–349, March 2010.

[28] R. Raiteri, H.-J. Butt, and M. Grattarola. Changes in surface stress at the liquid/solid interface measured with a microcantilever. *Electrochimica Acta*, 46(2):157 – 163, 2000.

[29] A. Ricci and E. Giuri. Fsi analysis of microcantilevers vibrating in fluid environment. *Proceedings of the COMSOL Conference 2009*, 2009.

[30] J. E. Sader. Frequency response of cantilever beams immersed in viscous fluids with applications to the atomic force microscope. *Journal of Applied Physics*, 84:1066–1069, 1998.

[31] J. E. Sader, T. P. Burg, et al. Energy dissipation in microfluidic beam resonators: Effect of poisson's ratio. *Physical Review E*, 84, 2011.

[32] J. E. Sader, T. P. Burg, and S. R. Manalis. Energy dissipation in microfluidic beam resonators. *J. Fluid Mech*, 650:215–250, 2010.

[33] J. E. Sader, J. Lee, and S. R. Manalis. Energy dissipation in microfluidic beam resonators: Dependence on mode number. *Journal of Applied Physics*, 108, 2010.

[34] S. Schmid, L. G. Villanueva, and M. L. Roukes. *Fundamentals of Nanomechanical Resonators*. Springer Publishing Company, Incorporated, 1st edition, 2016.

[35] J. Tamayo, A. Humphris, A. Malloy, and M. Miles. Chemical sensors and biosensors in liquid environment based on microcantilevers with amplified quality factor. *Ultramicroscopy*, 86(1):167 – 173, 2001. Proceedings of the second International Conference on Scanning.

[36] J. Tamayo, P. M. Kosaka, J. J. Ruz, A. San Paulo, and M. Calleja. Biosensors based on nanomechanical systems. *Chem. Soc. Rev.*, 42:1287–1311, 2013.

[37] Y. T. Yang, C. Callegari, X. L. Feng, K. L. Ekinci, and M. L. Roukes. Zeptogram-scale nanomechanical mass sensing. *Nano Letters*, 6(4):583–586, 2006. PMID: 16608248.

[38] D. J. Young, C. A. Zorman, and M. Mehregany. *MEMS/NEMS Devices and Applications*, pages 225–252. Springer Berlin Heidelberg, Berlin, Heidelberg, 2004.

[39] I. Yunus, A. Kurniawan, D. Adityawarman, and A. Indarto. Nanotechnologies in water and air pollution treatment. 1:136–148, 09 2012.